The Effect of Oil Supply on Piston-ring Lubrication in an Internal Combustion Engine

Jost Institute for Tribotechnology

Graham Calderbank

A thesis submitted in partial fulfillment for the requirements for the degree of
Doctor of Philosophy at the University of Central Lancashire

5th February, 2019

uclan
University of Central Lancashire
School of Engineering

uclan
University of Central Lancashire
School of Engineering

Student Declaration Form

Type of award: Doctor of Philosophy

School: School of Engineering

Concurrent registration for two or more academic awards

I declare that while registered as a candidate for the research degree, I have not been a registered candidate or enrolled student for another award of the University or other academic or professional institution.

Material submitted for another award

I declare that no material contained in the thesis has been used in any other submission for an academic award and is solely my own work.

Collaboration

No collaboration.

Use of a Proof-reader

No proof-reading service was used in the compilation of this thesis.

Signature of Candidate ______________________________

Print name: Graham Calderbank

The Effect of Oil Supply on Piston-ring Lubrication in an Internal Combustion Engine

Graham Calderbank

Abstract

A drive for efficiency and tightening emissions legislation are imposing increasing constraints on the piston-ring lubrication of large marine internal combustion engines, motivating engine manufacturers to invest in improved lubricating systems. In order to enable a new generation of systems to be developed more understanding is needed of the interaction between lubricant supply, oil-film thickness, and the development of the lubricant film on the cylinder liner.

The methods used for delivering lubricant to the ring pack in large marine diesel engines are focussed on improvements in timing, metering, and spread, but there is still a reliance on lubricant transport to distribute lubricant to many areas of the cylinder liner away from the area of injected lubricant. With corrosive and abrasive wear being consequences of inadequately balancing the lubrication needs of the piston-rings, it is important to understand how lubricant supply influences oil-film thickness and lubricant transport both near to, and more distant from the area of injected lubricant.

To address these issues a test apparatus has been developed to allow delivery of a metered dose of lubricant to selected regions of the cylinder. Capacitance based transducers were used to measure oil-film thickness over a number of cycles as the lubricant film develops. Investigations into the response of the lubricating film following a change in lubricant supply were conducted, and a method of evaluating the rate at which lubricant is transported using oil-film thickness data has been devised, and used to map lubricant transport on the liner at a number of lubricant supply rates. A two-dimensional piston-ring lubrication model has been developed and validated, with oil-film thickness predictions within 30% of experimental data in the top half of the stroke. The model is capable of predicting the development of the lubricant film over a number of cycles following the delivery of a non-uniform oil-film to the cylinder.

Oil-film thickness has been observed to follow a first order response with time constants in the range 10 to 20 seconds (20 to 40 cycles) following a change in lubricant feed-rate. The response is due to circumferential lubricant transport, and follows a fast response resulting from axial lubricant transport. The time constant is not dependent on lubricant supply but does vary over the stroke. By characterising the relationship between oil-film thickness and lubricant injector feed-rate a system model for oil-film thickness as function of lubricant supply can be determined allowing an oil-film thickness control system to be developed and reducing risk of over- and under-lubricating during fuel switching. The lower limit of lubricant supply before the onset of corrosive wear or scuffing can be found leading to reductions in oil consumption.

Keywords: Piston-ring, lubrication, lubricant supply, internal combustion engine, marine engine, lubricant consumption.

Contents

1 Introduction **1**
- 1.1 Motivation for the Study . . . 1
- 1.2 Aims and Objectives of the Study . . . 3
- 1.3 Structure of Thesis . . . 4
- 1.4 Original Contributions of the Research . . . 6

2 Literature Survey **8**
- 2.1 Introduction . . . 8
- 2.2 Relevance and Justification . . . 8
  - 2.2.1 The Impact of Gaseous Emissions from Marine Engines on a Global Scale 9
  - 2.2.2 Methods Proposed to Reduce Emissions from Marine Engines . . . 13
  - 2.2.3 Summary . . . 18
- 2.3 Piston-ring and Ring-pack Lubrication in Large Two-stroke Engines . . . 18
  - 2.3.1 The Function of Piston-rings and the Ring Pack . . . 18
  - 2.3.2 Common Piston-ring Types in Modern Marine Diesel Engines . . . 19
  - 2.3.3 Influence of Piston-rings on Engine Performance . . . 21
  - 2.3.4 Lubrication Systems in Large Two-stroke Engines . . . 24
- 2.4 Marine Engine Lubricants . . . 26
  - 2.4.1 The Function of Low-speed Engine Lubricants . . . 26
  - 2.4.2 Lubricant Types Used in Marine Diesel Engines . . . 28
  - 2.4.3 Additives for Improving Various Aspects of Lubricant Performance . . . 29
  - 2.4.4 Categorisation of Marine Cylinder Lubricants . . . 31
  - 2.4.5 Evolution and Development of Marine Lubricants . . . 32
- 2.5 Oil-film Thickness Measurement . . . 34
  - 2.5.1 The Tribological Significance of Oil-film Thickness . . . 34
  - 2.5.2 Measurement of Oil-film Thickness . . . 36
  - 2.5.3 Commercially Available Oil-film Thickness Sensors . . . 40
- 2.6 Summary . . . 41

3 Piston-ring Lubrication - Theory and Modelling **44**
- 3.1 Introduction . . . 44
- 3.2 Hydrodynamic Lubrication Theory . . . 44
  - 3.2.1 Steady, Laminar Flow between Parallel Plates - Couette and Poiseuille Flow 46
  - 3.2.2 Starvation and Cavitation . . . 49
  - 3.2.3 Assumptions and Simplifications . . . 50
  - 3.2.4 Initial Lubricant-film Distribution . . . 51
- 3.3 Numerical Modelling of Hydrodynamic Lubrication . . . 53
  - 3.3.1 Flow-continuity Algorithm . . . 55
  - 3.3.2 Equilibrium of Forces . . . 60
  - 3.3.3 Crank-angle Stepping . . . 63
  - 3.3.4 Minimum Oil-film Thickness Algorithm . . . 63
  - 3.3.5 Implementation . . . 65
- 3.4 Summary . . . 72

4 Development of Experimental Apparatus 74
4.1 Introduction . . . 74
4.2 Rationale . . . 74
  4.2.1 Large Two-stroke Marine Engines . . . 74
  4.2.2 Scaling of the Experimental Apparatus . . . 75
  4.2.3 Motored Conditions . . . 76
  4.2.4 Isolating the Cylinder Lubrication . . . 76
  4.2.5 The Ring Pack . . . 77
  4.2.6 Lister-Petter TR1 Experimental Engine . . . 77
4.3 Dynamic Similarity . . . 77
  4.3.1 Viscosity Selection . . . 77
  4.3.2 Surface Roughness of Piston-ring and Cylinder . . . 81
4.4 Lubricant Injection System . . . 85
  4.4.1 Lubricant Injector Flow-rate Requirements . . . 85
  4.4.2 Lubricant Flow Rate Validation . . . 86
  4.4.3 Lubricant Distribution . . . 89
  4.4.4 Lubricant Injection Control . . . 89
4.5 Engine Modifications . . . 91
4.6 Oil-film Thickness Measurement . . . 94
  4.6.1 Transducer Specification . . . 94
  4.6.2 Transducer Positioning . . . 97
  4.6.3 Transducer Quality . . . 98
  4.6.4 Transducer Calibration . . . 100
4.7 Summary . . . 103

5 The Effects of Spray Lubrication on Piston-ring Oil-film Thickness 113
5.1 Introduction . . . 113
5.2 Method . . . 113
5.3 Capacitance based oil-film thickness transducer results . . . 115
  5.3.1 Oil-film thickness results at top and bottom dead centres . . . 118
  5.3.2 Minimum Oil-film Thickness . . . 122
  5.3.3 Film Extent . . . 123
5.4 Result Verification Using Video Footage . . . 132
5.5 Discussion . . . 134
5.6 Conclusions . . . 136

6 The Influence of Lubricant Injection Volume and Time on Oil-film Thickness Development 138
6.1 Introduction . . . 138
6.2 Method . . . 138
6.3 Results . . . 139
  6.3.1 Minimum Oil-film Thickness . . . 139
6.4 Transient Response Characterisation . . . 146
  6.4.1 Evaluation of System Time Constant . . . 146
  6.4.2 Periodic Effects . . . 149
  6.4.3 Initial Oil-film Thickness, H . . . 152
6.5 Discussion . . . 154
6.6 Conclusions . . . 157

7 Axial and Radial Oil-transport in the Cylinder 158
7.1 Introduction . . . 158
7.2 Method . . . 158
7.3 Results . . . 160
  7.3.1 Minimum Oil-film Thickness . . . 160
  7.3.2 Evaluating the Rate of Lubricant Transport . . . 164
  7.3.3 Result Verification Using Film Extent . . . 166
  7.3.4 Result Verification Using Video Footage . . . 168
7.4 Discussion . . . 171
7.5 Conclusions . . . 174

8 Validating a Model for Oil-film Thickness Development 175
8.1 Introduction 175
8.2 Method 175
8.3 Validation of Piston-ring Lubrication Model 176
  8.3.1 Minimum Oil-film Thickness 176
  8.3.2 Starvation and Cavitation 182
8.4 Discussion 186
8.5 Conclusions 189

9 Conclusions and Recommendations for Further Work 190
9.1 Introduction 190
9.2 Achievement of Aims 191
9.3 Conclusions 192
9.4 Further Work 194
  9.4.1 Experimental Research 194
  9.4.2 Computational Research 196

Appendices A1

A Finite Difference Expressions in Full A2
A.1 Finite difference expressions for conservation of mass: hydrodynamic pressure and degree of filling A2

B Engineering Drawings B1
B.1 Transducer Grinding Clamp B2
B.2 Drilling of Holes for Transducers B4
B.3 Hall Effect Trigger Bracket B5

C Specification Sheets C1
C.1 Signal Amplifier Datasheet C2
C.2 Epoxy Resin Datasheet C4
C.3 Formlabs Grey Datasheet C6

List of Figures

1.1 Variations in hydrodynamic pressure on the piston-ring face due to non-uniform lubricant distribution leading to circumferential lubricant flow 2
1.2 Block diagram of a typical feedback control system, where h_0 is the minimum oil-film thickness, and the subscripts d and m represent the demand and measured minimum oil-film thickness values, and q_{ave} is the average injector flow-rate per cycle. 3

2.1 Carbon emission levels for the four major freight transport modes (Penner et al., 2000) 9
2.2 Estimated annual transport related emissions of C0_2, NO$_x$, SO$_2$ and 10um Particulate Matter, and fuel consumption, in Tg (1 Tg $= 1 \times 10^{12}$ g $= 1$ Mt) for the year 2000 (Eyring et al., 2007) 10
2.3 Global temperature response due to shipping emissions with and without sulphur dioxide (Fuglestvedt et al., 2009) 11
2.4 Temperature change due to emissions from transport sectors in the period from 1900 to 2100, using the four scenarios for future emissions taken from Skeie et al. (2009) 12
2.5 Cardiopulmonary mortality attributable to ship PM$_{2.5}$ emissions (Corbett et al., 2007) 13
2.6 SOx emissions by fuel type (Corbett and Winebrake, 2008) - IFO 380 and IFO 180 are bunker fuels, MGO is marine gas oil, and DMB and DMC are marine diesel oils. 15
2.7 Speed reduction vs. reduction of CO$_2$ emissions for each scenario using different fuel prices (Corbett et al., 2009). 17
2.8 Ramsbottom type piston rings with square butts (a), and angle or scarf butts (b) . . 20
2.9 Double Lap joint on Man B&W 'Controlled Pressure Relief' Piston-ring 21
2.10 Pressure Relief Grooves on the Running Face of Man B&W's 'Controlled Pressure Relief' Ring 21
2.11 The Stribeck curve – showing the variation in friction coefficient with the quantity $\eta U/W$ for a lubricated sliding bearing, where η is viscosity, U is sliding speed and W is the normal load (Hutchings, 1992). 22
2.12 Cutaway of a Cylinder Liner showing the Zigzag Lubricating Grooves 24
2.13 An example of clover leafing on a cylinder liner. The positions where oil is injected have been highlighted (Bhushan, 2001b). 27
2.14 Types of mineral oils: a) straight paraffin, b) branched paraffin, c) naphthene, d) aromatic (Lansdown, 2004). 29
2.15 Regimes of lubrication as a function of oil film thickness to composite r.m.s. surface roughness, λ (Bhushan and Gupta, 1991; Hutchings, 1992) 34
2.16 Fully-flooded (a) and starved (b) piston ring, both cases show cavitation at the trailing edge. 37

3.1 Oil-film thickness parameters, where $b =$ ring-face height, $h =$ distance from cylinder liner to ring-face, $h_0 =$ minimum oil-film thickness, $q =$ lubricant flow-rate, $R =$ ring-face radius, $U =$ piston-ring speed. 45
3.2 A typical hydrodynamic pressure distribution under a piston-ring. 45
3.3 Pressure and viscous forces on an incompressible control volume ($ABCD$) within a flow between flat, parallel plates (Douglas, 2005) 47
3.4 Oil-film thickness parameters, where $b =$ ring-face height, $h =$ distance from cylinder liner to ring-face, $h_0 =$ minimum oil-film thickness, $q =$ lubricant flow-rate, $R =$ ring-face radius, $U =$ piston-ring speed. 49

3.5 Schematic diagram of lubricant spray onto cylinder liner 52
3.6 Cell area normal to lubricant spray vector 53
3.7 Initial oil-film distribution on cylinder liner 54
3.8 Computational mesh definition and notation 54
3.9 Finite difference cell showing co-ordinate, dimensions, and flow-rate terms through each face. 59
3.10 Major forces acting on the piston-ring 62
3.11 Computational flowchart 64
3.12 Grid dependency check against load capacity 66
3.13 Grid dependency check against lubricant flow-rate 66
3.16 Comparison of flow-continuity model with Purday's empirical relationship 72
3.17 Comparison of flow-continuity algorithm against solution of Reynolds equation ($h_{oil} = 2\mu$m, $U = 0.32$ m/s, $\eta = 0.25$ Pa.s) 73

4.1 Cross-section of a typical marine diesel crosshead engine (Leduc, 2001) 75
4.2 Dynamic viscosity test results 81
4.3 Raw Talysurf measurement profile of top piston-ring face 83
4.4 Band-pass filtered Talysurf measurement profile of top piston-ring face 83
4.5 Raw Talysurf measurement profile of cylinder surface 84
4.6 Band-pass filtered Talysurf measurement profile of cylinder surface 84
4.7 Cross-section of SL-43 injector (Lincoln-Industrial, 2002) 86
4.8 Diagram of the injection system circuit 87
4.9 Average injection volumes for injectors 1 to 4. Error bars indicate 95% confidence level 88
4.10 Calibration charts for injectors 1 to 4 88
4.11 Distribution of lubricant on cylinder liner 89
4.12 Schematic of microcontroller circuit 90
4.13 Hall-effect sensor, and trigger bracket fitted to engine flywheel 90
4.14 Replacement cylinder head assembly 92
4.15 Engine mounted in the dynamometer cell 93
4.16 Replacement cylinder head assembly with lubricant injectors fitted 93
4.17 Transducer located in the cylinder liner with schematic of the intrumentation hardware 94
4.18 Cross-section of oil-film thickness transducer 96
4.19 Sensor numbers described by their block number and axial location 97
4.20 Images of oil-film thickness transducers post-honing 99
4.21 Calibration of channels on amplifier A 101
4.22 Calibration of channels on amplifier B 102
4.23 Cross-section of transducer showing offset distance - here the electrode is recessed 103
4.24 White light interferometer scan of sensor I-1, with axial and circumferential cross-sections through the electrode 104
4.25 White-light inteferometer scans of sensor replicas 1 to 8 for block I 106
4.25 White-light inteferometer scans of sensor replicas 1 to 8 for block I 107
4.25 White-light inteferometer scans of sensor replicas 1 to 8 for block I 108
4.26 White-light inteferometer scans of sensor replicas 1 to 8 for block II 110
4.26 White-light inteferometer scans of sensor replicas 1 to 8 for block II 111
4.26 White-light inteferometer scans of sensor replicas 1 to 8 for block II 112

5.1 Location of lubricant and transducers on the cylinder liner, with transducer numbers being described by their block number and axial location 114
5.2 Measured vs simulated signals (fully flooded) : flow-rate 0.04 ml inj^{-1}, sensor II-4, upstroke 116
5.3 Measured vs simulated signals (starved) : flow-rate 0.04 ml inj^{-1}, sensor I-4, upstroke 116
5.4 Measured vs simulated signal with spatial coordinates on the horizontal axis . . . 117
5.5 The simulated signal is produced by accounting for partial coverage of the electrode by the piston-ring 118
5.6 Sensor 8 : Piston-ring signals for sensor at bottom dead centre 119
5.7 Sensor 8 : Piston-ring signals showing contact and cavitation at the bottom dead centre transducer 120

5.8 Sensor 8 : Piston-ring signal for sensor at bottom dead centre on 50th Cycle showing a step change in signal output in the absence of lubricant 120
5.9 Sensor 8 : Piston-ring signal for transducer at bottom dead centre showing oscillatory signal during contact with the piston-ring 122
5.10 Minimum oil-film thickness on upstrokes at sensor I-4 during tests at four lubricant injector flow-rates 124
5.11 Minimum oil-film thickness on downstrokes at sensor II-4 during tests at four lubricant injector flow-rates (film thicknesses with $\lambda < 3$ are likely to involve metal to metal contact (Hutchings, 1992) 124
5.12 Film extent at sensor I-4 on selected upstrokes 125
5.13 Film extent at sensor II-4 on selected upstrokes 125
5.14 Experimental inlet and cavitation boundaries taken on the upstrokes at 5 cycle intervals 126
5.15 Experimental inlet and cavitation boundaries taken on the downstrokes at 5 cycle intervals 126
5.16 Minimum oil-film thickness on upstroke and downstrokes at sensors I-4 and II-4 (31.2mm from top dead centre) : Flow-rate = 0.04 ml inj^{-1} 127
5.17 The scraping mechanism of the lubricant volume exceeding that which can be consumed past the piston-ring 128
5.18 Experimental inlet and cavitation boundaries taken at 5 cycle intervals for (a) upstroke and (b) downstroke 129
5.19 Minimum oil-film thickness on upstroke and downstrokes at sensor II-5 (58.5 mm from top dead centre) 130
5.20 Comparison of experimental inlet and cavitation boundaries on upstroke and downstroke taken at 5 cycle intervals for both injector flow-rates 131
5.21 Video stills: Flow-rate = 0.04 ml inj^{-1} 132
5.22 Graphs of minimum oil-film thickness vs time at sensors I-3 to I-6 133
5.23 Graphs of minimum oil-film thickness vs time at sensors II-3 to II-6 133

6.2 Effect of flow-rate on oil-film thickness - Sensor II-4 : Period = 3. The markers indicate the cycles on which lubricant is injected into the cylinder. 145
6.3 Oil-film thickness at maximum and minimum average flow-rates - Sensor II-4 . . . 146
6.4 Comparison of oil-film thickness result with a first order exponential system response to a step input 147
6.5 Determination of time constant at transducers II-4 and II-6 148
6.6 Time constant in seconds evaluated at transducer II-4, II-5, and II-6 over a range of average injector flow-rates 149
6.7 Periodic oil-film thickness oscillations at sensor IV-4 in response to periodic lubricant injection 150
6.8 Periodic effects at different axial positions (period = 10) 151
6.9 Periodic effects at different circumferential locations (period = 10) 151
6.10 Factors affecting the magnitude of oil-film thickness oscillations at transducer IV-4 152
6.11 Upstroke inlet and cavitation boundaries taken every cycle : Flow-rate = 0.04 ml inj^{-1} 152
6.12 Comparison of oil-film at the highest and lowest average lubricant injector flow-rates, at transducers I-6 and II-4 153
6.13 Development of lubricant film thickness on the cylinder liner 154
6.14 Lubricant film control volume 155

7.1 Location of lubricant injection and sensors 159
7.2 Upstroke minimum oil-film thickness around the cylinder liner at sensor S6, for lubricant injection with a period = 3 161
7.3 Minimum oil-film thickness development at a number of axial and circumferential locations : Flow-rate 0.04 ml inj^{-1} : Period = 3 162
7.4 Minimum oil-film thickness development at a number of axial and circumferential locations : Flow-rate 0.08 ml inj^{-1} : Period = 3 162
7.5 Noisy measurements of minimum oil-film thickness at sensor II-4 resulting from contact between piston-ring and cylinder liner 163
7.6 A more typical oil-film thickness signal at II-4 as lubricant becomes available . . . 163
7.7 Ring signals at S4: Flow-rate = 0.04 ml inj^{-1}, Period = 3 166

7.8 Ring signals at S4: Flow-rate = 0.08 ml inj^{-1}, Period = 3 167
7.9 Ring signals for sensor V-4: Flow-rate = 0.08 ml inj^{-1}, Period = 3 169
7.10 Video stills: Flow-rate = 0.04 ml inj^{-1}, Period = 3 170
7.11 Video stills: Flow-rate = 0.08 ml inj^{-1}, Period = 3 170
7.12 Map of lubricant transport : Flow-rate 0.04 ml inj^{-1} : Period = 3 171
7.13 Map of lubricant transport : Flow-rate 0.08 ml inj^{-1} : Period = 3 172
7.14 Scatter plot of time taken for lubricant to reach a transducer against the inverse of the lubricant coverage parameter 173

8.1 Distribution of lubricant following injection event at flow-rate 0.04 ml inj^{-1} 176
8.2 Time-variation of minimum oil-film thickness on upstrokes at axial transducer positions 2 to 8 (dashed = predictions, solid = experimental) 177
8.3 Time-variation of minimum oil-film thickness on downstrokes at transducer positions 2 to 8 (dashed = predictions, solid = experimental) 177
8.4 Thickness of the lubricant film on the cylinder liner following each labelled cycle a lubricant injector flowrate of 0.04 ml/rev and injection period = 3 179
8.5 Upstroke and downstroke oil-film thickness at transducers II-3 and II-4, for a lubricant injector flow-rate 0.01 ml inj^{-1} 180
8.6 Simulated lubricant transport at the axial location of sensors 3 to 7 181
8.7 Simulated lubricant flow past the leading and trailing edge of the piston-ring (sensor position II-4, flow-rate 0.01 ml inj^{-1}). The inset shows oil-film thickness on the 4th and 8th cycles, to highlight the rapid change in oil-film thickness near midstroke, leading to squeeze effects as the lubricant film develops 183
8.8 Comparison of upstroke inlet and cavitation boundaries taken at 5 cycle intervals at transducers II-4 and II-5 184
8.9 Degree of filling showing the increased area of piston-ring generating hydrodynamic pressure at the location of sensor 4, at a lubricant injector flow-rate 0.01 ml/rev . . 185
8.10 Degree of filling showing the increased area of piston-ring generating hydrodynamic pressure at the location of sensor 5, at a lubricant injector flow-rate 0.01 ml/rev . . 185
8.11 Degree of filling showing the increased area of piston-ring generating hydrodynamic pressure at the location of sensor 4, at a lubricant injector flow-rate 0.01 ml/rev . . 186
8.12 Comparison of first and second order models to experimental results 188

A.1 Oil-film thickness parameters, where $b =$ ring-face height, $h =$ distance from cylinder liner to ring-face, $h_0 =$ minimum oil-film thickness, $q =$ lubricant flow-rate, $R =$ ring-face radius, $U =$ piston-ring speed. A2

List of Tables

2.1 Technical data for Castrol cylinder oils (Castrol, 2013; Castrol, 2017; Castrol, 2014) 31
2.2 Capacitive sensor data for Micro Epsilon transducers (Micro-Epsilon, 2012) 43

3.1 Summary of Couette flow terms in different regions of the domain 59
3.2 Summary of Poiseuille flow terms in different regions of the domain 59
3.3 Principle of mass conservation 60
3.4 Coefficients of the flow continuity equations 61

4.1 Engine parameters for the Lister-Petter TR1 (Lister-Petter, 2011) 77
4.2 Dimensions of variables which affect oil-film thickness 78
4.3 Physical properties of Castrol Magnatec Stop-Start 5W-20 E engine lubricant (Castrol, 2015) 80
4.4 Comparison of the similarity parameter at different stages of the engine cycle . . . 80
4.5 Viscometer data for Motaquip 20W-50 mineral oil 81
4.6 Average injection quantity at each setting for the 4 injectors 86
4.7 Approximate lubricant flow-rates 87
4.8 Mechanical and thermal properties for Formlabs Grey (FormLabs, 2017) 96
4.9 Relationships between transducer voltage and oil-film thickness (in μm) on each amplifier channel 100
4.10 Post-experiment sensor offsets (μm) 103

5.1 Lister-Petter TR1 engine geometry and operating conditions (Lister-Petter, 2011) . 115
5.2 Ratio of electrode area between calibrating transducer and installed transducers (A_{cal}/A_n) 117

6.1 Evaluated time constants at transducers II-3, II-4, II-5, and II-6, for injector periods of 3, 6, and 10. 148

7.1 Offset values for sensor I-4 and II-4 164
7.2 Timing (in seconds) of lubricant availability based on oil-film thickness changes - flow-rate 0.04ml inj^{-1} 165
7.3 Timing (in seconds) of lubricant availability based on oil-film thickness changes - flow-rate 0.08ml inj^{-1} 165
7.4 Timing of lubricant availability based on piston-ring signals - flow-rate 0.04ml inj^{-1} 168
7.5 Timing of lubricant availability based on piston-ring signals - flow-rate 0.08ml inj^{-1} 168

Acknowledgements

There are many people who have supported me through the duration of this project, who have all helped enormously in many different ways. First and foremost, though, I would like to extend my gratitude to Ian Sherrington and Ted Smith for helping to guide me, encourage me, and also to shape me since I started on this journey. Thank you also to Rob Wallace and the School of Engineering for funding me throughout, I fully appreciate your extended support.

I would also like to thank several members of my close family for being patient with me, for supporting me when the intensity rose, and for ensuring that I persevered to the end. So Nik, mum, dad, Sonya, and several others including Isabella and Sebi - thank you from the bottom of my heart.

A big thank you is also warranted for Matt Dickinson, for being my sounding board and for sharing the journey - even if mine was a touch longer. Equally, an important thank you is warranted for Simon Hindle, Dennis Boyle, Martin Holmes, Duncan Taylor, Phil Spence and Mark Grundy, for technical advice, helping with the manufacture of components and systems for the experimental engine, and for assisting with the testing itself.

Mark Dempsey deserves gratitude for helping me to escape and clear my head on countless weekends throughout, the value of being able to unwind and step back from the project is not to be underestimated.

Many other colleagues and students also deserve a big thank you for tolerating me when my focus was more on this project rather than yours.

—

Nomenclature

Roman Nomenclature

b	Axial height of compression ring
C_b	Nominal radial clearance between piston and cylinder liner
d	Nominal cylinder bore diameter
F_e	Load due to ring elasticity
F_g	Gas pressure load
F_z	Hydrodynamic load
F_{tb}	Axial force due to boundary friction
F_{th}	Axial force due to viscous friction
g	Switch variable
h	Oil-film thickness
h_0	Minimum oil-film thickness
h_{oil}	Lubricant film thickness
i, j	Computational loop counters for grid location
l	Connecting-rod length
N	Rotational frequency of engine
n_x	Number of cells in the axial direction
n_y	Number of cells in the circumferential direction
p	Pressure
p_l	Pressure at the leading edge of the piston-ring
p_t	Pressure at the trailing edge of the piston-ring
p_{in}	Pressure at the inlet boundary
p_{out}	Pressure at the cavitation boundary

q	Flow-rate
q^c	Couette flow
q^p	Poiseuille flow
q_{ave}	Average flow-rate
R	Radius of curvature of ring face
r	Crank radius
R_a	Arithmetic average roughness
R_b	Nominal cylinder bore radius
R_q	Root mean squared average roughness
t	Time
U	Axial velocity
V	Circumferential velocity
w_0	Radial velocity (initial)
w_h	Radial velocity (final)
x	Axial co-ordinate
y	Circumferential co-ordinate
z	Radial co-ordinate

Greek Nomenclature

η	Lubricant viscosity
γ	Relaxation factor for oil-film thickness adjustment
λ	Lambda ratio for lubrication regimes
λ_1	Relaxation factor for oil-film thickness adjustment
λ_2	Relaxation factor for Euler scheme
μ	Friction coefficient
ω	Angular velocity of crank-shaft
ϕ	Crank angle
ρ	Lubricant density
τ	System time constant
θ	Degree of filling

List of Abbreviations

ASTM	American Society for Testing and Materials
BHP	Brake horsepower
EU	European Union
IMO	International Maritime Organisation
MEP	Mean effective pressure
MGO	Marine gas oil
OFT	Oil-film thickness
PM	Particulate matter
SAE	Society of Automotive Engineers
SECA	Sulphur Emissions Control Area
TBN	Total base number
UNFCCC	United Nations Framework Convention on Climate Change

Chapter 1

Introduction

1.1 Motivation for the Study

The internal combustion engine has been used to power commercial marine vessels for over 100 years. While there was originally a contest between the adoption of four-stroke and two-stroke diesel engines, the success of the latter was boosted in the 1950's by the the adoption of turbochargers with increased efficiency, and soon after cemented by the increasing availability of cylinder lubricants capable of neutralising the acidic combustion products from the burning of cheaper and lower grade bunker fuels (Woodyard, 2004).

Sixty years on and the merchant fleet is still growing ([Anon], 2017). In the intervening period, two-stroke marine engines have undergone significant development. For a long time large marine diesel engines have adopted a crosshead configuration, with a stuffing box to isolate the cylinder from the crankcase, engine speeds have since been reduced to allow direct coupling to propellors of increased efficiencies. Engine size has also increased, the most powerful engines have stroke to bore ratios greater than 4, bore sizes of over a metre, up to 14 cylinders, mean effective pressures of almost 20 bar, combustion pressures of around 150 bar, and power ratings nearing 100 MW (Woodyard, 2004).

Since the turn of the century the lubrication of the piston-rings in large, two-stroke marine diesel engines has been subjected to increasingly challenging constraints. Developments in engine design, and the desire for higher efficiency and lower fuel consumption, has led to longer stroke lengths and larger bores. This, along with the slow engine speeds employed in this type of large engine have led to increasingly high combustion pressures, and high temperatures for longer portions of the stroke (Woodyard, 2004). Additionally, ”slow steaming” has been used to address rising fuel costs, resulting in increased corrosion due to condensation of combustion gases.

In addition, the desire of the operators is to use cheaper bunker fuels with high sulphur content. The sulphur content of the fuel leads to acidic gases being formed during combustion, and these must be neutralised to prevent excessive corrosion and corrosive wear of the piston rings and

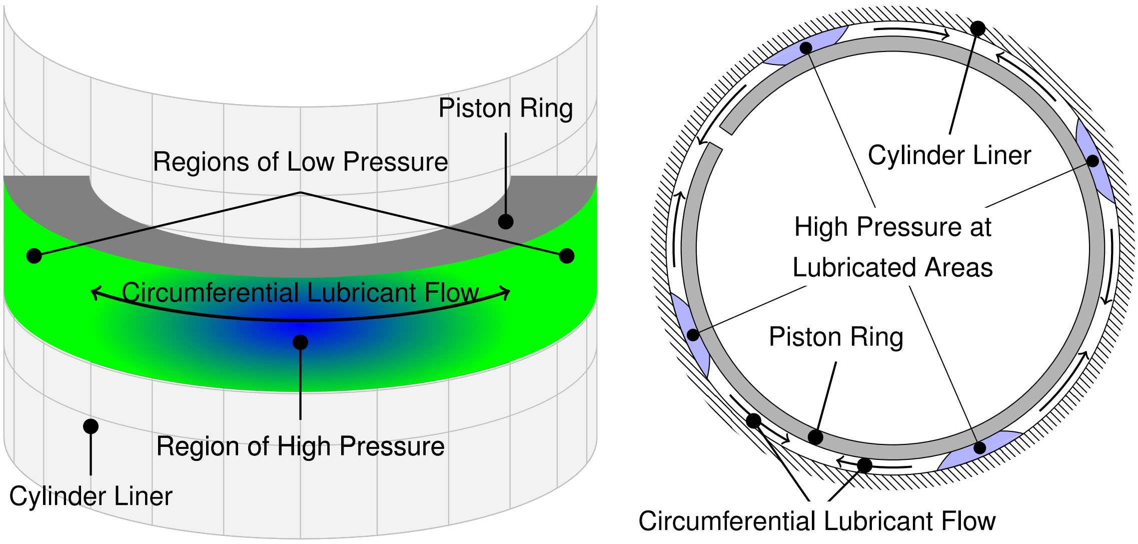

Figure 1.1: Variations in hydrodynamic pressure on the piston-ring face due to non-uniform lubricant distribution leading to circumferential lubricant flow

cylinder liner. Supplying too much lubricant, or using a lubricant with too high a base number, can lead to abrasive wear from the hard calcium deposits that form (Bhushan, 2001b).

A number of studies have linked the effect of emissions from high sulphur fuels to climate change and issues relating to human health (Fuglestvedt et al., 2009; Skeie et al., 2009; Corbett et al., 2007). These are thought to be significant enough to prompt the introduction of legislation to help curb these emission levels, namely the introduction of sulphur emission control areas within which the operators must use a fuel with much lower sulphur content ([Anon], 2006a). With operators largely choosing to switch between higher and lower sulphur fuels on entry and exit from these areas, this further complicates the balance between effective lubrication of the piston-rings, and adequate neutralisation of the acidic gases from combustion. This, in turn, has a knock on effect on the lubrication, friction and wear of the engine components and their subsequent design.

Novel solutions to help meet these needs include the design of improved lubricant delivery systems. Traditionally, a number of quills situated around the circumference of the cylinder liner allow drops of lubricant to be injected into a zigzag groove (Pevzner, 1998b). Greater hydrodynamic pressures are generated in areas near to the injected lubricant as the piston-ring passes and the pressure differential leads to lubricant spreading in the circumferential direction (figure 1.1).

Examples include the pulse lubricating system (Christensen, 2010), which allows more precise metering and timing of lubricant injection. Specifically, shorter injection times of 8–10 ms allow timed lubrication such that lubricant can be injected into piston ring pack as the piston rings pass the quills. In addition, the frequency at which a pre-defined quantity of lubricant is delivered is calculated by the control system based on engine load, speed and crankshaft position, and based on the requested feed rate (Christensen, 2010).

The swirl injection principle system uses spray nozzles to inject lubricant tangentially onto the cylinder liner, improving the spread of lubricant circumferentially upon delivery to the cylinder liner. This occurs in the upper part of the cylinder liner, with axial lubricant transport being needed to spread the lubricant vertically from this area (Eriksen, 2003).

An alternative approach involving a lubrication control system has also been proposed (Sherrington, 2000), whereby the requirements for lubricating the piston-rings, and for neutralising corrosive acids are decoupled. The benefits of such a system are the potential for reduced cylinder lubricant consumption, while maintaining a (just) satisfactory hydrodynamic lubricating film between piston-rings and cylinder liner. Effective acid neutralisation can be achieved by adjusting the dosage of base additive within the lubricant. Figure 1.2 shows a block diagram for the oil-film thickness control element of this system, where the controlled variable is the oil-film thickness, and the controlling variable lubricant supply. Measurements of oil-film thickness could be made using a suitable transducer.

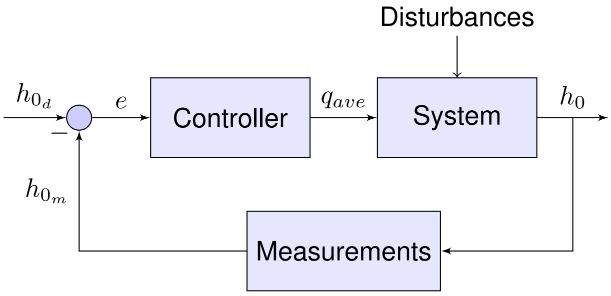

Figure 1.2: Block diagram of a typical feedback control system, where h_0 is the minimum oil-film thickness, and the subscripts d and m represent the demand and measured minimum oil-film thickness values, and q_{ave} is the average injector flow-rate per cycle.

Before a control system such as this can be implemented, the interaction between lubricant supply and oil-film thickness needs to be understood in more detail. Additionally, with lubricant being delivered to limited areas of a large cylinder liner, there remains a reliance on lubricant transport in order to successfully neutralise acidic gases further from the injected lubricant. As such further understanding regarding the transport of lubricant away from these areas is needed.

1.2 Aims and Objectives of the Study

The aim of this project is to determine the effect of lubricant supply on piston-ring lubrication in internal combustion engines, with a particular focus of the effects on large, two-stroke marine diesel engines, where lubrication of the piston-rings is achieved using the injection of oil at discrete locations on the cylinder liner. In order to achieve this goal, the following objectives were proposed.

1. To develop a test apparatus whereby lubricant can be delivered to the cylinder liner at a number of different supply rates, and where oil-film thickness can be measured using capacitance transducers
2. To conduct experiments at a number of lubricant supply rates, in order to investigate the effect of lubricant supply on piston-ring oil-film thickness at different locations on the cylinder liner
3. To develop methods for characterising the development of the lubricant film, and to investigate the mechanisms by which this lubricant film development occurs
4. To develop a piston-ring lubrication model capable of simulating a developing lubricant distribution over a number of engine cycles, following lubricant injection to different areas of the cylinder liner

1.3 Structure of Thesis

Chapter 2: Literature Survey

Following on from this introduction, the impact of the shipping industry on human health and climate change is reviewed in more detail, along with the legislation that has been introduced to help improve the environment in the context of shipping and the implications this has on cylinder lubrication. Following this, aspects of piston-ring lubrication are covered, namely the composition of the ring pack in marine engines and its influence on performance. The function and types of lubricants used in marine engines are also reviewed, along with methods for measuring oil-film thickness in internal combustion engines.

Chapter 3: Piston-ring Lubrication - Theory and Modelling

Theory relating to the hydrodynamic lubrication of piston-rings is outlined and explained, including the use of Reynolds equation for the prediction of the hydrodynamic pressure fields and lubricant flow past the piston-ring. The use of numerical methods for solving Reynolds equation is described, with their implementation to develop a flow-continuity model for predicting the development of a lubricant film over a number of cycles, along with oil-thickness, lubricant flow past the piston-ring, film extent, and lubricant transport. The model implemented considers a single compression ring concentric within the cylinder, and lubricant viscosity is assumed constant throughout the stroke. An algorithm has also been developed to determine the distribution of lubricant on the cylinder liner from given lubricant injector specifications.

Chapter 4: Development of Experimental Apparatus

The development of an engine based apparatus incorporating a spray lubricant injector system and capacitance based oil-film thickness transducers is outlined. A system for control of the lubricant injection is also described, alongside a validation of the lubricant flow-rate from the injectors throughout their range of supply settings. Calibration of the oil-film thickness transducers is included, so too is lubricant selection.

Chapter 5: The Effects of Spray Lubrication on Piston-ring Oil-film Thickness

The effects of the spray lubrication system on oil-film thickness are presented and examined in detail. Features observed in the development of oil-film thickness and film extent over the course of sixty cycles and at several lubricant injector flow-rates are inspected, analysed, and discussed. The development of the oil-film near top and bottom dead centre is also discussed.

Chapter 6: The Influence of Lubricant Injection Volume and Time on Oil-film Thickness Development

At reduced lubricant injector flow-rates (achieved through periodic lubricant injection), and over a longer period (120 cycles), the influence of lubricant injection volume and time on oil-film thickness development is investigated in more detail. The response of oil-film thickness to ongoing lubricant delivery is analysed, and an attempt to categorise and quantify this response made. Causes for this behaviour observed are discussed.

Chapter 7: Axial and Radial Oil-transport in the Cylinder

Results from an investigation looking at axial and radial oil-transport are presented. This involves only a single lubricant injector, and using analysis of oil-film thickness and film extent over the course of 120 cycles, a method has been developed to determine the transition from boundary to hydrodynamic lubrication. Based on this analysis, contour maps showing the development of the lubricant film over time on the cylinder liner have been constructed. An equation for the rate of lubricant transport from the injected area has been proposed.

Chapter 8: Validating a Model for Oil-film Thickness Development

Results from the model described in chapter 3 have been compared to experimental data to validate the model, to support arguments relating to discussed mechanisms of lubricant transport, and to confirm the cause of behaviour observed in the oil-film thickness response seen in the experimental investigations.

Chapter 9: Conclusions and Recommendations for Further Work

Conclusions arising from the presented work are outlined, along with suggestions for investigating a number of matters arising from this work in more detail. This includes further development of equipment, investigations using this modified equipment, and the theoretical model employed during this project, along with other ideas for original future investigation.

1.4 Original Contributions of the Research

1. A test-rig apparatus has been developed with the capability to allow investigations involving a developing lubricant film in a motored internal combustion engine. The system incorporates lubricant injectors that can deliver lubricant to the cylinder over a range of flow-rates and injection frequencies and position. A pneumatic lubricant injection system has been developed, using a Hall-effect sensor and microcontroller, to periodically trigger the lubricant spray onto the cylinder liner. Capacitance based oil-film thickness transducers have been manufactured without the use of fracture-prone ceramic insulators that until now have been needed for sensors of this type (Garcia-Atance Fatjo et al., 2017). The transducers have been installed and calibrated at a number of locations in the cylinder to provide information about the changing oil-film thickness and lubricating film.

2. A method has been developed for measuring the rate at which lubricant is transported both axially and circumferentially. Lubricant flow has previously been determined through investigations into the residency time of lubricant within the piston-ring pack (Stark et al., 2005). Here the timing of changes in oil-film thickness or film extent at different cylinder locations has been interpolated to generate a contour map showing the development of the lubricant film as lubricant is transported in the cylinder. This is the first time lubricant transport data has been presented in this way.

3. Comparison of the oil-film thickness signal to a simulated signal has been made to ascertain the variation in time of inlet and cavitation boundaries following a change in operating conditions. Fatjo et al. (2014) evaluated oil-film extent using capacitance transducers for an

engine operating in the steady state. The technique has been developed such that variations of film extent in time can now be measured.

4. A theoretical model, originally described and used by Ma et al. (1996) to model the starved lubrication of a piston-ring in distorted bores, has been developed to predict the development of a lubricant film over time from an initial non-uniform distribution. The model solves Reynolds equation to determine an initial estimate of the hydrodynamic pressure distribution. This estimate is modified to satisfy conservation of mass leading to predictions of the inlet and cavitation boundaries and a solution for hydrodynamic pressure and degree of filling at each computational cell. Oil-film thickness is determined by considering an equilibrium of the forces acting on the piston-ring. The model includes an algorithm to generate non-uniform lubricant distributions. Oil-film thickness predictions to within 15% of experimental data have been computed.

5. The impact of a change in lubricant injector supply rate to the cylinder on the development of oil-film thickness and film extent can be quantified. The response of oil-film thickness at a given location can be modelled using a time delay, a fast increase approximated as a step, and a slow increase represented as a first order response with a time constant. A system model for this behaviour has been proposed, with coefficients that can be determined by experiment.

6. Time-dependent oil-film thickness data at a number of axial and circumferential locations on the cylinder liner has been presented in a novel manner to allow comparison of oil-film thickness development at these locations during the course of an experiment.

7. A method for predicting upstroke and downstroke inlet supply upon engine startup, during periods following a change in the rate of lubricant supply rate, and following a change in operating conditions has been developed.

8. A range of investigations have been proposed to elucidate the behaviour of the oil-film and rate of lubricant transport at different engine conditions, thus enabling an oil-film thickness control system for large marine engines - such as that proposed by Sherrington (2000) - to be developed and potentially leading to reductions in cylinder oil consumption.

Chapter 2

Literature Survey

2.1 Introduction

This literature survey aims to provide an overview of the relevant areas of current knowledge, and recent or ongoing research, relating specifically to the study of the lubrication of the piston ring pack in an engine of this type. It provides a foundation for further investigation into the field, to allow the development of a lubrication control system for the piston rings in a large marine diesel engine.

The tribological aspects of piston rings are covered, as are details of lubricants and lubricating systems used in large marine diesel engines. Where appropriate, reference is made to implemented and expected changes to legislation and how this effects the lubrication in these engines. This mainly relates to the introduction of limits on the sulphur content of bunker fuels in a few busy shipping areas.

Finally, methods of investigating the oil film thickness in such systems are reviewed. This is not only important in terms of carrying out the study, but also because a lubrication control system requires a means for monitoring the oil film thickness in order to deliver the correct quantity of lubrication. The review covers the advantages and disadvantages of the different methods as well as briefly describing how they work, and finds that at least two of these methods (capacitance and ultrasonic) would be suitable for use in an operational engine.

2.2 Relevance and Justification

Prior to covering the technical aspects relating to this study, the motivation for the study is outlined. This includes the environmental impact that large marine diesel engines have on the environment and on human health, as well as considering economic aspects. In short, although the level of gaseous emissions of a single container ship are quite small, considering the size of its cargo and the distance it covers with it, and the large and ever increasing size of the world fleet, means the industry as a whole contributes to a significant portion of the harmful emissions produced by the transport sector. The resulting effect on climate and human health is thought to be significant enough to prompt the introduction of new legislation to help curb these emission levels. This, in turn, has a knock on effect on the lubrication, friction and wear of the engine components and their subsequent design.

2.2.1 The Impact of Gaseous Emissions from Marine Engines on a Global Scale

As with many forms of industry and transportation, the emissions from shipping have a significant impact on climate and health on both a local and global scale. There are currently many studies to try to both quantify these effects and to estimate their impact from now until sometime in the future (Fuglestvedt et al., 2009; Skeie et al., 2009; Corbett et al., 2007).

It appears to be accepted that freight transport by sea is one of the cleanest and most efficient methods available if consideration is made for the amount of cargo carried and the distance covered with it (Eyring et al., 2007; Corbett and Koehler, 2003). Figure 2.1 suggests that shipping is of the order of 10 to 100 times less polluting than road and air freight, respectively.

However, as the levels of international trade have grown, so too have the maritime emissions (Schrooten et al., 2009). Figures from 'The World Merchant Fleet in 2005' ([Anon], 2010b), and supported by Collins et al. (2009), suggest that the world merchant fleet has increased by 35$\%$ - to over 60,000 vessels – over the last 50 years. Further to this, the increase in activity of each vessel has resulted in growth of over 170$\%$ in seaborne trade between 1970 and 2005 – with levels rising

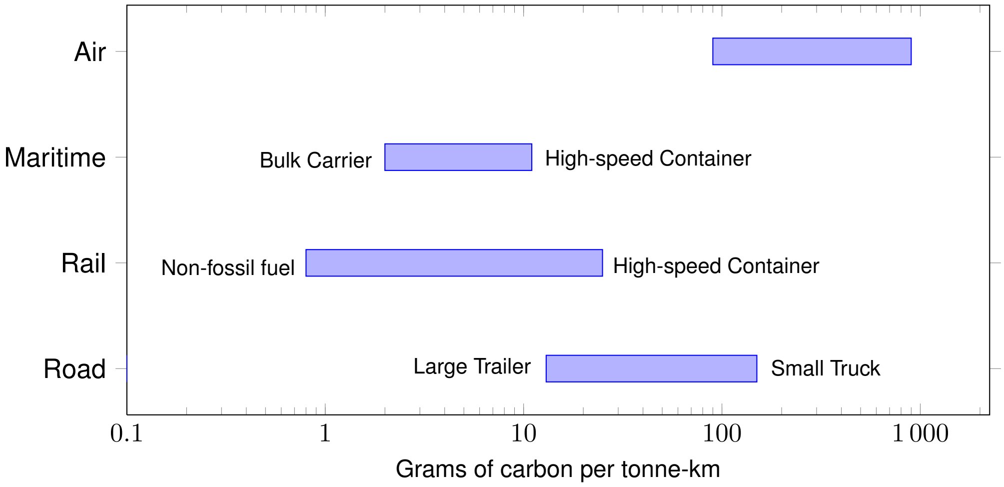

Figure 2.1: Carbon emission levels for the four major freight transport modes (Penner et al., 2000)

from 10,654 bn ton-miles to 29,045 bn ton-miles according to the 'Review of Maritime Transport' ([Anon], 2006b), accounting for 90% of international transport by tonnage (French, 2008).

The significance of this increased activity means that between 1990 and 2004, shipping contributed at least a 45% increase in carbon dioxide (CO_2) emissions in Europe (Eyring et al., 2005), and in 2007 it accounted for total CO_2 emission levels of the same order as aviation (Eyring et al., 2007). The same report estimated that ocean-going ships consumed 280 million metric tons of fuel globally, and emitted approximately 800 million tonnes of CO_2 in 2000 – contributing about 2.7% to all anthropogenic CO_2 emissions that year (Eyring et al., 2007). This is comparable with the contribution from aviation, which accounted for 2% of global CO_2 emissions and 12% of CO_2 emissions from all transport sources – a total of 666 million tonnes of CO_2 for 2008 (Association et al., 2009). Emissions from shipping increased to an estimated 1000 million tonnes/year for 2006 – a 25% increase from the year 2000 resulting in 3.3% of total anthropogenic CO_2 emissions for that year (Fuglestvedt et al., 2009).

Figure 2.2 shows the shipping industry to be as much as 10, 100 and 1000 times more polluting than aviation for oxides of nitrogen (NO_x), sulphur dioxide (SO_2) and particulate matter of size 10 μm or less (PM_{10}) emissions respectively, as well as more thirsty in terms of total fuel consumption.

Emission levels and total consumption of heavy fuel oil and diesel are expected to rise yet further over the next 20 years, in line with the expected rise in maritime transport activity. It was predicted that growth of +183% of ship miles in the period 1997-2030 would be made, the largest increase being a +518% increase for container ships (Schrooten et al., 2009) which are

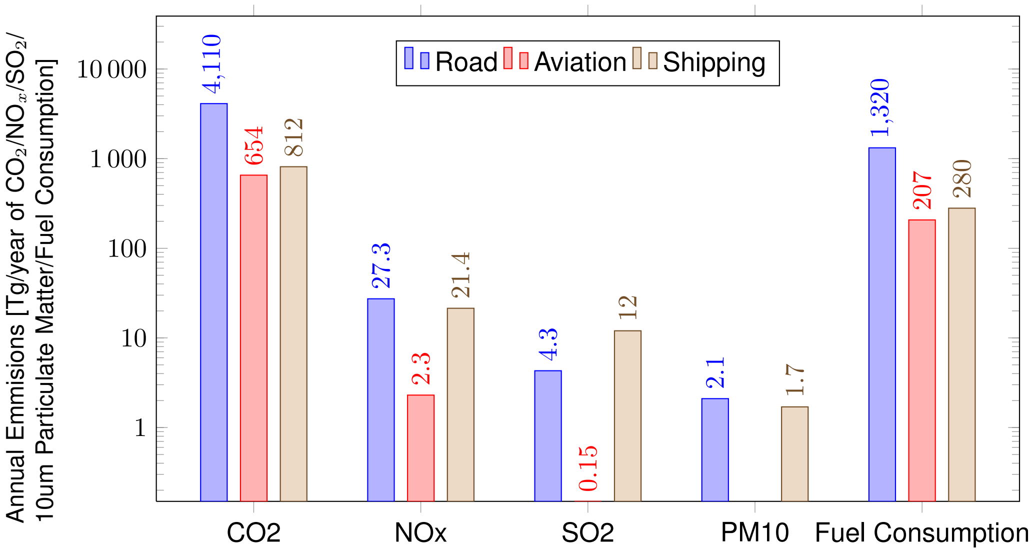

Figure 2.2: Estimated annual transport related emissions of $C0_2$, NO_x, SO_2 and 10um Particulate Matter, and fuel consumption, in Tg (1 Tg $= 1 \times 10^{12}$ g $= 1$ Mt) for the year 2000 (Eyring et al., 2007)

the biggest polluters in the industry. One reason for a continued rise could be the lack of growth in the aviation freight transport sector, which – if UK trends are anything to go by – stalled in 2000 (‘Air freight – the impacts’, Airportwatch, 2009; various IATA press releases, 2009-10) because of increasing costs (IATA press release, September 2009). Whatever the cause, the growth is expected to lead to an increase in shipping emissions of 150% to 250% from 2007 levels if current practice is maintained (Ritch, 2009). The impact of all these emissions on the climate and human health is complex, with the different types of emissions having varying effect both locally and globally, and in the short and long term. For example Fuglestvedt et al. (2009) have modelled the global temperature response for two scenarios (figure 2.3) – one where sulphur dioxide emissions from the shipping industry remain constant (scenario A), and another where they are reduced by 90% with all other emissions remaining constant (scenario B).

The total global temperature response from each of the different transport sectors is shown as the bold line in figure 2.4, alongside the predicted temperature response due to each individual emission type – carbon dioxide (CO_2), sulphur dioxide (SO_2), nitrogen oxides (NO_x), ozone (O_3), methane (CH_4) and ozone particulate matter (O_3PM). For scenario A, the total global temperature response due to the emissions is negative (ie. global cooling) for the next 200 years, with a minimum about 35 years into the future. If SO_2 emissions are reduced by 90% as per scenario B, the minimum turning point remains approximately 30 years in the future, but shipping emissions are contributing to global warming after only about 75 years. Fuglestvedt et al. (2009) suggest the reason that sulphur emissions lead to a more long term cooling effect is a result of the sulphur dioxide particles oxidising to become sulphates (SO_4^{2-}) when they are released into the atmosphere. These sulphates form particles that scatter solar radiation and reduce radiation heating of the earth’s surface. The second cause is because sulphur dioxide leads to the forming of cloud condensation nuclei, which increases water droplet density and thus increases the reflectance

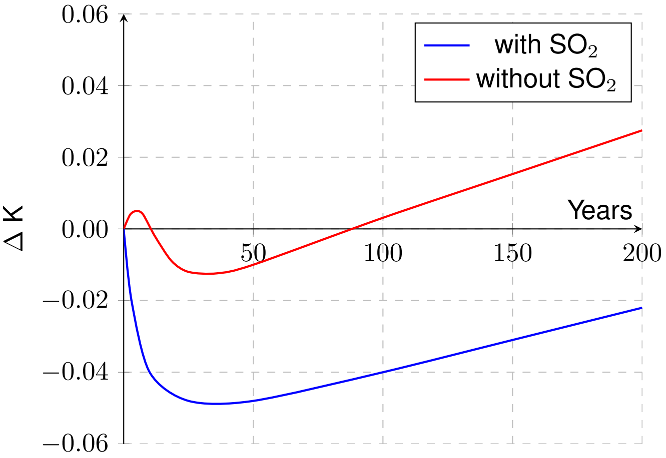

Figure 2.3: Global temperature response due to shipping emissions with and without sulphur dioxide (Fuglestvedt et al., 2009)

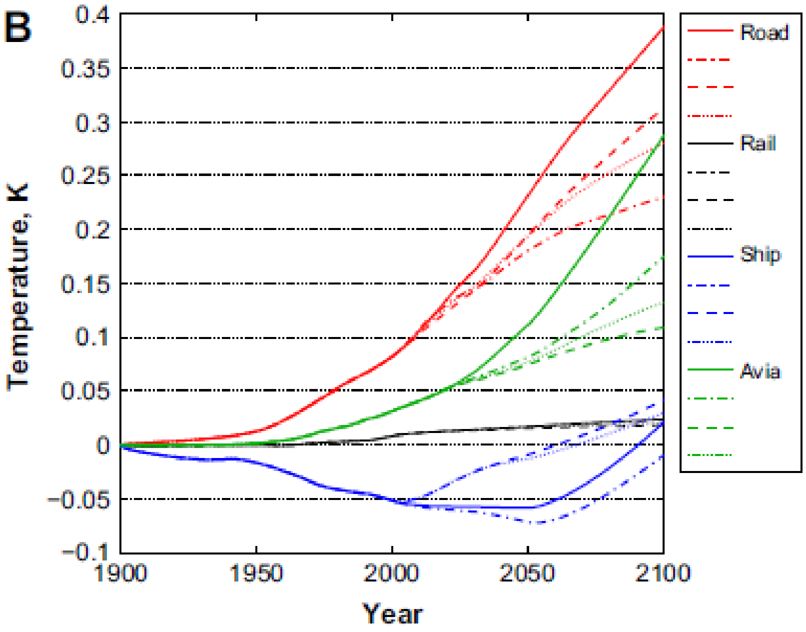

Figure 2.4: Temperature change due to emissions from transport sectors in the period from 1900 to 2100, using the four scenarios for future emissions taken from Skeie et al. (2009)

.

and lifetime of clouds – particularly crucial because shipping lanes tend to be in areas of clean air with low clouds. The temperature response from this phenomena is of the order of decades, in part because the residency of the sulphate particles is only a matter of days. This compares to the long term response to CO_2 emissions of several hundred years. It could be argued then, that global cooling from shipping is in fact a good thing, since the world is currently in the grip of a global warming 'crisis', and that emissions should be left as they are. The contribution of a few hundredths of a degree certainly appears to be minimal when combined with the effects of the rest of the transport sector and global industry as a whole, and when other factors such as human health are considered.

Skeie et al. (2009) plotted the temperature response due to emissions from road, rail, shipping and aviation transport (figure 2.4). There is obvious agreement with Fjugelstvedt that the response due to shipping is negative and of the order of -0.05 K over the next 100 years. However aviation alone would counter this and more, with a response rising from 0.05 K at present to 0.28 K in the year 2100. The temperature response from road transport is even higher again, so in the year 2050, for example, the total temperature response from road, rail and air transport is 0.39 K while the cooling effect of the shipping industry is -0.05 K. What is clear, certainly from figure 2.3, is that CO_2 emissions will have an increasingly significant impact on global warming if left unrestricted. The media are already picking up on this and it is more than likely that it will lead to the introduction of new regulations, as shipping is currently exempt from the current Kyoto protocol. This will

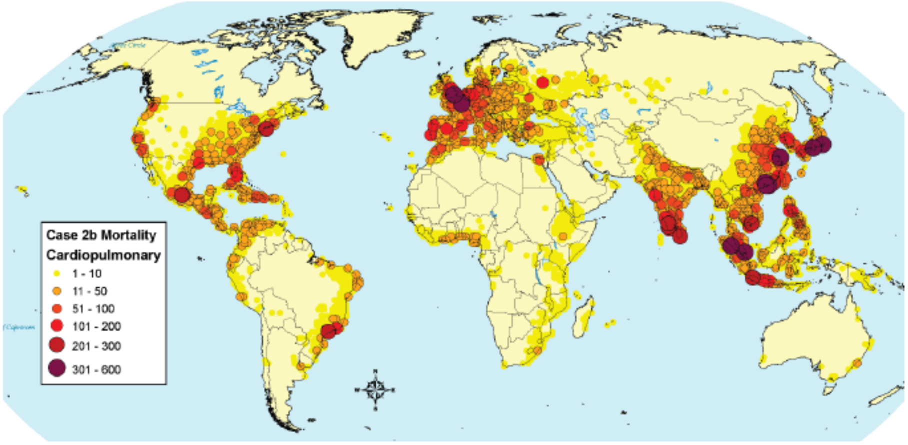

Figure 2.5: Cardiopulmonary mortality attributable to ship $\mathrm{PM}_{2.5}$ emissions (Corbett et al., 2007)

.

be discussed further in the next section, ‘Methods proposed to reduce emissions from marine engines’.

The effect of these emissions on human health is also important. For example, near busy shipping lanes, particulate matter from ship emissions (particularly sulphur) up to 400 km offshore can be transported to any adjacent coastal regions. These particles – which can also lead to acid rain – will contribute to a range of health problems such as asthma, heart attacks and cancer. A study by Corbett et al. (2007) modelled premature mortality due to this particulate matter in order to assess the scale of the problem.

As would be expected, Figure 2.5 shows that the largest concentrations of mortality due to shipping emissions are in areas of high population along the major shipping lanes (straights of Dover, Malacca straights). This study suggests that shipping contributes to 60,000 premature deaths annually as a result of emitting particulate matter. Fuglestvedt et al. (2009) agree with this, but also suggest that over 40,000 of these deaths would be spared if the sulphur content of fuel were restricted to 0.5% by weight for ships within 200 nautical miles of the coast.

So shipping appears to be one of the cleanest forms of moving freight when considered in terms grams of carbon emitted per tonne-kilometre of cargo, and the media tends to focus on road and air traffic as the major contributors to air pollution. Nevertheless, the size and level of activity of the world fleet means that shipping emissions have a significant impact on climate and health. As a result shipping emissions are likely to become a more significant political issue.

2.2.2 Methods Proposed to Reduce Emissions from Marine Engines

There are a range of proposals and possibilities that exist for reducing emissions from marine engines. These vary from advanced engine design, to changes to fuel and operating conditions. The primary driver for these changes is the introduction of new regulations, of which there are some in place, with more expected in the future.

Currently there are Nitrous Oxide (NO$_x$) and Sulphur Dioxide (SO$_2$) emissions limits that have been introduced and regulated by the International Maritime Organisation (IMO) under the Marpol Annex VI ([Anon], 2007), as ratified in 2004. These regulations must be met either through changes in the type of fuel used, exhaust gas scrubbing, emissions trading schemes, or technological advances.

A global fuel-oil sulphur cap to limit fuel sulphur content to 4.5% by weight was introduced in May 2005, and was further reduced to 3.5% in January 2012. In 2020 this limit will be tightened again with a cap of 0.5% fuel sulphur content. There are currently three corresponding sulphur emission control areas (SECA's), in which the fuel oil sulphur cap is 0.1% (alternatively, this target can be met by exhaust gas scrubbing to reduce sulphur emissions to 6 g/kWh). The first area to be established was the Baltic Sea in May 2006, the North Sea and English Channel being added in 2007. California was added in July 2009, and expanded to include the remainder of North American and Canadian coastline in 2012. The most recent addition was the US Caribbean.

The NO$_x$ emissions cap is dependent on engine speed. It must be less than 17 g/kWh for engine speeds below 130 rpm, between 17 g/kWh and 9.8 g/kWh for engine speeds between 130 rpm and 2000 rpm (based on the formula $45n^{-0.2}$ g/kWh, where n is the engine speed in revolutions per minute), and for engine speeds above this the NO$_x$ emissions must be less than 9.8 g/kWh.

The obvious method of meeting the sulphur caps is to reduce the sulphur content in the fuel (because the level of emissions is proportional to this), and to reduce fuel consumption. An alternative is to switch from bunker fuel to marine gas oil or marine diesel oil. These fuel types are cleaner, but at the cost of requiring more CO$_2$ to produce. However, it has been shown using a total fuel cycle analysis (Corbett and Winebrake, 2008) – which includes emissions from raw material extraction right through to combustion of the fuel in the vessel – that switching to these fuel types could lead to reductions in the emissions of sulphur oxides (SOx) of between 70% and 85% (6% of total anthropogenic SOx emissions), with only a 1% increase in CO$_2$ (figure 2.6).

Not considered in the above study were the financial costs of switching fuel type. Although cleaner fuel would lead to more efficient engines and remove the need for purifiers, the heating of fuel tanks, sludge control and emission-abatement equipment, and the disposal of residues, would result in a fuel cost rise of approximately $200-$250 per tonne (25%-30%) (French, 2008). Oil refiners would also lose out because bunker fuel is an otherwise unsellable residual product.

One final possibility is to remove the SOx emissions from the exhaust gases, but this is expensive, and requires bulky equipment and the disposal of effluent (Schmid and Weisser, 2005).

Since January 2000, marine engines have been manufactured to comply with the new regula-

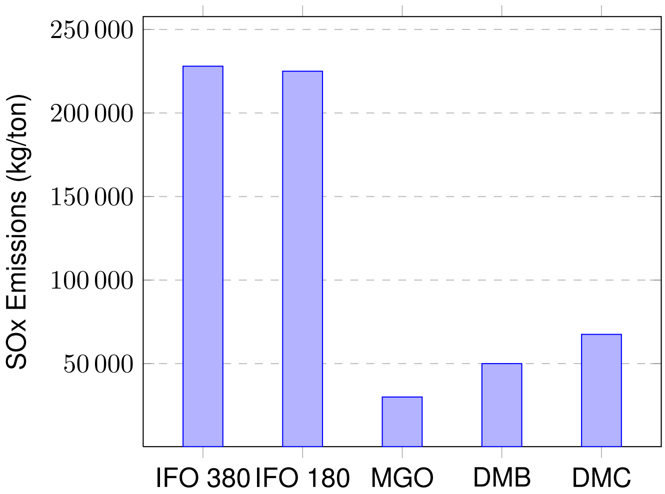

Figure 2.6: SOx emissions by fuel type (Corbett and Winebrake, 2008) - IFO 380 and IFO 180 are bunker fuels, MGO is marine gas oil, and DMB and DMC are marine diesel oils.

tion on NO_x emissions. This has already resulted in emissions reductions of between 25%-30% (of the order of 4.4 million tonnes/year, globally). These reductions have been made possible through optimised ship design and careful operation. It is also expected that further reductions are possible, through similar optimisation and use of more modern common rail injection systems (such as the Wartsila RT-Flex) which can achieve the optimum tuning for either efficiency, reduced emissions or power. These technologies are detailed in a document released by Wartsila (Schmid and Weisser, 2005) and include tuning the engine for low NO_x emissions, making further reductions of these emissions through introducing selective fuel injection patterns and timing on engines with common-rail injection systems, and the use of water-fuel emulsions and direct water injection to optimise the combustion conditions for low NO_x emissions.

Along with the existing regulations are a couple of proposals under consideration. The first of these is a plan to tax bunker fuel; a suggestion which was supported by developed countries in the run-up to the Copenhagen conference in December 2009 (Mason, 2009). The money would go to a climate aid fund, and the International Maritime Organisation (IMO) would reportedly be happy to administer this. An alternative currently under consideration by the IMO, is a levy on a vessel's charterer for the fuel used and cargo imported to developed nations, which, according to the Professional Engineering report, 'Shipping Emissions Levy Proposed' ([Anon], 2009), account for a disproportionate amount of worldwide shipping. The motivation for this is the difficulty in apportioning responsibility for emissions, since a ship delivering to the UK could sail under the flag of a less developed nation and get its fuel from a country which is not currently required to adhere to any emission reduction targets set by the Kyoto protocol. For this scheme the money would go into a fund that could be used to develop green technologies.

Despite political and media pressure to include shipping in the greenhouse gas emissions targets for the second period of the Kyoto protocol(2013 to 2020), these never came into force due to a lack of support from a number of parties following the Doha Amendment. This led to a separate agreement known as the Paris Agreement, from which shipping was again excluded ([Anon], 2018b). As a result the principle regulations on shipping emissions remain those implemented by the International Maritime Organisation, which restrict sulphur emissions by limiting fuel sulphur content to 3.5% globally and to 0.1% in a number of busy shipping lanes such as the English Channel. The global cap is set to further reduce to 0.5% in 2020 ([Anon], 2018a; George and Ghaddar, 2018).

Options for complying with the sulphur emissions regulations include swicthing between high and low sulphur content fuel and exhaust gas scrubbing, with operators typically using a financial model to choose which option with no consideration as to the benefits (Schinas and Stefanakos, 2014). To date the sulphur emissions regulations have been met principally through switching between high and low sulphur fuels on entering a sulphur emission control area. While exhaust gas scrubbing can be effective equipment costs are typically between $1m and $6m, and with long installation times it could take several decades for operators to retrofit all their vessels (George and Ghaddar, 2018).

Other technologies for complying with these, or other future regulations include the use of kite sails, upgrades to hulls, engines and propellers, or simply operating in more efficient ways such as at lower speeds. It is thought that CO_2 reductions between 25% and 75% are possible by use of one or several of these techniques (Ritch, 2009). BP shipping has also started to use electricity from the national grid (rather than let ships use their own generators) to help curb harbour emissions (Maung, 2007).

With regards to the speed reductions, a study by Corbett et al. (2009) was performed on container ships. These ships may only account for 4% of the world fleet, but alone they contribute to 22% of the energy consumptions and CO_2 emissions from international shipping, and are expected to be the fastest growing sector of the shipping industry. The study considered the percentage of speed reductions required to maintain maximum profit margin for two different scenarios. The first – scenario 1 – that vessels carry more containers to meet constant demand, and the second – scenario 2 – that additional ships are added to the route to serve the existing demand. The study also looked at the impact of increasing fuel prices on the speed reductions.

The graph in Figure 2.7 shows that as the cost of fuel increases, so does the incentive for greater speed reductions in order to maintain maximum profit margins. It also shows that greater CO_2 reductions are possible for the scenario where container ships carry more cargo. Figure 5.2.3 shows the effect of introducing fuel tax on incentivising speed reductions for the same two scenarios, and that a $60 /tonne tax would lead to reductions of CO_2 of around 20% and 10%

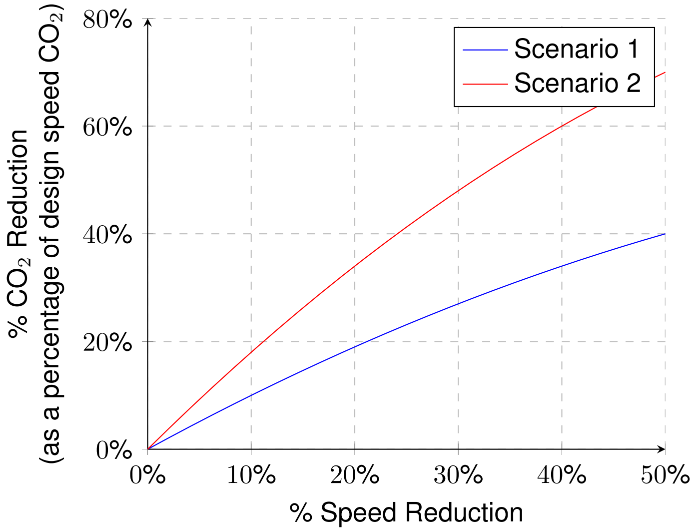

Figure 2.7: Speed reduction vs. reduction of CO_2 emissions for each scenario using different fuel prices (Corbett et al., 2009).

for scenarios 1 and 2, respectively. This would increase to 60% and 33% for a fuel tax of $570 /tonne, although this represents approximately 50% of the current bunker fuel price.

Having been operating to the sulphur caps for a number of of years, operators now have a better understanding of the challenges associated with fuel switching. These include operational matters such as ensuring vessels carry compliant fuel and manage the switching of fuel to ensure the correct sulphur level fuel is being consumed without cross contamination (ExxonMobil, 2017). In order to satisfy the administrative bodies fuel changeovers must be logged and samples held for up to a year (Adamkiewicz and Drzewieniecki, 2018).

Of the technical challenges, different viscosities of heavy fuel oil, low sulphur fuels, and marine gas oil require a maximum temperature change of 2°C per minute to avoid thermal shock. Use of a lower base number lubricant is also advised to correctly neutralise any corrosive acidic sulphur in the fuel and minimise liner wear or acid corrosion (ExxonMobil, 2017). For fuels with sulphur content below 1% a lubricant with base number BN40 or BN50 is recommended, and for fuels with sulphur content above 1.5% a lubricant with base number BN70 is advised, with the feed rate being adjusted based on the actual fuel sulphur content (Adamkiewicz and Drzewieniecki, 2018). However the minimum feed rate for satisfactory lubricant distribution is 0.6 g/kWhr, and even with the lowest base number lubricants this is reached at fuel sulphur content of 3%.

The sulphur limits have led to change in the composition of marine fuels as a result of concerns over issues with fuel quality, compatability and stability ([Anon], 2015). Monitoring of the fuel switching process through testing of viscosity and fuel compatibility, and monitoring of liner wear is essential to ensuring engine performance is not compromised.

Zetterdahl et al. (2016) carried out a study of the impact of fuel sulphur content legislation on emissions to air based on measurements taken on the same ship and engine using different marine fuels, finding that emissions of SOx were reduced by 85% after the introduction of the reduced cap in 2015.

2.2.3 Summary

Due to the scale of the industry, emissions from shipping impact seriously on both the climate and on human health. Carbon dioxide and ozone emissions lead to global warming, and sulphur dioxide, nitrous oxide and particulate matter emissions result in increased asthma, heart disease and cancer problems.

Some changes have already been made to combat these negative impacts, such as the introduction of SECAs in busy shipping lanes, and the development and exploitation of new engine technology such as common-rail injection systems.

Unfortunately, this can introduce different problems, particularly with regards to ease and cost of operation. For example, low sulphur fuels are expensive, so there is a cost for using it for an entire journey just to comply with a SECA near the destination. An alternative is to use fuels with different sulphur content, but this introduces the need to vary the quantity and type of lubricant also, in order to correctly balance the acidity of the fuel and keep corrosion and wear to a minimum. Such complications could easily lead to mistakes, resulting in costly engine maintenance.

There are other proposals to reduce emissions, including reducing speed and taxing fuel imported into developed nations. No legislation exists as yet, however, and the motivation to adopt such strategies is immediately dampened by the perceived impact on profits. This could all change if the International Maritime Organisation introduce emissions targets for the shipping industry.

2.3 Piston-ring and Ring-pack Lubrication in Large Two-stroke Engines

2.3.1 The Function of Piston-rings and the Ring Pack

The introduction of the split piston ring to steam engines in the nineteenth century had a dramatic effect on engine efficiency and the life of the piston (Dowson, 1993). The operating principle was that the elasticity of the ring would ensure an effective seal was maintained to prevent loss of pressure past the piston, thus improving engine performance. It also served to reduce friction and wear, resulting in an improved lifespan of the engine components.

Since their introduction, piston rings have remained an important feature of the piston assembly in all internal combustion engines, and are designed to perform several key functions that contribute to effective and efficient running. Firstly, they must provide an effective seal between the piston and cylinder wall, so the high pressures in the combustion chamber during compression, combustion, and exhaust do not leak to the crankcase. Any pressure that is lost will reduce power and efficiency of the engine (Dowson, 1993; Munro, 1999). Second, they are vital to the lubrication between piston and cylinder, as they help to spread the lubricant evenly across the cylinder walls. They also play a role in the cooling of the piston components, as the rings provide a path for the transfer of heat to the cylinder walls, from where it can be transferred to the coolant in the cylinders water jacket (Dowson, 1993). Finally they play a part in minimising friction and wear of the cylinder walls, which has a direct impact on oil consumption, reliability and time between engine overhauls (Dowson, 1993).

2.3.2 Common Piston-ring Types in Modern Marine Diesel Engines

Historically, large bore marine diesel engines have incorporated a ring pack of five or six piston rings. The majority of newer engines – manufactured by MAN B&W, Mitsubishi or Sulzer, incorporate only four rings (Woodyard, 2004).

These low speed engines incorporate a once-through lubrication-system, where the lubricating oil is injected into the cylinder and burnt with the fuel. The quantity of oil being injected can be controlled by setting the pumps to match expected engine load, and so no excess oil is expected after combustion and an oil control ring, or scraper ring, is therefore not required (Blau, 1992; Clark, 1970). Unlike automotive engines, all four rings are compression rings that help prevent pressure loss both after combustion on the expansion stroke and on the compression stroke. Even if all the sealing faces are perfect, some pressure loss will occur through the ring gap, which is essential to the design of piston rings as it allows for easy fitting and their expansion when hot, while keeping the radial pressure against the cylinder walls to an acceptable level. Too much radial pressure would lead to high friction and occasionally seizure (Clark, 1970). While some pressure is exerted against the cylinder wall due to the tension in the ring, the main contributor to the radial pressure against the cylinder is in fact from the compressed gases in the combustion chamber. According to Clark, the pressure behind the top ring is approximately 75% of the gas pressure, which after combustion leads to around 3600 kPa of radial pressure compared to 100 kPa from ring tension. Loading from the gas pressure behind the second ring is of the order 1380 kPa, and is less again on subsequent rings (Clark, 1970). What this shows is that some leakage does occur through the ring gaps and that several compression rings are therefore necessary to get the best performance from the engine.

At the other end of the cycle, when the pressure is low, the initial radial pressure from the piston ring becomes very important as it is relied upon to create the seal at the start of the compression stroke. If it is too weak, the seal will not form, which can lead to ring flutter (defined by Tian (2002a) as “the phenomenon that the ring oscillates inside the groove several times within a portion of a cycle”), this can adversely affect blow-by and could lead to increased friction and accelerated wear (Tian, 2002a; Tian, 2002b). In extreme cases it could also result in breakage through fatigue failure (Clark, 1970).

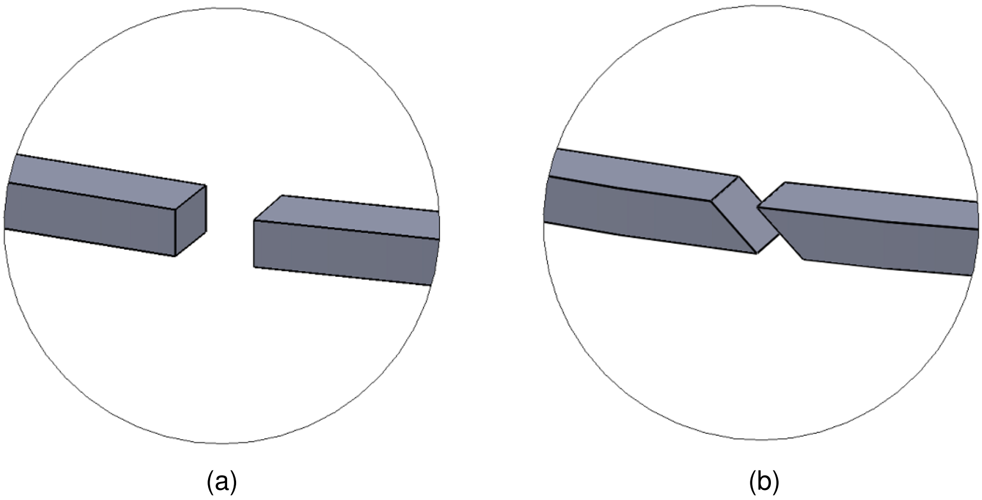
(a) (b)

Figure 2.8: Ramsbottom type piston rings with square butts (a), and angle or scarf butts (b)

The piston rings used in large bore marine diesel engines are predominantly of the Ramsbottom type with either scarf butts or square butts (see figure 2.8). These rings are manufactured with a square profile, which would lead to the lubricating oil being scraped off the cylinder wall rather than spread over it. These sharp corners are therefore removed by rounding off to promote more effective lubrication of the cylinder during the important running in stage of the cylinder assembly (Clark, 1970). Sulzer go further than this, as they supply pre-profiled piston rings for all new engines and for retrofitting of older engines, for all the rings on a piston (Woodyard, 2004). It is thought to be difficult to predict exactly what shaped profile the ring will form naturally – due to the variety of engine sizes and operating conditions, but pre-profiling has been shown by Sulzer to give improved running in performance, with a more reliable and consistent oil film from the very first cycle resulting in less friction and low wear rates (Amoser, 2001).

Man B&W have introduced the ‘controlled pressure relief’ ring on some of their largest engines (Woodyard, 2004). This is installed as the top ring, and has a double lap joint (figure 2.9) that has been developed to achieve a completely tight upper ring, and so greatly reduces blow-by through the ring gap. This helps prevent the hot combustion gases causing localised overheating on the cylinder liner and second piston ring, and reduces load on the lower piston rings (Schenk et al., 2000; [Anon], 2010a). Relief grooves (figure 2.10) are manufactured in the running face to ensure optimum pressure drop across the top ring, these ensure the loading on the oil film is at an optimum level. An aluminium-bronze alloy coating is applied to the sliding surfaces to ensure safe

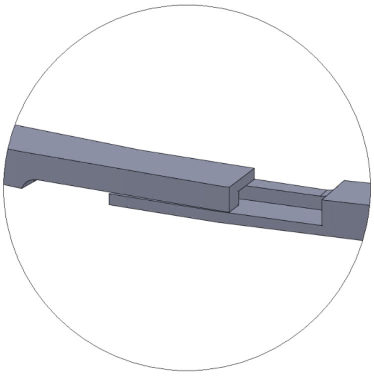

Figure 2.9: Double Lap joint on Man B&W 'Controlled Pressure Relief' Piston-ring

running in.

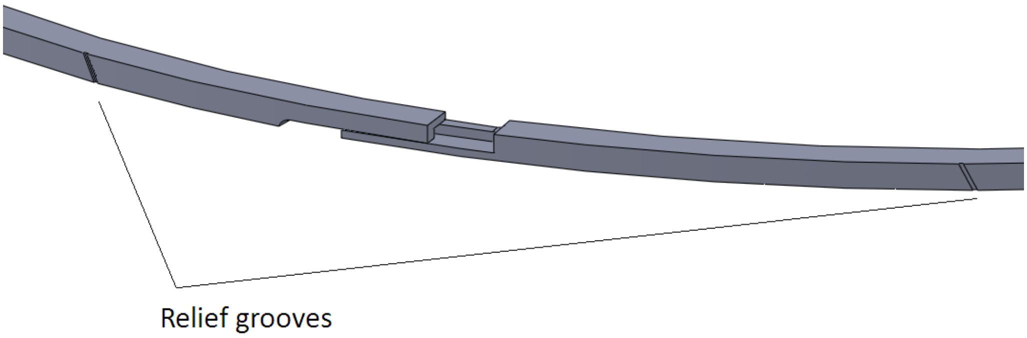

Figure 2.10: Pressure Relief Grooves on the Running Face of Man B&W's 'Controlled Pressure Relief' Ring

2.3.3 Influence of Piston-rings on Engine Performance

According to the Stribeck curve (figure 2.11), it is inevitable that some metal to metal contact will occur in these large, slow engines. Typically this contact happens at top dead centre when the pressure in the combustion chamber is high and the speed of the piston is low, and the hydrodynamic forces are too weak to maintain even a very thin oil film (Hutchings, 1992). This results in high friction and wear rates due to the contact between asperities.

Problems resulting from this contact are particularly common during the running-in phase of the piston and cylinder components. This is when the surfaces are at their roughest with many asperities and more chance of them engaging, especially if load and speed are applied too rapidly (Blau, 1992). Scuffing is one such problem, which is a surface damage problem caused by rapid wear resulting from localised welding between two effectively unlubricated surfaces (Hutchings, 1992). Similar hard metals – such as the cast irons used in piston ring and cylinder liner manufac-

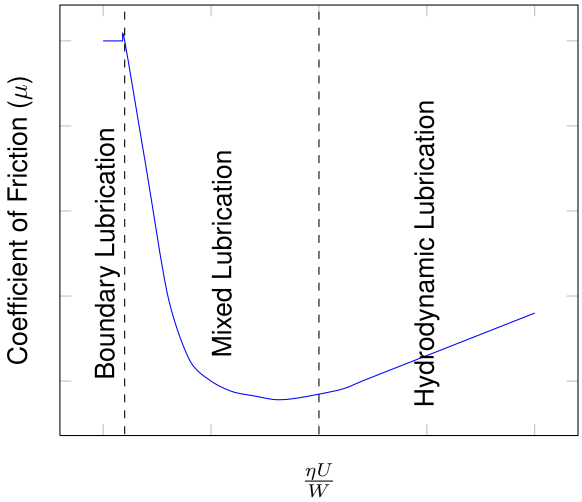

Figure 2.11: The Stribeck curve – showing the variation in friction coefficient with the quantity $\eta U/W$ for a lubricated sliding bearing, where η is viscosity, U is sliding speed and W is the normal load (Hutchings, 1992).

ture – are a particularly poor bearing combination because of the high adhesion force (Stachowiak and Batchelor, 2005). This leads to the shearing-off of asperities and will eventually result in scuffing (Gohar and Rahnejat, 2008).

Scuffing is a serious problem in these diesel engines because the resultant wear will eventually lead to blow-by, reducing performance of the engine (Bhushan, 2001a). Other problems caused by scuffing include high oil consumption, and in the worst cases seizure of the engine (Blau, 1992). Two common methods for reducing friction and wear during running in are by profiling the running face of the piston rings, or by applying a coating to the surface of the ring (Blau, 1992; Clark, 1970).

Running-in coatings are typically phosphate oxide, graphite, or soft metal such as tin or cadmium, and are often applied to all piston rings to maximise time between overhaul (Woodyard, 2004). The phosphorous compounds allow the asperities to flow without surface seizure due to their low shear strength. Graphite based coatings adsorb and form chemical bonds with combustion gases. This weakens the bonding forces and reduces the shear strength of the coating, resulting in it, rather than the cylinder liner, being worn (Bhushan and Gupta, 1991). Soft metal coatings such as the aluminium-bronze alloy used by Man B&W are applied by plating; when the asperities engage, the temperature rises and melts the coating, which then acts as a liquid lubricant. Coatings such as this give protection against seizure in the event of the piston ring being insufficiently lubricated, which is particularly vital during the running in phase of the engine (Bhushan and Gupta, 1991; Clark, 1970).

Some coatings have been developed for more long term benefits. They are often only applied to the top piston ring, since it is under the highest loads and therefore most susceptible to high friction and wear from marginal lubrication conditions (figure 2.11). These coatings have better wear, friction and scuff-resistant properties than cast iron (Blau, 1992).

Long term coatings include plated chromium, as used by Man B&W and Mitsubishi (Woodyard, 2004). It gives a good compromise between scuffing, wear and corrosion resistance with low friction and a resistance to oxidisation at high temperatures. This is achieved in part due to the increased hardness – 700-900 HV for plated chromium as opposed to 200-400 HB for cast iron (approximately 210-425 HV), which increases wear resistance by reducing the surfaces susceptibility to being ploughed by hard, sharp particles (Gohar and Rahnejat, 2008). Plasma sprayed coatings of molybdenum, as used by Man B&W and also found in some Sulzer engines (Woodyard, 2004), are even harder with a rating of over 1000 HV, and are believed to have higher scuffing resistance as a result. Unfortunately oxidisation occurs at 500°C, and the oxidised layer will vaporise at 730°C. Plasma sprayed ceramic (Cr_2O_3), cermet (WC-Co, Cr_3C_2-Ni & Cr_3C_2-Mo) or alloy (Mo-Cr-Ni) coatings have also been developed for improved wear and scuffing resistance under marginal lubrication conditions. A plasma sprayed chromium ceramic type coating is widely used by Sulzer for the top rings in their Tribopack, in order to improve wear resistance (Amoser, 2001; Woodyard, 2004).

There are other factors that affect performance. Research on a low speed MAN-B&W engine led to moving the two uppermost piston rings 30% higher, and plasma-coating or chrome-plating the uppermost ring. This has led to an increased time between overhauls. Sulzer have been testing a top ring which is thicker in the axial direction. This has been shown to reduce wear (Pevzner, 1998a).

Piston ring attitude has also been found to change depending on the speed and load of the engine, and the position at which it is measured. Dragsted et al. (2004) observed the piston ring flicking from one attitude to another on the compression stroke, between mid-stroke and top dead centre. It is expected that the phenomenon also occurs on the expansion stroke, although this has not yet been investigated. According to Mittler et al. (2009), the twisting phenomenon is a result of the changing moment forces acting on the piston ring. These forces are composed of the spring force of the piston ring, the gas pressure acting on it, and the friction and inertia forces. Dragsted suggests the flicking could affect performance by disrupting the oil film at the point of flicking, and by the ring acting as a scraper rather than having a good inlet for squeeze film (a phenomenon that maintains an oil film as a result of the perpendicular motion of the bearing surfaces due to varying normal loads (Hutchings, 1992)), while Mittler and Mierbach add that it will have a significant effect on blow-by.

2.3.4 Lubrication Systems in Large Two-stroke Engines

Large marine diesel engines have a crosshead construction, with the cylinders being lubricated independently of the crankcase. Although this requires a separate system with its own power and maintenance issues, it gives the benefit that the acidic fuels can be kept separate from the crankcase and the rest of the engine by a diaphragm (Pevzner, 1998a), and an appropriate lubricant can be used within the cylinder. This is crucial for preventing corrosion and the associated wear and fatigue problems that it causes (Bhushan, 2001a). Lubrication in these types of engine covers several key functions. Eriksen (2003) summarised these in order of importance as reducing friction between piston rings and cylinder liner, neutralising the acidic nature of the fuel, creating an effective seal between piston rings and cylinder liner, and cleaning by carrying away debris from wear, and the fuel and lubricant. It is only possible to satisfy all these requirements by utilising an independent lubricating system. There are two types of lubricating system that have been implemented extensively in low speed marine engines. These are the timed and accumulator lubrication systems. Both systems have performed effectively for a number of years, as their widespread use confirms, but Eriksen (2003) suggests their efficiency can be questioned based on an increase of cylinder oil consumption in more recent years and the fact that cylinder oil accounts for approximately 70% of cylinder operating costs. Both systems inject drops of the lubricating oil into the cylinder via 4 to 8 lubricating quills positioned circumferentially around the cylinder liner (Pevzner, 1998b). This is distributed circumferentially via a zigzag groove in the liner (figure 2.12) due to the pressure from the piston ring pressing the oil along the groove as it passes, and is vertically distributed by movement of the piston rings (Eriksen, 2003).

Timed lubrication systems inject the oil at a specific point in the engine cycle, typically as the piston rings pass the lubricating orifices during the upward stroke. The lubricators are driven

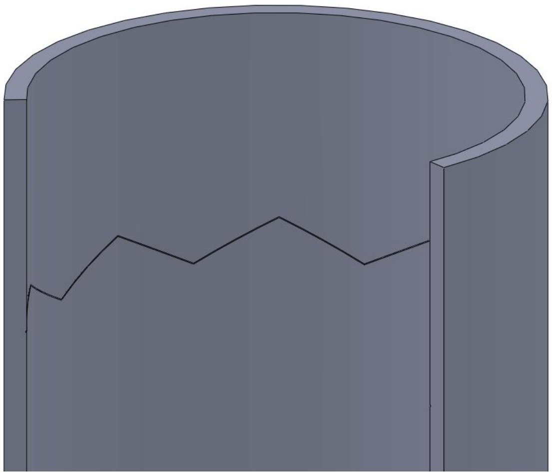

Figure 2.12: Cutaway of a Cylinder Liner showing the Zigzag Lubricating Grooves

mechanically and synchronously with the engine, and the pressurised lubricating oil supply is delivered via a non-return valve on every engine stroke (Eriksen, 2003). The quantity of oil delivered is adjusted – either manually or automatically – to a feed-rate recommended by the manufacturer. The required feed-rate is dependent on several engine design factors and the operating conditions (Pevzner, 1998a). Accumulator lubrication systems inject oil into the cylinder when the pressure in the cylinder is lower than the pressure in the accumulator or non-return valve. Controlling delivery in this way means oil can be injected above, on or below the piston rings (Eriksen, 2003). Sulzer have introduced a modification whereby the oil is injected at two levels on the cylinder liner, which Eriksen suggests will give a better distribution of lubricating oil than by injecting at one level (Eriksen, 2003). Since lubrication is not synchronised with piston position, an independent drive can be used. The advantages of this are the ability to pre-lubricate the cylinder, and adjust the quantity of oil injected – as determined by load conditions – by regulating the pumping frequency of the cylinder lubricator (Eriksen, 2003).

These systems have been used for many years and there is evidence to suggest they are nearing the limit of their capabilities in more modern engines. For example, Pevzner (1998a) found that a current trend to increase oil feed-rate is a result of high specific cylinder power rates, increases in combustion and mean effective pressures, and higher combustion gas temperatures. The result, he said, is that, “The oil film is exposed to blowing and burning, leading to adhesive/corrosive wear in the cylinder-piston complex.” Special devices now have to be installed to control oil supply and prevent excessive feed rates at part engine loads.

There have been some developments in the design of lubrication systems in order to compensate for the insufficient non-return valve pressures that have caused mistimed lubricant delivery for timed systems installed on modern engines. Oil supply can be controlled by linking it to the mean effective pressure (MEP) or brake horsepower (BHP) of the engine, and involves an adjustment of the lubricating oil pump stroke to correspond to the mean effective pressure or load of the engine. Load change dependent systems increase the quantity of injected lubricant for short periods when changes in load lead to thermal instabilities, which increases risk of corrosive and frictional wear. The increased quantity of lubricating oil neutralises acid build-up and reduces friction. Intermittent lubrication allows the frequency of injection to be altered to meet the engines need. The necessary frequency is determined by sensors and an algorithm, but the system is currently uncommon due to a lack of trust in the validity of signals from the control system (Eriksen, 2003).

New systems have also been developed with the aim of achieving improved timing and efficiency. These systems are the Alpha lubrication system and swirl injection lubrication system.

The Alpha lubrication system has much in common with traditional timed systems, but is electronically synchronised with the engine rather than being mechanically synchronised. This allows improved timing based on the position of the crankshaft, and gives the possibility of reducing cylinder oil consumption by altering the injection timing whilst the engine is running. Lubricant is not often injected on each piston stroke, but more typically in the range of each 4th to 7th stroke. Each lubricator has several supply pistons that supply a pre-adjusted quantity of oil on each injection. The quantity of lubricant injected is controlled by the number or revolutions during which injection is skipped. Lubricant quantity is typically regulated by engine load and speed, but a modification of the system also allows regulation to be based on sulphur content of the fuel (Eriksen, 2003).

Dragsted et al. (2004) compared the Alpha system to a mechanical timed lubrication system, and found that for a feed rate of 0.45 grams/BHP-hour (the basic setting on this particular engine being 1.0 g/BHP-hour), the Alpha lubricating system gave consistently thicker oil film thickness. The average increase near top dead centre was about 40% during compression and 44% for the expansion stroke.

Swirl injection lubrication is a development of how the oil is injected and distributed on the cylinder liner, and aims to provide a good oil film distribution with as little oil as possible. Rather than using non-return valves and a zigzag groove, the swirl injection system uses pressurised valves and spray nozzles to inject a fine spray of oil droplets tangentially onto the cylinder liner wall. Delivery is on the upstroke, and effectively covers the circumference of the upper part of the liner, where the wear is typically at its most acute. The piston rings spread the oil vertically as they pass. In contrast to Alpha lubrication, injection is intended to occur on each stroke in order to effectively neutralise the acid from the combustion of sulphurous fuel (Eriksen, 2003).

As a result of serving several purposes, the rate of application of lubricating oil is very important. If the cylinder is under-lubricated the alkaline nature of the lubricant is neutralised before it spreads over the entire cylinder. The result is that although the sulphuric acid in the fuel will be neutralized close to where the lubricating oil is injected, it will remain acidic further away leading to “clover leafing” (see figure 2.13), where corrosion-fatigue wear and corrosion-abrasive wear occurs between the quills but not near them (Bhushan, 2001b). If the cylinder is over lubricated, fouling of the cylinder can occur, as can post-cylinder fires in the engine – particularly in the turbocharger. Over lubrication can also add to maintenance costs (Bhushan, 2001b).

2.4 Marine Engine Lubricants

2.4.1 The Function of Low-speed Engine Lubricants

Lubricants perform a range of tribological functions as required by the application. These, typically, would be to reduce or control friction, reduce wear, prevent overheating and to prevent

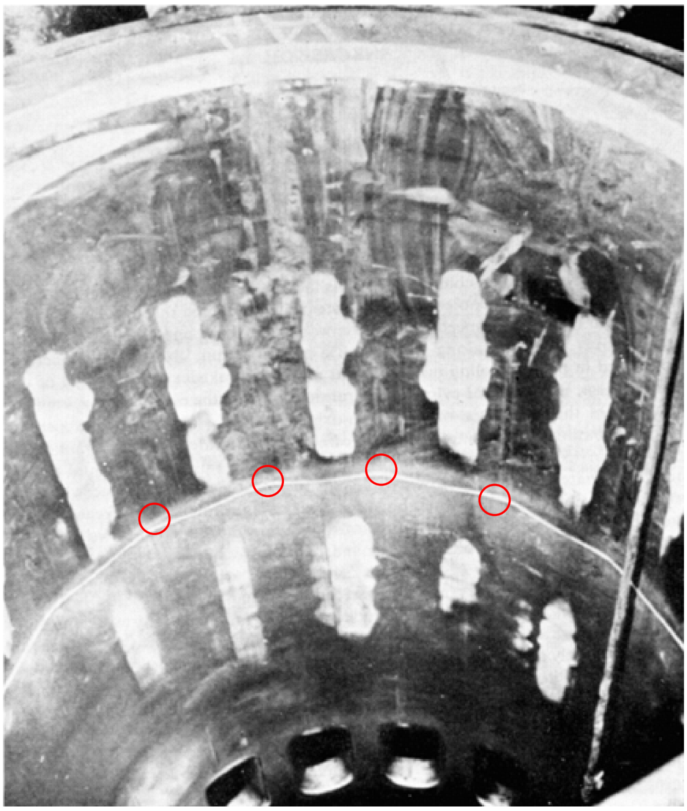

Figure 2.13: An example of clover leafing on a cylinder liner. The positions where oil is injected have been highlighted (Bhushan, 2001b).

corrosion (Lansdown, 2004). Lubricants used in the cylinders of low-speed marine diesel engines certainly need to perform these functions, but can be described more specifically for this application (Woodyard, 2004);

- To assist the formation of the gas seal between piston rings and cylinder wall
- To minimise contact between piston rings and cylinder wall
- To neutralise the corrosive acids in the bunker fuel, and also those created during combustion
- To transport any combustion deposits away from the ring pack and to minimise deposit build up on any of the piston, piston rings and cylinder liner

All these functions serve to maximise performance and increase the life of the cylinder and piston assembly. Under certain conditions the lubricant will attain a sufficient pressure and thickness to support the load between the piston ring and cylinder liner, creating an effective seal between piston ring and cylinder liner and minimising blow-by. This maximises the combustion pressure and in turn maximises the power output from the engine. The separation of the components caused by this lubricant seal will also reduce asperity contact between the metals, and because the shear strength of the lubricant is much less than that of the components the coefficient of friction is reduced (Hutchings, 1992). Furthermore, less metal to metal contact means less welding and shearing of asperities that is typical of the adhesive wear found in low-speed marine engines (Woodyard, 2004). Both frictional losses and wear are therefore reduced – which helps to maximise power output and increase the life of the piston ring and cylinder liner.

Corrosive acids are neutralised by the alkaline nature of the cylinder oil, and any deposits, from combustion or otherwise, can be held in suspension in the oil and carried away as the oil is transported (Woodyard, 2004).

2.4.2 Lubricant Types Used in Marine Diesel Engines

At the most basic level, lubricants are classed as liquid, semi-solid, gas or dry lubricant. Oil is a liquid lubricant, greases are oils that are artificially thickened to become semi-solid, gas lubricants often use air, although any other suitable gas could be used, and dry lubricants are typically powders, solid coatings or some other bulk solid. As with most internal combustion engines the lubricant type most suitable for lubricating the cylinder is oil, because it flows easily and the oil can be easily fed directly to the bearing surfaces as required (Lansdown, 2004).

In some applications it is possible, or necessary, to use a fluid that is not specifically a lubricant but is already present in the system. These are known as process fluids. In chemical industries it could be a coolant, refrigerant or fuel, it could be syrup in the food industry, or some other treatment liquid in tanning or paper making. The properties of these fluids are not intended to make them good lubricants, and often cannot be changed. In these cases the bearing must be carefully designed to function with the process fluid (Lansdown, 2004).

There are several classes of oil: biological, mineral and synthetic. Biological oils are animal or vegetable oils, and are used for applications where risk of contamination must be kept to a minimum. Mineral oils are the naturally occurring petroleum (or crude) based mixes of hydrocarbons. These are extracted and processed, and widely used as lubricants throughout industry. Synthetic oils are developed artificially when superior properties to those provided by mineral oils are required (Stachowiak and Batchelor, 2005). In the case of low-speed marine engines, the combination of viscosity, thermal stability and cost of petroleum mineral oils make them the ideal choice (Woodyard, 2004).

Petroleum is largely composed of hydrocarbons, but these come in a variety of different forms (see figure 2.14). There are three basic types; the most common is paraffin in either straight or branched configuration, naphthene is the second most common type and has most of the carbon atoms incorporated into a cyclic molecule, the third are aromatic molecules which make up a small percentage of petroleum, these also incorporate the carbon ring although the proportion of hydrogen is reduced (Stachowiak and Batchelor, 2005; Lansdown, 2004).

The high viscosity index, good thermal stability and lubricating properties, resistance to oxidisation, high pour point and flash point, and low volatility of paraffinic lubricants make them suitable

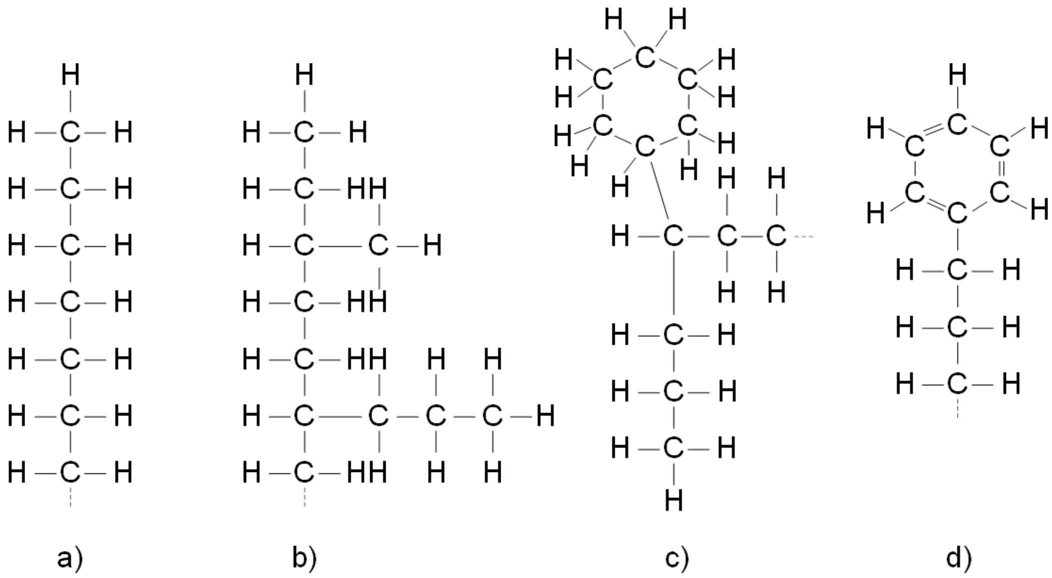

Figure 2.14: Types of mineral oils: a) straight paraffin, b) branched paraffin, c) naphthene, d) aromatic (Lansdown, 2004).

for marine cylinder oils. One drawback is they tend to form hard carbon deposits during combustion, although this can be reduced with suitable blending with naphthenic oils (Mortier et al., 2010)

2.4.3 Additives for Improving Various Aspects of Lubricant Performance

The performance of the base lubricating oils can be significantly improved with the use of carefully chosen additives. Viscosity and durability of the lubricant, and wear and corrosion of the components, can all be enhanced with the addition of small amounts of organic or organo-metallic chemicals (Stachowiak and Batchelor, 2005). Some of these additives are common in many lubricants, as the benefits apply universally. Some additives are more specific to engine oils or the marine environment, or more specifically to cylinder oils for large two-stroke marine diesel engines. Alkaline detergents are added to neutralise any acids formed during combustion. The additives used in marine engines are typically over-based calcium detergents with base number (see section 2.4.4) between 250 and 400. The high alkalinity is necessary because of the high sulphur content of the fuel. The detergents often have a 40% soap content to maintain engine cleanliness and provide additional protection against corrosion and rust (Stachowiak and Batchelor, 2005; Mortier et al., 2010).

Oxidation inhibitors are usually present in lubricating oils to delay the onset of severe oxidation of the oil, which can cause an increase in friction and wear of the engine and consequently affect its performance and lifespan. The oxidisation process occurs in three stages: dissociation of the hydrocarbon molecules to form radicals, a reaction between the hydrocarbons and dissolved oxygen to form peroxides, and the production of hydroperoxides which catalyse further oxidisation (Stachowiak and Batchelor, 2005).

Natural sulphur or nitrogen containing compounds are present naturally in mineral oils, and act as inhibitors by scavenging the radicals produced during the first stage of the oxidation process. The naphthenic oils used for marine lubricants contain less of these natural anti-oxidants than paraffinic oils, and are more prone to oxidation as a result. There are two types of anti-oxidant additive that are commonly used in marine lubricants – radical inhibitors and peroxide decomposers. Radical inhibitors, such as hindered phenols and amines, function by neutralising the peroxide radicals. They have a low volatility and long lifespan and are used in small quantities of around 0.5%-1% by weight. Peroxide decomposers neutralise the hydroperoxides which would otherwise catalyse the oxidation process. Dialkyldithiophosphate is one example of this type of antioxidant which is often added to engine oils in amounts of approximately 1%-2% by weight (Stachowiak and Batchelor, 2005; Mortier et al., 2010).

Marine oils are sometimes contaminated with water, and although this is largely removed by a centrifuge further protection is sought by the addition of rust inhibitors such as sulphonates and phosphonates, or amine succinates. These protect the uncoated ferrous components by attaching themselves to the surface to prevent oxidisation of the ferrous material. Corrosion inhibitors are also added to protect non-ferrous surfaces from the acidic products of combustion. This is through neutralisation with alkaline detergents similar to those already discussed, and the formation of a protective barrier on the surface using an additive such as zinc diethyldithiophosphate, zinc diethyldithiocarbamate or trialkyl phosphites (Mortier et al., 2010; Stachowiak and Batchelor, 2005).

Zinc dialkyldithiophosphate is commonly used as an antioxidant in marine engine oils, but has also been found to protect contacting surfaces from wear under conditions of low load but high temperature. It works by forming a very durable surface layer through the reaction process of chemisorption (the creation of a new chemical species on a surface due to the formation of strong chemical bonds between the surface and additive), which helps to protect the two surfaces. Some compounds are designed to react under extreme conditions of load and velocity. The additive (usually sulphur, iodine or chlorine based) reacts with the metallic surfaces to create a low shear strength film that reduces friction and protects from wear under high loads (Stachowiak and Batchelor, 2005; Mortier et al., 2010).

Dispersants have been developed as a result of problems specific to internal combustion engines. They are added to neutralise any acids formed during combustion, prevent lacquer and varnish forming on the engine components, and to prevent the flocculation or agglomeration of particles and deposits that may clog the oil systems. This need arises firstly because the oil becomes contaminated with products of the fuel and the combustion process, wear deposits, calcium deposits from acid neutralisation, and any other debris from the atmosphere or the fuel. Secondly, the presence of water can accelerate oxidation of the oil, and the sulphur content of the fuel can accelerate corrosion and corrosive wear. An ashless (or mild) dispersant such as polyisobutylene-succinimide is used in marine applications because it will give better diesel performance by reducing lacquer formation, despite not being very effective at dispersing the sludge that is often found in this type of engine (Stachowiak and Batchelor, 2005; Mortier et al., 2010).

Finally there are pour-point depressants and anti-foam additives. Pour-point depressants prevent the generation of wax crystals at low temperatures. Most marine cylinder lubricants are produced with a pour-point in the region of -10C, which is usually adequate without the need for depressants. Anti-foam additives are silicone based and oil insoluble, and are to destabilise any foam generated during operation. They are used only in very small quantities (0.05% to 0.5%) and must be well dispersed to be effective (Stachowiak and Batchelor, 2005; Mortier et al., 2010).

2.4.4 Categorisation of Marine Cylinder Lubricants

Lubricants are often categorised by their SAE viscosity grade. This is a number that indicates the viscosity of the lubricant as standardised by the Society of Automobile Engineers (SAE). However, all current marine cylinder oils have an SAE viscosity grade of 50, so they are categorised primarily by the total base number (TBN) of the lubricant. The total base number is defined in Engineering Tribology (Stachowiak and Batchelor, 2005) as “the amount of potassium hydroxide in milligrams necessary to neutralise the hydrochloric acid (HC1) which would be required to remove the basicity in 1 gram of oil.”

For example, Castrol have a range of three crosshead engine cylinder oils, where the major difference between them is the total base number (table 2.1).

Typical Characteristics	Cyltech 50S	Cyltech 70	Cyltech 80AW
Density at 15C (kg/l)	0.930	0.940	0.950
Viscosity at 100C (cSt)	19.5	19.5	19.5
SAE Number	50	50	50
Base Number	50	70	80
Closed Flash Point (C)	$>$190	$>$190	$>$180
Pour Point (C)	-9 or below	-9 or below	-9 or below

Table 2.1: Technical data for Castrol cylinder oils (Castrol, 2013; Castrol, 2017; Castrol, 2014)

The different base numbers allow for use with fuels of differing sulphur content, which is now required as a result of the introduction of sulphur emission control areas in the Baltic Sea, North Sea and English Channel, and the Californian coast. Cyltech 70 is the standard cylinder oil which has sufficient alkalinity for use with the standard bunker fuels. These fuels currently have high sulphur content, typically over 4.5% by weight. The Cyltech 50S oil is formulated for prolonged operation with fuels with less than 1.5% sulphur content in order to minimise the formation of calcium carbonate deposits. Cyltech 80AW has an increased base number which offers higher neutralising capability and offers increased protection against corrosive wear.

There are also subtle differences in the additives of these oils, which are combined to best suit the proposed application of that lubricant. For example, both the Cyltech 70 and Cyltech 80AW oils have acid-neutralising, detergent and ashless dispersant additives to maintain the cleanliness of the cylinder and piston-rings. In addition to this, the Cyltech 80AW has a blend of anti-wear (AW) additives that give extra protection against scuffing from metal to metal contact in the event of oil film breakdown under extreme operating conditions.

This form of categorisation is not limited to Castrol products. Equivalent methods can also be seen in the literature for Shell, BP and Exxon-Mobil marine cylinder lubricants, although some of these companies also represent the SAE viscosity grade in the lubricant name for consistency with their entire engine lubricant range.

2.4.5 Evolution and Development of Marine Lubricants

There has always been a need for lubricants to develop in line with progress in engine design and the subsequent improvements in performance. The increased temperatures and pressures that have arisen from the demand for more power or better fuel economy, and the higher stroke to bore ratios that have been introduced to satisfy the desire to burn cheaper, poorer quality fuels have dictated the trends in lubrication development. There is also an increasing need for lubricants to evolve due to the introduction of new environmental legislation (such as the introduction of SECA's) and ever increasing oil costs (Woodyard, 2004).

The most significant trends over the last twenty years have been in response to the changes in engine design. The demand for more efficient and economic engines has resulted in longer piston strokes, reduced engine speed, and higher firing pressures and temperatures. This causes several issues for the lubricant. Achieving a satisfactory spread of lubricant on the cylinder liner can be difficult, and maintaining a satisfactory oil film thickness at the increased pressures and temperatures becomes problematic (Smith, 1986).

The spreadability problems from increased stroke lengths have led to improved lubricating systems to ensure the top of the cylinder is adequately lubricated, as this is typically where the highest wear takes place (Lauritsen et al., 2001). Different solutions exist and include an increased number of lubricant delivery quills that are split between two levels on the cylinder liner, or the new alpha and swirl injection systems that are described in section 2.3.4.

The trend towards increased pressures caused problems because the oil film has to support a greater load. As cylinder temperatures rise the oil becomes less viscous, resulting in it being less capable of supporting this load – as shown by Reynolds tilted pad slider bearing theory (Hutchings, 1992) – and leading to the onset of adhesive wear. Base oil and additive combinations have been developed to enhance oil film thickness by reacting with the bearing surface to form a thin, non-corrosive chemical film. This has lower shear strength than the metal surface of the bearing and is removed as the piston ring slides past before reforming ahead of the next pass. The effectiveness of this film reduces with increasing temperature because the chemical bonds break causing de-absorption of the additives from the surface, although the lubricants were systematically improved to function at temperatures greater than 250C (Woodyard, 2004; Bhushan, 2001a).

One of the key drivers of lubricant development has been the introduction of legislation dictating the use of fuels with low sulphur content. The requirement to run low sulphur fuels is currently limited to a few busy shipping areas, and because it is less economic ships will often switch between the standard and low sulphur fuels as they enter and leave these zones. The lower sulphur content results in less acidic by-products being produced during combustion, and leaving the lubricant and feed rate unchanged can lead to the formation of hard calcium deposits on the piston top land which in turn can lead to abrasive wear (Welsh, 2002; Havil, 2008).

The first solution, and particularly appropriate if it is only for a short period, is to reduce the lubricant feed rate. Wärtsilä have shown this is possible providing the components are in good condition (although there is a risk that there will be insufficient oil to form a stable oil film), although the low feed rate will lead to corrosive wear should the engine load be reduced over a long period because the temperature and pressure in the cylinder will be below the dew point curve of the sulphur trioxide. The alternative is to use a low base number lubricant, since there will be less sulphuric acid to neutralise. Typical low base number lubricants have base number between 30 and 50, the best of which are produced by substituting some of the high base number additives with other additives as opposed to simply diluting with suitable base oil. Adjustments to the feed rate can be made in the event that a risk of corrosive wear arises (Welsh, 2002; Aabo, 2005).

A development that provides an alternative to the above is the introduction of Lubmarine's Talusia Universal cylinder oil. This has been developed for use with fuels having sulphur content between 0.5% and 4.5% by weight using additives that have never before been used in marine cylinder oils. These were reported in Marine Engineering Review to "enhance the speed and efficiency of the lubricant while neutralising the acidity formed during the combustion process". Precise details regarding the additives and how the lubricant functions effectively on such a broad range of fuels are as yet unpublished, although sea trials have been successfully completed by a number of operators (Havil, 2008; [Anon], 2008).

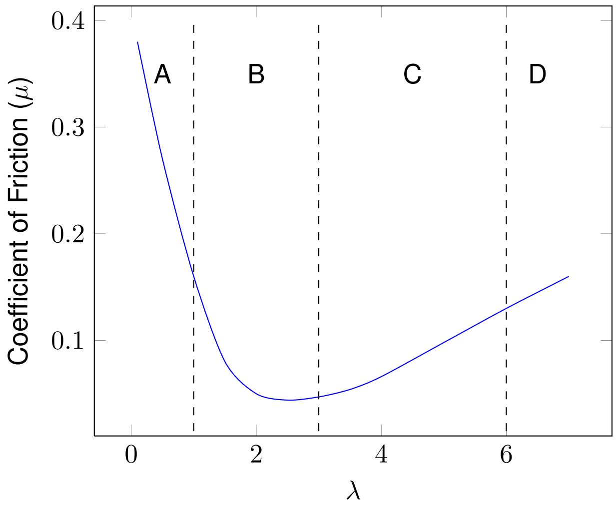

Figure 2.15: Regimes of lubrication as a function of oil film thickness to composite r.m.s. surface roughness, λ (Bhushan and Gupta, 1991; Hutchings, 1992)

It is not foreseen that improving engine design and the introduction of new legislation will exceed the lubrication capabilities of mineral based oils, although the ever-increasing cost of oil could eventually influence a shift to the use of synthetic oils for marine engine applications (Smith, 1986).

2.5 Oil-film Thickness Measurement

2.5.1 The Tribological Significance of Oil-film Thickness

The significance of oil film thickness lies in the fact it influences the frequency of asperity contact between the surfaces in the system. This relationship has a direct impact on friction and wear, which – as explained in section 2.4.1, affect engine performance in terms of the power lost to heat and in deformation of the bearing surfaces. The latter is an important factor regarding the durability of an engine. It also plays a vital role in creating an effective seal to maximise the power extracted from the combustion pressures.

The relation between oil film thickness and asperity contact is categorised into three broad lubrication regimes by using surface roughness to represent asperity contact. These regimes are boundary lubrication, mixed lubrication and hydrodynamic lubrication (Bhushan and Gupta, 1991).

Figure 2.15 shows how friction coefficient varies as a function of λ, the ratio of oil film thickness to composite r.m.s. surface roughness for these different regimes. Boundary lubrication occurs in region A, where the oil film is not thick enough to separate the two surfaces and there will be considerable interaction between asperities. This can be caused by high pressures or very low sliding speeds, and will result in high friction and wear rates unless a lubricant with suitable extreme-pressure additives is used (Hutchings, 1992).

Regions C and D are where a full oil film exists and there is negligible asperity interaction, leading to much lower wear rates. These regimes are known as elastohydrodynamic and hydrodynamic lubrication respectively. In hydrodynamic lubrication the pressure that supports the load is generated by the sliding action between the two bearing surfaces, which must be converging in order for the hydrodynamic film to form. As seen in figure 2.11, the friction coefficient (μ) is proportional to the dynamic viscosity (η) of the lubricant, the relative velocity of the sliding surfaces (U) and the load the lubricant is supporting (W) (Hutchings, 1992; Lansdown, 2004).

$$\mu \propto \frac{\eta U}{W} \tag{2.1}$$

Elastohydrodynamic lubrication is a special case of hydrodynamic lubrication which occurs in some heavily loaded contacts, typically those with counterformal surfaces, that results in a point or line contact. Examples of cases with counterformal faces include gears, cams and their followers, or ball and roller bearings. The film thickness between the two surfaces is very small because the loads are high, and so the lubricant is subjected to very high pressures as it enters into this space. The result is an increase in the viscosity of the lubricant and a subsequent increase in the film thickness. Also, because the load between the bearing surfaces is high, it causes one or both of the surfaces to deform elastically, such that the load is spread over a larger, flatter area (Lansdown, 2004; Hutchings, 1992).

In the mixed lubrication regime – region B in figure 2.15, the load is supported in part by a full hydrodynamic oil film and partly by boundary lubrication. Consequently there is some asperity interaction and the wear rate will be higher than for hydrodynamic lubrication, but lower than for boundary lubrication (Gohar and Rahnejat, 2008; Hutchings, 1992).

The oscillatory nature of motion of a piston ring results in it operating in a range of these regimes. This has been demonstrated by Moore (1998), who showed the film thickness on a large marine diesel engine decreasing from over 100 μm to 1 μm in the time it took for the top piston ring to arrive and depart from the oil film thickness transducer at top dead centre. The reason the range is so wide is due to the variation in the speed of the piston and the pressure in the cylinder. In fact Moore suggests that were it not for the squeeze film effect (described in section 2.3.3) metal-to-metal contact would occur at top dead centre due to the very low velocity and the sudden rise in gas pressure. Understanding piston ring tribology is critical for the design of effective components that will maximise performance in terms of power and efficiency, and minimise the wear to ensure the components are long-lasting and trouble-free.

In relation to the lubrication of piston rings in a marine diesel engine, the level of lubrication in the cylinder is also important because of its acid neutralising capabilities. The new SECA sulphur limits have led to vessel operators having to either reduce lubricant feed-rate or switch to a low base number lubricant. Whichever method is chosen, it is important the correct amount of lubricant is introduced into the cylinder to maintain an adequate oil film and to balance the acidity of the combustion gases. Failure to do this correctly could lead to unwanted levels of corrosive or abrasive wear, as discussed in section 2.4.5.

2.5.2 Measurement of Oil-film Thickness

The complex nature of lubrication and wear in an operating engine (summarised in section 2.4.4) has led to a great deal of research being carried out in this field. One aspect of this research is the monitoring of oil film thickness using a variety of techniques. These methods can be grouped as electrical, optical or acoustic. The electrical methods are based on the principles of electrical resistance, capacitance or induction. The optical methods are laser-induced fluorescence and optical interferometry. The acoustic method uses ultrasound techniques.

Although these methods serve the same purpose they all have different advantages and disadvantages. For example, some can only be used in the laboratory, while others can provide instant results from a firing engine; and they all vary in the range of film thicknesses they measure. The following sections aim to summarise these differences along with an overview of how each method functions.

A review of these methods is important in the context of this study because a lubrication control system will have to monitor the oil film in order to provide the necessary feedback to deliver the appropriate amount of lubricant. If a transducer is to be installed on an operational vessel it would need to be accurate, reliable and durable in the harsh environment of a marine diesel engine cylinder.

Electrical Methods for Measuring Oil-film Thickness

Electrical Resistance It is possible to investigate the oil film thickness in a bearing or an engine by passing a current through the lubricating oil and calibrating the potential drop in terms of resistance. This method allows measurements to be made on a running engine by insulating the piston ring, or part of it, from the piston and using it as one electrode, and using the cylinder wall as the other. According to Courtney-Pratt and Tudor (Courtney-Pratt and Tudor, 1946) the method is simple and quick to configure and use.

If the bearing is hydrodynamically lubricated, the resistance will be very high because of the low conductivity of the oil. However, if there is a break-down in the oil film and the bearing surfaces come into contact with each other, or within close enough proximity for the electric current to spark the gap, the resistance will drop considerably (Courtney-Pratt and Tudor, 1946; Furuhama and Sumi, 1960).

The method allows the oil film thickness to be tracked for the entire engine cycle, although large differences in resistance make observation of small variations in oil film thickness difficult.

Electrical Capacitance The electrical capacitance method also uses the piston ring as an electrode, but in this case the opposing electrode is an insulated transducer in the cylinder liner. These make the two plates of a capacitor, the dielectric between them being the lubricating oil, for which the dielectric constant must be known. The oil film thickness can measured because the capacitance is inversely proportional to the distance between the plates. The capacitances are only small (according to Grice et al. (1990) between 0.1 pF and 5 pF), but a specially developed charge amplifier is employed to generate an output voltage proportional to the gap size (Grice et al., 1990; Moore, 1993).

This method has been commonly used since its inception, and as long as the system has been properly calibrated and the engine run-in to ensure the transducer is flush with the liner, it has proven to be accurate with good repeatability of results. It is also robust and reliable enough for extended use in a firing engine (Grice et al., 1990; Moore, 1993). Use of capacitance is ideal for measuring piston-ring oil-film thickness because its range covers from 0.5 μm to 20 μm, which is typical of what is expected in an internal combustion engine. The major drawback here, as with the resistance method, is that an electrical short will produce erroneous results should there be any contact between the bearing surfaces (Moore, 1993; Hamilton and Moore, 1974; Grice et al., 1990).

The good resolution that is possible allows the piston ring profiles to be determined, as long as the piston ring is fully flooded and with no cavitation (see figure 2.16). If cavitation occurs the measured value will be higher than the true value due to the change in dielectric constant (Grice et al., 1990; Hamilton and Moore, 1974).

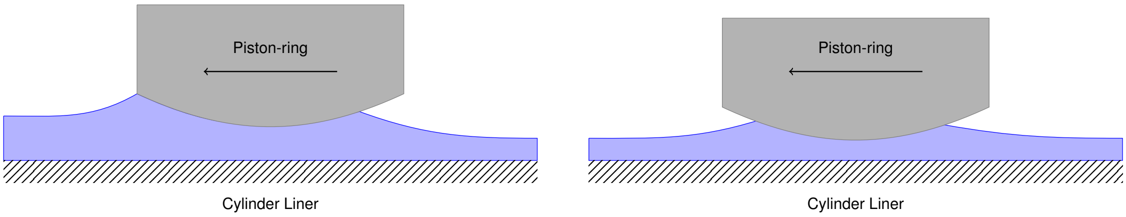

(a) Fully-flooded piston-ring

(b) Starved piston-ring

Figure 2.16: Fully-flooded (a) and starved (b) piston ring, both cases show cavitation at the trailing edge.

Inductance This method uses the electromagnetic principle of inductance to measure the distance between the piston ring and the cylinder liner. A proximity transducer is made from a magnetic armature and a core that has a certain number of wire windings around it. The core is mounted in the cylinder liner and the piston ring is the armature. As the piston ring moves past the core the magnetic flux crosses the gap and induces a current in the windings. This current can be measured to give the size of the clearance between the two components, which is determined by the oil film thickness. The method is most sensitive in the range 5 μm to 250μm, and has a resolution as fine as around 0.1 μm. (Lewis, 1974; Dow et al., 1983; Hamilton and Moore, 1974).

The main issue with the inductance method is that it measures the size of the gap between piston ring and cylinder as opposed to the thickness of the oil film. The consequence of this is there is no indication of whether the piston ring is fully flooded or starved at the leading edge, or if there is cavitation at the trailing edge (Lewis, 1974).

Other problems include needing a rapid response from the probes because the ring is only thin and passes the probe quickly, errors resulting from temperature changes affecting the resistance of the windings, and the system having low electrical efficiency as a result of resistive losses dominating the inductance of the coil (Lewis, 1974; Dow et al., 1983).

Optical Methods for Measuring Oil-film Thickness

Laser Induced Fluorescence The laser induced fluorescence method is based on the concept that oil will fluoresce when laser light is shined onto it. The intensity with which it fluoresces is related to the thickness of the oil film, thus allowing it to be measured (Richardson and Borman, 1991). This method originally required the use of a transparent cylinder, and gave only uncalibrated, qualitative data (Richardson and Borman, 1991). In modern methods the laser is carried along fibre optic cable to a probe, which can be mounted in the cylinder liner or in the piston ring – the latter allowing for continuous oil film thickness measurements to be taken during the entire engine cycle. The wavelength of the exciting laser radiation is typically 488nm, while the fluorescence radiation – which has a wavelength of 540nm, is picked up by a photo-multiplier (Weimar and Spicher, 2003).

Laser induced fluorescence gives a linear measurement between 4 μm and 40 μm, and can show clearly the ring pack allowing for evaluation of piston ring profiles (Richardson and Borman, 1991). There are several important problems with this method though. When the oil is first exposed to laser light the intensity of the fluorescence will be high, but will decrease upon subsequent exposures. This phenomenon is known as bleaching, and because the level of bleaching is non-linear, and depends on factors such as laser-intensity, oil-film thickness and temperature, an oil change is required for any subsequent measurements (Richardson and Borman, 1991).

If the technique is to be employed in a fired engine it requires a dynamic calibration technique due to the changing composition and temperature of the oil affecting its fluorescence. This has been achieved successfully by Sanda et al. (1993) by using a piston ring with stepped grooves of a known depth, and a fluorescent die that is less severely affected by the temperature and oil composition. The effects of bleaching, temperature and oil oxidisation were found to have a negligible impact on their results. Reduction in the intensity of the fluorescence is only 5% in 30 minutes if laser intensity is reduced and filtered, and the issue with changing temperature can be overcome by using the stepped groove calibration as long as the temperature variance is small and the relationship between fluorescence and oil film thickness remains linear. The calibration technique is not without its own difficulties though. For example, it requires steps of height less than 15 μmm to be ground or etched onto the piston ring, and the re-calibration process to be executed for each engine cycle.

Other problems with the technique exist. If employed in a firing engine, the fibre optics are susceptible to becoming dirty. In some cases, for example on the skirt of the piston, the system will measure the thickness of two oil films (one on the skirt and the other on the cylinder liner) (Richardson and Borman, 1991).

Interferometry With interferometry white or monochromatic light is shone on the oil film, and the intensity of the reflected interference pattern analysed to give the oil film thickness. The method can be applied using white light, which gives better resolution such that film thicknesses of less than 1 μm can be measured, or monochromatic light that allows the measurement of film thicknesses of up to “several micrometers” (Bassani and Ciulli, 1996). With either method the minimum oil film thickness detectable is 0.1 μm, although the resolution using white light is 0.03-0.06 μm as opposed to 0.1 μm using monochromatic light (Bassani and Ciulli, 1996).

One of the major concerns with this technique is that the colours (which represent oil film thickness) can be interpreted inaccurately. However, it does allow for quick evaluation of the results over the measured region (Bassani and Ciulli, 1996). Marklund and Gustafsson (2001) developed an algorithm to analyse the results, and as a result have achieved a higher accuracy than originally possible. They also implemented a calibration-based method that allows the measurement of thin films between 80 nm and 750nm. This is done using white light, although a major difficulty with this method is the required construction of look-up tables.

The key limitation of this method is that it requires one of the bearing surfaces to be transparent, or for one of them to have a transparent window. This currently restricts its use to the laboratory (Bassani and Ciulli, 1996). Finally, there is an issue with the refractive index of the lubricant being pressure dependent. This makes it very difficult to implement in an engine cylinder because the pressure of the oil film varies constantly due to the relation between the velocity of the piston and crank angle (Marklund and Gustafsson, 2001).

Acoustic Methods for Measuring Oil-film Thickness

Ultrasound Ultrasonic methods involve focussing ultrasonic waves on the oil film and processing the reflected pulses to compute the film thickness. To do this an ultrasonic transducer must be positioned on the outermost bearing surface to emit and receive the pulses. If the oil film thickness is greater than 40 μm, ultrasound can be easily employed by measuring the difference between the time of flight for the ultrasonic pulse reflections from the front and back surfaces of the bearing. Alternatively, oil films greater than 10 mm can be estimated by finding the resonant frequency for the lubricant film by obtaining the impulse response, which is related to the film thickness and acoustic properties of the oil. If the oil film is thinner than this it is necessary to find its stiffness. By relating the density, speed of sound and the thickness of the layer to the reflection coefficient it is possible to measure the thickness of very thin films, as long as the properties of the oil can be determined (Dwyer-Joyce et al., 2003).

Between them these methods allow the measurement of oil film across a wide range of thicknesses, for both hydrodynamic and elastohydrodynamic lubrication regimes. The method is non-invasive too, because the pulses will propagate through the bearing shell. The method can therefore be used to provide measurements on real bearing components.

Ultrasonic methods have been used for non-invasive studies of piston-ring oil-film thickness in both motored and firing engines (Mills et al., 2015; Avan et al., 2010b), showing favourable measurements compared to those using other techniques. These authors have also adopted ultrasonic transducers to map piston skirt oil-film thickness, allowing observations of piston skirt compliance and secondary motion of the piston (Mills et al., 2014; Mills, 2014), and to perform simultaneous oil-film thickness and friction measurements in a piston-ring-liner reciprocating test rig (Avan et al., 2010a; Avan et al., 2011). The use of ultrasonic sensors has been further developed to allow in-situ measurements of journal bearing lubricant viscosity by use of a quarter-wavelength matching layer that increases acoustic response (Schirru et al., 2015; Schirru and Dwyer-Joyce, 2016). The technique has been used to show the effects of shear heating on local viscosity - particularly in the high temperature and high load region of the contact - by comparison with an isothermal solution to Reynolds equation (Schirru et al., 2018).

2.5.3 Commercially Available Oil-film Thickness Sensors

There are a range of transducers available that could be used for oil film thickness, but all have significant drawbacks if being considered for use in an operating engine. Capacitance, inductance and ultrasonic transducers are the most commonly available commercial sensors.

A wide range of capacitance transducers are available at IFM Electronic (www.ifm.com). Many of these would not sit flush in an engine cylinder, and of those that would the smallest available had diameter 12 mm and length 60mm. The key dimension on a transducer of this type is the diameter of the central conductor, which according to Moore (1993) should be less than 1 mm if the piston ring has thickness less than 10 mm, or should be 2 mm is the thickness is greater than this. IFM do not disclose this information with their product data, so it is not possible to determine how suitable this transducer would be. Regardless of this their range is from 1 mm to 6mm, and with a temperature range of between -25C and 70C they would not be suitable for installation in an operational engine.

An alternative sensor was found at Lion Precision (www.lionprecision.com) with a range of 10 mm to 6mm. The outer diameter was only 5mm, but the temperature range – 4C to 50, would still render it unsuitable for installation in an engine.

Table 2.2 shows the technical data for a range of cylindrical sensors (with integrated cable) by Micro Epsilon (www.micro-epsilon.com). Sensors of this type would potentially be suitable due to the wide temperature range and the appropriate sensitivity and measuring range. The company also do a range of inductive sensors, but with a minimum resolution of 2 μm these would not be as suitable.

2.6 Summary

The literature survey has highlighted a number of challenges facing marine engine operators. The widespread adoption of fuel switching as a strategy for meeting emissions regulations when entering and leaving the sulphur emission control areas leads to a need also for a change in cylinder oil and hence viscosity. As a result, the lubricant feed rate must be adjusted appropriately while maintaining a satisfactory distribution of lubricant on the cylinder liner for both neutralising acidic content of the fuel and for providing a hydrodynamically lubricated contact between the piston-rings and cylinder liner.

The relationship between oil-film thickness (as a multiple of the composite surface roughness) and coefficient of friction shows a minimum exists at approximately three times the composite surface roughness, which corresponds with the lower limit for hydrodynamic lubrication. This, along with increasing cylinder oil costs, motivates a reduction in lubricant consumption. A number of different systems for delivering lubricant to the cylinder exist, and while these have successfully led to reductions in lubricant feed-rates, it is shown that there are currently no systems incorporating oil-film thickness measurement to reduce this further towards the lower limit of hydrodynamic lubrication.

While commercial oil-film thickness sensors have drawbacks, the capacitance and ultrasound techniques for oil-film thickness measurement have the potential to enable the realisation of a feedback system for controlling lubricant feed-rate and hence oil-film thickness. A system of this kind, with lubricant base number controlled independently of lubricant feed-rate, could lead to both reduced cylinder oil consumption as well as a reduction in frictional losses. The subsequent chapters present the theory associated with hydrodynamic lubrication, and its adoption for the development of an algorithm for predicting oil-film thickness following specific initial distributions on the cylinder liner. In addition, the results of experimental investigations into the relationship between lubricant feed-rate and oil-film thickness and lubricant transport are presented.

Sensor Type	CSH02-CAm1,4	CSH05-CAm1,4	CSH1-CAm1,4	CSH1,2-CAm1,4
Article number	6610086	6610087	6610088	6610089
Measuring range	0.2 mm	0.5 mm	1 mm	1.2 mm
Linearity 1)	± 0.05 % FSO	± 0.05 % FSO	± 0.05 % FSO	± 0.05 % FSO
Resolution 1) (static, 2Hz)	0.15 nm	0.38 nm	0.75 nm	0.9 nm
Resolution 1) (dynamic. 8.5kHz)	4 nm	10 nm	20 nm	24 nm
Temperature stability zero 4)	-19 nm/°C	-19 nm/°C	-19 nm/°C	-19 nm/°C
Temperature stability sensitivity	-12 ppm/°C	-12 ppm/°C	-12 ppm/°C	-12 ppm/°C
Temperature range (operation)	-50 . . . +200°C	-50 . . . +200°C	-50 . . . +200°C	-50 . . . +200°C
Temperature range (storage)	-50 . . . +200°C	-50 . . . +200°C	-50 . . . +200°C	-50 . . . +200°C
Air humidity 2)	0 . . . 95% r.H.	0 . . . 95% r.H.	0 . . . 95% r.H.	0 . . . 95% r.H.
Sensor dimensions	⌀8 × 14 mm	⌀8 × 14 mm	⌀12 × 14 mm	⌀12 × 14 mm
Active measuring area	⌀2.6 mm	⌀4.1 mm	⌀5.7 mm	⌀6.3 mm
Guard ring width	1.9 mm	1.2 mm	2.4 mm	2.1 mm
Minimum target diameter	⌀7 mm	⌀7 mm	⌀11 mm	⌀11 mm
Weight (incl. cable and connector)	30 g	30 g	33 g	33 g
Material (housing)	1.4104 (magn.)	1.4104 (magn.)	1.4104 (magn.)	1.4104 (magn.)
Integrated cable	⌀2.1mm× 1.4m axial	⌀2.1mm× 1.4m axial	⌀2.1mm× 1.4m axial	⌀2.1mm× 1.4m axial
Mounting	radial clamp	radial clamp	radial clamp	radial clamp

Table 2.2: Capacitive sensor data for Micro Epsilon transducers (Micro-Epsilon, 2012)

Chapter 3

Piston-ring Lubrication - Theory and Modelling

3.1 Introduction

This chapter outlines the implementation of a piston-ring lubrication algorithm. The purpose of this algorithm is to help study the spatial and temporal distribution of lubricant on the cylinder liner over one or more cycles, following an initial, non-uniform distribution of oil. To enable this, oil-film thickness between piston-ring and cylinder liner must be simulated, and the subsequent transport of lubricant around the cylinder liner must be included. Friction force is also estimated over the cycle to help determine the lower limit of lubricant injector flow-rate. The algorithm allows the calculations to continue for a number of revolutions of the engine, with lubricant being injected at intervals, to allow the oil-film thickness and lubricant transport during this time to be assessed.

Theoretical aspects underpinning the model are described, most notably the fluid dynamics involved. So too are details on the implementation of this theory, with reference to the finite difference method and the flow-continuity algorithm employed to compute the hydrodynamic pressure, along with oil-film thickness and other variables. Further to this, verification of the model is presented using a series of tests against reliable data. Also detailed is the method used for estimating the initial oil-film distribution from the four lubricant injectors.

3.2 Hydrodynamic Lubrication Theory

Hydrodynamic lubrication involves a relatively thin layer of lubricant between two surfaces (Hutchings, 1992), and according to Stachowiak and Batchelor (2005) there are two conditions that must be satisfied for this to occur:

- The surfaces must be moving at sufficient velocity relative to one another
- The surfaces must be inclined at some angle to each other

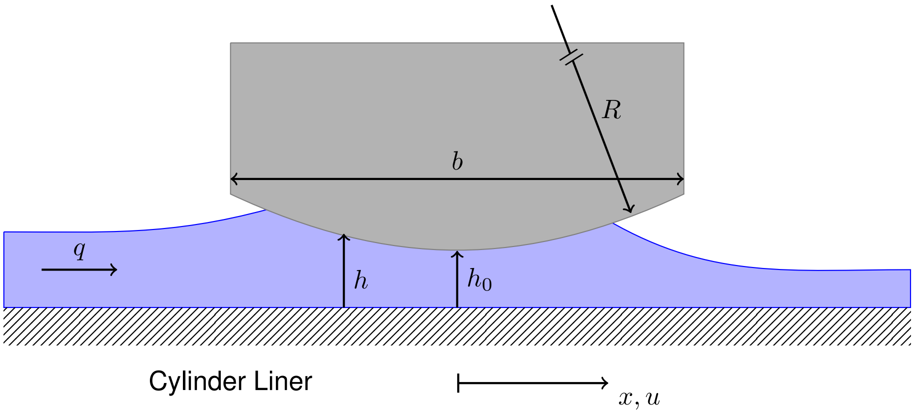

Figure 3.1: Oil-film thickness parameters, where $b =$ ring-face height, $h =$ distance from cylinder liner to ring-face, $h_0 =$ minimum oil-film thickness, $q =$ lubricant flow-rate, $R =$ ring-face radius, $U =$ piston-ring speed.

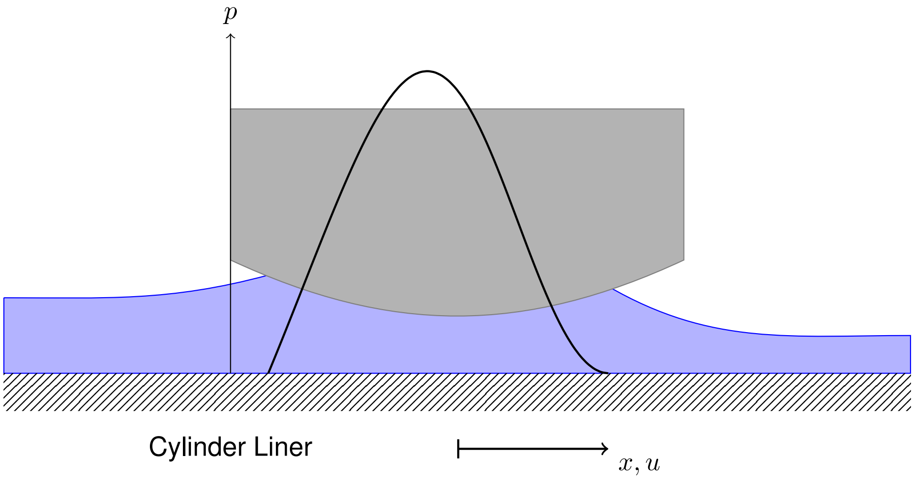

Figure 3.2: A typical hydrodynamic pressure distribution under a piston-ring.

In the case of a piston-ring (figure 3.1) these two conditions are met for a considerable portion of the engine stroke, as such it is reasonable to assume hydrodynamic lubrication during this time - as long as lubricant is present. The separation is achieved by the hydrodynamic pressure generated in the fluid between the two surfaces supporting the normal load (figure 3.2). Osborne Reynolds (1886) derived an analytical theory for hydrodynamic lubrication and this can be used to compute the pressure distribution as long as the parameters for the surface and lubricant are known. This model is reliant on a number of simplifying assumptions, such as the lubricant must be a Newtonian fluid, any lubricant flow must be laminar, and density must be constant throughout the lubricant (Stachowiak and Batchelor, 2005). The full Reynolds equation in 2-dimensions is given in equation 3.1.

$$\frac{\partial}{\partial x}\left(\frac{h^3}{\eta}\frac{\partial p}{\partial x}\right) + \frac{\partial}{\partial y}\left(\frac{h^3}{\eta}\frac{\partial p}{\partial y}\right) = 6\left(U\frac{dh}{dx} + V\frac{dh}{dy}\right) + 12(w_h - w_0) \tag{3.1}$$

Where x and y are the distances in the two directions of sliding, U and V are the sliding velocities in the axial and circumferential directions respectively, h is the distance between the surfaces, p is the hydrodynamic pressure, and w_h and w_0 are the fluid velocities in the direction normal to the sliding plane (Stachowiak and Batchelor, 2005).

It is possible to ensure that one of the axes (x in this case) is in the direction of sliding, and as such V can be assumed to be zero and the equation can be simplified (3.2).

$$\frac{\partial}{\partial x}\left(\frac{h^3}{\eta}\frac{\partial p}{\partial x}\right)+\frac{\partial}{\partial y}\left(\frac{h^3}{\eta}\frac{\partial p}{\partial y}\right)=6U\frac{dh}{dx}+12(w_h-w_0) \tag{3.2}$$

This relationship is used to find the pressure distribution in the lubricant and to evaluate it against other forces acting on the piston-ring. Consequently the piston-ring oil-film thickness can be found for which these forces equate.

3.2.1 Steady, Laminar Flow between Parallel Plates - Couette and Poiseuille Flow

While the calculation of the pressure distribution acting on the piston-ring face is key to evaluating the oil-film thickness, it is also important to establish the flow rate of lubricant under the piston-ring. This is necessary to compute the level of starvation in the event of the piston-ring inlet not being flooded, and also to ensure that flow continuity is satisfied. This fluid flow is driven by a combination of Couette flow and Poiseuille flow - the former being caused solely by movement of one or both surfaces (Massey, p. 205), while the latter is caused by a difference in pressure at two ends of the system. Conservation of momentum can be applied in order to ascertain the flow rate of lubricant through the conjunction.

The conservation of momentum principle, which is a statement of Newton's second law, can be stated as shown in equation 3.3.

$$\text{Time Rate of Change of Momentum} = \text{Resultant Force} \tag{3.3}$$

The right hand side of this equation, the resultant force, is the sum of forces acting on the lubricant (ρf_x), and the pressure and viscous forces ($\mathbb{F}_{viscous}$) acting on the control volume. These forces can be expressed mathematically as shown in equation 3.4.

$$\text{Resultant Force} = -\frac{\partial p}{\partial x}+\rho f_x+\mathbb{F}_{viscous} \tag{3.4}$$

The left hand side of Newton's second law is a combination of momentum changes with time due to unsteady fluctuations of flow inside the fluid, and the net flux of momentum out of the

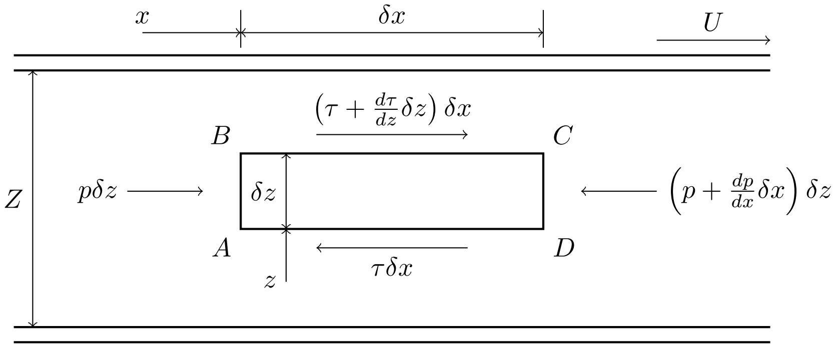

Figure 3.3: Pressure and viscous forces on an incompressible control volume ($ABCD$) within a flow between flat, parallel plates (Douglas, 2005)

control volume. Again, applying this to fluid flow gives equation 3.5.

$$\text{Time Rate of Change of Momentum} = \frac{\partial(\rho u)}{\partial t} + \nabla.(\rho u\underline{\mathbf{V}}) \tag{3.5}$$

Giving the full momentum equation in the axial direction of the cylinder as shown in equation 3.6.

$$\frac{\partial(\rho u)}{\partial t} + \nabla.(\rho u\underline{\mathbf{V}}) = -\frac{\partial p}{\partial x} + \rho f_x + \mathbb{F}_{viscous} \tag{3.6}$$

Where ρ is the lubricant density, u is the velocity in the axial direction (x), $\underline{\mathbf{V}}$ is the velocity vector, p the static pressure, and f the force per unit mass acting on the lubricant.

It is safe to assume in this case that no significant momentum change in the radial or circumferential directions occurs, and that the effect of the weight of lubricant is small relative to other forces acting on the control volume. In the case of the piston ring, the restriction can be considered infinitely wide, negating any circumferential (∂y) terms. Also, the fluid flow will be considered steady ($\frac{\partial(\rho u)}{\partial t} = 0$) and uniform ($\nabla.(\rho u\underline{\mathbf{V}}) = 0$) - which renders the entire left-hand side of the momentum equation to zero (equation 3.7).

$$-\frac{\partial p}{\partial x} + \mathbb{F}_{viscous} = 0 \tag{3.7}$$

The diagram in figure 3.3 shows the pressure and viscous forces acting on each side of a control volume within a laminar flow between parallel plates. Equilibrium of the pressure forces can be expressed as per equation 3.8.

$$-\frac{\partial p}{\partial x}\delta x\delta z = p\delta z - \left(p + \frac{dp}{dx}\delta x\right)\delta z \tag{3.8}$$

While the viscous forces acting on the control volume can be expressed using shear stress acting over the area (equation 3.9).

$$\mathbb{F}_{viscous}\delta x\delta z = -\tau\delta x + \left(\tau + \frac{d\tau}{dz}\delta z\right)\delta x \tag{3.9}$$

Some of the above expressions can be simplified, combining these the momentum equation can be rewritten as in equation 3.10.

$$-\frac{dp}{dx}\delta x\delta z + \frac{d\tau}{dz}\delta z\delta x = 0 \tag{3.10}$$

Since the fluid quantities are small and the pressures and viscous forces high, the weight shall be neglected in this case. As a result, the expression can be simplified somewhat further, to equation 3.11.

$$\frac{d\tau}{dz} = \frac{dp}{dx} \tag{3.11}$$

Integrating this twice with respect to the radial direction (z), with a substitution for τ after the first of these using the principle that the shear stress for laminar flow can be expressed as the product of velocity gradient and viscosity ($\tau = \eta\frac{du}{dz}$) produces the expression in 3.12.

$$u = \frac{1}{\eta}\frac{dp}{dx}\frac{z^2}{2} + \frac{C_1}{\eta}z + C_2 \tag{3.12}$$

Using the no slip condition at each surface ($u = 0$ at $z = 0$ and $u = U$ at $z = h$) yields equation 3.15.

$$C_2 = 0 \tag{3.13}$$

$$C_1 = \eta\frac{U}{h} - \frac{h}{2}\frac{dp}{dx} \tag{3.14}$$

$$u = U\frac{z}{h} - \frac{1}{2\eta}\frac{dp}{dx}\left(hz - z^2\right) \tag{3.15}$$

Integrating this again with respect to z, from $z = 0$ to $z = h$ gives an expression for the volumetric flow rate, q. This is useful as it should be equal at all points between the cylinder and piston-ring, and can therefore be used to find the inlet boundary.

$$q = \int_0^h u dz = \int_0^h \left(U\frac{z}{h} - \frac{1}{2\eta}\frac{dp}{dx}\left(hz - z^2\right)\right) dz \tag{3.16}$$

$$q = \left[\frac{U}{h}\frac{z^2}{2}\right]_0^h - \frac{1}{2\eta}\frac{dp}{dx}\left[h\frac{z^2}{2} - \frac{z^3}{3}\right]_0^h \tag{3.17}$$

This gives the flow rate per unit width as

$$q = \frac{Uh}{2} - \frac{h^3}{12\eta}\frac{dp}{dx} \tag{3.18}$$

The first term in this expression represents the Couette flow, while the second gives the Poiseuille flow. These can be written for the flow-rate into or out of a cell (in this case for the axial direction) as

$$q^c = \Delta y \frac{Uh}{2} \tag{3.19}$$

$$q^p = -\Delta y \frac{h^3}{12\eta}\frac{dp}{dx} \tag{3.20}$$

3.2.2 Starvation and Cavitation

If there is insufficient lubricant to fully flood the piston ring (figure 3.4), starved lubrication is said to occur. In this case flow continuity must be conserved, such that the flow of oil in the conjunction between piston-ring and cylinder liner is equal to the rate of lubricant flow upstream of the piston-ring. The inlet boundary can be initially estimated by equating the couette flow (equation 3.19) with the approaching lubricant flow rate - as shown in equation 3.22. Following this estimation, mass conservation can be assessed in order to compute the true inlet boundary.

$$q^c = \Delta y U h_{oil} = \Delta y \frac{Uh_{in}}{2} \tag{3.21}$$

$$h_{in} = 2h_{oil} \tag{3.22}$$

The cavitation boundary is initially estimated to be equal to that for the previous crank angle. Following this estimate Reynolds boundary condition is applied (equation 3.23), for which there will be no pressures below the boundary pressure because the pressure gradient at the rupture boundary should be zero. The cavitation is found iteratively by checking these conditions are

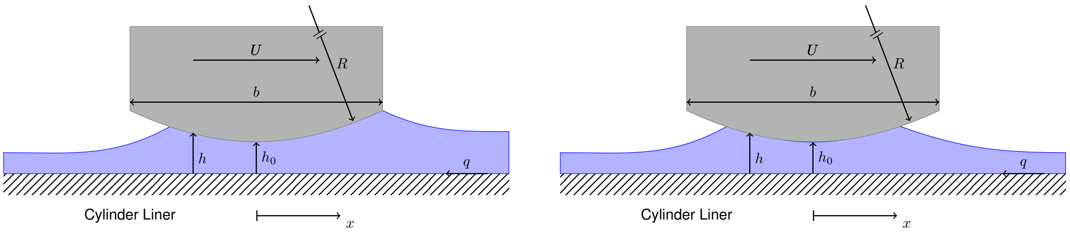

(a) Fully-flooded (b) Starved

Figure 3.4: Oil-film thickness parameters, where b = ring-face height, h = distance from cylinder liner to ring-face, h_0 = minimum oil-film thickness, q = lubricant flow-rate, R = ring-face radius, U = piston-ring speed.

satisfied, and moving the boundary estimate and re-solving Reynolds equation should this not be the case.

$$p_{in} = p_1 \; ; p_{out} = p_t \; ; \frac{dp}{dx} = 0 \tag{3.23}$$

In the partially filled region the pressure on the piston-ring face is equal to the boundary pressure. This will be the combustion chamber pressure or crank-case pressure depending on the direction of travel of the piston. This is true also at the inlet of the full oil-film and at the rupture boundary, hence the boundary conditions given in equation 3.23.

3.2.3 Assumptions and Simplifications

For the purposes of this work, the lubrication of only one compression ring is modelled. This piston-ring is assumed to be circular, and concentric with the cylinder liner such that minimum oil-film thickness does not vary in the circumferential direction. Piston-ring twist is typically less than 1 degree at typical engine operating speeds, and due to the low speeds (120 rpm) and low pressures expected in the experiments it is assumed piston-ring twist will be negligible. Piston tilt is also not included in the model, and again for the low speeds of the experiments the connecting rod force should be adequately balanced by lubricant pressure adjacent to the piston skirt. No piston tilt should occur with large marine diesel engines with their having a crosshead configuration. While it is possible to define axial variations in viscosity, the work herein follows an assumption of isothermal conditions, implying constant lubricant viscosity throughout the stroke.

When oil-film thickness is greater than three times the combined average roughness it is assumed axial piston-ring friction is due to hydrodynamic pressure forces and viscous shear. When oil-film thickness is below this threshold the contact is assumed to be in the boundary lubrication regime, and axial friction is computed from the product of hydrodynamic pressure and friction coefficient. The friction coefficient has been shown to be dependent on a number of parameters, such as the ring face topography and geometry, lubricant formulation and temperature, ring-bore conformability, and piston and piston-ring kinetics (Gore et al., 2017; Leighton et al., 2017). Typical values for friction coefficient vary between 0.15 and 0.25 over the stroke (Gore et al., 2017; Bewsher et al., 2019), and for this work a constant value of 0.2 has been assumed. The friction force in the radial direction due to contact between the piston-ring top or bottom land and the piston-ring groove on the piston is assumed negligible.

The system is considered to be quasi-steady, that is that while some dynamic forces are considered - namely the squeeze-film effect, the algorithm uses static equilibrium of forces at each crank angle position to find the oil-film thickness.

While the flow-continuity algorithm used is based on that published by Ma et al., 1996, this has been developed further to allow investigation of a variety of initial cylinder lubricant-film distributions and volumes, and their development over a number of cycles. This will allow for spatial and temporal investigations of lubricant transport, along with its impact on piston-ring oil-film thickness over these cycles. This is important since two-stroke marine engines have systems that inject lubricant onto regions of the cylinder liner in an uneven distribution every few strokes.

3.2.4 Initial Lubricant-film Distribution

An algorithm has been developed utilising vector algebra in order to estimate the initial distribution of lubricating oil on the cylinder liner (see figure 3.5). By discretizing the surface of the cylinder liner into a mesh of a $m \times n$ nodes (where m is the number of nodes axially, and n the number circumferentially), it is possible to assign the Cartesian co-ordinates of these nodes into an array of the same dimensions. This is achieved from knowledge of the nominal cylinder bore geometry (such as diameter and stroke), and converted from these cylindrical co-ordinates using equations 3.25 and 3.27.

$$x_{p_{i,j}} = rcos\theta_{i,j} \tag{3.24}$$

$$y_{p_{i,j}} = rsin\theta_{i,j} \tag{3.25}$$

$$z_{p_{i,j}} = z_{i,j} \tag{3.26}$$

$$\vec{P}_{i,j} = [x_{p_{i,j}} y_{p_{i,j}} z_{p_{i,j}}] \tag{3.27}$$

The location ($\vec{S}$) and direction of each lubricant injector is also known, the latter being determined by inspecting the lubricant distribution on the liner. This allows the axial co-ordinate of the intersection ($\vec{C}$) between a line from the injector (representing the centreline of the cone of lubricant spray) and the cylinder liner to be determined (equation 3.28). A vector can then be defined for the line connecting the injector and the intersection point.

$$\vec{L} = \vec{C} - \vec{S} \tag{3.28}$$

The angle subtended between the vector from each cell ($\vec{P}_{i,j}$) to the injection point ($\vec{S}$), and the vector $\vec{L}$ is assessed (equation 3.29) to determine if it is within the limits of the cone of lubricant spray from the injector (figure 3.5). The injectors have been specified to have a cone angle of 25°, and thus the angle between vectors must lie below 12.5°. A logical array is generated in which all cells lying within this limit are given the value 1.

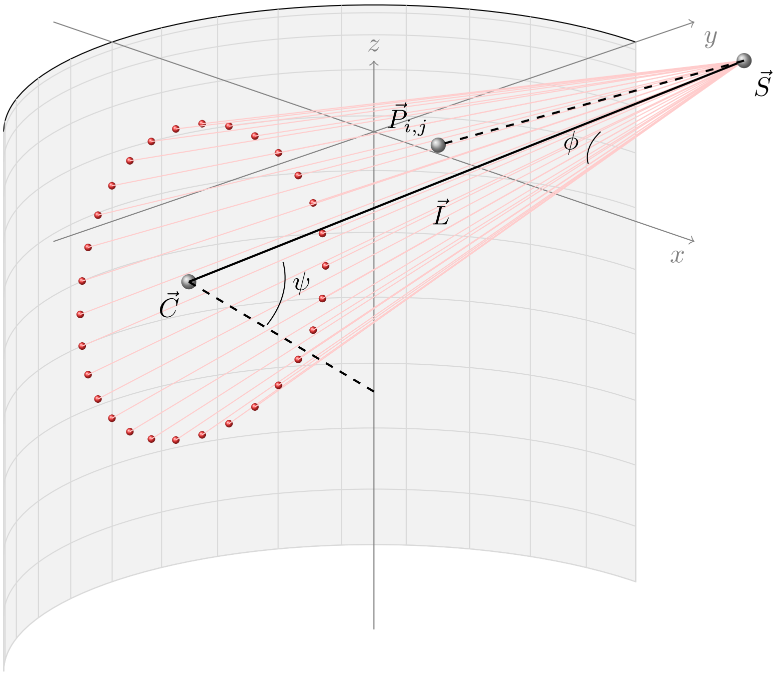

Figure 3.5: Schematic diagram of lubricant spray onto cylinder liner

$$\phi_{i,j} = \frac{\arccos\left(\left[\vec{P}_{i,j} - \vec{S}\right].\vec{L}\right)}{\left|\vec{P}_{i,j} - \vec{S}\right|\left|\vec{L}\right|} \tag{3.29}$$

While the lubricant spray is assumed to be distributed equally throughout the cone, the volume of lubricant within each cell on the liner will not be uniform because of the varying incidence angle for each cell relative to the injection point. The area of each mesh cell (A_p) on the liner can be calculated with equation 3.30. The normal to each cell intersects the axis of the cylinder liner ($x = 0.\ y = 0$), and this normal (A_{norm}) is given by equation 3.31.

$$A_p = \frac{d}{2} d\theta dz \tag{3.30}$$

$$A_{norm} = [x_p y_p 0] \tag{3.31}$$

This allows the angle between line $\vec{L}$ and the normal to each cell area to be computed using equation 3.32.

$$\psi_{i,j} = \frac{\arccos\left(\left[\vec{P}_{i,j} - \vec{S}\right].\vec{A}_{norm}\right)}{\left|\vec{P}_{i,j} - \vec{S}\right|\left|\vec{A}_{norm}\right|} \tag{3.32}$$

And so the projected area in the direction of the source of lubricant spray is computed with equation 3.33 (figure 3.6).

$$A_{ps} = A_p \cos\psi \tag{3.33}$$

The total volume of lubricant is then shared between the incident cells based on their proportional areas facing the injection point, and this volume divided by the cell area (A_p) to find the oil-film thickness on the liner.

$$V_p = \frac{A_{gs}}{A_{total}} V_{total} \tag{3.34}$$

$$H_p = \frac{V_p}{Ap} \tag{3.35}$$

The oil-film thickness calculated above is then repeated about the cylinder axis every 90 degrees. Where there are overlapping sections the oil-film thicknesses are summed. The totals are then added to any residual oil-film present on the cylinder liner (figure 3.7).

3.3 Numerical Modelling of Hydrodynamic Lubrication

The governing differential equations in section 3.2 represent a continuous system, which must be discretised in order to compute a numerical approximation to the solution. A discrete mesh is defined for the region in the conjunction between piston-ring and cylinder liner. This region is one cell thick in the radial direction, while there are n_x and n_y cells in the axial and circumferential directions respectively. Figure 3.8 shows how the mesh domain relates to the piston-ring geometry.

At each node the hydrodynamic pressure and lubricant flow-rate are calculated, and summed over the domain to determine the hydrodynamic load capacity. This is used to determine oil-film thickness. The flow-continuity algorithm used here has several steps in order to determine the oil-film thickness over the lubrication cycle. This process is summarised briefly below, while the following sections will elaborate on the workings of each of these processes.

- For a given oil-film thickness, the Reynolds equation is first solved to estimate the pressure

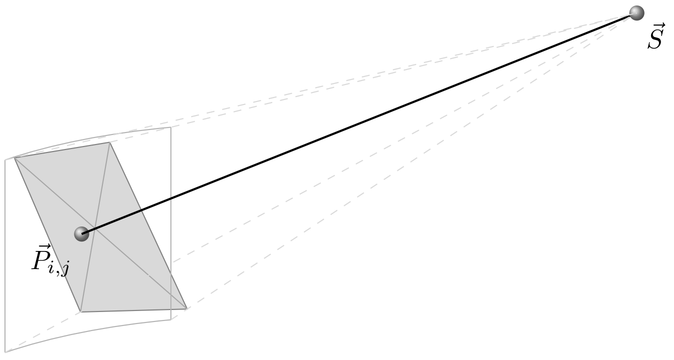

Figure 3.6: Cell area normal to lubricant spray vector

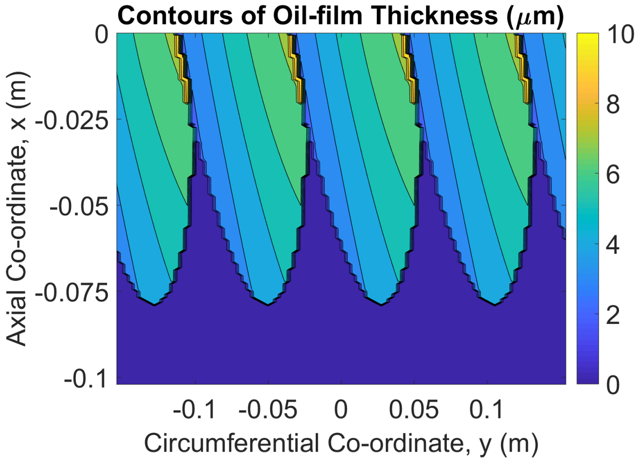

Figure 3.7: Initial oil-film distribution on cylinder liner

Figure 3.8: Computational mesh definition and notation

distribution caused by the flow of lubricant through the conjunction of piston-ring and cylinder liner. Following this estimation, flow-continuity is checked for each cell in the mesh, and the pressure distribution adjusted to enforce conservation of momentum throughout the domain.

- Once the pressure distribution has been determined, the forces acting on the piston-ring are computed. The oil-film thickness is found when static equilibrium of these forces is satisfied. If the forces do not equate the oil-film thickness is adjusted and the forces re-calculated.
- After the oil-film thickness for crank-angle ϕ^{n-1} is found, the crank angle is incremented and the oil-film thickness for the next crank-angle (ϕ^n) estimated using an Euler first-order forward method. Oil-film thickness, degree-of-filling, oil availability, and lubricant flow-rate are recorded.

3.3.1 Flow-continuity Algorithm

Finite Difference Equations

The derivatives of the governing equations - namely the Reynolds equation and the flow rate expression - are approximated throughout the discretized system using finite difference approximations (Hoffman, 1993).

Using a central difference approximation, the first order derivatives can be expressed in the form shown in equation 3.36.

$$f_i' = \frac{f_{i+1} - f_{i-1}}{2\Delta} \tag{3.36}$$

While the second order derivatives can be expressed as in equation 3.37

$$f_i'' = \frac{f_{i+1} - 2f_i + f_{i-1}}{\Delta^2} \tag{3.37}$$

Numerical Solution of Reynolds Equation

Reynold's equation, as shown previously, can be written as in equation 3.38.

$$\frac{\partial}{\partial x}\left(\frac{h^3}{\eta}\frac{\partial p}{\partial x}\right) + \frac{\partial}{\partial y}\left(\frac{h^3}{\eta}\frac{\partial p}{\partial y}\right) = 6U\frac{dh}{dx} + 12\frac{dh}{dt} \tag{3.38}$$

Non-dimensional expressions using the scheme of Ma et al. (1996) are defined for oil-film thickness ($H = h/C_b$) and axial piston-ring width ($X = x/b$), circumferential length ($Y = y/R_b$), and an expression relating time and engine speed ($d\alpha = \omega dt$). The parameters C_b and R_b are the nominal clearance between piston and cylinder liner, and the radius of the cylinder bore respectively. Additional non-dimensional ratios of some geometric parameters of the engine are defined as $\psi = C_b/R_b$, $\lambda = R_b/b$, and $K = b\omega/U$. This allows Reynolds equation to be written in non-dimensional form as in equation 3.39.

$$\lambda^2\frac{\partial}{\partial X}\left(H^3\frac{\partial P}{\partial X}\right) + \frac{\partial}{\partial Y}\left(H^3\frac{\partial P}{\partial Y}\right) = 6\frac{dH}{dX} + 12K\frac{dH}{d\alpha} \tag{3.39}$$

To rewrite Reynolds equation with the finite difference expressions, the derivatives must first be expanded as follows (3.40).

$$\lambda^2\frac{d\left(H^3\right)}{dX}\frac{dP}{dX} + \lambda^2 H^3\frac{d^2P}{dX^2} + \frac{d\left(H^3\right)}{dY}\frac{dP}{dY} + H^3\frac{d^2P}{dY^2} = 6\frac{dH}{dX} + 12K\frac{dH}{d\alpha} \tag{3.40}$$

Substituting the finite difference terms for the derivatives in the Reynolds equation produces the finite difference approximation given in 3.41.

$$\begin{aligned}\lambda^2\left(\frac{H^3_{i+1,j}-H^3_{i-1,j}}{2\Delta X}\right)\left(\frac{P_{i+1,j}-P_{i-1,j}}{2\Delta X}\right)+\lambda^2 H^3_{i,j}\left(\frac{P_{i+1,j}-2P_{i,j}+P_{i-1,j}}{\Delta X^2}\right)\\+\left(\frac{H^3_{i,j+1}-H^3_{i,j-1}}{2\Delta Y}\right)\left(\frac{P_{i,j+1}-P_{i,j-1}}{2\Delta Y}\right)+H^3_{i,j}\left(\frac{P_{i,j+1}-2P_{i,j}+P_{i,j-1}}{\Delta Y^2}\right)\\=6\left(\frac{H_{i+1,j}-H_{i-1,j}}{2\Delta X}\right)+12K\left(\frac{H^n_{i,j}-H^{n-1}_{i,j}}{2\Delta\alpha}\right)\end{aligned} \tag{3.41}$$

The above equation can be expanded, factorised for the pressure terms, and expressed in the form shown in 3.42.

$$AP_{i,j-1}+BP_{i-1,j}+CP_{i,j}+DP_{i+1,j}+EP_{i,j+1}=F \tag{3.42}$$

Where the coefficients A to F are given by the expressions below.

$$\begin{aligned}A=&\left[\frac{H^3_{i,j}}{\Delta Y^2}-\frac{H^3_{i,j+1}-H^3_{i,j-1}}{4\Delta Y^2}\right]\\B=&\lambda^2\left[\frac{H^3_{i,j}}{\Delta X^2}-\frac{H^3_{i+1,j}-H^3_{i-1,j}}{4\Delta X^2}\right]\\C=&-2\left[\frac{\lambda^2 H^3_{i,j}}{\Delta x^2}+\frac{H^3_{i,j}}{\Delta Y^2}\right]\\D=&\lambda^2\left[\frac{H^3_{i,j}}{\Delta X^2}-\frac{H^3_{i+1,j}-H^3_{i-1,j}}{4\Delta X^2}\right]\\E=&\left[\frac{H^3_{i,j}}{\Delta Y^2}-\frac{H^3_{i,j+1}-H^3_{i,j-1}}{4\Delta Y^2}\right]\\F=&\left[6\left(\frac{H_{i+1,j}-H_{i-1,j}}{2\Delta X}\right)+12K\left(\frac{H^n_{i,j}-H^{n-1}_{i,j}}{\Delta\alpha}\right)\right]\end{aligned}$$

A matrix system of simultaneous equations can thus be compiled for each of the discretised nodes of the piston-ring (in the form $A\mathbf{x}=\mathbf{b}$), and solved for the pressure distribution using the MATLAB function *mldivide*. This function selects the most efficient solver based on the nature of the square matrix, A (MathWorks, 2018).

To increase efficiency, the extent of the starved region is first estimated by satisfying the flow-rate equation for the case where the pressure gradient is zero.

$$Q=Uh_{oil}=\frac{Uh}{2}-\frac{h^3}{12\eta}\frac{dp}{dx}\approx\frac{Uh}{2} \tag{3.43}$$

As such, the inlet is estimated to be at the point where the oil-film thickness is twice the oil availability. Since the pressure in the starved region will be equal to the boundary pressure, the

Reynolds equation need only be solved for the region downstream of the oil inlet.

Reynolds boundary condition (Stachowiak and Batchelor, 2005) is applied to determine the extent of the cavitated region. This is initially estimated, and the separation point adjusted to satisfy the conditions in equation 3.44.

$$P_t = P_b \text{ and } \frac{dP}{dX} = 0 \tag{3.44}$$

Conservation of Mass

Following estimation of the hydrodynamic pressure using Reynolds equation, flow continuity in each cell is enforced through application of the conservation of momentum. This ensures the rate of change of mass of lubricant in each cell is equal to the net mass flux of lubricant into the control volume. Since density is assumed to be constant in the entire flow domain, the mass flow rates can be represented by the product of this density and the volumetric flow-rate. Figure 3.9 shows the volumetric flow-rate of lubricant through each face of the cell (i, j) due to both Couette and Poiseuille flow. The Couette term is neglected in the circumferential direction because the sliding velocity in the y-direction is assumed to be zero. The Poiseuille flow in the y-direction can be non-zero, however. This will be the case when the lubricant supply is non-uniform resulting in pressure differential in the y-direction. The flow-rates are quantified using equations 3.19 and 3.20, while the rate of change of mass content of the cell due to the squeeze effect is proportional to the change in volume between piston-ring and cylinder liner is expressed as shown in equation 3.45.

$$\frac{\partial m}{\partial t} = \rho \left.\frac{\partial V}{\partial t}\right|_{i,j} = \rho \Delta x \Delta y \left.\frac{\partial h}{\partial t}\right|_{i,j} \tag{3.45}$$

To account for how the flow-rate differs for cells that are partially and fully filled with lubricant, a switch function is used as adopted by Elrod and Adams (2017). This has two components to it - the first is a parameter θ, which gives the degree of filling of a cell, such that a cell that is completely filled with lubricant has $\theta = 1$, while a cell that is half filled with lubricant has $\theta = 0.5$. The second parameter is the switch variable, g - this is defined such that $g = 1$ for a filled cell, and $g = 0$ for a cell that is only partially filled. The equations for Couette and Poiseuille flow, and that for the rate of change of mass content of a cell must be rewritten to account for this function as follows (3.46 and 3.47).

$$\left(q^c_{x,in}\right)_{i,j} = \Delta y \frac{U}{2}\left\{\theta_{i-1,j} h_{i-1,j}\left(1 - g_{i-1,j}\right) + g_{i-1,j} h_{i-1,j} + g_{i-1,j} g_{i,j}\left(\frac{h_{i,j} - hi - 1, j}{2}\right)\right\} \tag{3.46}$$

$$\left(q^p_{x,in}\right)_{i,j} = -\Delta y \frac{1}{12\eta}\left(\frac{h_{i-1,j} + h_{i,j}}{2}\right)^3 \frac{\left(g_{i,j} p_{i,j} - g_{i-1,j} p_{i-1,j}\right) - \left(g_{i,j} - g_{i-1,j}\right) p_b}{\Delta x} \tag{3.47}$$

$$\Delta x \Delta y \left. \frac{\partial \theta h}{\partial t} \right|_{i,j} = \Delta x \Delta y \left\{ \left(\theta_{i,j} \frac{h_{i,j} - h_{i,j}^{n-1}}{\Delta t} \right) + h_{i,j} \left(\frac{\theta_{i,j} - \theta_{i,j}^{n-1}}{\Delta t} \right) \right\} \tag{3.48}$$

Equivalent expressions to 3.46 and 3.47 can be derived for the flow out of the cell (by using the subscripts (i and $i+1$ in place of $i-1$ and i, respectively). Likewise, the expression for flow in circumferential direction can be similarly derived. Tables 3.1 and 3.2 show how the flow equations change in different regions of the mesh.

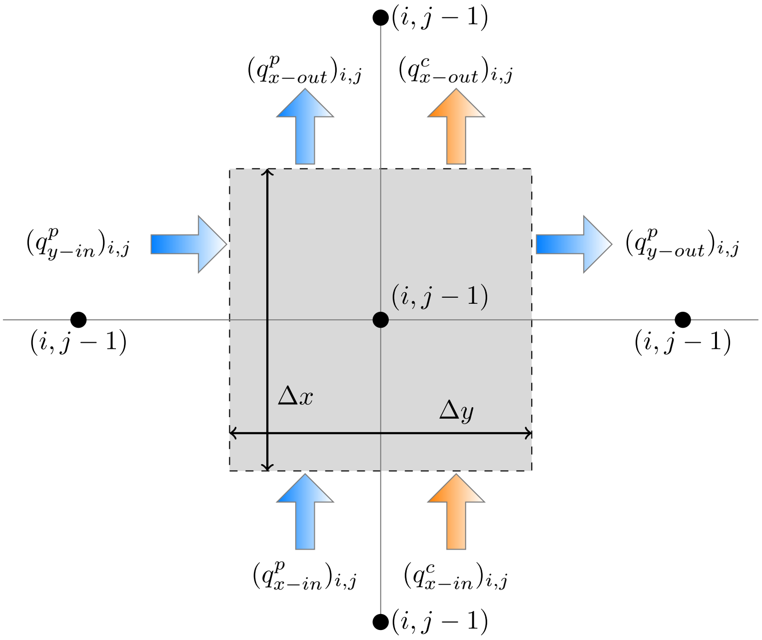

Figure 3.9: Finite difference cell showing co-ordinate, dimensions, and flow-rate terms through each face.

Region	Switch Function	Couette Term
Starved Region	$g_{i,j}=0,\, g_{i-1,j}=0$	$\left(q^c_{x,in}\right)_{i,j}=\frac{U\Delta y}{2}\left(\theta_{i-1,j}h_{i-1,j}\right)$
Inlet Boundary	$g_{i,j}=1,\, g_{i-1,j}=0$	$\left(q^c_{x,in}\right)_{i,j}=\frac{U\Delta y}{2}\left(\theta_{i-1,j}h_{i-1,j}\right)$
Fully filled Region	$g_{i,j}=1,\, g_{i-1,j}=1$	$\left(q^c_{x,in}\right)_{i,j}=\frac{U\Delta y}{2}\left(\frac{h_{i-1,j}+hi,j}{2}\right)$

Table 3.1: Summary of Couette flow terms in different regions of the domain

Region	Switch Function	Poiseuille Term
Starved Region	$g_{i,j}=0,\, g_{i-1,j}=0$	$\left(q^p_{x,in}\right)_{i,j}=0$
Inlet Boundary	$g_{i,j}=1,\, g_{i-1,j}=0$	$\left(q^p_{x,in}\right)_{i,j}=-\frac{\Delta y}{12\eta}\left(\frac{h_{i-1,j}+h_{i,j}}{2}\right)^3\frac{(p_{i,j}-p_b)}{\Delta x}$
Fully filled Region	$g_{i,j}=1,\, g_{i-1,j}=1$	$\left(q^p_{x,in}\right)_{i,j}=-\frac{\Delta y}{12\eta}\left(\frac{h_{i-1,j}+h_{i,j}}{2}\right)^3\frac{(p_{i,j}-p_{i-1,j})}{\Delta x}$

Table 3.2: Summary of Poiseuille flow terms in different regions of the domain

The principle of conservation of mass can be expressed as shown in table 3.3. For any computational cell the terms showing mass-flux into and out of the cell are shown in figure 3.9, for which the expressions are given in equations 3.46 and 3.47. These are combined with the term for rate of change of mass in a cell, or the squeeze term, (equation 3.48) to give equation 3.49.

Rate of change of mass in a control volume	$+$	Mass flux out of a control volume	$=$	Mass flux into of a control volume

Table 3.3: Principle of mass conservation

$$\rho \Delta x \Delta y \left.\frac{\partial \theta h}{\partial t}\right|_{i,j} + \rho\left(q^c_{x,out}\right)_{i,j} + \rho\left(q^p_{x,out}\right)_{i,j} + \rho\left(q^p_{y,out}\right)_{i,j} = \rho\left(q^c_{x,in}\right)_{i,j} + \rho\left(q^p_{x,in}\right)_{i,j} + \rho\left(q^p_{y,in}\right)_{i,j} \tag{3.49}$$

As with the Reynolds equation, this can be non-dimensionalised using the same parameters used to derive equation 3.39, along with an additional parameter to account for the squeeze term, $dt = d\alpha/\omega$. Once the expressions for the respective lubricant flow and squeeze terms are substituted in, the resulting equation is rather unwieldy. However grouping pressure terms and degree-of-filling terms allows this to be expressed as shown in equation 3.50 and 3.51. The full derivation of these equations can be found in appendix A.1.

$$\begin{aligned} P_{i,j} = \{&A1_{i,j}\theta_{i-1,j}\left(1 - g_{i-1,j}\right) + A2_{i,j}g_{i-1,j} + A3_{i,j} + A4_{i,j}g_{i+1,j} + A5_{i,j} \\ &+ A6_{i,j}g_{i+1,j}\left(P_{i+1,j} - P_b\right) + A7_{i,j}g_{i-1,j}\left(P_{i-1,j} - P_b\right) \\ &+ A8_{i,j}g_{i,j+1}\left(P_{i,j+1} - P_b\right) + A9_{i,j}g_{i,j-1}\left(P_{i,j-1} - P_b\right)\}/A10_{i,j} + P_b \end{aligned} \tag{3.50}$$

$$\begin{aligned} \theta_{i,j} = \{&\left[A1_{i,j}\theta_{i-1,j}\left(1 - g_{i-1,j}\right) + g_{i-1,j}\right] \\ &+ A6_{i,j}g_{i+1,j}\left(P_{i+1,j} - P_b\right) + A7_{i,j}g_{i-1,j}\left(P_{i-1,j} - P_b\right) \\ &+ A8_{i,j}g_{i,j+1}\left(P_{i,j+1} - P_b\right) + A9_{i,j}g_{i,j-1}\left(P_{i,j-1} - P_b\right) + A11_{i,j}\}/A12_{i,j} \end{aligned} \tag{3.51}$$

The coefficients A1 to A12 are as presented in table 3.4:

3.3.2 Equilibrium of Forces

Figure 3.10 shows the forces acting on the piston-ring. To determine the oil-film thickness, a quasi-static equilibrium assumption is used such that the hydrodynamic load generated (F_z) must equal the sum of the forces from the ring tension (F_e) and that due to the gas-pressure acting on the back face of the piston-ring (F_g). In the case of this study all pressures are set to ambient

$$\begin{aligned}
A1_{i,j} &= C_1 H_{i-1,j} \\
A2_{i,j} &= C_1 \left(H_{i,j} - H_{i-1,j}\right)/2 \\
A3_{i,j} &= -C_1 H_{i,j} \\
A4_{i,j} &= -C_1 \left(H_{i+1,j} - H_{i,j}\right)/2 \\
A5_{i,j} &= -C_2 \left\{H_{i,j}\left(1 - \theta_{i,j}^{n-1}\right) + \left(H_{i,j}^{n} - H_{i,j}^{n-1}\right)\right\} \\
A6_{i,j} &= C_3 \left(H_{i,j} + H_{i+1,j}\right)^3 \\
A7_{i,j} &= C_3 \left(H_{i,j} + H_{i-1,j}\right)^3 \\
A8_{i,j} &= C_3 \left(H_{i,j} + H_{i,j+1}\right)^3 \\
A9_{i,j} &= C_3 \left(H_{i,j} + H_{1,j-1}\right)^3 \\
A10_{i,j} &= A6_{i,j} + A7_{i,j} + A8_{i,j} + A9_{i,j} \\
A11_{i,j} &= C_2 H_{i,j} \theta_{i,j}^{n-1} \\
A12_{i,j} &= C_1 H_{i,j} + C_2 \left\{H_{i,j} + \left(H_{i,j}^{n} - H_{i,j}^{n-1}\right)\right\}
\end{aligned}$$

Where $C_1 = 48\Delta X$, $C_2 = 96K\left(\Delta X\right)^2/\Delta\alpha$, $C_3 = \lambda^2$, $C_4 = \left(\Delta X/\Delta Y\right)^2$.

Table 3.4: Coefficients of the flow continuity equations

pressure, and therefore only the ring tension is used to balance the hydrodynamic forces. Oil-film thickness is considered to be converged when equation 3.52 has been satisfied. Changes in the shape of the piston-ring face due to contact pressures and tilting of the ring are assumed negligible for this study.

$$\frac{(F_g + F_e) - F_z}{F_g + F_e} < 0.1\% \tag{3.52}$$

Ring tension (F_e) has been estimated using a finite element analysis of the compression ring, where the pressure (acting on the ring-face) needed to close the ring gap has been computed and used to determine the resulting tension. The gas force acting on the back of the piston-ring (F_g) is computed as the product of the gas pressure and the area upon which it is acting. This pressure can be either the combustion chamber pressure or the crank case pressure, depending on where the piston-ring sits in the ring groove, although pressure variations have been set to zero in this case because the combustion chamber is open to atmosphere. A balance of the axial forces is used to determine which pressure value is used. The axial forces are the gas pressure force on top and bottom lands (F_1 and F_2), the weight of the piston-ring (Mg) and its inertia force (Ma_c), and the friction due to one or more of asperity contact, viscous shear stresses, and hydrodynamic pressure (F_t).

The forces F_1 and F_2 result from the pressures in the crank-case and combustion chamber acting on the bottom and top lands of the piston-ring respectively. The area upon which these pressures act will depend on whether the ring sits at the top or bottom of the groove. This is determined following assessment of the forces at each crank angle. The weight of the ring (Mg), and the inertia force (Ma_c) is found from the piston acceleration. Finally, the friction force is also calculated. Since the friction will depend on whether the lubrication is in the hydrodynamic or boundary regimes, it is determined using one of two methods.

In areas of the ring-face where the separation from the cylinder liner is greater than three times the combined average roughness of these two surfaces, the friction will be considered to be due to hydrodynamic pressure and viscous shear forces. These can be expressed using equation 3.53.

$$F_{th} = \frac{\eta U}{h} - \frac{h}{2}\frac{dp}{dx} \tag{3.53}$$

In areas of the ring-face where the separation is less than three times the combined average roughness of the two surfaces, asperity contact will also cause friction. This is estimated with equation 3.54, where μ is the coefficient of friction. A value for $\mu = 0.2$ has been used for coefficient of friction.

$$F_{tb} = sign(U)\mu p \tag{3.54}$$

These forces are integrated over the surface of the ring-face depending on whether the local film-thickness falls above or below the hydrodynamic lubrication threshold.

Once the pressure distribution and degree of filling has been computed, the hydrodynamic force is computed using equation 3.55.

$$F_z = \int_{-\pi R_b}^{\pi R_b} \int_{-b/2}^{b/2} p dx dy \tag{3.55}$$

If these forces are not balanced, the oil-film thickness is adjusted using equations 3.56 and 3.57 (k is the iteration number). The constants γ and λ_1 determine the magnitude of the change in oil-film thickness for the following iteration. Here $\gamma = 0.12$ and $\lambda_1 = 0.18$.

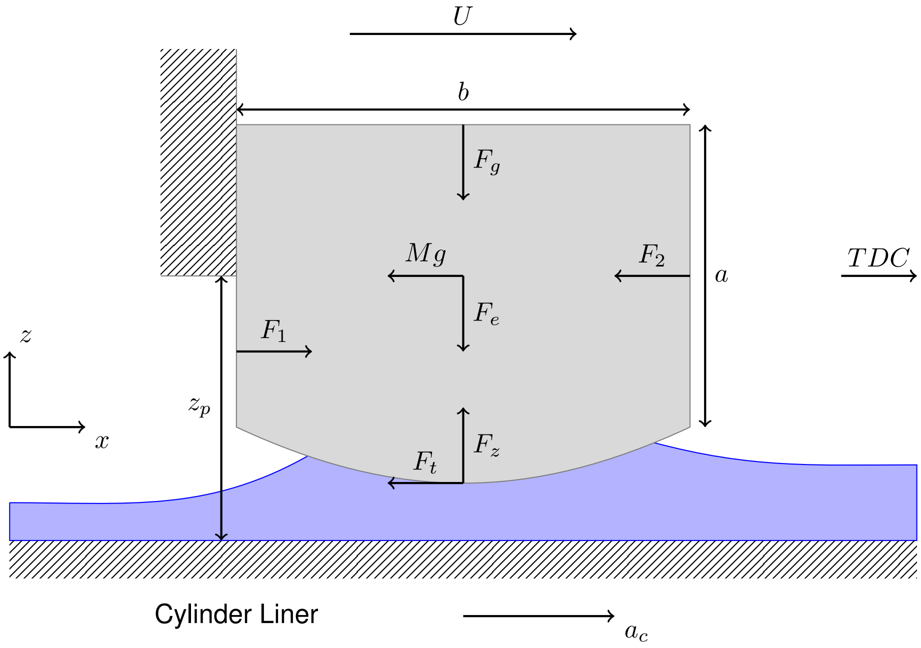

Figure 3.10: Major forces acting on the piston-ring

$$h^n_{0,\text{est}} = \left(\frac{F_z}{F_g + F_e}\right)^\gamma h^n_{0,k-1} \tag{3.56}$$

$$h^n_{0,k} = h^n_{0,k-1} + \lambda_1 \left(h^n_{0,\text{est}} - h^n_{0,k-1}\right) \tag{3.57}$$

Following satisfaction of static equilibrium of piston-ring forces, the lubricant flow-rate is calculated at the inlet and cavitation boundaries using the equations 3.46 and 3.47. From this, should the lubricant flow at the inlet be less than the lubricant supply, the difference is assumed to be transported, and is added to the lubricant available at the following crank-angle location.

Under certain conditions (ie. when oil-film thickness was increasing), the lubricant flow-rate was found to be greater than lubricant supply. This would occur to satisfy flow continuity, since additional lubricant would be required to fill the increase in volume in the conjunction. To do this oil was 'borrowed' from upstream, which in practice is not possible. This action needed to be suppressed, by limiting the maximum lubricant flow at the inlet boundary to the lubricant availability at that crank-angle.

Lubricant flow-rate at the cavitation boundary is used to determine the quantity of lubricant remaining on the cylinder liner once the piston-ring has passed. This becomes the lubricant availability on the following engine stroke.

3.3.3 Crank-angle Stepping

Once the oil-film thickness is determined, the remaining piston-ring forces can be determined. These include the friction force, inertia force, and gas-pressure forces on the top and bottom lands. Not only does this provide a means for power-loss to be estimated, it also allows the algorithm to determine whether the piston-ring sits on the upper or lower face of the piston-ring groove, and subsequently whether it is the combustion chamber pressure or crank-case pressure that acts on the rear face of the piston-ring (used for the static equilibrium phase of the algorithm).

Finally, oil-film thickness for the following crank-angle is estimated using an Euler first-order forward scheme (equation 3.58), with $\lambda_2 = 0.3$. While this is a simple method, it is adequate for providing a first guess that will subsequently be refined to satisfy static equilibrium.

$$h^n_{0,\text{est}} = h^{n-1}_0 + \lambda_2 \frac{dh_0}{d\phi}\left(\phi^n - \phi^{n-1}\right) \tag{3.58}$$

3.3.4 Minimum Oil-film Thickness Algorithm

The algorithm for computing the minimum oil-film thickness at all crank angles over a number of engine cycles is summarised in the data-flow diagrams shown in figure 3.11.

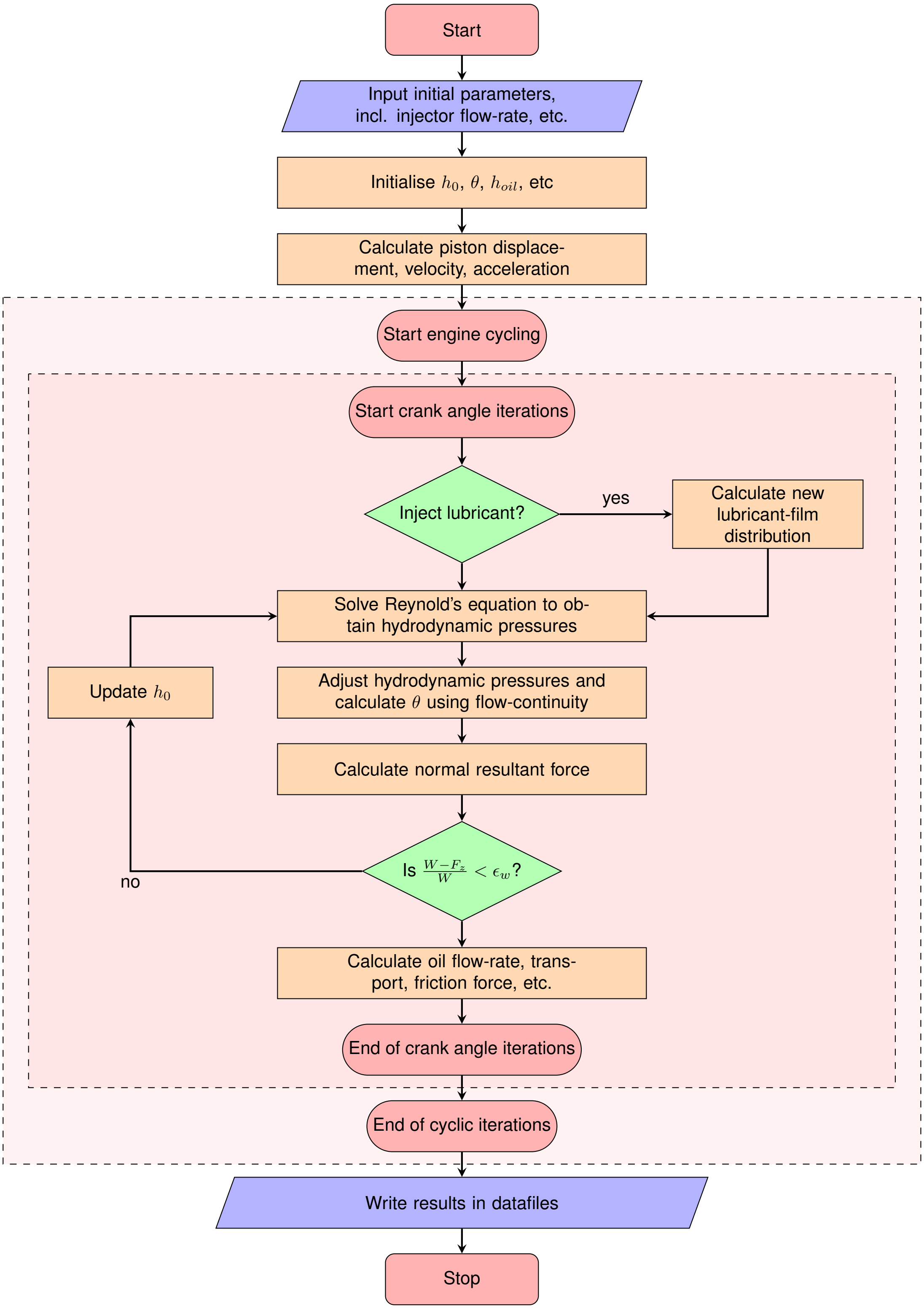

Figure 3.11: Computational flowchart

3.3.5 Implementation

Grid-dependency Check

A grid dependency check was carried out to assess the effect of node count in both the axial and circumferential directions. Figure 3.12 shows the hydrodynamic load carrying capacity as the number of nodes were increased, while figure 3.13 shows the relative error in lubricant flow-rate at the starvation and cavitation boundaries. Additionally, figures 3.14 and 3.15 show the changes in degree of filling and hydrodynamic pressure over the ring-face as the number of nodes is increased.

Figure 3.12 shows that increasing the number of co-ordinates in the axial direction has relatively little affect, certainly above the minimum node count attempted. In contrast, the circumferential node-count has a more profound impact - likely due to the non-uniform nature of the oil-supply around the circumference of the ring. This is further supported by figure 3.14, which shows a near equal pressure distribution in all cases, while in figure 3.15 there are notable differences. If the node count is decreased too far, no hydrodynamic pressure is generated, and as it increases the true extent of the full-film lubrication is seen.

Inspection of the error in the lubricant-flow rate shows a similar trend, although there is a significantly larger error shown here for an axial node count of 32.

Based on the results of these tests, an axial node count of 48 has been chosen. Additionally, while a circumferential node count of 96 or more would be considered ideal, it was found to be too computationally intensive. As a result a node count of 72 was selected. This would provide adequate resolution in a more efficient manner.

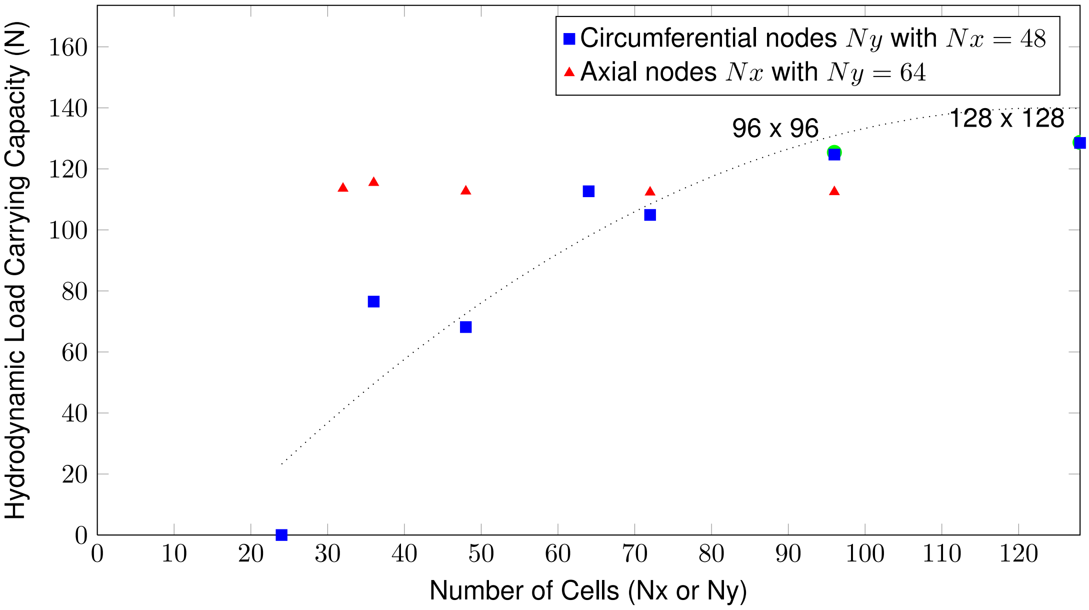

Figure 3.12: Grid dependency check against load capacity

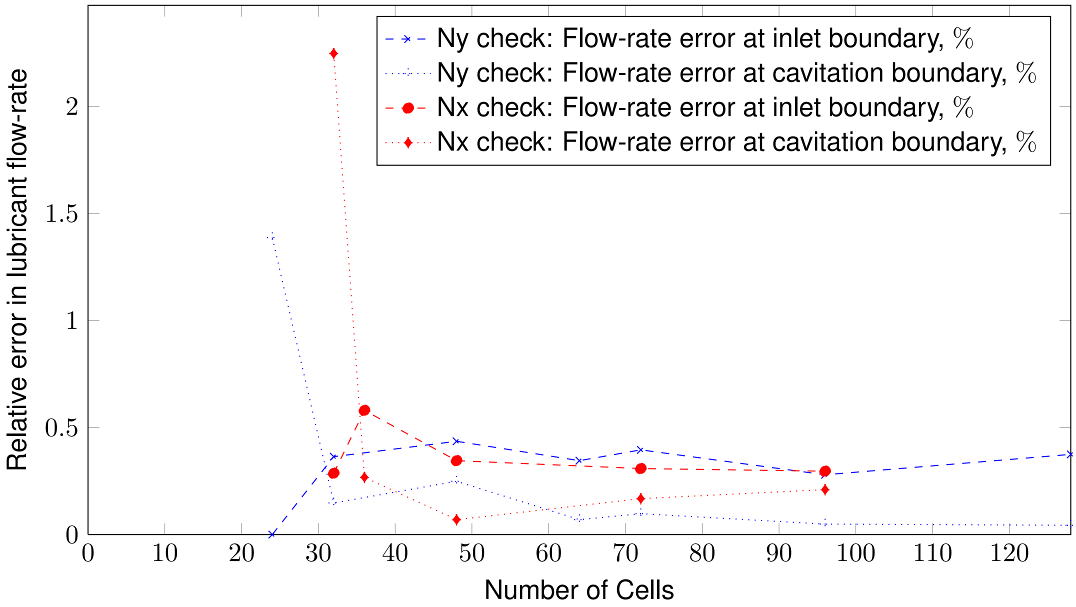

Figure 3.13: Grid dependency check against lubricant flow-rate

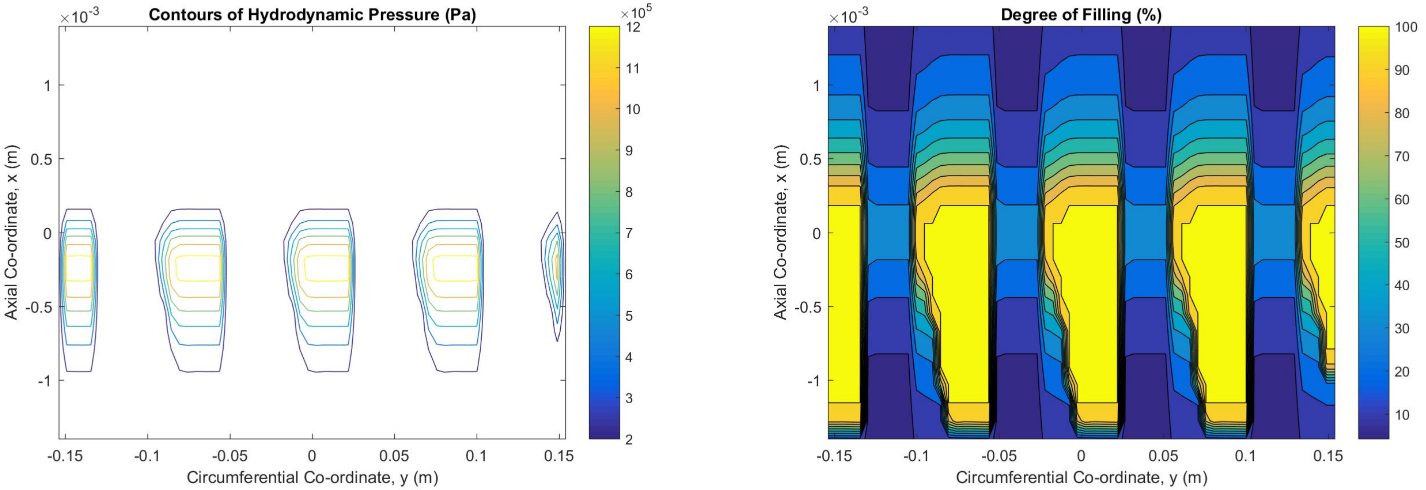

(a) Nx = 32 ; Ny = 64

(b) Nx = 32 ; Ny = 64

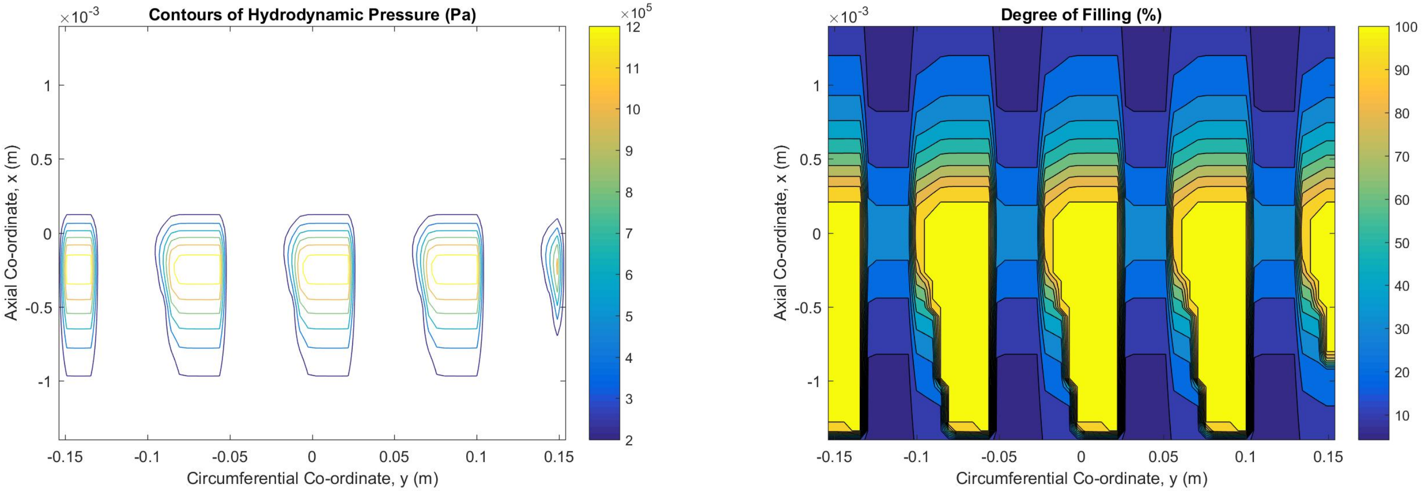

(c) Nx = 48 ; Ny = 64

(d) Nx = 48 ; Ny = 64

Figure 3.14: Pressure contours (left) and degree of filling (right) for different axial cell counts

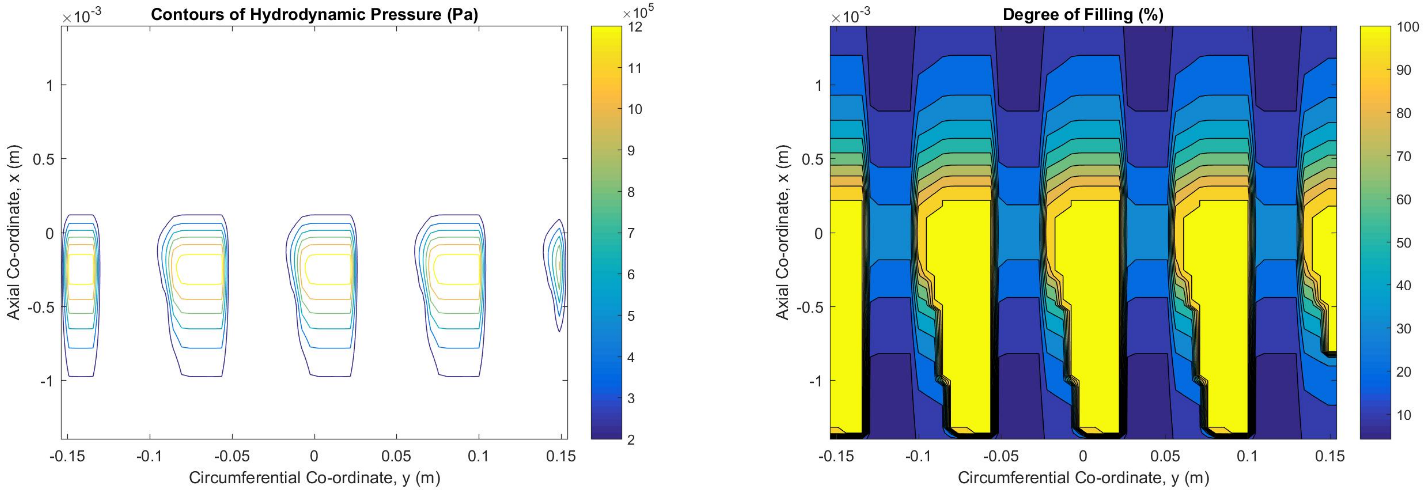

(e) Nx = 72 ; Ny = 64

(f) Nx = 72 ; Ny = 64

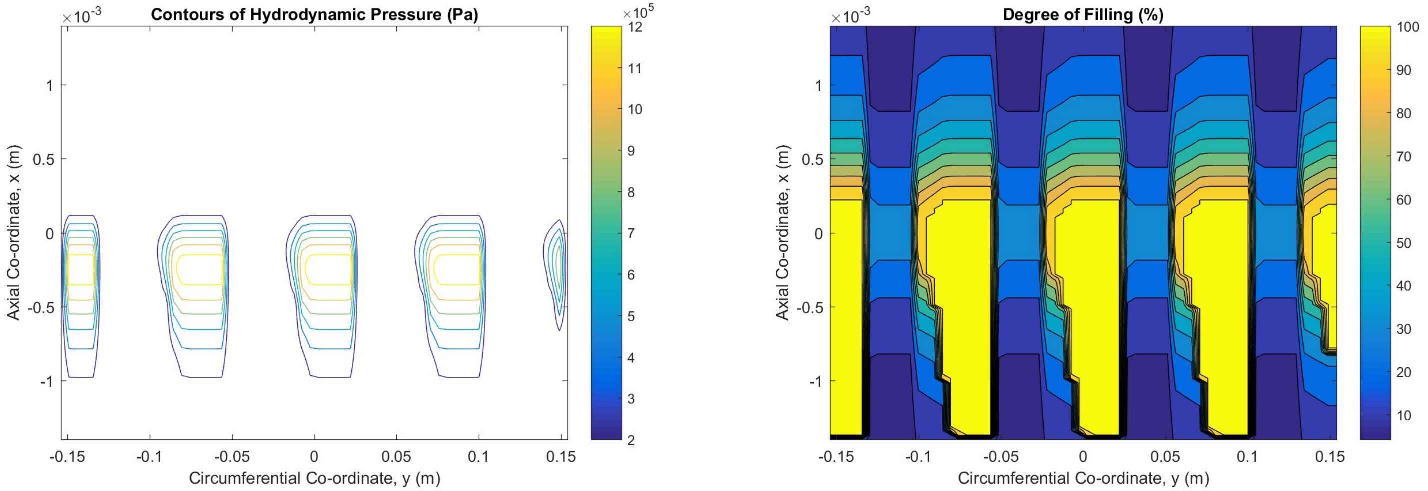

(g) Nx = 96 ; Ny = 64

(h) Nx = 96 ; Ny = 64

Figure 3.14: Pressure contours (left) and degree of filling (right) for different axial cell counts

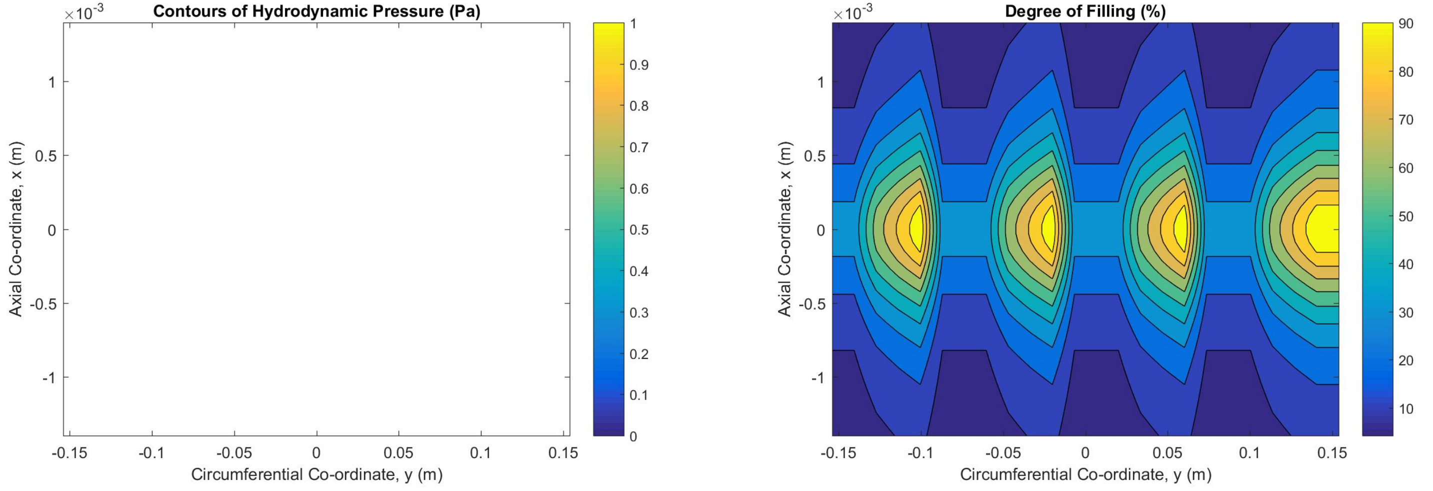

(a) Nx = 48 ; Ny = 24 (b) Nx = 48 ; Ny = 24

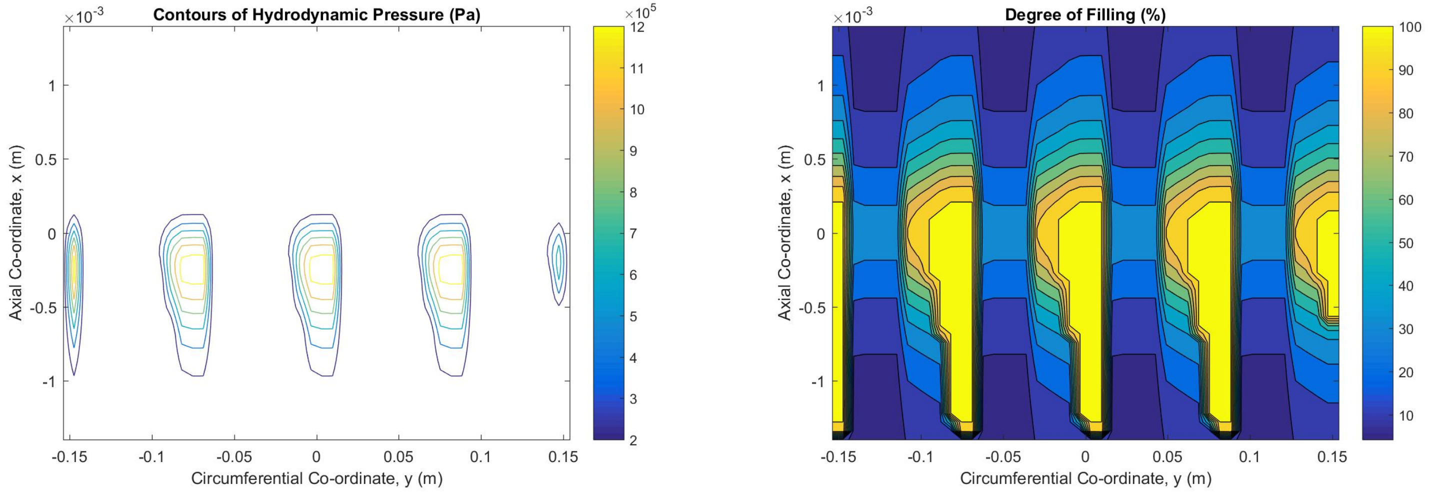

(c) Nx = 48 ; Ny = 48 (d) Nx = 48 ; Ny = 48

Figure 3.15: Pressure contours (left) and degree of filling (right) for different circumferential cell counts

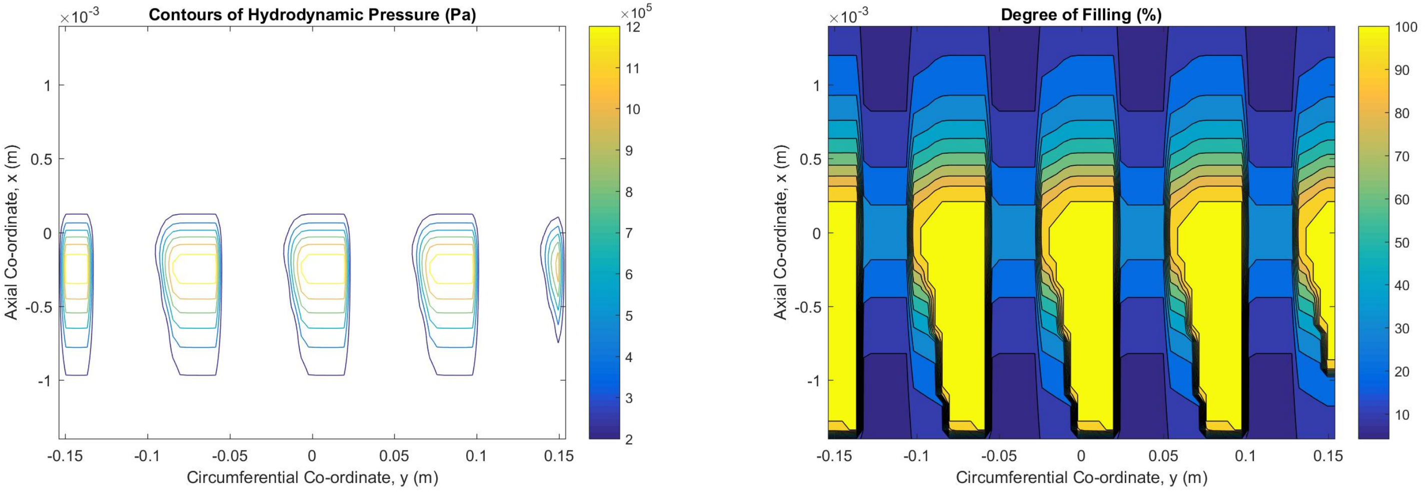

(e) Nx = 48 ; Ny = 72

(f) Nx = 48 ; Ny = 72

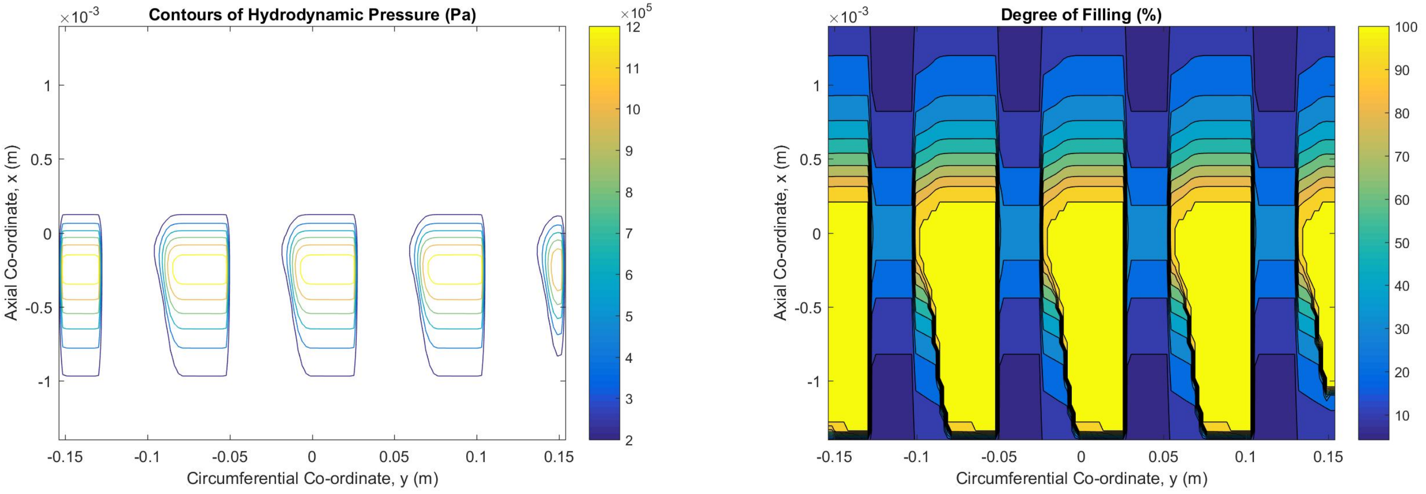

(g) Nx = 48 ; Ny = 128

(h) Nx = 48 ; Ny = 128

Figure 3.15: Pressure contours (left) and degree of filling (right) for different circumferential cell counts

Verification of the Model

In order to verify the model, a number of simulations were performed for a system with known inputs and results. These tests assessed the scheme for the computation of pressure distribution and minimum oil-film thickness, along with prediction of the appropriate starvation and cavitation conditions.

The solution of Reynold's equation for a rigid parabolic cylinder is presented in Dowson's classic text on elasto-hydrodynamic lubrication (Dowson and Higginson, 1977). This states the dimensionless force component normal to the surface is given as per equation 3.59. It continues to show there is strong correlation between this result and his own experiments, which considered circular cylinders rather than parabolic ones.

$$\overline{P}_y = 2.44\frac{R}{h_0} \tag{3.59}$$

Given the dimensionless load is defined as per equation 3.60, a relationship between the parameters of a parabolic surface such as a piston-ring face, and the hydrodynamic load capacity, can be defined. This relationship is shown in equation 3.61.

$$\overline{P}_y = \frac{P}{2\eta U} \tag{3.60}$$

$$\frac{h_0}{R} = 4.88\frac{\eta U}{P_y} \tag{3.61}$$

This result is used for verification of the computational results using the flow-continuity algorithm. Results for a number of different boundary conditions have been computed and plotted below in figure 3.16. These results show a strong correlation with Purday's empirical relationship, and verifies that, for uniform oil-films at least, the results of the flow-continuity algorithm are acceptable.

In addition to the above test, the results of the hydrodynamic pressure calculations were compared to the finite-difference solution of Reynolds equation for a series of lubricant supply boundary conditions. Results showed a good correlation between the two for all tests, as evidenced in figure 3.17.

The above comparisons show the algorithm employed here gives a good indication of minimum oil-film thickness for a range of lubricant supply conditions, which is essential for the this study, and also that the conditions used for flow continuity and lubricant flow-rate are accurate.

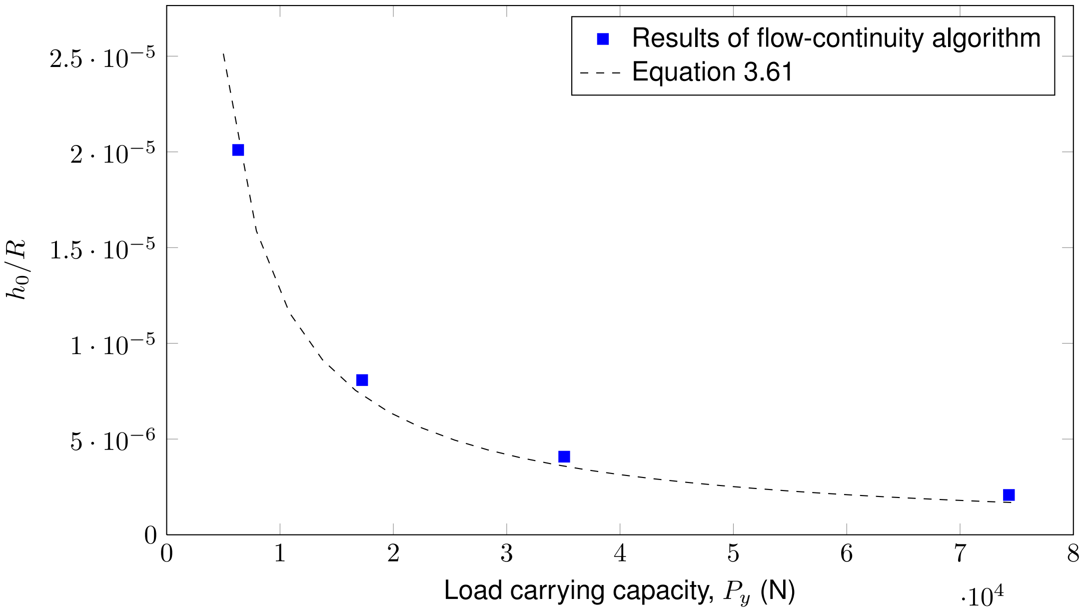

Figure 3.16: Comparison of flow-continuity model with Purday's empirical relationship

3.4 Summary

A flow-continuity algorithm has been developed for predicting the spatial and temporal distribution of lubricant in the cylinder over multiple engine cycles, following an initial non-uniform distribution of lubricant. The lubrication of only one compression ring is modelled, and this is assumed circular and concentric within the cylinder. The flow continuity algorithm estimates the pressure distribution using Reynolds equation, and corrects this through satisfaction of conservation of mass for each computational cell in a grid of the area in the conjunction, assuming lubricant flow is due to only the relative velocity between the piston-ring and cylinder and the pressure differential across the piston-ring. The use of a switch function and a variable for the degree of filling of a computational cell thus allows the inlet and cavitation boundaries to be computed along with the hydrodynamic pressure.

An algorithm for computing the distribution of lubricant following an injection event has also been developed. This uses the direction and spread of lubricant from the spray nozzle, and the position of the nozzle relative to the cylinder to predict the volume of lubricant delivered to different areas of the cylinder.

A grid-dependency check has been performed and the algorithm has been verified using empirical data, and shows strong correlation for a range of oil-film thickness. Validation of the model, including comparison between experimental data and predictions from the model for oil-film thickness, the position of the inlet boundary and lubricant transport is presented in chapter 8.

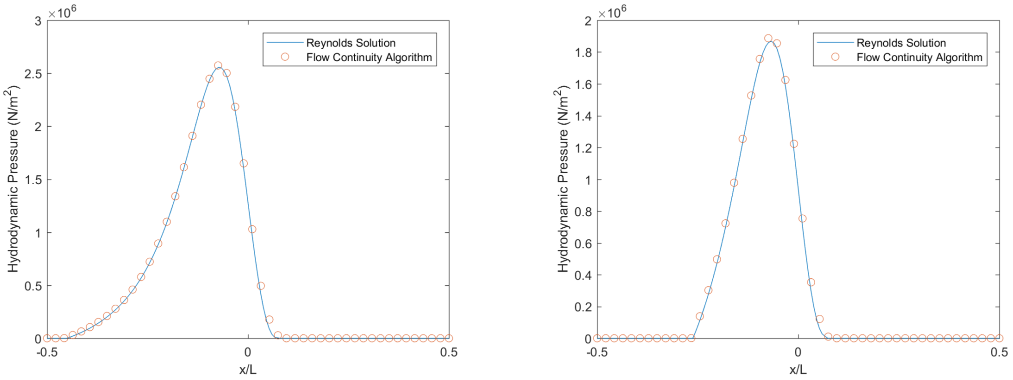

(a) $h_0 = 3.1\mu$m, $W = 455.4$ N

(b) $h_0 = 3.3\mu$m, $W = 272.1$ N

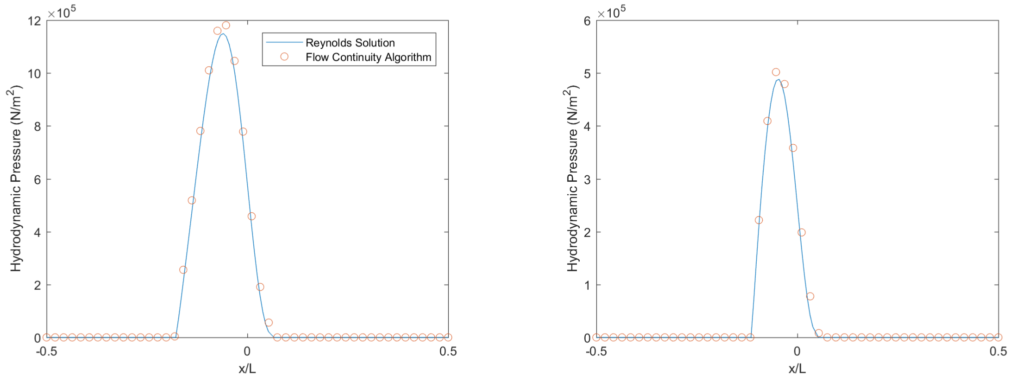

(c) $h_0 = 3.5\mu$m, $W = 136.5$ N

(d) $h_0 = 3.7\mu$m, $W = 40.9$ N

Figure 3.17: Comparison of flow-continuity algorithm against solution of Reynolds equation ($h_{oil} = 2\mu$m, $U = 0.32$ m/s, $\eta = 0.25$ Pa.s)

Chapter 4

Development of Experimental Apparatus

4.1 Introduction

In order to carry out the desired investigations, an apparatus is needed in which lubricant delivery is closely controlled, and in which there is suitable instrumentation for measuring piston-ring oil-film thickness. This chapter outlines the selection of an appropriate engine for testing, along with subsequent modifications, design of the lubricant injection system, manufacture and calibration of the oil-film thickness transducers, and lubricant selection.

Firstly, the rationale behind the use of this apparatus is detailed, along with the key differences between the ring packs of marine engines and that of the apparatus used for the following investigations.

4.2 Rationale

4.2.1 Large Two-stroke Marine Engines

Large two-stroke marine diesel engines are typically adopted for merchant vessels such as container ships. These engines are normally of the crosshead type, which is a mechanism involving guide rails and a sliding bearing contact at the little end of the connecting rod. A piston-rod then connects this to the piston through a stuffing box. A cross section of a typical crosshead engine is shown in figure 4.1.

The primary function of the crosshead and stuffing box are to allow isolation of the combustion chamber from the crank-case, which allows the use of cheap but dirty bunker fuels. This isolation prevents residual products of the combustion process, such as corrosive and abrasive contaminants from the fuel, from affecting other components in the engine. It also takes the forces generated by the connecting rod in the direction normal to the cylinder liner, allowing for better

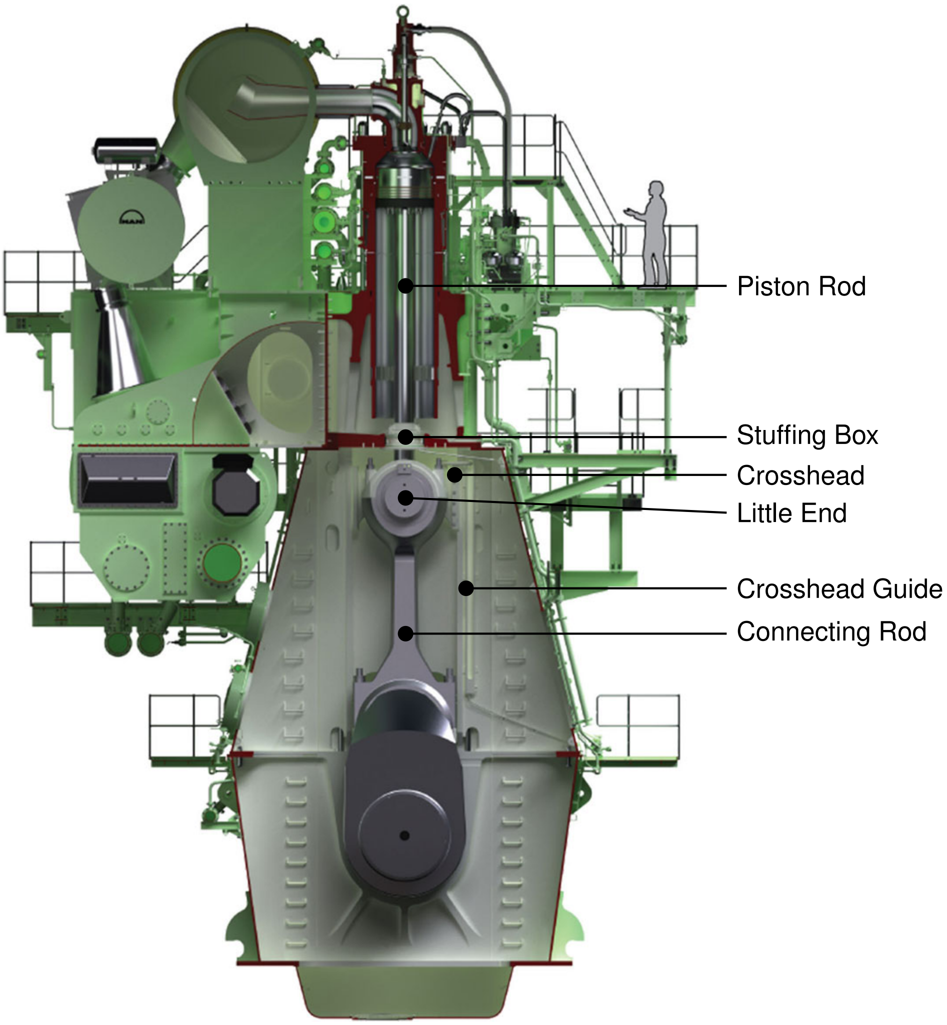

Figure 4.1: Cross-section of a typical marine diesel crosshead engine (Leduc, 2001)

lubrication and reduced friction and wear in the combustion chamber, where conditions are most harsh. This configuration dictates the need for a system to provide lubrication for the piston-rings. The independence of this lubricating system from the engine oil and its specific purpose allows the lubricant to be chosen to mitigate some of the detrimental effects of the fuel.

As discussed in the chapter 2, the lubricant must therefore serve several purposes, including the provision of a sufficient oil-film to form a gas seal, minimising contact between piston-rings and cylinder liner, and to neutralise the corrosive acids in the combustion gases due to the fuel sulphur content.

4.2.2 Scaling of the Experimental Apparatus

At the outset of the project, the objective was to conduct testing on a large marine engine, preferably of the crosshead type relevant to the aims of the research. Despite a prolonged period of inquiries to identify an appropriate facility and to negotiate relationships with manufacturers to allow this to happen, these efforts were unfortunately not successful.

To mitigate against being unable to conduct testing on a marine engine, a decision was made to modify a smaller engine for the purpose of the experiments. Several iterations of designs were proposed and prototypes manufactured. These included a crosshead type configuration, and plans for injecting through the wall of the cylinder. Limitations in the capabilities of injection systems available for the low flow-rates required, and difficulties with ensuring that lubricant injection through the wall of the cylinder liner did not adversely affect the lubrication of the piston-rings ultimately led to several key compromises in order to ensure the experimental equipment and process was feasible and reliable.

4.2.3 Motored Conditions

One of the more significant compromises has been to carry out the experiments under non-firing, or motored, conditions. This is due to several factors.

Unfortunately, the procurement and the complexity to integrate a lubricating system that operates at engine speed and injects through the cylinder liner or from the cylinder head, proved particularly challenging. As such, it was decided to run the investigations under motored conditions.

Because there will be no combustion during the engine cycle there will not be any lubricant consumption by evaporation. For a study on the use and consumption of lubricant, this is clearly an important factor. However, the absence of evaporation will permit consumption of lubricant by other means, such as the lubricant transport axially and circumferentially, to be monitored in isolation. In an engine the size of those used in the marine industry, lubricant transport is an important consideration for allowing proper piston-ring lubrication throughout the stroke.

4.2.4 Isolating the Cylinder Lubrication

During normal running the piston-rings would be lubricated by the splash lubrication from the crank case. Since the investigations require tightly controlled lubrication of the piston-rings, some means for preventing this was needed - either by using a barrier or baffle, or by conversion of the engine to the crosshead type. Both of these options were explored in some depth, and while the latter was considered to be more feasible, consequential effects relating to engine balancing, the need for additional sliding contacts, and the complexity involved in doubling the distance between cam-shaft and cylinder head, ultimately led to this option not being pursued. The tests will be carried out under motored conditions and the sump will remain dry in order to ensure only lubricant from the injectors will be present on the cylinder wall.

4.2.5 The Ring Pack

The ring pack of large two-stroke marine engines consists of up to five piston-rings to ensure an effective gas seal for the high pressures during combustion. Typically, the top two rings are asymmetrical barrel shaped and the remainder symmetrical, to encourage the spreading of lubricant to where it is needed around the cylinder liner. Anti-polishing rings are now also conventional to prevent the build-up of deposits and reduce scuffing, particularly when running on low sulphur fuels (Woodyard, 2004).

The ring pack in small diesel engines of the type used in this research is somewhat different, typically involving only two compression rings and an oil-control ring. These help to limit the flow of oil upwards to the combustion chamber (Bhushan, 2001b).

Only one symmetrical barrel shaped piston-ring will be used for this research, since the formation of the gas seal is not a concern. This will also simplify analysis since it will be certain that any phenomena observed are caused by this piston-ring. While there may be some differences between the precise behaviour of the lubricant film and oil-film thickness in these experiments, the basic mechanism of flow will be similar and the methods adopted will be applicable to trials on engines of any size and with ring packs of any configuration.

4.2.6 Lister-Petter TR1 Experimental Engine

A Lister-Petter TR1 was chosen for this research project due to its simplicity, and because the air-cooled cylinder liner is easily removed from the crank-case, making it ideal for the installation of oil-film thickness transducers and lubricant injectors. The Lister-Petter TR1 is a single cylinder, fixed speed, stationary engine. Other characteristics are that it is a naturally aspirated, direct injection diesel 4-stroke. Further details can be found in table 4.1.

Nominal Cylinder Bore	mm	98.42
Stroke	mm	101.6
Cylinder Capacity	litre	0.773
Compression Ratio	-	15.5:1
Minimum Idling Speed	rev/min	850

Table 4.1: Engine parameters for the Lister-Petter TR1 (Lister-Petter, 2011)

4.3 Dynamic Similarity

4.3.1 Viscosity Selection

Similitude is required between the experimental and operational conditions in the conjunction between piston-ring and cylinder liner to ensure results of the experiments are representative and relevant. To achieve similitude, geometric, kinematic, and dynamic similarity must be satisfied. Geometric similarity is achieved through use of the stock piston-rings, while non-dimensional analysis is required to find a suitable lubricant to develop a hydrodynamic oil-film over the majority of the stroke.

The expression relating these variables for a piston-ring of infinite width can be derived using Rayleigh's method for dimensional analysis. This method uses the dimensions of the variables to form an expression relating them. In this case it can be assumed that the oil-film thickness is a function of lubricant viscosity, ring-speed, hydrodynamic load, and ring-face radius. The resulting function can be expressed using indices for each of these variables, as in equation 4.1.

$$h = f(R^a, w^b, U^c, \eta^d) = k(R^a w^b U^c \eta^d) \tag{4.1}$$

	h	R	w	U	η
SI Unit	metre	metre	Newton per metre	metre per second	Pascal second
Dimensions	L	L	MT^{-2}	LT^{-1}	$ML^{-1}T^{-1}$

Table 4.2: Dimensions of variables which affect oil-film thickness

$$1 = a + c - d \tag{4.2}$$

$$0 = b + d \tag{4.3}$$

$$0 = -2b - c - d \tag{4.4}$$

The solution to these equations gives $a = 1$, $b = -d$, and $c = d$, such that the function for h can be written as

$$h = k(Rw^{-d}U^d\eta^d) = kR\left(\frac{U\eta}{w}\right)^d \tag{4.5}$$

The dimensions of the independent variables are given in table 4.2. Equating these dimensions gives three simultaneous equations (equations 4.2, 4.3, and 4.4), the solution of which gives the function shown in 4.5. The coefficients k and d can be found through experimentation or more detailed theoretical analysis, and the quotient $(\eta U/w)$ is the dimensionless group that governs hydrodynamic lubrication. It can be concluded from this analysis that should all geometric parameters remain the same (which would be true for a comparison between firing and motored tests), then to maintain the oil-film thickness the value of the dimensionless group must remain constant.

Further analysis of the Reynold's equation (Stachowiak and Batchelor, 2005) gives further confirmation of the relationship between these variables and verifies the reduction used for the numerical investigation is appropriate.

$$\frac{\partial}{\partial x}\left(\frac{h^3}{\eta}\frac{\partial p}{\partial x}\right)+\frac{\partial}{\partial y}\left(\frac{h^3}{\eta}\frac{\partial p}{\partial y}\right)=6U\frac{dh}{dx}+12\frac{dh}{dt} \tag{4.6}$$

Non-dimensional expressions are defined for oil-film thickness ($H = h/C_b$) and axial piston-ring width ($X = x/b$), circumferential length ($Y = y/R_b$), and an expression relating time and engine speed ($d\alpha = \omega dt$). This allows Reynold's equation to be re-written

$$\frac{C_b^2 b}{\eta U R_b^2}\frac{R_b^2}{b^2}\frac{\partial}{\partial X}\left(H^3\frac{\partial p}{\partial X}\right)+\frac{C_b^2 b}{\eta U R_b^2}\frac{\partial}{\partial Y}\left(H^3\frac{\partial p}{\partial Y}\right)=6\frac{dH}{dX}+\frac{12b\omega}{U}\frac{dH}{d\alpha} \tag{4.7}$$

Substituting for the geometric parameters of the piston assembly using $\psi = C_b/R_b$, $\lambda = R_b/b$, and $K = b\omega/U$, and rearranging, gives

$$\frac{\psi^2 b}{\eta U}\lambda^2\frac{\partial}{\partial X}\left(H^3\frac{\partial p}{\partial X}\right)+\frac{\psi^2 b}{\eta U}\frac{\partial}{\partial Y}\left(H^3\frac{\partial p}{\partial Y}\right)=6\frac{dH}{dX}+12K\frac{dH}{d\alpha} \tag{4.8}$$

$$P=\frac{\psi^2 b}{\eta U}p \tag{4.9}$$

The equation in 4.9 can be found by inspection, and since integrating the pressure per unit width (or length) gives hydrodynamic load, it follows that the non-dimensional load-carrying capacity is given as per equation 4.10.

$$W=\int P dX=\frac{\psi^2 b}{\eta U}\int p dx=\frac{\psi^2 b}{\eta U}w \tag{4.10}$$

Equivalence of this non-dimensional load-carrying capacity for the conditions present during the engine firing and the engine being motored should ensure the oil-film thickness is similar in both cases, and equation 4.11 shows this equivalence. The subscripts e and f represent the experimental and firing conditions respectively. This equation corresponds with the dimensional analysis, since maintaining oil-film thickness should ensure a constant ratio between oil-film thickness to ring-face radius (h/R).

$$W=\frac{\psi_f^2 b_f}{\eta_f U_f}w_f=\frac{\psi_e^2 b_e}{\eta_e U_e}w_e \tag{4.11}$$

The recommended lubricant for this engine in operation is the synthetic oil SAE 5W-20. This oil has kinematic viscosity and density as shown in table 4.3.

Similarity was considered for the cases where the piston-ring is near top-dead centre on both a power and induction stroke, and also at midstroke on an induction stroke. Since the piston-ring geometry is unchanged, and because the required load capacity is proportional to the combustion chamber pressure, the similarity requirement is reduced to that in equation 4.12. The value of this

Kinematic Visosity	$40\,\mathrm{deg}$	43.51	mm^2/s (cSt)
	$100\,\mathrm{deg}$	8.2	mm^2/s (cSt)
Relative Density		0.847	

Table 4.3: Physical properties of Castrol Magnatec Stop-Start 5W-20 E engine lubricant (Castrol, 2015)

	η (mPa.s)	U (m/s)	p (bar)	$\frac{\eta U}{p}$
@5 deg after TDC (Power Stroke)	120	1.1	60	0.22
@5 deg after TDC (Induction Stroke)	120	1.1	0.86	15.0
@90 deg after TDC (Induction Stroke)	120	8.0	1.4	60.0

Table 4.4: Comparison of the similarity parameter at different stages of the engine cycle

similarity parameter is tabulated for the three cases in table 4.4.

$$\frac{\eta_f U_f}{p_f} = \frac{\eta_e U_e}{p_e} \tag{4.12}$$

Evaluating the similarity parameter for lubricant viscosity during the experiments is performed using a pressure of 1 bar at all crank angles (since the cylinder head will be removed for the tests), and with velocities of $1/25^{th}$ of those shown in the table.

For the compression and power strokes, ensuring similarity is challenging due to the peak combustion pressure far exceeding the pressure at the other end of these strokes. While a viscosity of 6 mPa.s should give equivalence at the top of the stroke, further down the low viscosity would result in small oil-film thicknesses, which is not ideal for these tests as it will be difficult to see any changes under different lubrication conditions.

Matching the similarity parameter near top dead centre on the induction stroke on the other hand suggest the use of an oil with dynamic viscosity 417 mPa.s, while matching at midstroke suggests a viscosity of 210 mPa.s is needed. Since it is beneficial to see clear differences in the oil-film thickness during the experiments the higher viscosity was chosen. Additionally, should the oil warm slightly during the tests the viscosity should still be sufficient to maintain a full lubricant film over the entire stroke.

Two lubricants were tested for viscosity using the Anton Parr SVM-3000 Stabinger viscometer. This performs a precise test for dynamic and kinematic viscosities, along with lubricant density. Results from these tests are shown in figure 4.2. Typical (British) room temperature would be slightly below 20 degrees, and at this temperature it is clear the 20W-50 lubricant is the better choice. The full test results for this oil are shown in table 4.5.

Temperature (Degrees)	Dynamic Viscosity (mPa.s)	Kinematic Viscosity (mm^2/s	Density (kg/m^3)
10	727.95	829.91	0.8779
15	517.42	591.56	0.8747
20	375.66	431.03	0.8715
25	276.29	318.16	0.8684
30	204.72	236.59	0.8653
35	155.70	180.59	0.8622
40	120.49	140.25	0.8591

Table 4.5: Viscometer data for Motaquip 20W-50 mineral oil

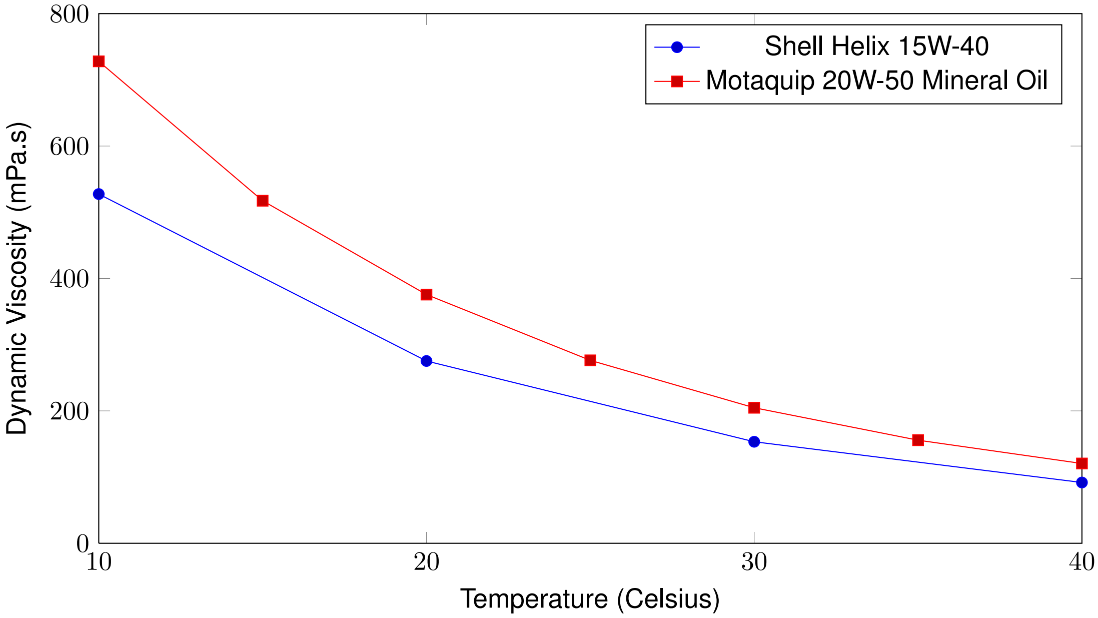

Figure 4.2: Dynamic viscosity test results

4.3.2 Surface Roughness of Piston-ring and Cylinder

It is important to supply enough lubricant to separate asperities and maintain hydrodynamic lubrication over most of the cycle. To do this it is useful to know the surface roughness average (Ra) of both cylinder liner and piston-ring. In this way the minimum required oil-film thickness can be estimated.

Roughness Average (Ra)

The roughness average (Ra) is defined as the arithmetical mean of the assessed profile, according to equation 4.13, as

$$Ra = \frac{1}{l}\int_0^l |Z(x)|dx \tag{4.13}$$

Where $Z(x)$ is the height of the profile above the mean line at any position (British-Standards-Institution, 1998). Shown in figures 4.3 to 4.6 are surface profiles (raw and modified) of both piston-ring and cylinder liner. The average roughness of the piston-ring was 0.12 μm, and the cylinder liner after honing 0.42 μm.

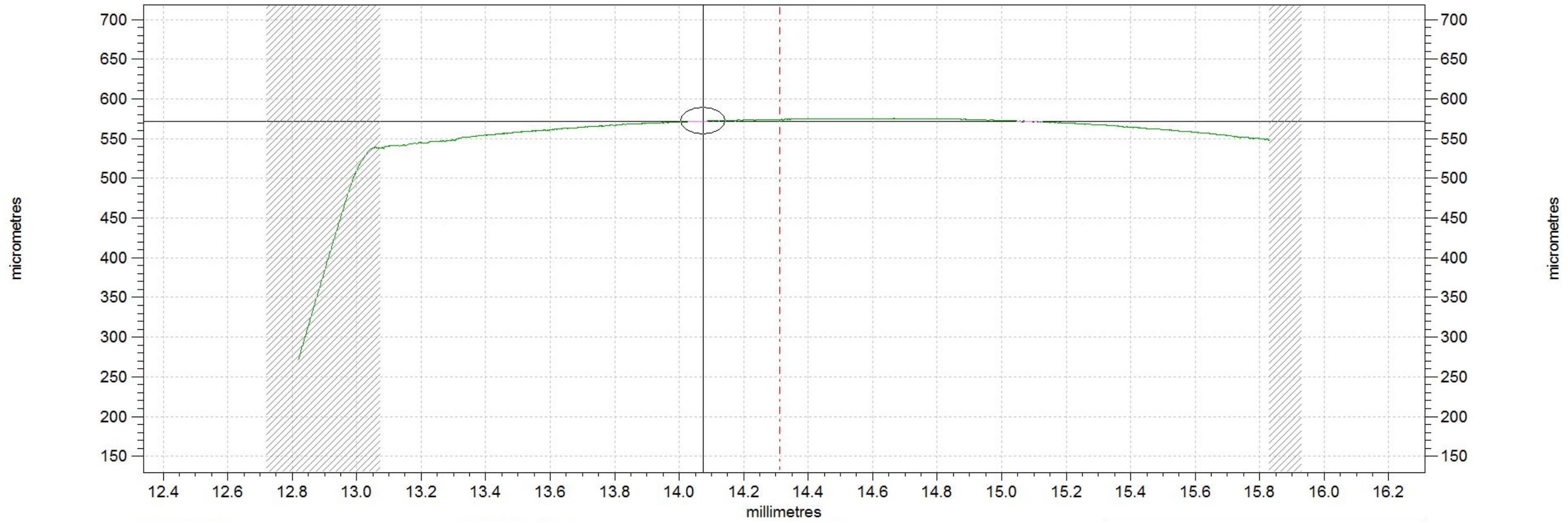

Figure 4.3: Raw Talysurf measurement profile of top piston-ring face

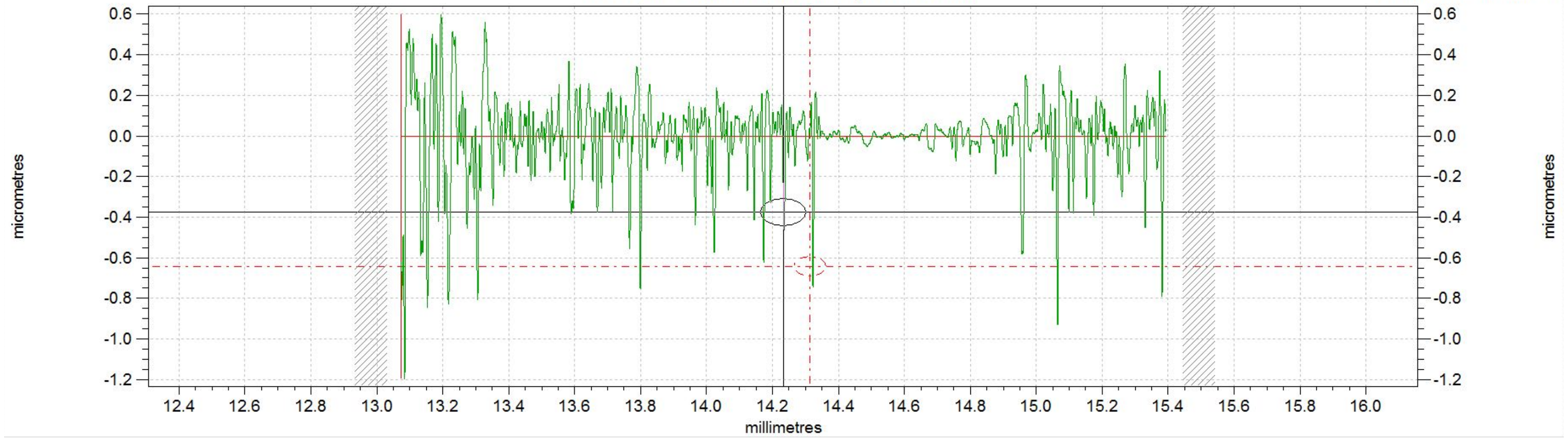

Figure 4.4: Band-pass filtered Talysurf measurement profile of top piston-ring face

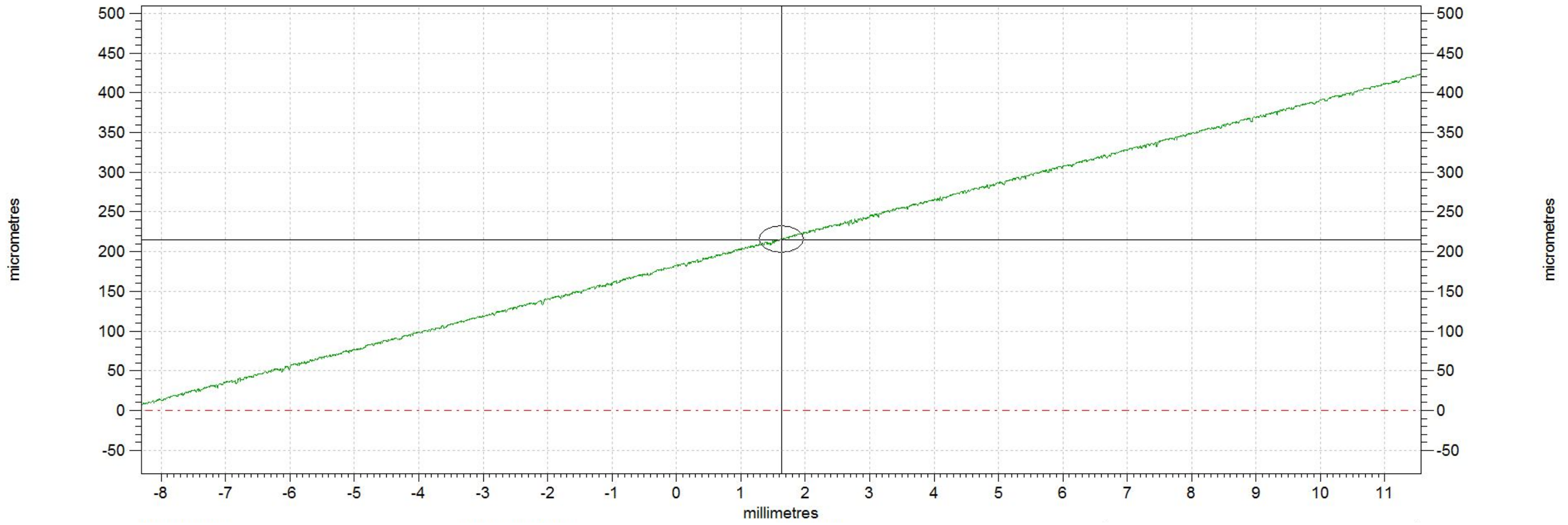

Figure 4.5: Raw Talysurf measurement profile of cylinder surface

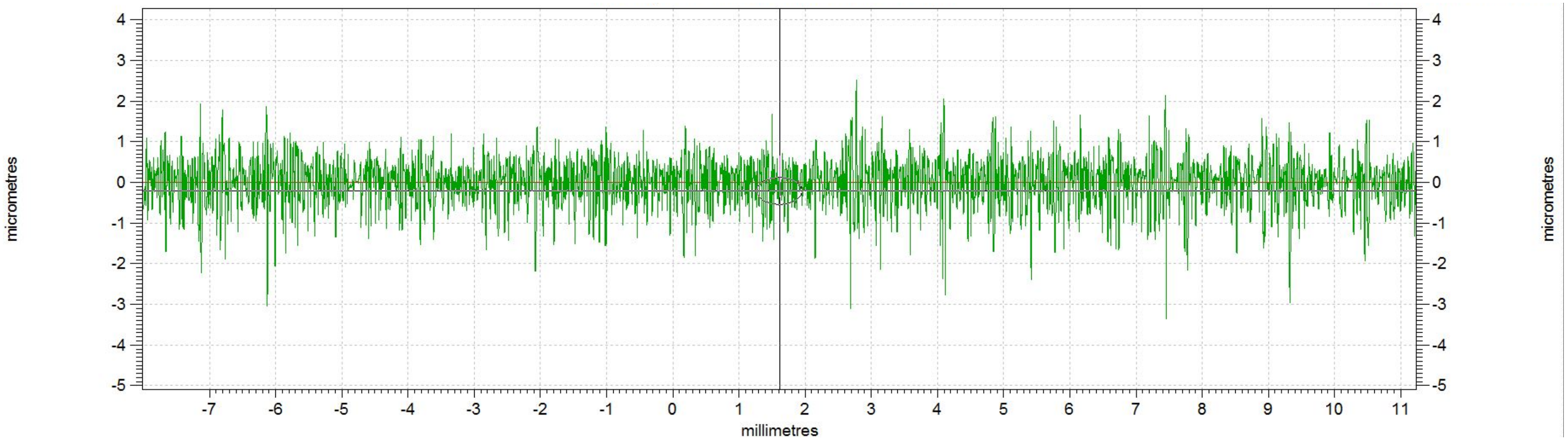

Figure 4.6: Band-pass filtered Talysurf measurement profile of cylinder surface

4.4 Lubricant Injection System

A lubrication system would need to be added to provide lubricant for the piston-rings. This system would need to

1. Deliver an appropriate quantity of lubricant onto the cylinder liner to ensure hydrodynamic lubrication of the piston-rings.
2. Distribute the oil sufficiently such that lubricant is transported down the liner to lubricate the bottom half of the stroke.
3. Allow the lubricant delivery to be adjusted such that the desired experiments can be carried out. This would include
    (a) Adjustable volumetric flow-rate of lubricant
    (b) Adjustable lubricant distribution
    (c) Adjustable lubricant injection frequency and timing
4. Automatically trigger the lubricant injection at the appropriate crank angle
5. Inject at a frequency of once per revolution at the maximum required engine speed

4.4.1 Lubricant Injector Flow-rate Requirements

To determine the rate at which lubricant is to be injected into the cylinder (q_r), a calculation was performed assuming a perfectly uniform distribution of oil on the cylinder wall. The calculation shown (equation 4.14) gives the required flow-rate for an oil thickness of 1 μm. The cylinder has a diameter of 98 mm and the stroke length is 101 mm.

$$q_r = \pi DL * h_{oil} = \pi \times 98 \times 101 \times 0.001 = 9.90mm^3 = 0.0099ml \tag{4.14}$$

The engine, having 4 injectors at this flow rate, could be considered to deliver a uniform oil-film on the cylinder liner of 4 μm. The lubricant film delivered will not of course be uniform (the true distribution is shown in 4.11), leading to regions in the lubricant film both thicker, and thinner, than this value. Additionally, since the lubricant will be injected from above the cylinder liner, only lubricant that is transported down the liner by the piston-ring will reach the lower portion of the stroke. As such it is expected that more oil will need to be delivered than would be needed if the oil-film were perfectly uniform as per the above calculation.

The SL-43 injector, shown in figure 4.7, allows for adjustable, metered delivery of lubricant to the spray nozzle, and subsequently to the cylinder liner. It operates by switching on and off the supply pressure to cycle the measuring and delivery processes. When the supply line is under pressure the plunger moves forward to force the lubricant in the discharge chamber through the outlet check valve to the feed line. Lubricant is also fed to the measuring chamber during this part of the cycle. The supply line is then vented, and as the plunger returns to it's retracted position draws lubricant from the measuring chamber to the discharge chamber. Flow from the feed line is blocked by the outlet check valve.

The injector is specified to be adjustable between 0.001 cubic inches to 0.008 cubic inches (0.0164 ml to 0.131 ml), by screwing the indicator cap through 5 full turns and tightening the lock-nut against it.

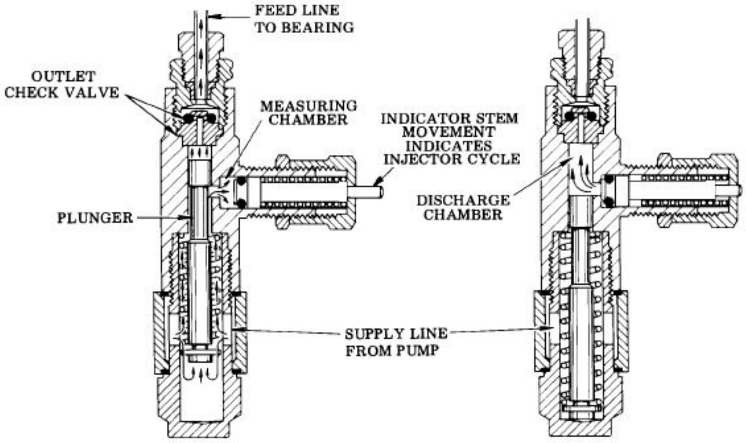

Figure 4.7: Cross-section of SL-43 injector (Lincoln-Industrial, 2002)

To cycle the pressure of the lubricant supply line, a pneumatic circuit was designed. This comprised of a 24 V solenoid valve that would electronically switch the air supply to the pneumatic pump feeding the SL-43 injectors and subsequently the spray-nozzles that deliver the lubricant to the cylinder liner. On a parallel circuit, following the solenoid, a pressure regulator and a manifold distribute the intermittently compressed air to operate 4 spray-nozzles to deliver the metered quantity of lubricant. A schematic of this circuit is pictured in figure 4.8.

4.4.2 Lubricant Flow Rate Validation

Tests were conducted in order to verify the system injects the quantity of lubricant stated in the specification documents. The test involved repeated cycling of the injector circuit to fire up to twenty shots of lubricant into a measuring cylinder. The supply pressure to the spray nozzles was set at 1 bar gauge, and the opening time for the solenoid set at 0.2 seconds. The test was repeated for each injector at half turn increments of the indicator cap.

Average results for all injectors are shown in figure 4.9 and below in table 4.6, with results for individual injectors being shown in figures 4.10a to 4.10d.

TURNS	0	0.5	1.0	1.5	2.0	2.5	3.0	3.5	4.0	4.5	5.0
AVERAGE	0.0101	0.0235	0.0384	0.0520	0.0657	0.0798	0.0929	0.1018	0.1125	0.1188	0.1267
STDEV	0.0042	0.0054	0.0040	0.0043	0.0028	0.0022	0.0021	0.0069	0.0051	0.0016	0.0075

Table 4.6: Average injection quantity at each setting for the 4 injectors

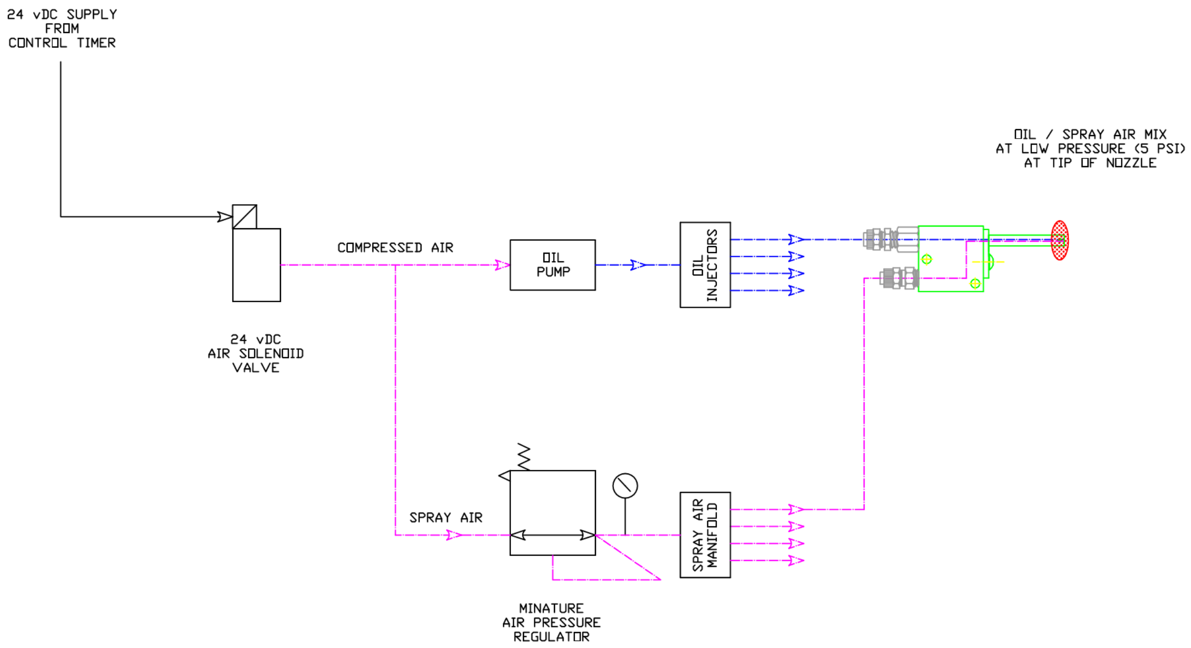

Figure 4.8: Diagram of the injection system circuit

Number of Turns	Approx. Flow Rate
0.0 turns	0.01 ml inj^{-1}
0.5 turns	0.02 ml inj^{-1}
1.0 turns	0.04 ml inj^{-1}
2.5 turns	0.08 ml inj^{-1}

Table 4.7: Approximate lubricant flow-rates

The graph in figure 4.6 shows a consistently linear relationship between the indicator cap setting and the injection quantity up to the third turn, after which there is a very slight reduction in the rate of change. The confidence level shown by the error bars suggests that there is very strong consistency in lubricant delivery though, so it should be possible to confidently relate the adjustment cap setting to the delivery quantity regardless of the non-linear trend seen at the higher injection quantities.

For simplicity going forward, the relationship between the number of turns and lubricant delivery will be rounded to one decimal place. These are summarised in table 4.7.

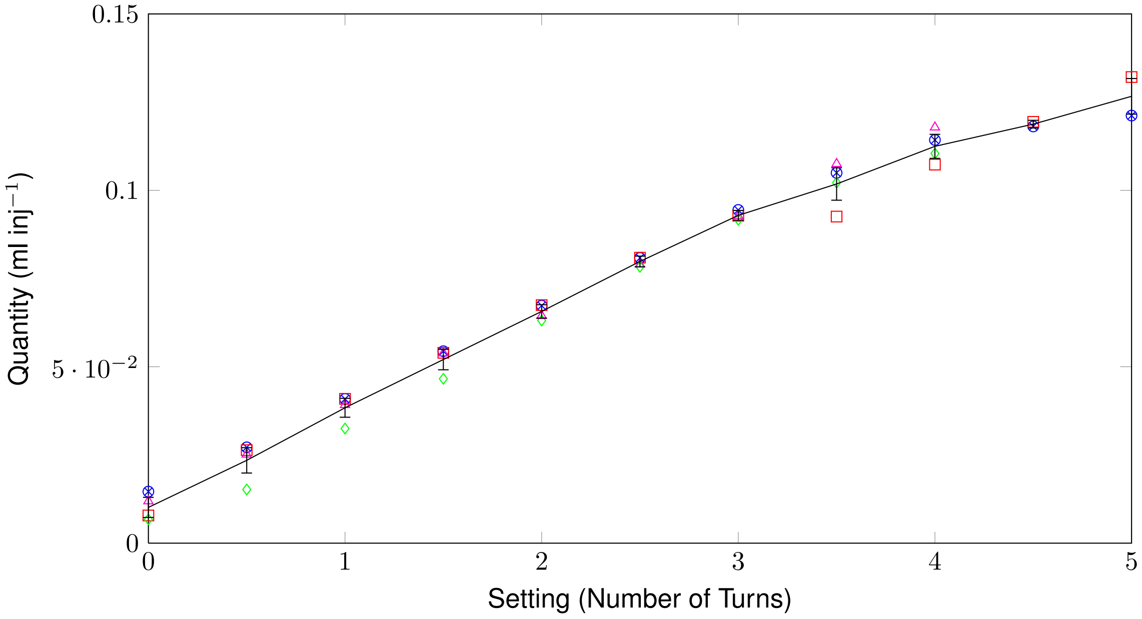

Figure 4.9: Average injection volumes for injectors 1 to 4. Error bars indicate 95% confidence level

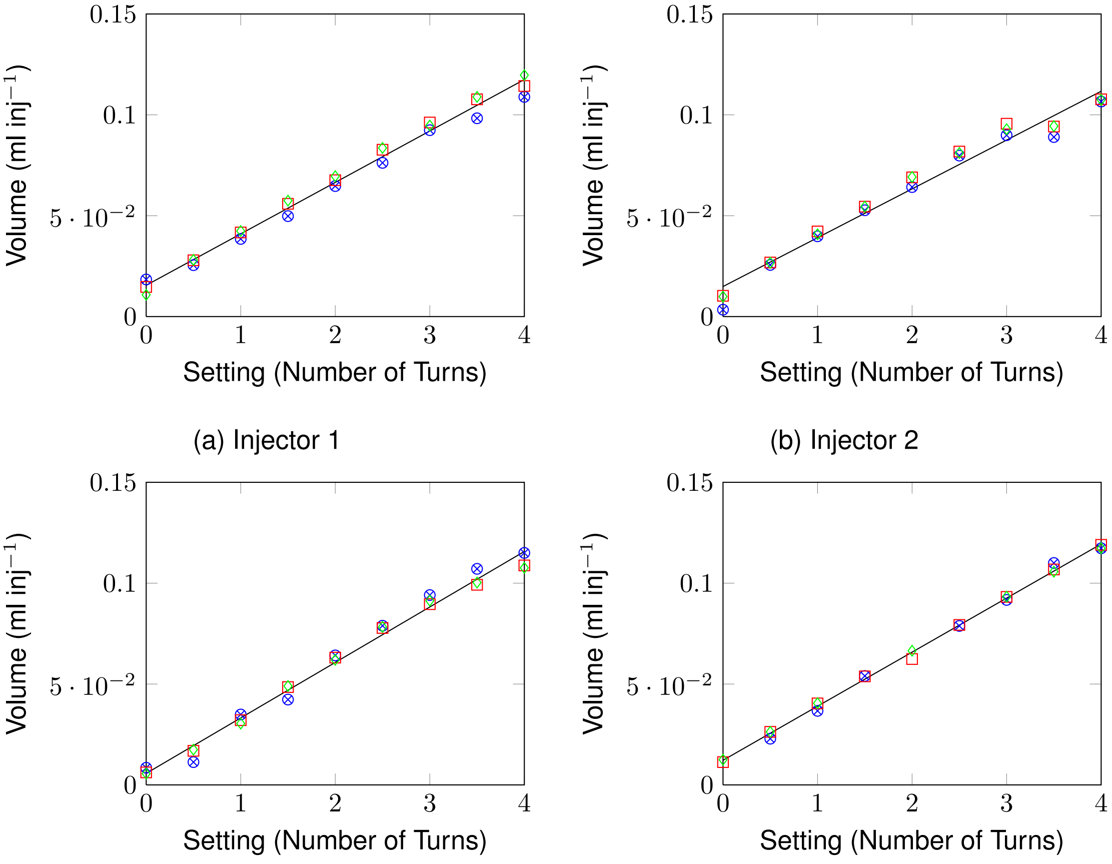

(a) Injector 1

(b) Injector 2

(a) Injector 1

(b) Injector 2

Figure 4.10: Calibration charts for injectors 1 to 4

4.4.3 Lubricant Distribution

To determine the distribution of lubricant on the cylinder liner a test was performed in which lubricant was sprayed onto a piece of paper inserted into the cylinder liner. Knowledge of the spread is important in order to ensure any simulations are comparable, and also to ensure the design intent of the experiments is met. The paper used for the test had height equal to the stroke length of the engine. A modified image of the result of this test is shown in figure 4.11, and shows the lubricant spread axially is from near top-dead-centre to approximately 60-80 degrees crank angle. Circumferentially there is not as much spread as expected, with each injected lubricant volume covering around 35 degrees to 40 degrees around the circumference.

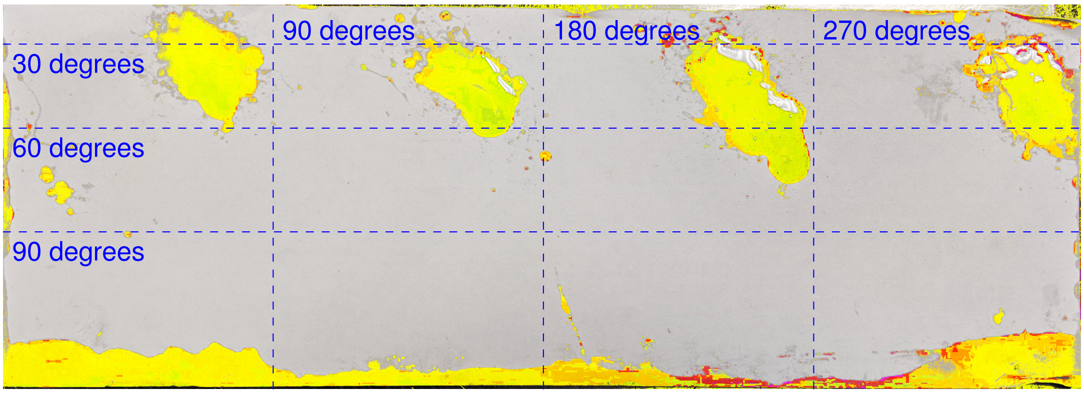

Figure 4.11: Distribution of lubricant on cylinder liner

While these volumes of lubricant are more focussed than originally intended, they are distinct enough to allow the transport of lubricant axially and circumferentially to be seen clearly - which is critical for the planned investigations. While the orientation of the injectors could be changed and perhaps optimised using a selection of different brackets, for this study they will remain unaltered.

The oil at the bottom of the sample originated from between the cylinder liner and piston (which sat at bottom-dead-centre). This was very difficult to eradicate, but does not detract from the result of the test.

4.4.4 Lubricant Injection Control

An electronic triggering system was developed and built to control the timing and frequency of lubricant injection. This incorporated a Hall-effect sensor mounted on the engine and a trigger on the flywheel. A voltage divider reduces the signal voltage from the Hall-effect sensor and is used as an input to the Nucleo development board micro-controller (STM32F4), which has been programmed (using MBED OS C++ compiler) to operate as a counter to determine whether or not to inject on a particular cycle. When it is correct to inject lubricant the output from the microcontroller is high, the transistor allows current to flow and the the solenoid opens the valve on the pneumatic lubricant injection circuit. The trigger position can be adjusted to allow the injection timing to be refined.

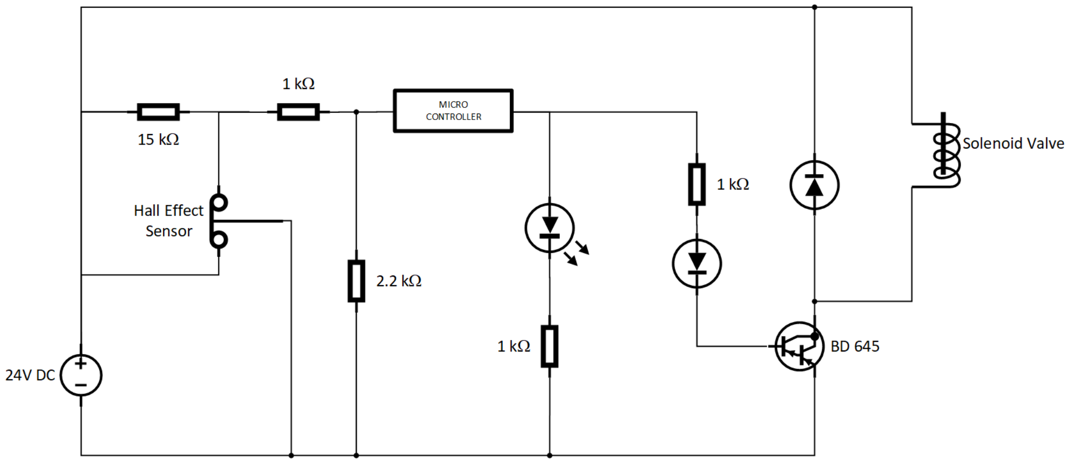

Figure 4.12: Schematic of microcontroller circuit

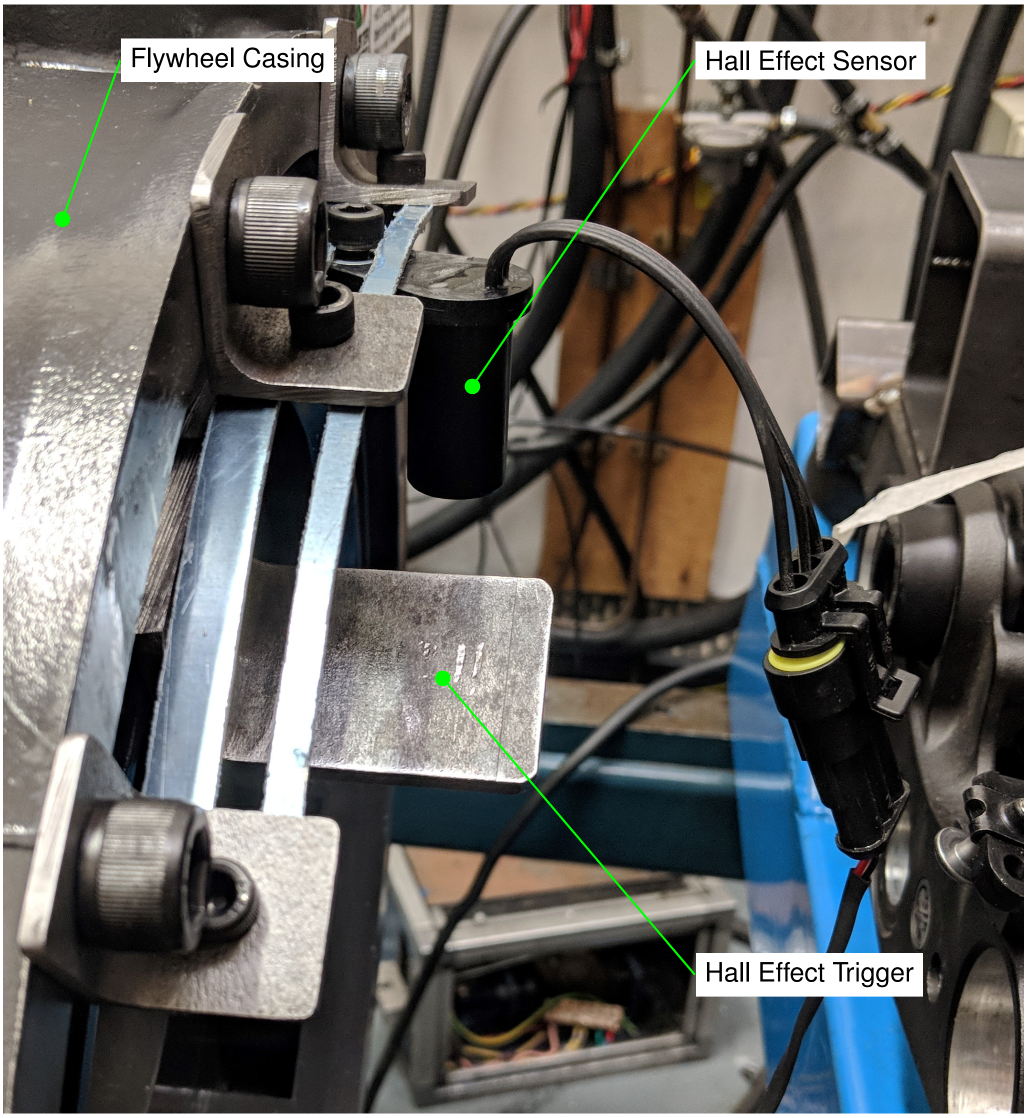

Figure 4.13: Hall-effect sensor, and trigger bracket fitted to engine flywheel

4.5 Engine Modifications

The installation of injectors should be such that delivery of lubricant is over a sufficient portion of the cylinder liner to provide hydrodynamic lubrication. To carry out the desired investigations it was also important to allow some adjustability in the direction of injection and spread of lubricant. Mounting the injectors to spray through the liner was considered - as per marine diesel engines with either swirl injection principle (Hans Jenson Lubricators), or the pulse lubricating system (Wartsila). However this would be difficult to achieve without having an impact on the lubrication of the piston-ring due to the size of the hole required.

Instead the lubricant was injected from above the cylinder - with injectors mounted on a bespoke cylinder head (figure 4.14). A variety of mounting brackets allows the vertical and radial position of the injector, as well as the direction of lubricant spray, to be easily modified.

Since the location of the injector nozzle was known from the distribution analysis (figure 4.11), and the injector dimensions are known, it was relatively straightforward to position a mounting bracket that could hold them in this position.

A three component system has been designed on which to mount the brackets, providing flexibility over the precise position of each injector. A large tubular section sits atop the cylinder, where the cylinder head had been originally. A circular plate - with a large hole in the centre is mounted above this. In this component there are 4 holes through which the original studs are fitted to clamp down the new head. Having this part of the assembly as two components allowed higher efficiency in the manufacturing, since the latter part could be quickly machined out of sheet metal on a waterjet cutter, while the first could be turned from extruded bar - meaning less processes involved and no need to move the work from one machine to another. Finally a bracket was secured on top of the plate onto which each injector was mounted.

The assembly is shown below in figure 4.14, and in figures 4.15 and 4.16.

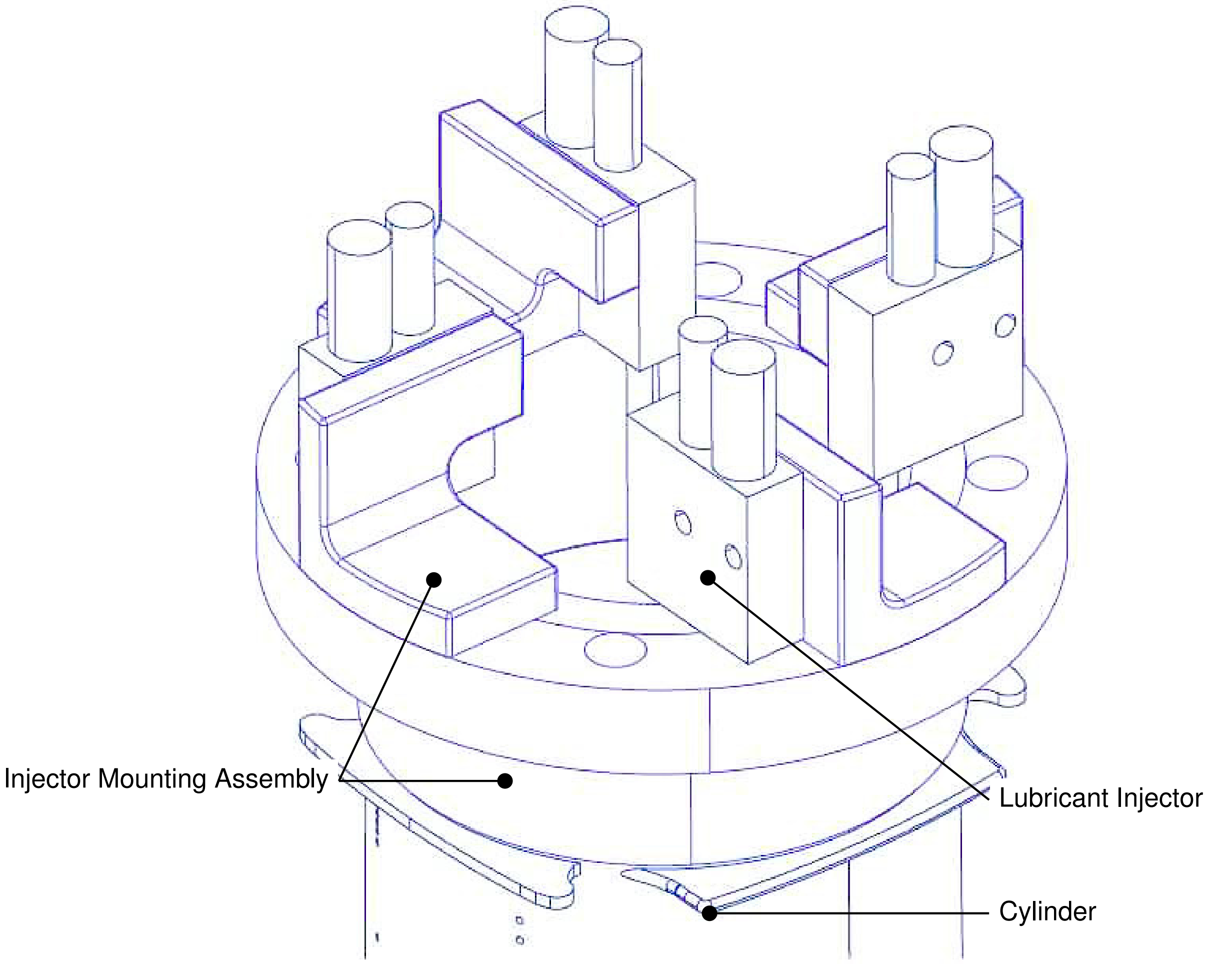

Figure 4.14: Replacement cylinder head assembly

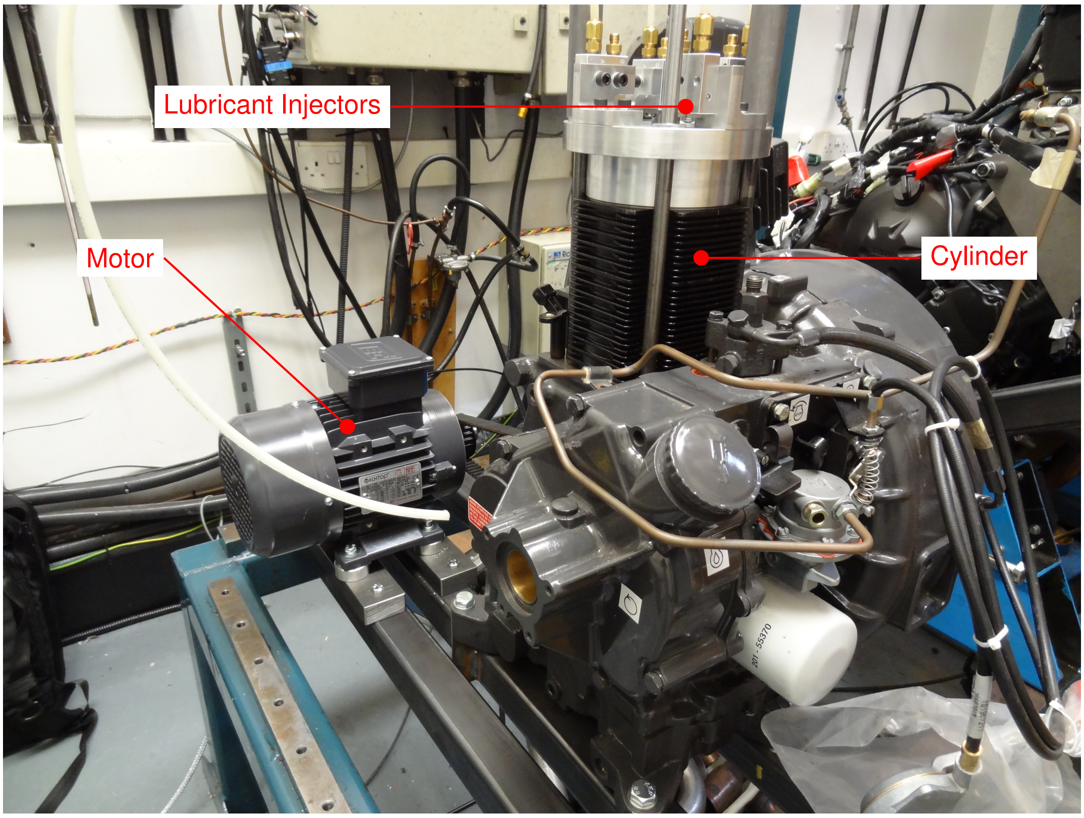

Figure 4.15: Engine mounted in the dynamometer cell

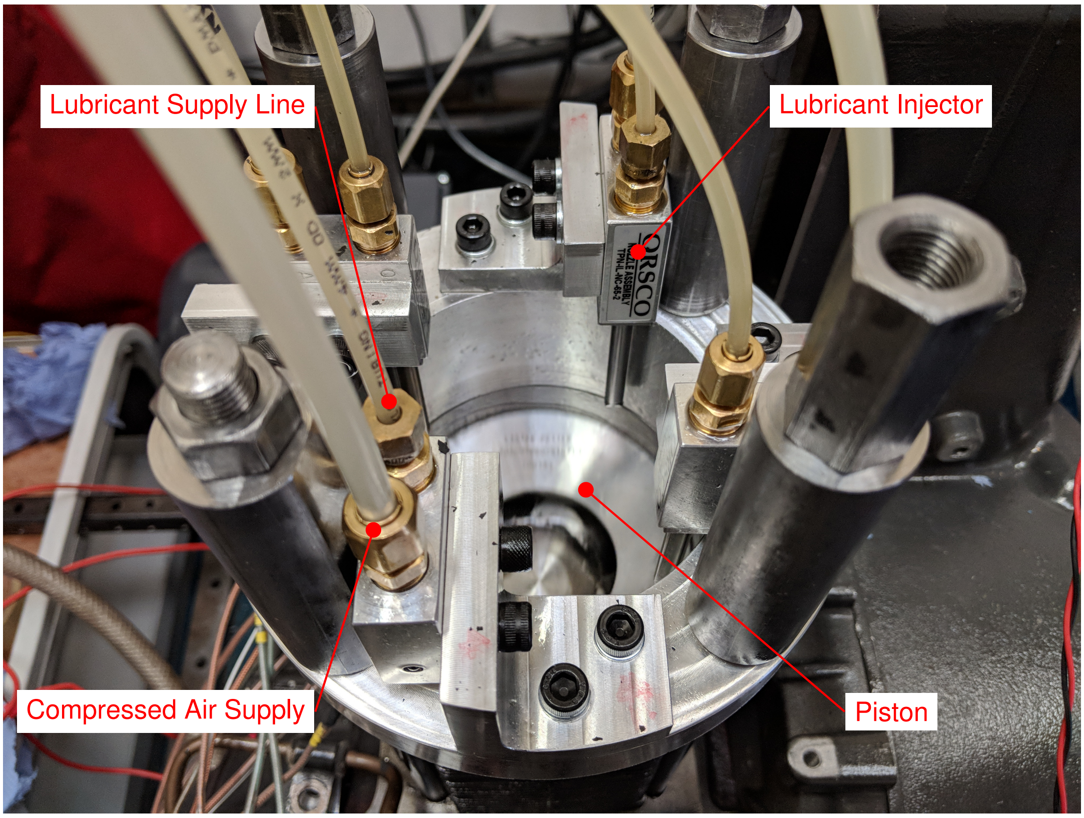

Figure 4.16: Replacement cylinder head assembly with lubricant injectors fitted

4.6 Oil-film Thickness Measurement

4.6.1 Transducer Specification

As discussed in the literature survey in chapter 2, there are a number of different types of oil-film thickness transducers that could be used in this type of investigation. For the purposes of this work, the transducers should be straightforward to calibrate, reliable, and accurate. They must also have a fast enough response and sample rate to record enough data points as the piston-ring passes, in order to provide a resolution that allows the ring-shape to be analysed and to ensure the minimum oil-film thickness is recorded.

The capacitance type transducer is ideal for satisfying these needs. This type of sensor has successfully been used in both firing and motored engines to measure the oil-film thickness to micron-level accuracy, and provides sufficient resolution to determine the shape of piston-ring face.

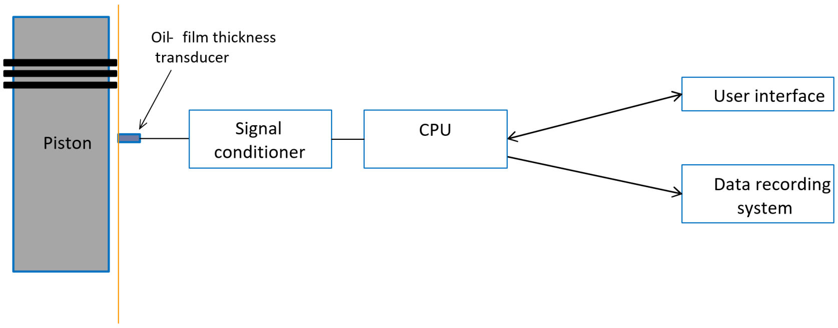

Figure 4.17: Transducer located in the cylinder liner with schematic of the intrumentation hardware

Figure 4.17 shows how a capacitance sensor is positioned in the cylinder liner, along with the systems needed for logging oil-film thickness measurements. The system consists of the transducer itself, a signal conditioner to provide a voltage to the sensor and amplify the resulting signal, and a means of logging, processing, and viewing the data - typically with a PC and some data acquisition hardware. In this case two National Instruments PXI-4472 dynamic signal acquisition modules are used in a PXI chassis. The signal voltage data is logged using a simple LabVIEW virtual instrument before writing to files for later analysis.

The equipment used is comparable to that used by (Grice et al., 1990) during the original development of the capacitance based technique for oil-film thickness of piston-rings. This system uses plate capacitor theory, for which capacitance is given by equation 4.15. Here, C_T is transducer capacitance, ϵ_0 the absolute permitivity, ϵ_r the relative permitivity of the lubricant, A the electrode area, and d the distance between transducer and piston-ring.

$$C_T = \frac{\epsilon_0 \epsilon_r A}{d} \tag{4.15}$$

The transducer is connected to a charge amplifier which excites the capacitor plates with a 12 kHz oscillator and produces a voltage that is proportional to the distance between the plates (d). The output voltage of the charge amplifier (V_{out}) is related to the transducer capacitance and hence oil-film thickness (d) as shown in equations 4.16 and 4.17 respectively. The oscillator input and capacitance are V_{osc} and C_{osc}. The constant k is determined during the calibration process, and is assumed to be consistent for all transducers for as long as the electrode area remains unaltered.

$$V_{out} = -\frac{V_{osc} C_{osc}}{C_T} \tag{4.16}$$

$$V_{out} = -\frac{V_{osc} C_{osc} d}{\epsilon_0 \epsilon_r A} = k\frac{d}{A} \tag{4.17}$$

For this work the transducer took the form shown in figure 4.18. While it is more common for a ceramic tube to be used for insulating the sensor from the cylinder liner and separating the electrode and screen, the low temperatures expected for the planned experiments allowed a polymer tube to be used - which has advantages in surface quality and hence measurement sensitivity following the honing process. The polymer tube was produced using stereolithography (SLA) 3D printing, which is motivated through limited options being available in tubes of the required size. The resin used is Formlabs Grey, for which the mechanical and thermal properties are shown in table 4.8. The sensors were cured and as such these properties should be referred to. The full data sheet can be found in appendix C.

The heat deflection temperature test described in ASTM D 648-07 covers the determination of the temperature at which an arbitrary deformation of a moulded component occurs. It involves a simple beam of rectangular cross-section being tested under two loads, the first to subject the beam to fibre stesses of up to 0.455 MPa (66 psi), and the second to 1.82 MPa (264 psi). The temperature is raised in 2 degree increments until the deflection reaches 0.25 mm. Given the stress of a simple, rectangular beam can be calculated using equation 4.18, and the deflection is given by equation 4.19, equating forces allows the expression for elastic modulus of the material to be derived as per equation 4.20.

$$\sigma = \frac{My}{I} = \frac{3FL}{2bd^2} \rightarrow F = \frac{2bd^2\sigma}{3L} \tag{4.18}$$

	Green	Post-cure	Method
Mechanical Properties			
Ultimate Tensile Strength	38 MPa	65 MPa	ASTM D 638-10
Young's Modulus	1.6 GPa	2.8 GPa	ASTM D 638-10
Elongation at Failure	12%	6.2%	ASTM D 638-10
Flexural Modulus	1.25 GPa	2.2 GPa	ASTM C 790-10
Notched IZOD	16 J/m	25 J/m	ASTM D 256-10
Thermal Properties			
Heat Deflection Temp. @ 264 psi	42.7 C	58.4 C	ASTM D 648-07
Heat Deflection Temp. @ 66 psi	49.7 C	73.1 C	ASTM D 648-07

Table 4.8: Mechanical and thermal properties for Formlabs Grey (FormLabs, 2017)

$$\delta = \frac{FL^3}{48EI} = \frac{FL^3}{4Ebd^3} \rightarrow F = \frac{4\delta Ebd^3}{L^3} \tag{4.19}$$

$$E = \frac{\sigma L^2}{6d\delta} \tag{4.20}$$

Using equation 4.20 with the data from the standard gives the elastic modulus as 0.23 GPa at 73.1 C for fibre stress 0.455 MPa, and 0.93 GPa at 58.4 C for applied stress of 1.82 MPa.

The epoxy is a two-part adhesive which is high stiffness (unspecified), has shear strength of approximately 20 MPa, has good chemical resistance properties, and is electrically insulating. Given the hydrodynamic pressure could feasibly reach the order of 10 bar, the maximum shear stress would be in the region of 0.1 MPa which is well below the shear strength.

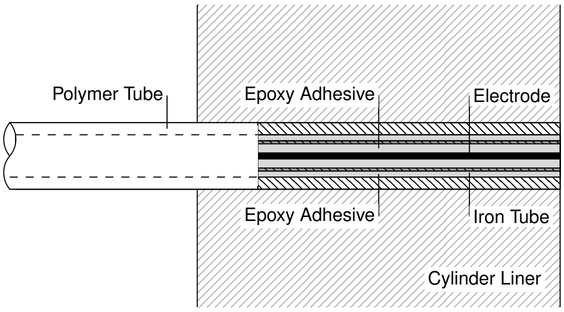

Figure 4.18: Cross-section of oil-film thickness transducer

Sample-rate/Resolution

Given the motored conditions, for which the engine speed will be in the region of 60 rpm, the minimum passing time for a piston-ring past any of the sensors in approximately 7.5 milliseconds (axial piston-ring width 2 mm, piston velocity 0.31 m/s). This is the second piston-ring passing the sensor at mid-stroke. Given a maximum sample rate of 10 kHz, past this sensor there should be over 75 data points. It will also ensure the time between datapoints is at least twice the 50 μs rise time of the amplifier.

4.6.2 Transducer Positioning

The transducers will need to be positioned carefully to successfully investigate the effects on oil-film thickness of lubricant flow rate and distribution. Since lubricant is delivered from four injectors, there will be a variable distribution around the circumference of the cylinder liner - ie. there is likely to be an overlapping region with the combined lubricant from two injectors, in addition to a region that has lubricant from a single injector. It is important to monitor the oil-film thickness in both of these regions to understand how lubricant is being distributed over the surface of the cylinder liner, and so a number of transducers will be placed axially, along a line through the centre of the delivery zone, as well as in the intersecting region. Eight sensors on each line (to be referred to as block I and block II) should be sufficient to measure the oil-film thickness over the course of a stroke, and allow the oil transport and oil-film thickness to be analysed.

In addition to the above sensors, three further sensors will be located around the circumference of the cylinder liner, at an axial location 31 mm below top dead centre (correspondent with a crank angle of 60° from top dead centre)

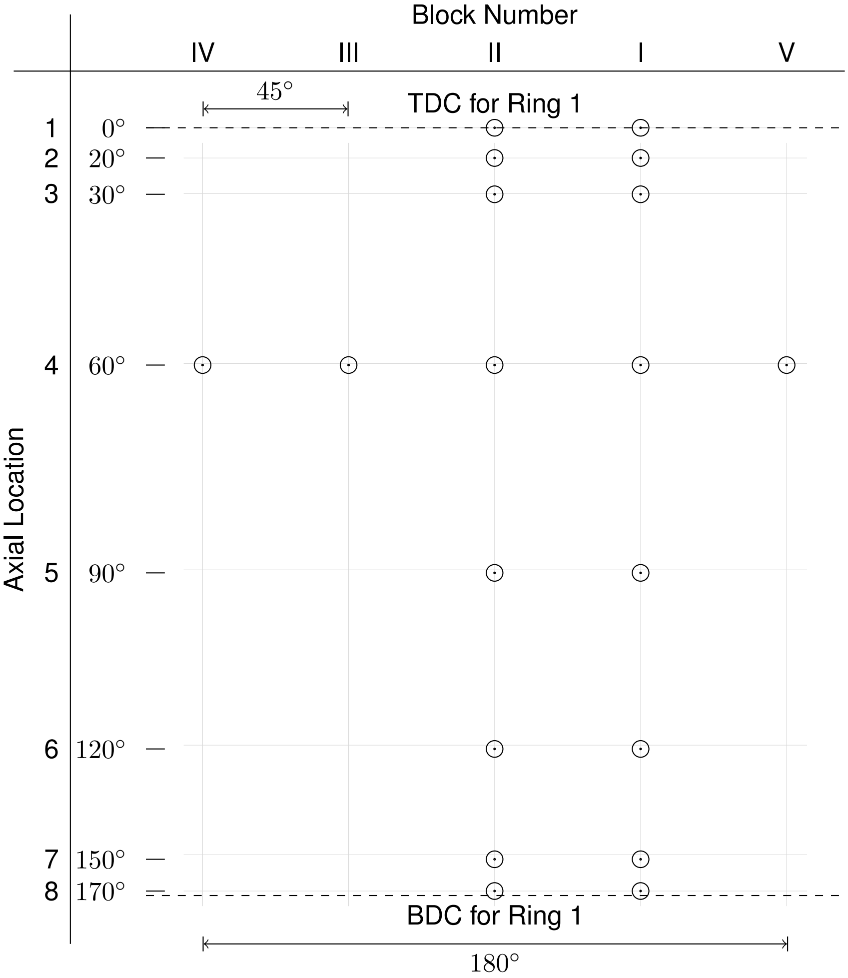

Figure 4.19: Sensor numbers described by their block number and axial location

4.6.3 Transducer Quality

Images of all the oil-film thickness transducers are shown in figure 4.20. These images have been taken to ensure there is not excessive smearing of the electrode during the honing process that may impact on the efficacy of the transducer outputs, and hence oil-film thickness results (Garcia-Atance Fatjo et al., 2017). Inspection of these images show that any smearing is minimal, and as such no corrections will be applied as it is consistent throughout. Smearing may be less evident than with previous studies (Garcia-Atance Fatjo et al., 2017) because the transducers are not made with ceramic tubes to insulate the conducting components. This ceramic is known to degrade when ground or honed, leaving large voids and leaving the electrode and iron tube unsupported.

Here, only an epoxy adhesive is used to insulate the electrode from the iron tube. Separation between these components during manufacture is achieved by applying tension to the electrode, and pinching the iron tube such that it grips the electrode to keep it centralised through the tube. Surface tension also helps to ensure there is no contact. Once the adhesive is cured, the pinched portion of the transducer is ground away and the electrical resistance between the electrode and the iron tube is checked to ensure it is above the required 1 MΩ. The 3D-printed iron tube is used to insulate the transducer from the cylinder liner, this does not fracture like the ceramic tube previously used, thus maintaining the integrity of the transducer.

A limitation of this manufacturing technique is that it could not be used for transducers installed in a firing engine, due to the temperatures that would be involved. However it should ensure the oil-film thickness measurements in this study are of an adequate quality.

Inspection of the images in figure 4.20 shows that sensors $I-3$, $II-1$, and $IV-4$ have been manufactured with iron tube of lower wall thickness. Since the area of the shield does not affect the capacitance of the transducer, then again no corrections are required.

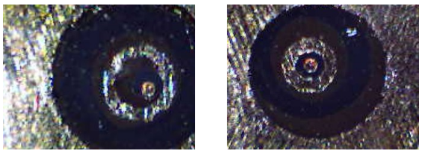

(a) Sensor II-1 (b) Sensor I-1

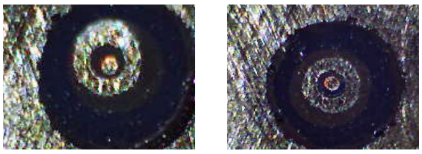

(c) Sensor II-2 (d) Sensor I-2

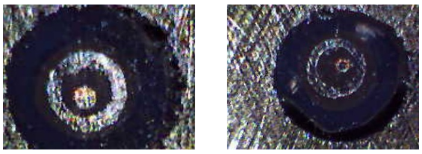

(e) Sensor II-3 (f) Sensor I-3

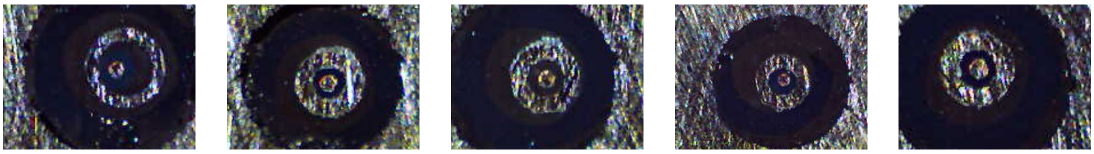

(g) Sensor IV-4 (h) Sensor III-4 (i) Sensor II-4 (j) Sensor I-4 (k) Sensor V-4

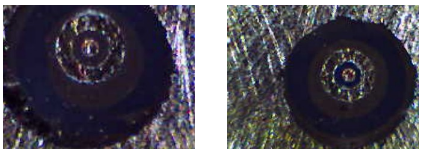

(l) Sensor II-5 (m) Sensor I-5

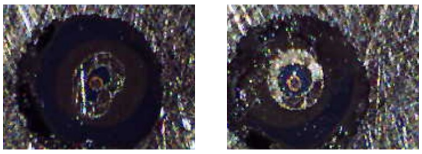

(n) Sensor II-6 (o) Sensor I-6

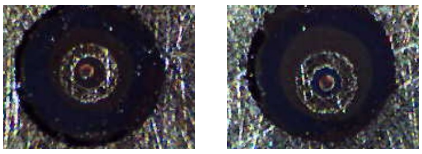

(p) Sensor II-7 (q) Sensor I-7

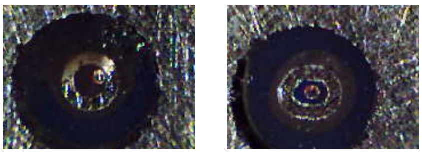

(r) Sensor II-8 (s) Sensor I-8

Figure 4.20: Images of oil-film thickness transducers post-honing

4.6.4 Transducer Calibration

Amplifier Calibration

Ten channels across 2 amplifiers (A and B) were calibrated to ascertain the relationship between voltage output and oil-film thickness on each channel. This was performed using a sensor mounted in a calibrating block, the lubricant used for the investigations (Motaquip 20W-50 mineral oil), and an micrometer capable of positioning a probe acting as a capacitor plate at a known distance from the transducer. This actuator is accurate at micrometer scale. The zero oil-film thickness posistion is identified by lowering the probe onto the transducer until the micrometer scale no longer changes. The amplifier output voltage is then recorded at a number of positions above this datum.

The results of this calibration process are shown in figures 4.21 and 4.22. Each plot shows the test data and a line of best fit for this data. The subsequent relationships based on each line of best fit are shown in table 4.9. These adjustments are applied to the voltage data logged during the experiments.

Transducer Offsets

Replicas of each sensor were obtained in order to determine the offset between each electrode of the transducers and the cylinder liner. This allows post-processing of the data to give accurate readings for oil-film thickness as a distance from the cylinder liner as opposed to a distance from the transducer electrode.

Each replica is scanned using a MicroXAM 10000 white-light interferometer to determine the surface height across a section of the sensor. The replica is carefully aligned in the axial direction in order to minimise height changes due to its curvature, and the table upon which it sits adjusted such that the replica is horizontal. To determine the offset between the cylinder liner and the

Channel	Equation
A1	$V = 0.211h - 0.4753$
A2	$V = 0.346h - 0.6897$
A3	$V = 0.360h - 1.8314$
A4	$V = 0.249h - 1.1481$
A5	$V = 0.270h - 0.4884$
A7	$V = 0.244h - 0.4703$
B1	$V = 0.261h - 0.3420$
B2	$V = 0.274h - 0.5518$
B3	$V = 0.273h - 0.7075$
B4	$V = 0.214h - 0.4652$

Table 4.9: Relationships between transducer voltage and oil-film thickness (in μm) on each amplifier channel

electrode, the mean surface height is taken on each side of the transducer, as well as the surface height at the electrode. The offset can then be calculated using the principle of similar triangles as shown in figure 4.23. If the electrode is recessed from the liner the offset must be subtracted from the measured oil-film thickness. If the electrode protrudes from the liner, the offset must be added to the measured value.

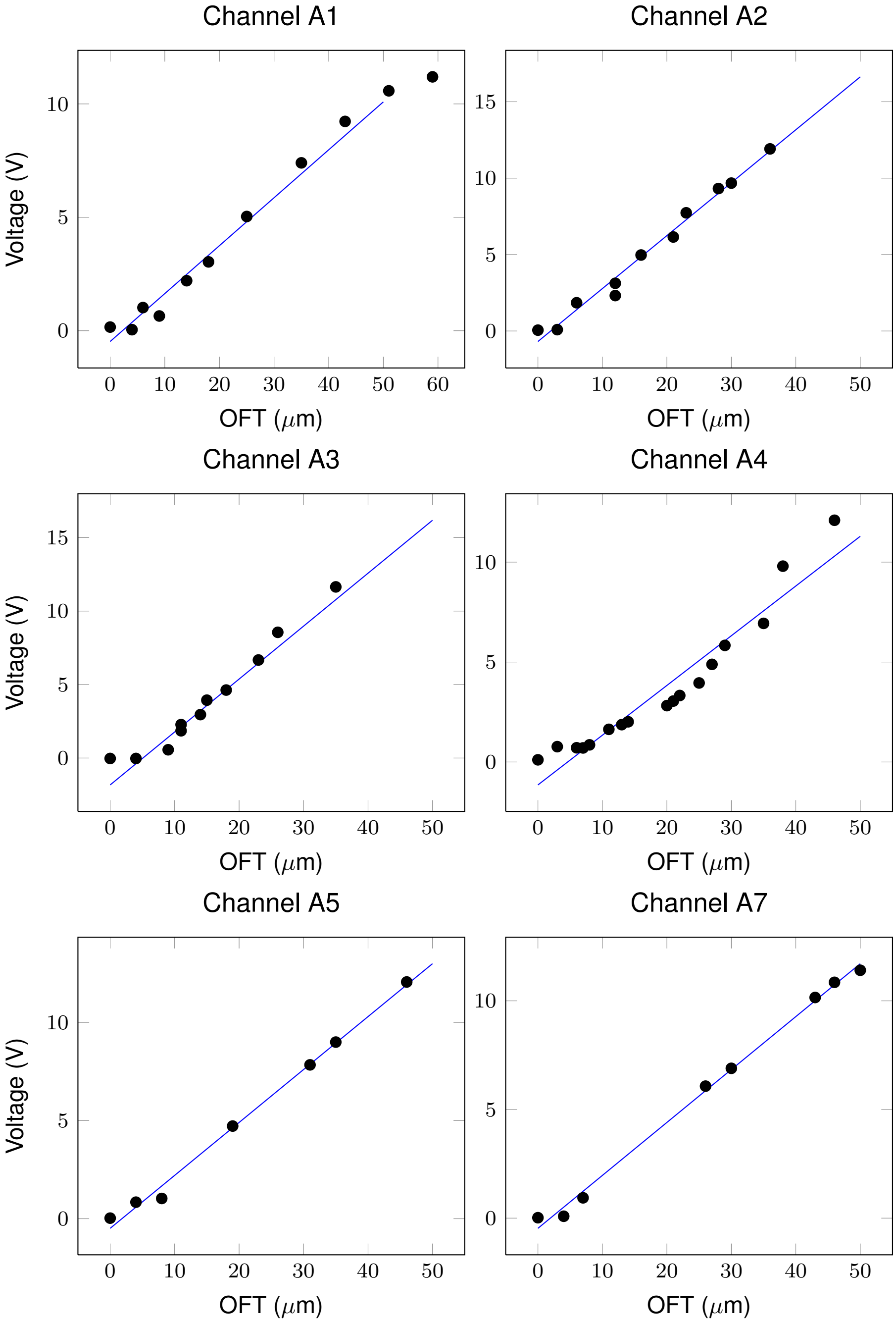

Figure 4.21: Calibration of channels on amplifier A

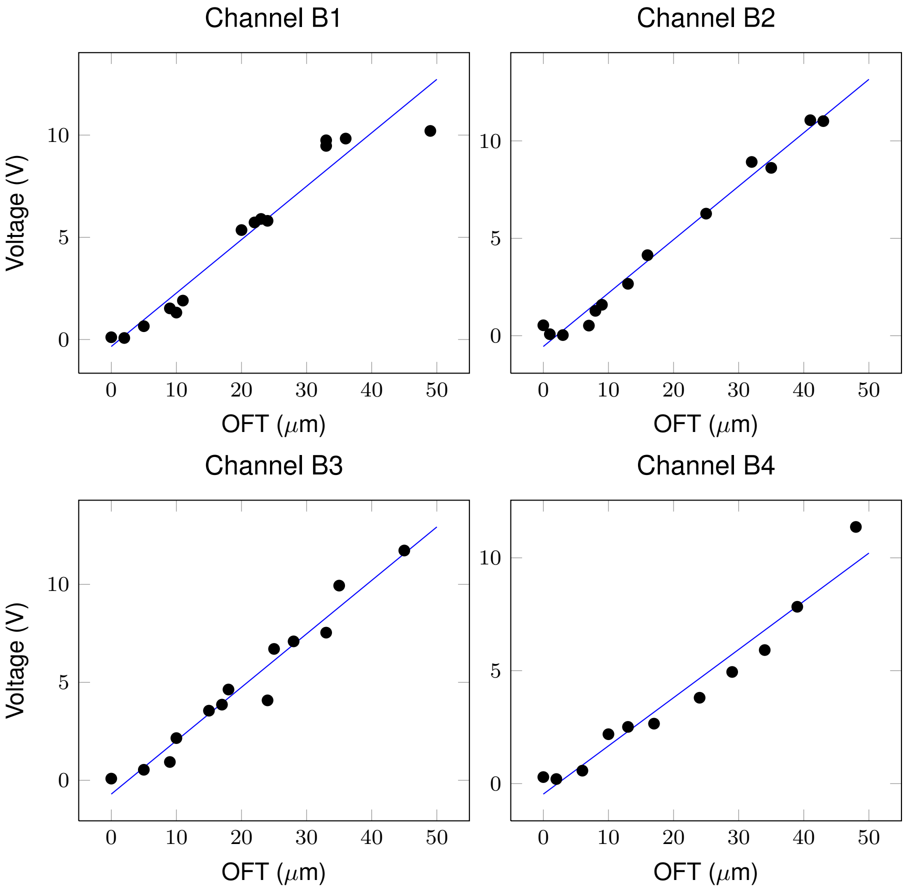

Figure 4.22: Calibration of channels on amplifier B

	Block Number				
Sensor	I	II	III	IV	V
1	4.5	0.4			
2	1.8*	4.5			
3	4.3	0.3			
4	5.0	-2.2	3.3	2.6	1.0
5	-3.1	-2.1			
6	-1.5	-0.5			
7	–	–			
8	1.6	-0.4			

Table 4.10: Post-experiment sensor offsets (μm)

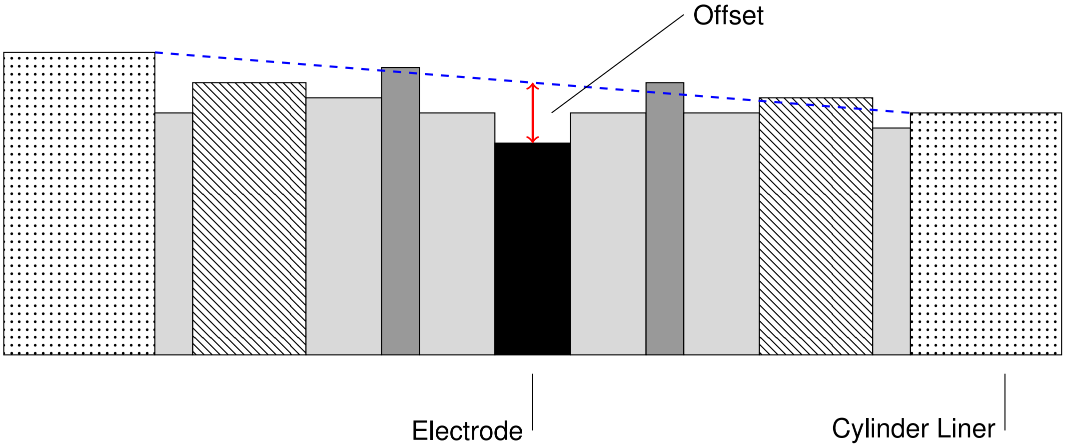

Figure 4.23: Cross-section of transducer showing offset distance - here the electrode is recessed

Some replicas were acquired prior to the experiment, although not all of these were of a quality that allowed the offsets to be determined. Replicas were also taken after the experiments and it is the offsets measured using these that will be applied. The post-experiment offsets are shown in table 4.10 - positive values are transducers where the electrode is proud of the liner, and negative values refer to electrodes that are recessed.

Images from white-light interferometer scans are included in figures 4.24 and 4.25. The surface map is shown, along with axial and circumferential cross-sections of the transducer, through the electrode.

4.7 Summary

The development of a test apparatus has been outlined, including the design of a lubricant injection system for delivering a range of quantities of lubricant to the cylinder. A sensor on the flywheel is used with a microcontroller that has been programmed to trigger lubrication events periodically after a given number of cycles. A lubricant has also been selected with suitable viscosity for the test programme outlined.

An array of capacitance based oil-film thickness transducers have been fitted to the cylinder liner to allow oil-film thickness measurements to be made and for lubricant transport both axially and circumferentially to be observed. Due to the low temperatures expected for these experiments it was possible to manufacture the transducers using a polymer casing and without the fragile ceramic insulating layers used in previous designs. This allowed for a higher quality surface finish after honing and hence better resolution from the transducer.

The apparatus described was used to carry out a number of investigations into the effects of lubricant supply on oil-film thickness and lubricant transport, the results of which are presented in the subsequent chapters. Chapter 5 details the method and results for the first of these, an investigation into the effects a non-uniform distribution of lubricant has on oil-film thickness and film extent.

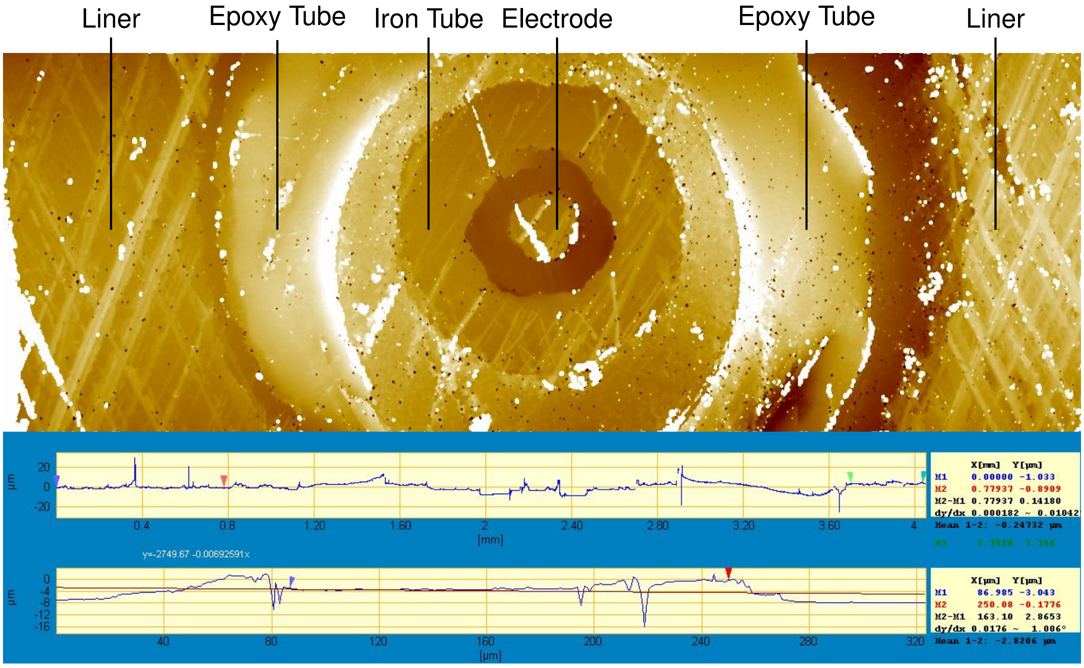

Figure 4.24: White light interferometer scan of sensor I-1, with axial and circumferential cross-sections through the electrode

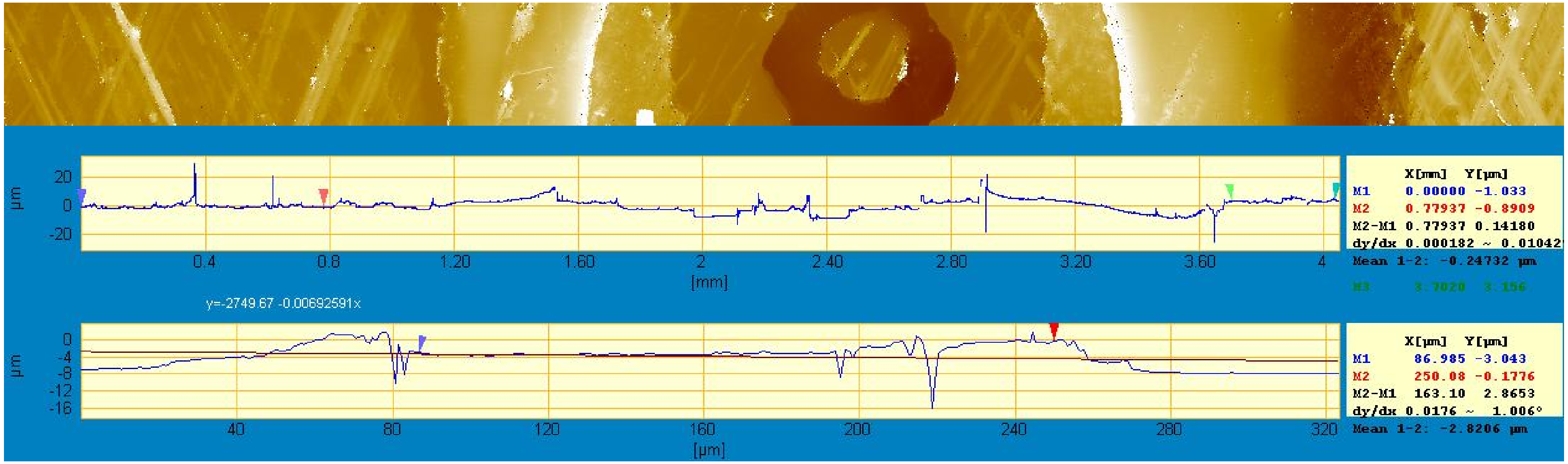

(a) Sensor I-1

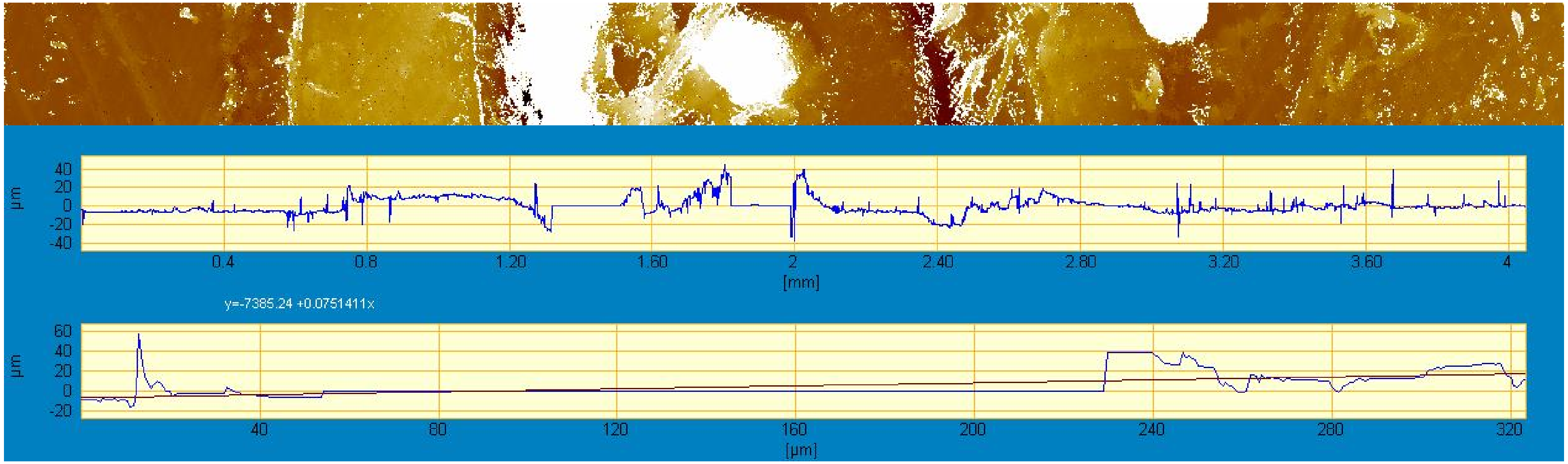

(b) Sensor I-2

Figure 4.25: White-light inteferometer scans of sensor replicas 1 to 8 for block I

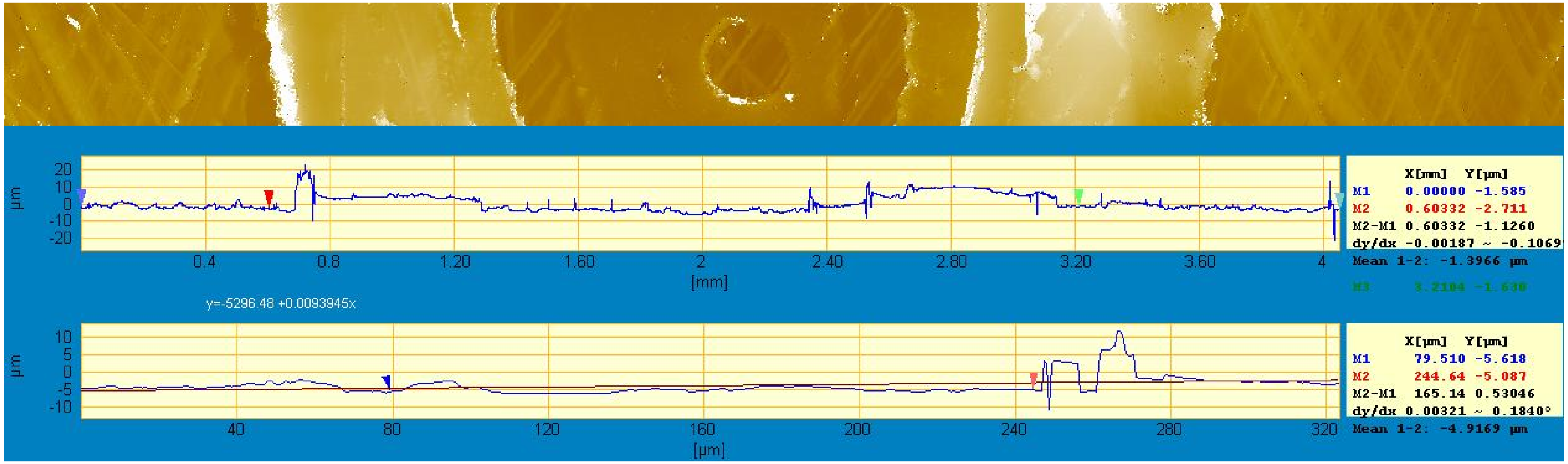

(c) Sensor I-3

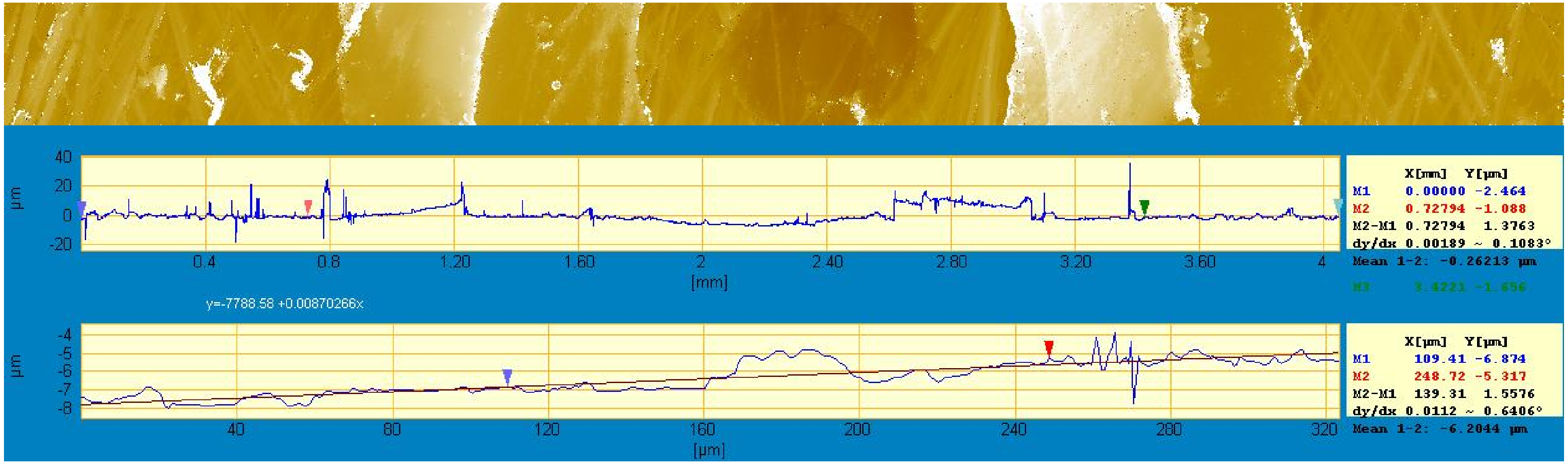

(d) Sensor I-4

Figure 4.25: White-light inteferometer scans of sensor replicas 1 to 8 for block I

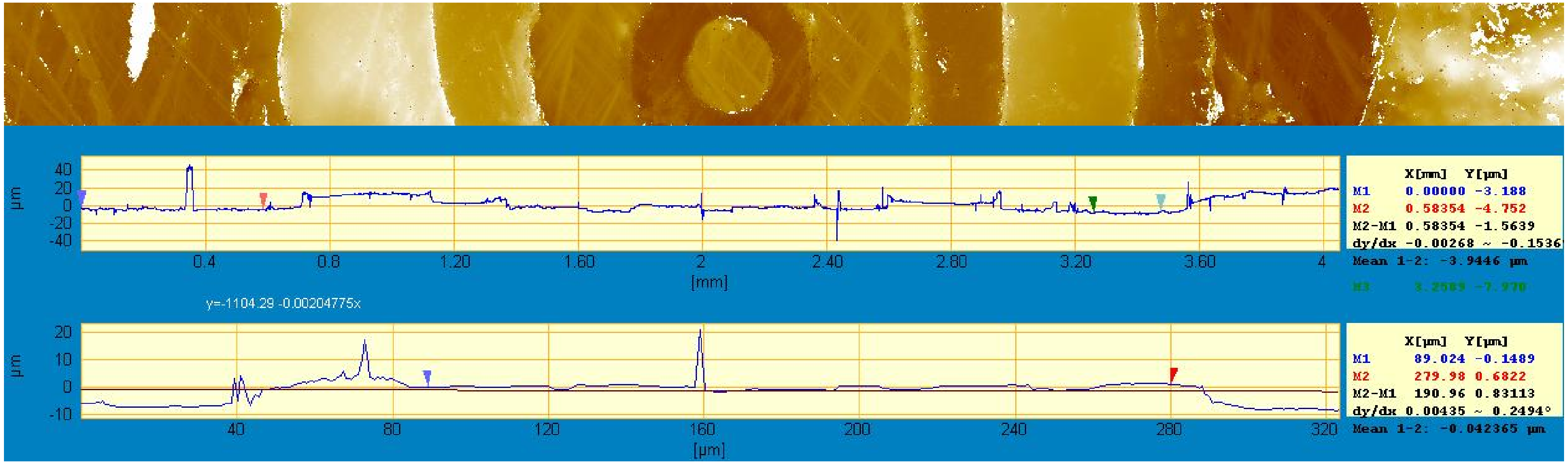

(e) Sensor I-5

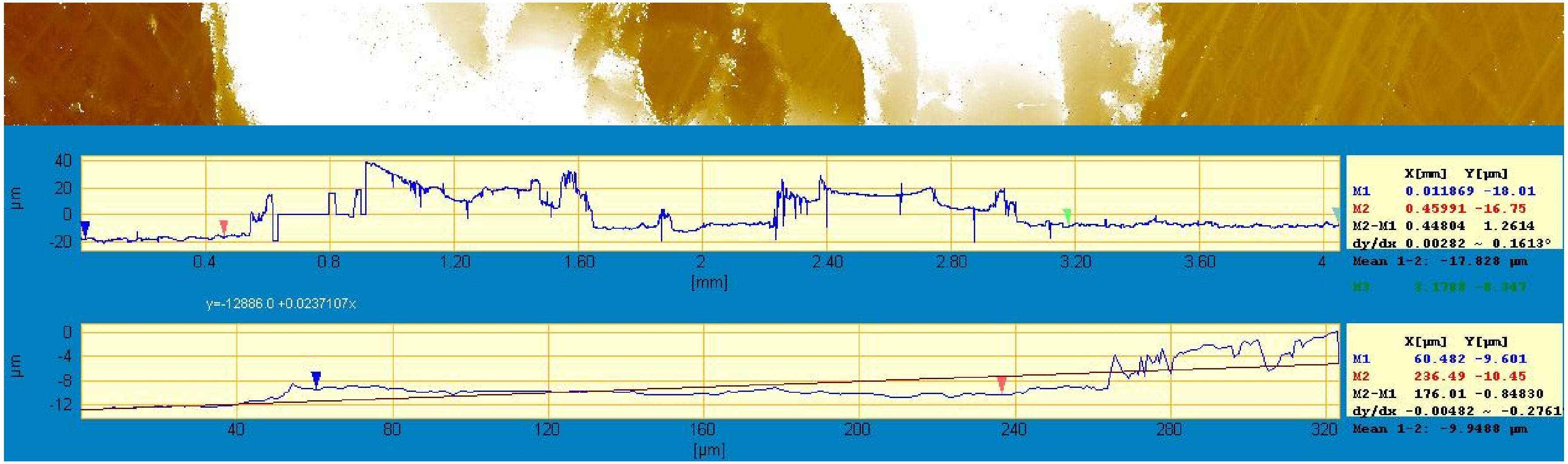

(f) Sensor I-6

Figure 4.25: White-light inteferometer scans of sensor replicas 1 to 8 for block I

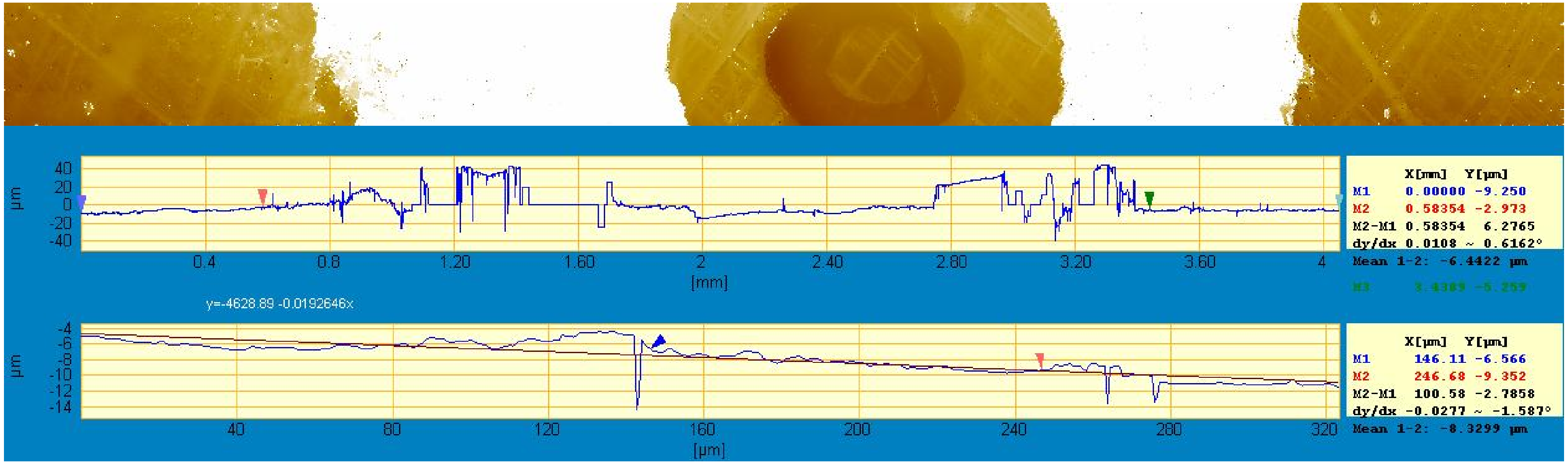

(g) Sensor I-8

Figure 4.25: White-light inteferometer scans of sensor replicas 1 to 8 for block I

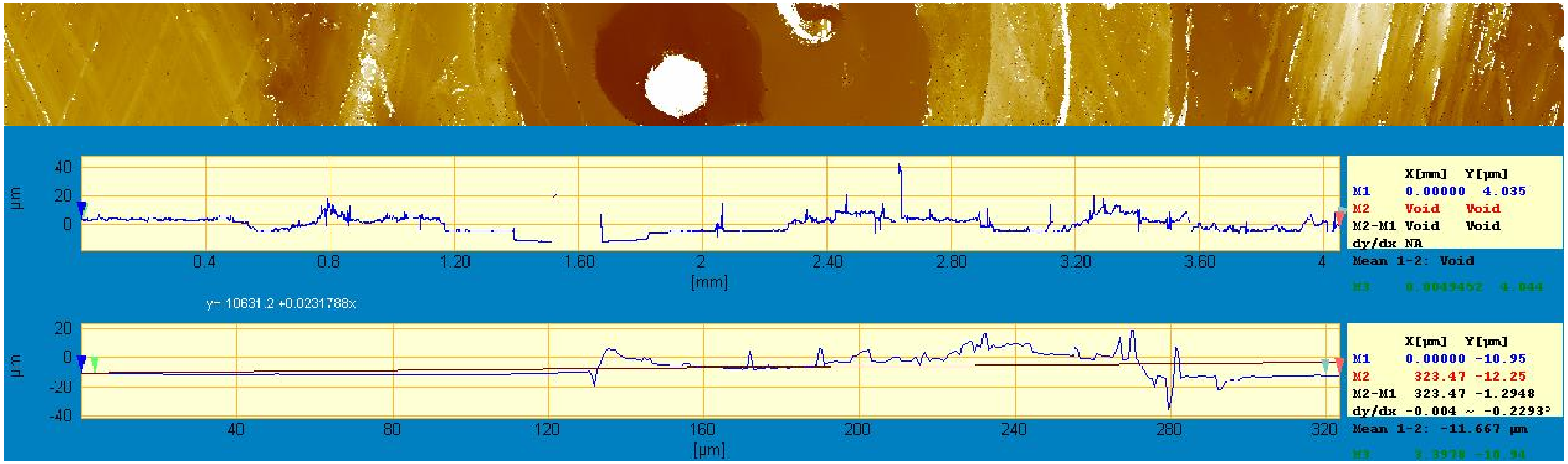

(a) Sensor II-1

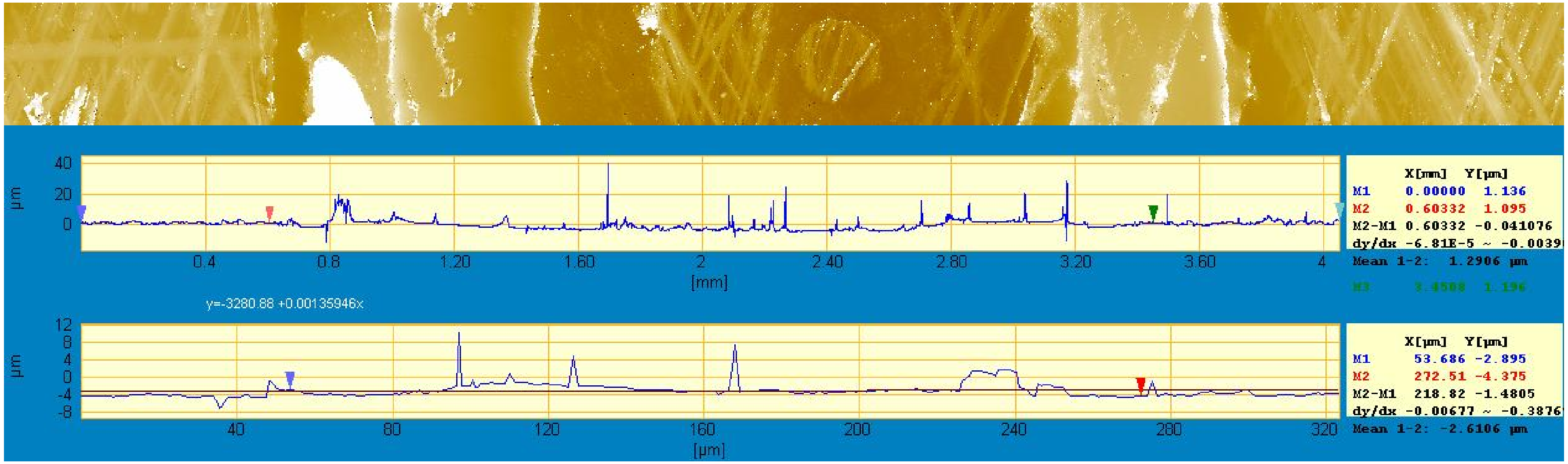

(b) Sensor II-2

Figure 4.26: White-light inteferometer scans of sensor replicas 1 to 8 for block II

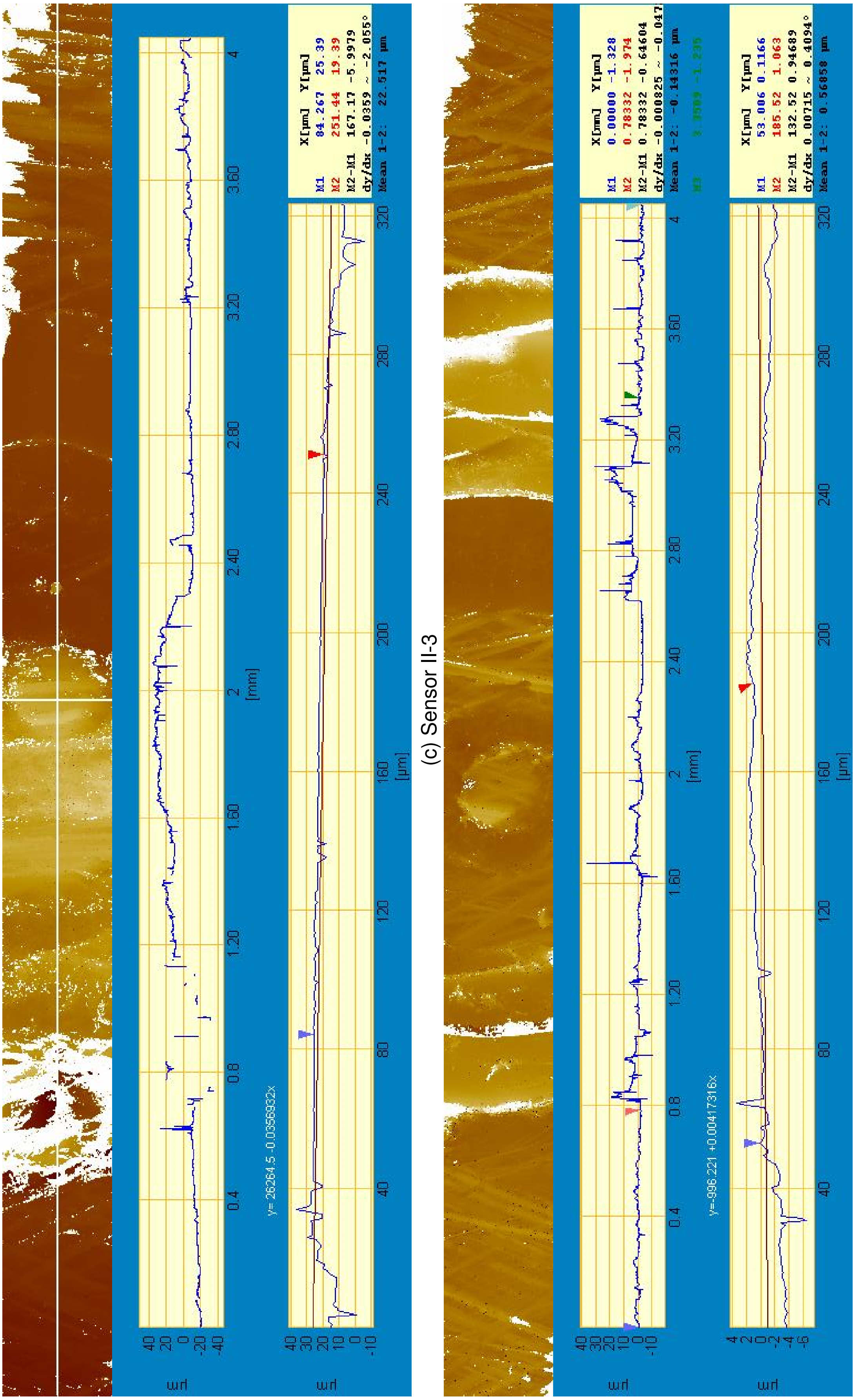

(c) Sensor II-3

(d) Sensor II-4

Figure 4.26: White-light inteferometer scans of sensor replicas 1 to 8 for block II

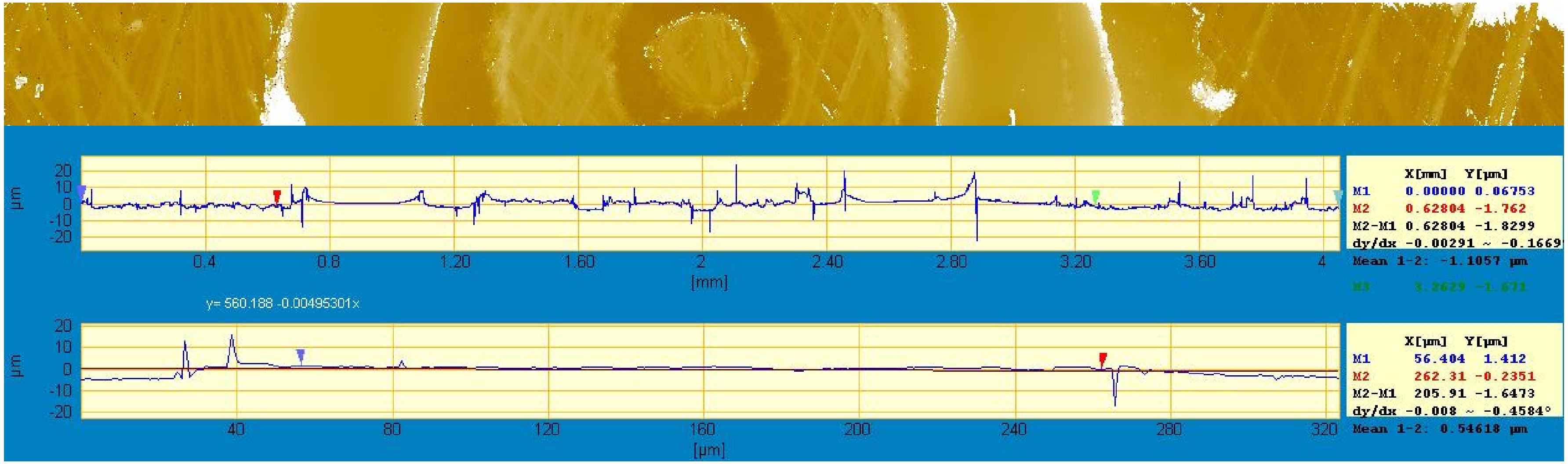

(e) Sensor II-5

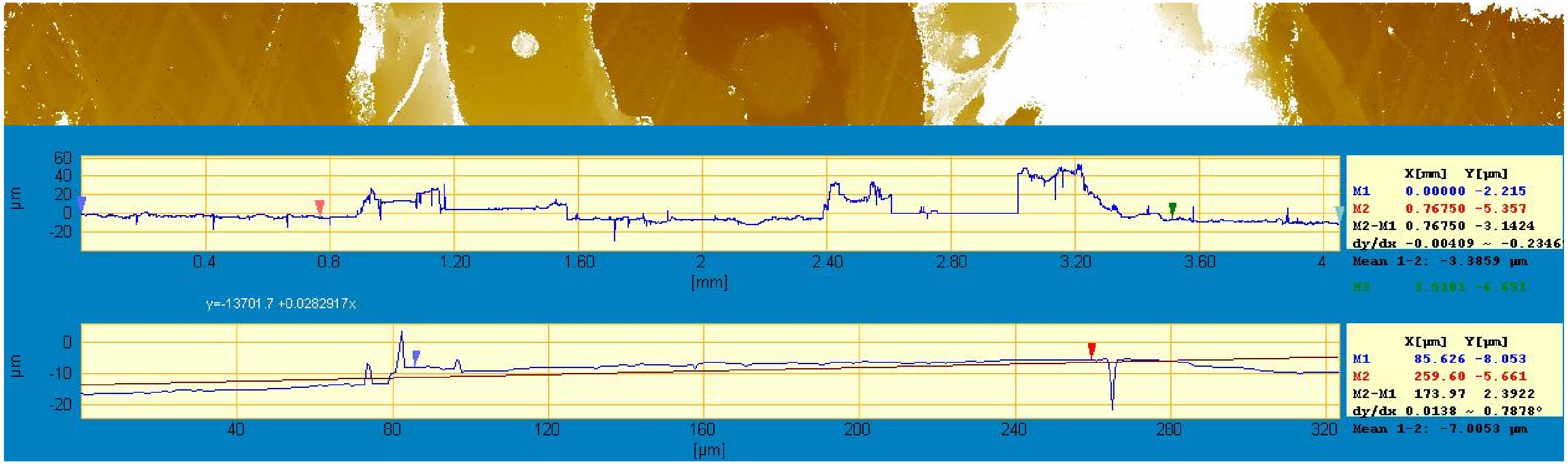

(f) Sensor II-6

Figure 4.26: White-light inteferometer scans of sensor replicas 1 to 8 for block II

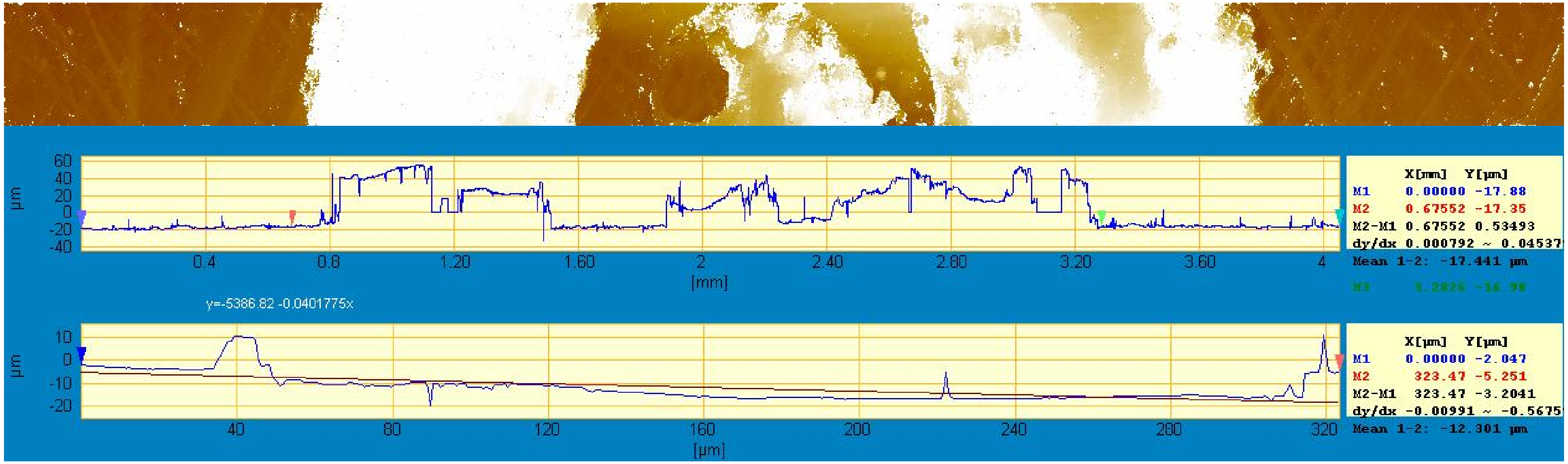

```
        X[mm]   Y[µm]
M1      0.00000 -17.88
M2      0.67552 -17.35
M2-M1   0.67552 0.53493
dy/dx   0.000792 ~ 0.04537
Mean 1-2: -17.441 µm

M3      3.2826 -16.98
```

```
        X[µm]   Y[µm]
M1      0.00000 -2.047
M2       323.47 -5.251
M2-M1    323.47 -3.2041
dy/dx   -0.00991 ~ -0.5675
Mean 1-2: -12.301 µm
```

(g) Sensor II-8

Figure 4.26: White-light inteferometer scans of sensor replicas 1 to 8 for block II

Chapter 5

The Effects of Spray Lubrication on Piston-ring Oil-film Thickness

5.1 Introduction

The lubrication of marine diesel engines involves the delivery of lubricant to selected areas at the top of the cylinder liner by either releasing lubricant through a number of quills (ie. Wartsila's pulse lubrication system), or by spraying it onto the cylinder liner from injector valves (ie. Hans Jensen Lubricators' swirl injection principle). In either case the initial lubricant distribution is uneven, leaving large areas of the cylinder liner without a replenished supply of lubricant. With the lubricant in two-stroke marine diesel engines serving the purpose of both lubricating the piston-rings as well as neutralising the acidic contaminants in the fuel (as discussed in chapter 2), the effect of having such a localised delivery needs to be understood.

A series of tests have been performed to investigate the effects a non-uniform distribution of lubricant has on piston-ring oil-film thickness and film extent. These tests have been carried out at a number of lubricant injector flow-rate settings to assess how the development of the oil-film thickness in time is affected. In this chapter the results of measurements from the oil-film thickness transducers for these tests are presented and explained, along with analysis and discussion of the effects caused by the non-uniform lubricant supply.

5.2 Method

An initial set of tests were carried out using the experimental equipment described in chapter 4 to examine the effect of localised lubricant delivery on oil-film thickness and lubricant transport.

The tests were performed at four lubricant injector flow-rates; 0.01 millilitres per injection event (ml inj^{-1}), 0.02 ml inj^{-1}, 0.04 ml inj^{-1}, and 0.08 ml inj^{-1}. At each cycle, lubricant was injected onto the cylinder liner in 4 locations as described in chapter 4, and shown in figure 5.1. Only the compression ring was employed in these tests. The oil-film thickness for this piston-ring was measured during each thirty second test using fourteen capacitance transducers arranged in an array, as shown in figure 5.1. The two columns of eight transducers (block I and block II) are located 22.5° circumferentially either side of the thrust face. The transducers positioned axially in each block allow oil-film thickness to be measured from top dead centre to just above bottom dead centre. Each transducer is identified by its block number and axial location, (ie. sensor I-4, or II-7).

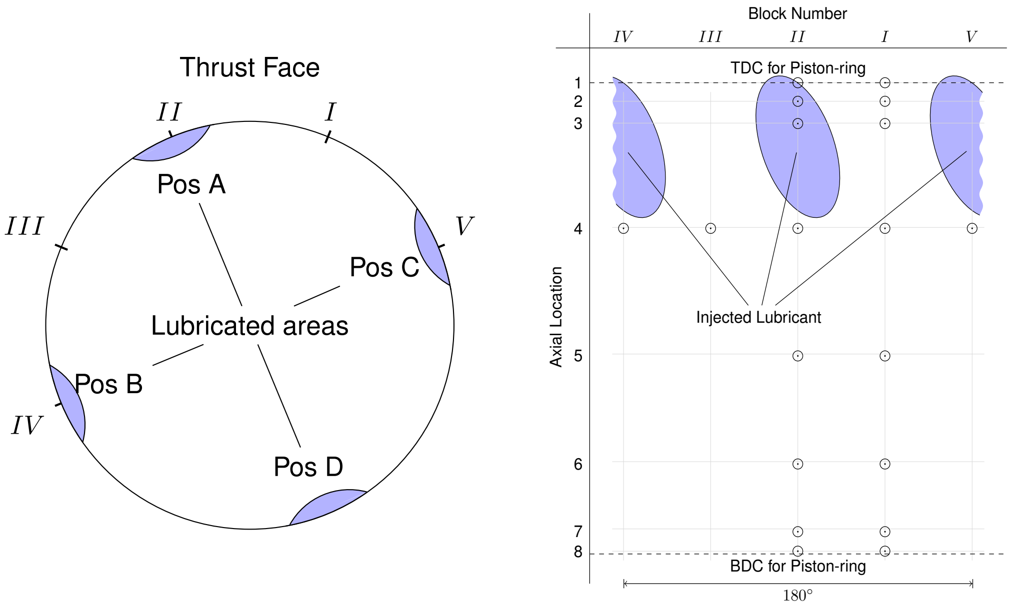

Figure 5.1: Location of lubricant and transducers on the cylinder liner, with transducer numbers being described by their block number and axial location

Lubricant injector valves were open for 200 ms on every cycle, commencing when the piston-ring was 82 mm below top dead centre. One of the spray lubricated areas covers the first three sensors in block II (top dead centre to 31 mm below top dead centre), while three additional lubricated areas are equally spaced in a circular pattern about the cylinder axis. Engine and experimental parameters for this experiment are detailed in table 5.1. The cylinder liner was cleaned thoroughly with solvent after each test to ensure there is no residual lubricant present at the start of each run.

In addition to the oil-film thickness measurements, video footage was acquired to provide visual evidence of lubricant film development.

Engine parameters for experimental and simulated tests		
Cylinder bore	d	98 mm
Crank radius	r	50.5 mm
Connecting-rod length	l	164 mm
Axial height of compression ring	b	2.75 mm
Radius of curvature of ring face	R	30 mm
Rotational frequency of engine	N	120 rpm
Lubricating oil		20W-50 Mineral Oil

Table 5.1: Lister-Petter TR1 engine geometry and operating conditions (Lister-Petter, 2011)

5.3 Capacitance based oil-film thickness transducer results

Each capacitance transducer produced a voltage output that could be converted to oil-film thickness. This was performed using the linear relationship obtained for each input channel of the amplifier during calibration, as described in section 4.6.4. This allowed a signal representing the piston-ring passing the transducer to be inspected (an example is shown in figure 5.2, with a further example shown in figure 5.4 with spatial coordinates on the horizontal axis, rather than time). This signal is from sensor II-4, which is positioned 31 mm below top dead centre. The time axis has been adjusted so the minimum oil-film thickness occurs at a time $t = 0$. The leading edge of the piston-ring is shown towards the left-hand side, with the trailing edge on the right.

A simulated signal representing the true profile of the piston-ring is superimposed on the same axes, using a method described by Fatjo et al. (2014). This simulated signal accounts for the change in effective capacitor area as the piston-ring moves over the face of the electrode by calculating the electrode area covered by the piston-ring at a number of discrete piston-ring positions (figure 5.5). Using the minimum oil-film thickness from the experimental data as a datum the expected signal at each position (h_{sim}) can be determined from the average oil-film thickness of the section of piston-ring covering the electrode (h_{ref}), adjusted by the ratio of total electrode area (A_{tot}) to covered area (A_{cov}). This effectively modifies the capacitor area in equation 4.17. There is also commonly a difference between the area of the electrode in the installed transducers from that used during calibration, due to smearing during the honing process. These areas were assessed using the white-light interferometer scans presented in section 4.6.4. An adjustment was then made in the simulated signal in a similar manner to that above, by adjusting the expected signal by the ratio of the electrode area from the calibrating transducer area (A_{cal}) and the installed transducer electrode area (A_n). The adjustment is summarised in equation 5.1, and the ratios of calibrating electrode area to installed transducer electrode areas presented in table 5.2.

$$h_{sim} = \frac{A_{tot}}{A_{cov}} \frac{A_{cal}}{A_n} h_{ref} \tag{5.1}$$

Since the axial co-ordinate of each electrode is known then so too is the velocity of the piston-

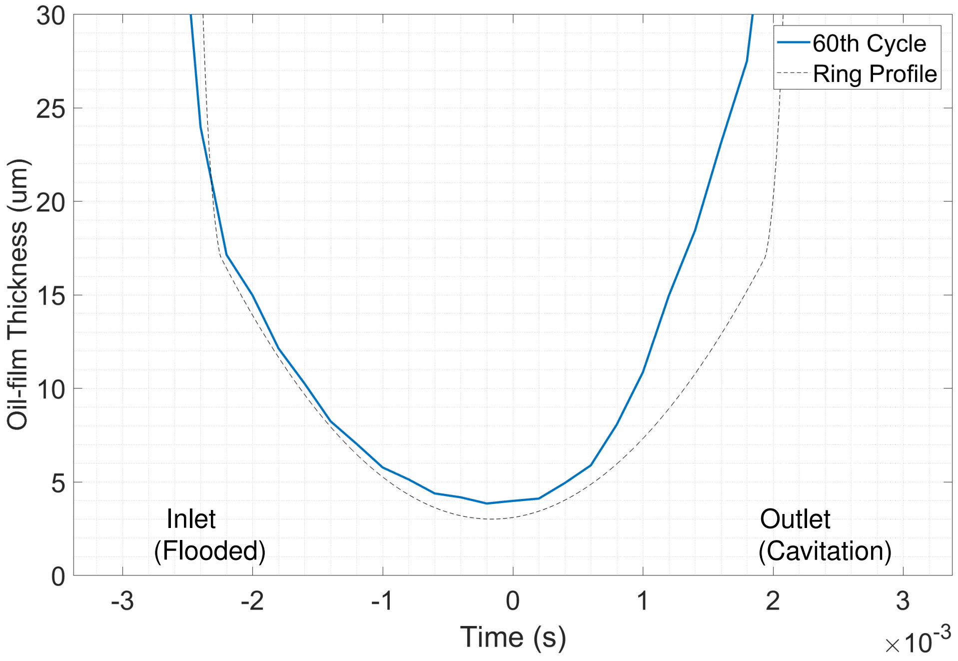

Figure 5.2: Measured vs simulated signals (fully flooded) : flow-rate 0.04 ml inj^{-1}, sensor II-4, upstroke

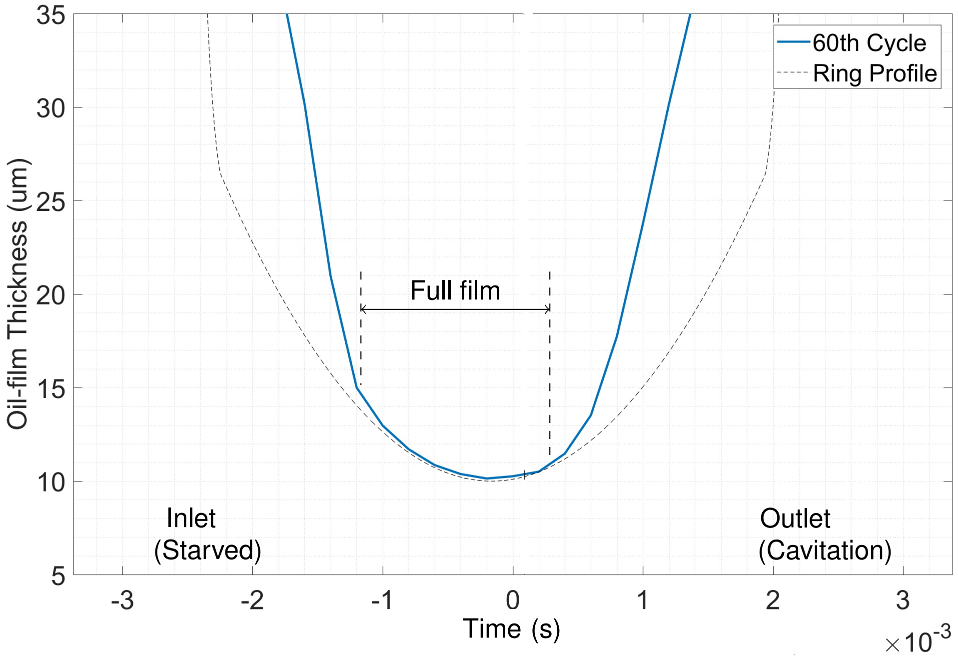

Figure 5.3: Measured vs simulated signals (starved) : flow-rate 0.04 ml inj^{-1}, sensor I-4, upstroke

ring. The time at each computed piston-ring position can therefore be determined, allowing the above signal to be plotted against time, enabling comparison of the measured signal and the expected signal.

The measured piston-ring shape follows the simulated signal closely in the inlet region, whereas shortly after the point of minimum oil-film thickness it diverges upwards from it, producing a higher

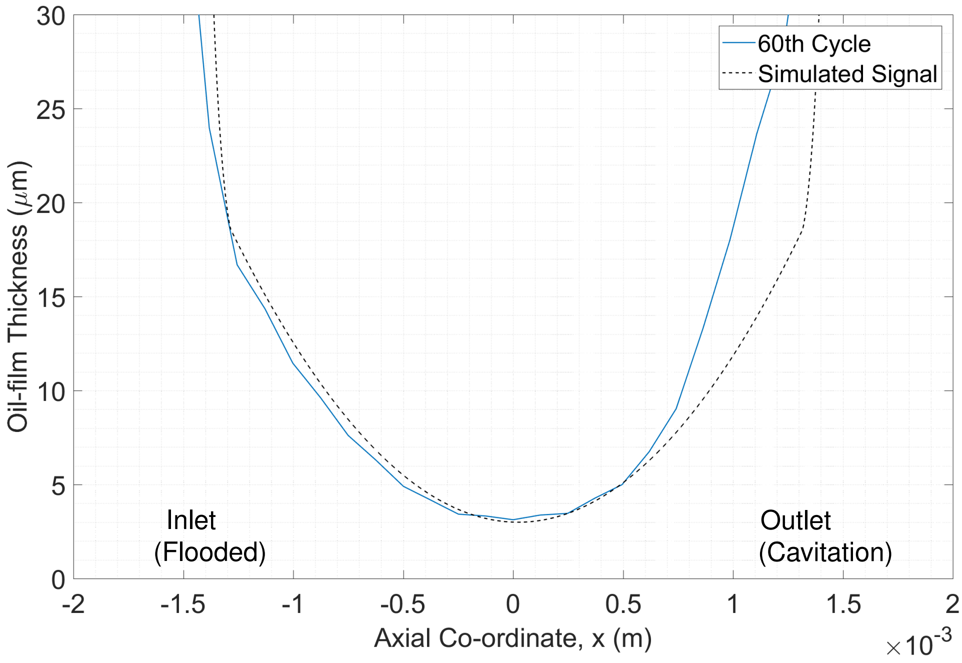

Figure 5.4: Measured vs simulated signal with spatial coordinates on the horizontal axis

Sensor	Block I	Block II
1	0.66	1.34
2	-	0.72
3	0.77	0.62
4	0.77	0.66
5	0.62	0.54
6	0.58	0.66
7	-	-
8	0.72	1.10

Table 5.2: Ratio of electrode area between calibrating transducer and installed transducers (A_{cal}/A_n)

measured value than is expected. The measured values in this region can be seen to be greater than the simulated values by a factor of approximately two. Typically, cavitation is expected at some point in the divergent part of the conjunction between piston-ring and cylinder liner. Recalling equation 4.17, which indicates the oil-film thickness is inversely proportional to the relative permitivity, and since the relative permitivity of mineral oil is approximately two times greater than that of air, the cavitation boundary can be determined as the point where the lines diverge.

Figure 5.3 shows a similar signal from sensor I-4. This is further from the spray lubricated area that is near to sensor II-4. Again the measured signal diverges from the predicted piston-ring signal towards the trailing edge, and in this case the signal does not follow the predicted shape in much of the convergent part of the conjunction either. As before, it would appear that air fills the gap in this region rather than lubricant, allowing the inlet boundary to be estimated in the same manner as the cavitation boundary. Assessing the inlet and cavitation boundaries in this way on

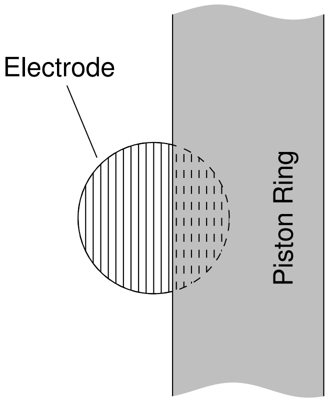

Figure 5.5: The simulated signal is produced by accounting for partial coverage of the electrode by the piston-ring

successive cycles allows their development in time to be evaluated.

5.3.1 Oil-film thickness results at top and bottom dead centres

Four of the transducers are positioned close to the dead centres, two of these at the top of the stroke and two at the bottom. Figure 5.6 shows two signals from sensor II-8, which is positioned 0.6 mm above bottom dead centre. One of these signals is from 10 cycles into the test (5 seconds), and one from 50 cycles in (25 seconds). Unlike other sensors, which have separate signals for upstroke and downstroke, the output from these have one continuous signal because the piston-ring does not pass completely over the transducer. Consequently, the left-hand side of the signal (-0.03 to zero seconds) shows the piston-ring moving over the transducer at the end of the downstroke, with the lower face of the piston-ring as the leading edge. The right-hand side shows start of the upstroke, with the same lower face becoming the trailing edge.

These signals have been overlaid, by translating the oil-film thickness for the signal on the 50th cycle, and by matching the time data, so they do not necessarily imply equal minimum oil-film thickness where the lines are coincident on the two signals. This allows any differences in the signal to be highlighted, in this figure for example, while the signals commence together there is a very slight difference as the piston-ring moves over the electrode, with the signal from the 50th cycle appearing to be rotated anticlockwise. This could be caused by the piston-ring having a marginally different angle of inclination. Also, the cycle from the 50th cycle shifts slightly rightwards as it moves away from the electrode - which may be the piston-ring shifting downwards in the ring-groove as the piston changes direction and accelerates upwards.

It is possible from the duration of the signals to determine the axial co-ordinate of the transducer. From the signal of the 10th cycle, the time the piston-ring covers the sensor is 45 ms, with half of this being the end of the downstroke, and half the beginning of the upstroke. From

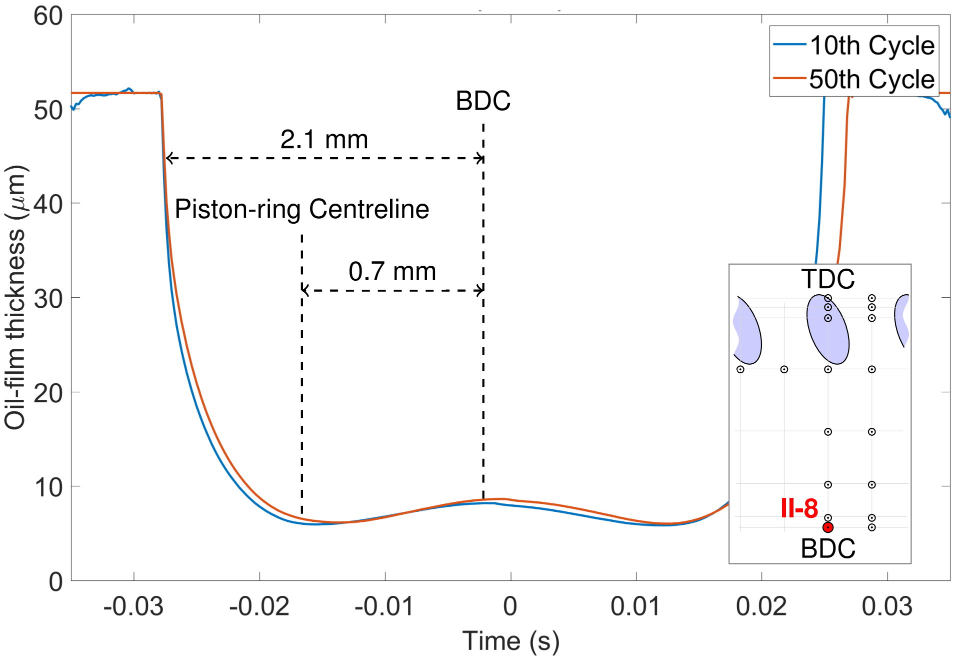

Figure 5.6: Sensor 8 : Piston-ring signals for sensor at bottom dead centre

the measured engine speed, the connecting-rod length and the stroke length, the relationship between time, crank angle, and axial position is known. This puts the crank angles at the beginning and end of the signal at 160.5° and 198.5° after top dead centre. This corresponds to the axial position of the transducer being 2.1 mm above the bottom of the piston-ring, or 0.7 mm above the centreline of the piston-ring at bottom dead centre. These two distances are at different scales on figure 5.6 as a result of the changing velocity of the piston-ring.

Not all of the signals are this noise-free, an example of which is shown in figure 5.7 - this time from sensor I-8. Again the piston-ring partially covers the transducer even at the turning point of the stroke, so both downstroke and upstroke are represented in each signal. The signal is clean as the piston-ring moves over the transducer. However, on the tenth cycle there is a rise in oil-film thickness shortly following the piston-ring centreline. It then drops again almost precisely at bottom dead centre. At around 0.006 seconds both signals rise in a similar manner to that seen at the end of the downstroke. Both signals are terminated by a brief spike, and then a smooth signal as higher parts of the piston ring cover the transducer as it departs of the upstroke.

During the central part of the signal (between $t = -0.015$ and $t = 0.015$ seconds) there is an irregular, oscillatory behaviour evident. Considering the low velocities at this part of the engine cycle (less than 0.15 m/s) these oscillations are thought to be caused by stick-slip contact between cylinder liner and piston-ring at some point around their circumference. During this time the piston-ring will be subjected to an increased friction force that opposes that imposed by the piston-ring groove. This may cause it to briefly stick to the cylinder liner, before it is forced to

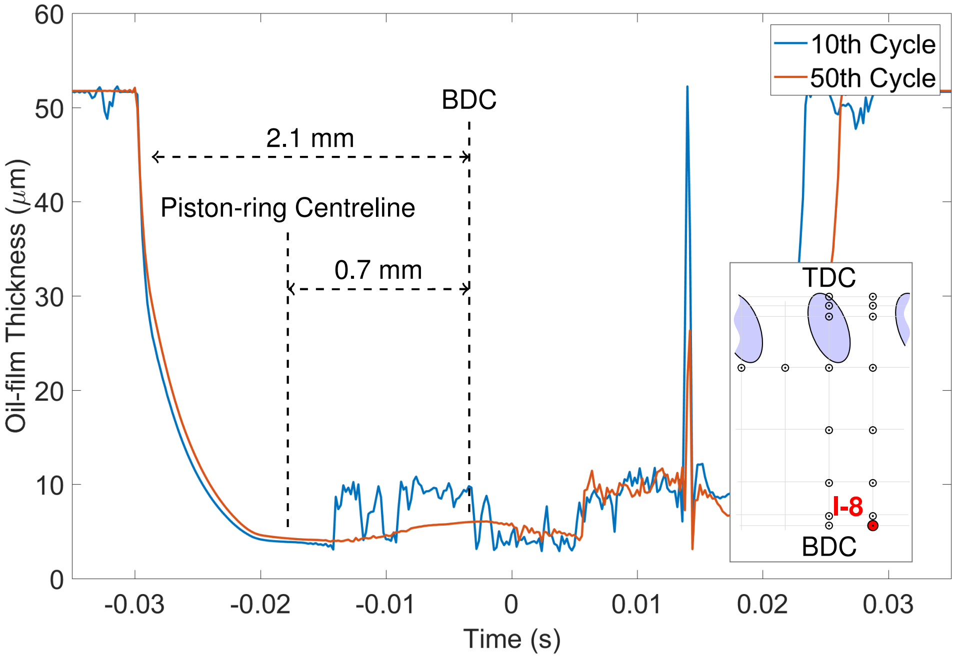

Figure 5.7: Sensor 8 : Piston-ring signals showing contact and cavitation at the bottom dead centre transducer

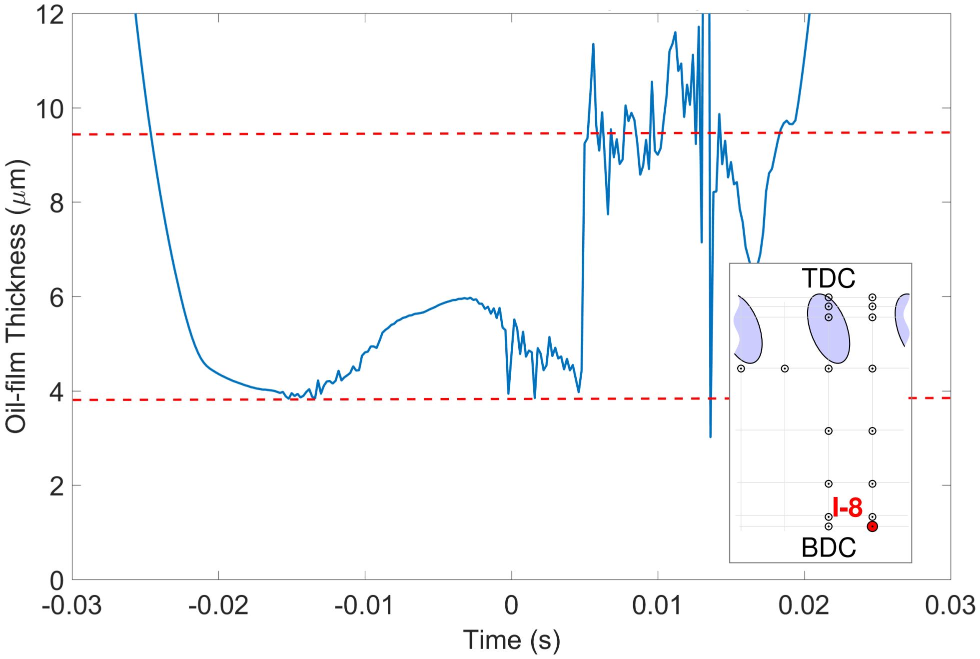

Figure 5.8: Sensor 8 : Piston-ring signal for sensor at bottom dead centre on 50th Cycle showing a step change in signal output in the absence of lubricant

release and suddenly change its position and orientation in the piston-ring groove. Also evident during the central part of the tenth cycle signal is a lower measured oil-film thickness between $t = -0.005$ seconds and $t = 0.005$ seconds. During contact a zero voltage is recorded, to which the calibration expression for the amplifier channel used is applied, along with the offset between transducer and cylinder liner. The combination of these calibrating factors for this transducer give an oil-film thickness of 3.8 μm when the voltage is zero - confirming this is indeed contact at this point.

Looking more closely at the signal for the 50th cycle (figure 5.8, the downstroke part of the signal shows minimum oil-film thickness of 3.8 μm, and the noisy signal on the upstroke has oil-film thickness between approximately 8 μm and 12 μm - two to three times higher. Equation 4.17 tells us the oil-film thickness is inversely proportional to the relative permitivity, and since the relative permitivity of mineral oil is about 2.1 times greater than the relative permitivity of air, the step change in oil-film thickness could be caused by an absence of lubricant for the upstroke part of the signal. It is also worth noting this transducer is 1.6 μm proud of the liner according to the white-light interferometer scan, and if the residual oil-film thickness is less than this is possible the conjuction between transducer and piston-ring is not filled by oil.

Figure 5.9 shows another sample signal for sensor II-8. This shows a piston-ring signal as it passes the transducer during a test with lower lubricant flow-rate than that in 5.6. Also shown on the figure are two simulated piston-ring shapes positioned to correspond with the leading and trailing edges of the piston-ring, and a line representing the lower limit of fluid film lubrication. This limit is determined using the definition described in Hutchings (1992), with $\lambda = 3$ being quoted as the limiting value (and where λ is defined in equation 5.2). The piston-ring and cylinder liner have average roughness values of $R_{q_p} = 0.19$ μm and of $R_{q_c} = 0.55$ μm respectively, giving a combined roughness of $R_{a_{p+c}} = 0.74\mu$m, and lower limit of fluid film lubrication of 1.75μm.

$$\lambda = \frac{h_{min}}{\sqrt{R_{q1}^2 + R_{q2}^2}} \tag{5.2}$$

As the piston-ring moves over the transducer the signal is again noise free. Indeed it is like this until just after bottom-dead centre (the meeting point of the two simulated signals). Following bottom dead centre the measured value drops to approximately 2 μm at $t = 1.545$ seconds. The measured value then oscillates before a sharp rise where the signal returns to a value suggesting the ring is no longer above the transducer. Following this the signal returns as the piston-ring departs at the beginning of the upstroke.

The initial oscillations at $t = 1.545$ seconds are very regular, with a time period in the region of 300 μs. This is closely followed by less regular oscillations before the signal increases. The latter show a similar form to those in figure 5.7, again suggesting contact leading to a stick-slip behaviour of the piston-ring. The earlier oscillations are far more regular in their frequency, and show an exponentially increasing amplitude typical of an unstable dynamic system. The time period of these oscillations corresponds to the higher of the two specified rise times of the signal amplifier (for a cutoff frequency of 1kHz), which may suggest it is an electronic effect rather than

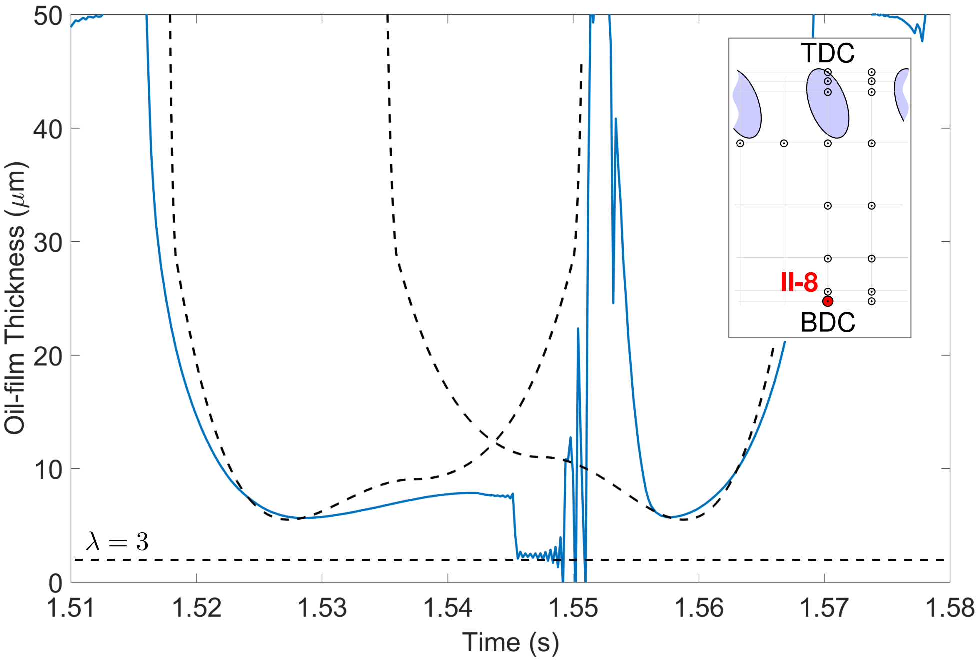

Figure 5.9: Sensor 8 : Piston-ring signal for transducer at bottom dead centre showing oscillatory signal during contact with the piston-ring

a mechanical one. Through the duration of the oscillations the measured signal shows an oil-film thickness at approximately the lower limit for fluid film lubrication.

Following these oscillations oil-film thickness appears to rise rapidly to beyond the range of the transducers. It remains distant for 3 ms before returning back to show the apex and the bottom land of the piston-ring as it moves upwards. Again, this could be caused by the piston-ring shifting in the ring groove, or the piston tilting over as the connecting rod swings under the crank shaft.

5.3.2 Minimum Oil-film Thickness

During the course of a thirty second test, the piston-ring passes each transducer many times (four times per second). An algorithm has been used to extract the minima from the oil-film thickness signals for each transducer every time the piston-ring passes. This allows the changes in time of oil-film thickness throughout the test to be evaluated. For a single transducer, the values for the upstrokes and downstrokes are separated. Recalling the cylinder liner is dry at the beginning of these tests, any changes in oil-film thickness are likely to be due to a change in lubricant availability.

Figures 5.10 and 5.11 show minimum oil-film thickness results from each upstroke and downstroke at sensor I-4 and II-4 (both 31.2 mm from top dead centre), for tests carried out at four different injector flow-rates. Figure 5.10 shows that for each flow-rate, there is an initial increase in oil-film thickness early during the test - during the first two cycles, most clearly seen at an injector flow-rate of 0.04 ml inj^{-1}. Since transducer I-4 is positioned such that lubricant is delivered to either side (recall figure 5.1), it is thought this increase is the result of the piston-ring responding to the sudden availability of lubricant in another location. While figure 5.11 suggests this movement is less at transducer II-4, it should be noted the results for block I and block II are acquired in separate runs of the same test due to having a limited number of amplifier channels. Following this initial rise in oil-film thickness, there is a plateau, until another increase approximately ten seconds into the tests. A similar increase is also seen in figure 5.11 at approximately the same time.

5.3.3 Film Extent

By comparing the piston-ring signals to the simulated signal representing the ring profile, the inlet and cavitation boundaries throughout the test can be assessed. Figures 5.12 and 5.13 show examples of such signals at different times throughout the tests with injector flow-rate 0.04 ml inj^{-1}, at both sensor I-4 and II-4. The first of these figures shows two signals where the measured signal deviates from the simulated signal very close to the centre of the piston-ring, indicating the highly starved conditions. That is until the 35th cycle, which corresponds to 17.5 seconds into the test. Curiously, by the 50th cycle (t = 25 seconds) the piston-ring is once again highly starved. This brief change in conditions could be because there is no longer lubricant in the region of sensor I-4, or it could be due to a reduction in piston-ring oil film thickness (or indeed an increase of piston-ring oil-film thickness on the 50th cycle) due to side-movement of the piston-ring from forces elsewhere around the circumference of the cylinder liner.

The second of these figures (figure 5.13) shows lubricant availability much earlier during the test, with the inlet boundary being almost halfway between the centre of the piston-ring and its leading edge by 10 seconds into the test. Following this the piston-ring becomes fully flooded. It should be expected that more lubricant is present, and hence the piston-ring is better lubricated in this part of the cylinder, as it is very close to where the lubricant is injected.

Inspecting signals such as this at regular intervals throughout the tests allows the lubricant availability to be assessed. This is the first time experimental data has been used to evaluate the development of film extent in time. Since the velocity of the piston-ring past the sensors is known, the axial piston-ring co-ordinates corresponding with the inlet and cavitation boundaries can be calculated. Figure 5.14 shows the result of this analysis at five cycle intervals for sensors I-4 (left) and II-4 (right), with a lubricant injector flow-rate of 0.04 ml inj^{-1}. Time is the vertical axis, and the axial co-ordinate of the piston-ring is represented horizontally, with the leading edge being at the extreme left-hand side of each diagram.

Firstly, for the block II sensor, there is a notable increase in lubricant availability at 10 seconds

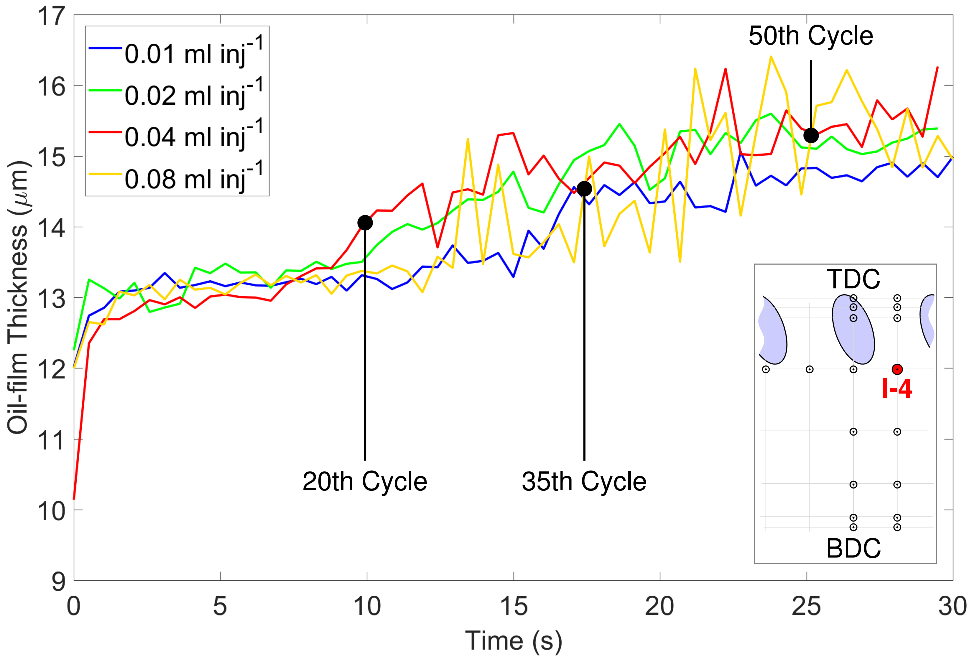

Figure 5.10: Minimum oil-film thickness on upstrokes at sensor I-4 during tests at four lubricant injector flow-rates

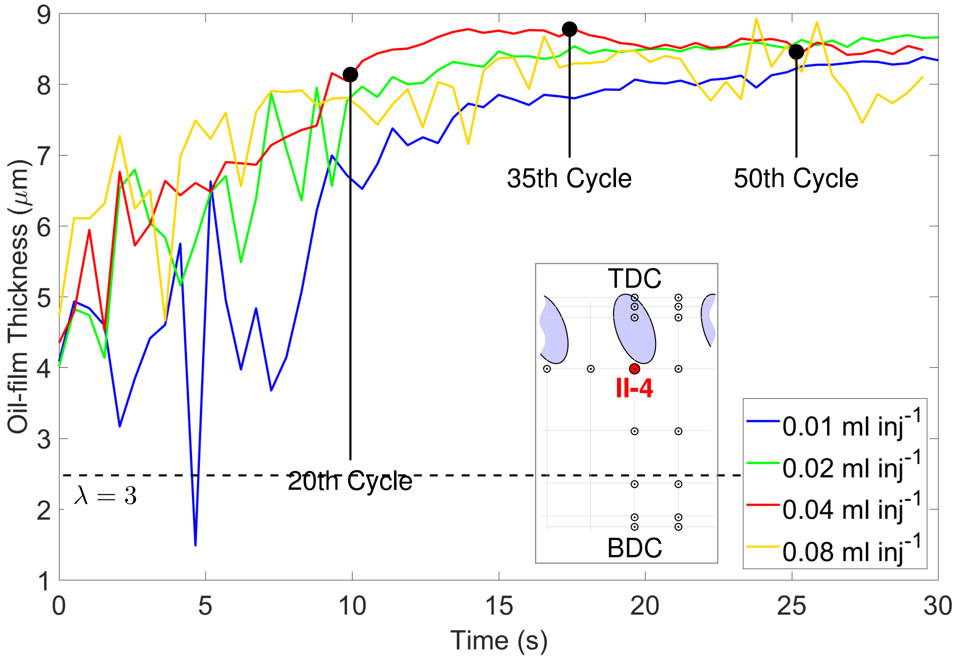

Figure 5.11: Minimum oil-film thickness on downstrokes at sensor II-4 during tests at four lubricant injector flow-rates (film thicknesses with $\lambda < 3$ are likely to involve metal to metal contact (Hutchings, 1992)

into the test - as seen on figure 5.14b. Prior to this time the piston-ring is very starved, and following this it is almost fully-flooded. The cavitation boundary is relatively stable throughout the test. For sensor I-4, the piston-ring is more highly starved until later in the test, with the exception of the period between 15 and 18 seconds. Towards the end of the test the lubricant availability is

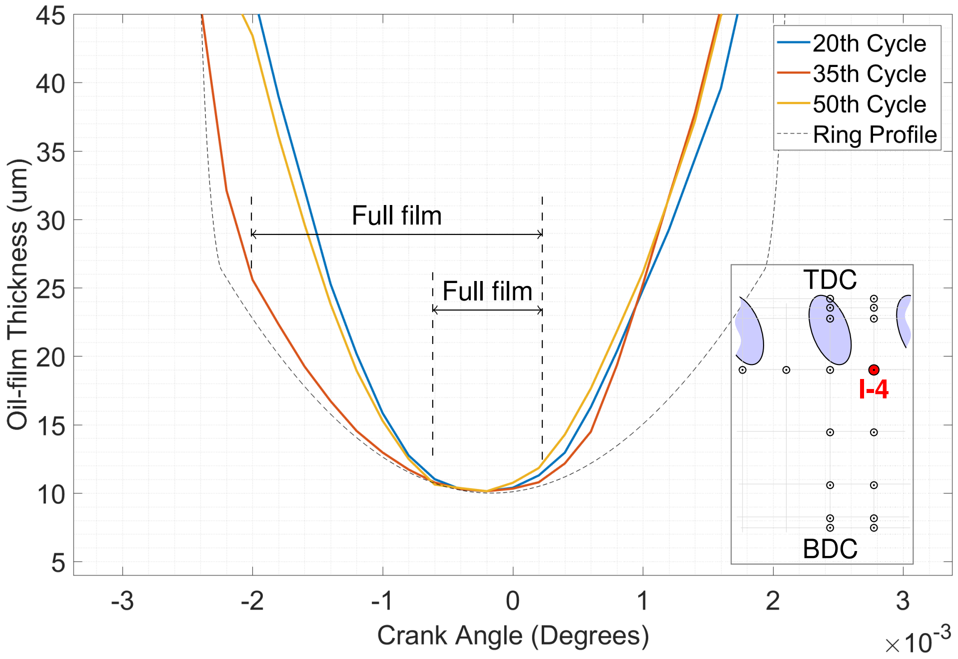

Figure 5.12: Film extent at sensor I-4 on selected upstrokes

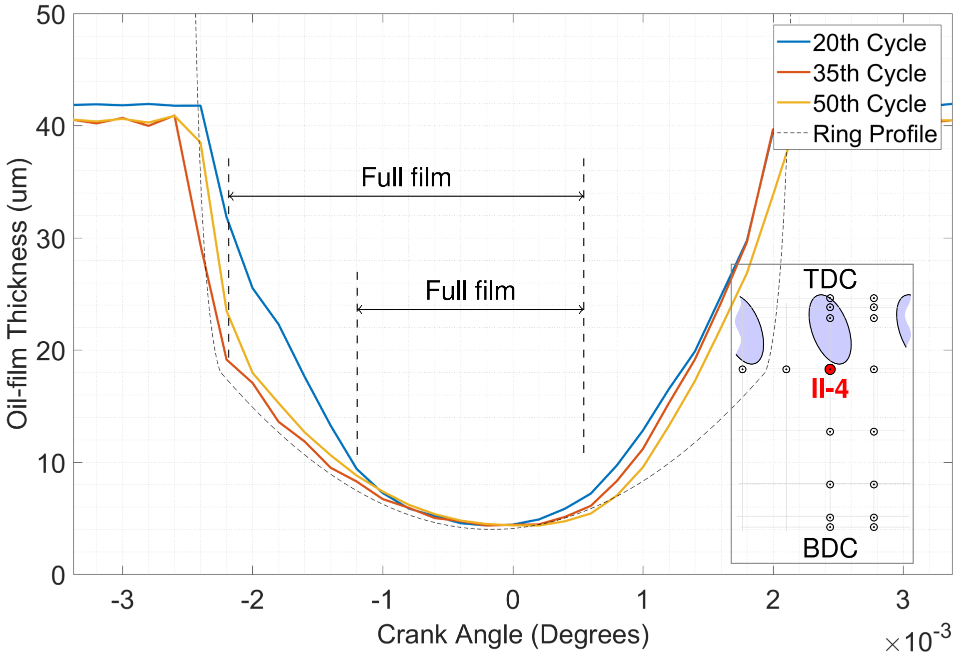

Figure 5.13: Film extent at sensor II-4 on selected upstrokes

increasing, indicated by the starvation boundary moving towards the leading edge. Inspection of video footage shows no apparent evidence to help explain this brief shift in starvation boundary, certainly not in terms of changing lubricant conditions in the region of the transducer.

A similar diagram is shown in figure 5.15, this time for the same sensors (I-4 and II-4) on the downstroke. Here the cavitation boundary is similarly positioned to that in figure 5.14, while the starvation boundary is more notably different in both cases. With sensor II-4, the piston-ring is

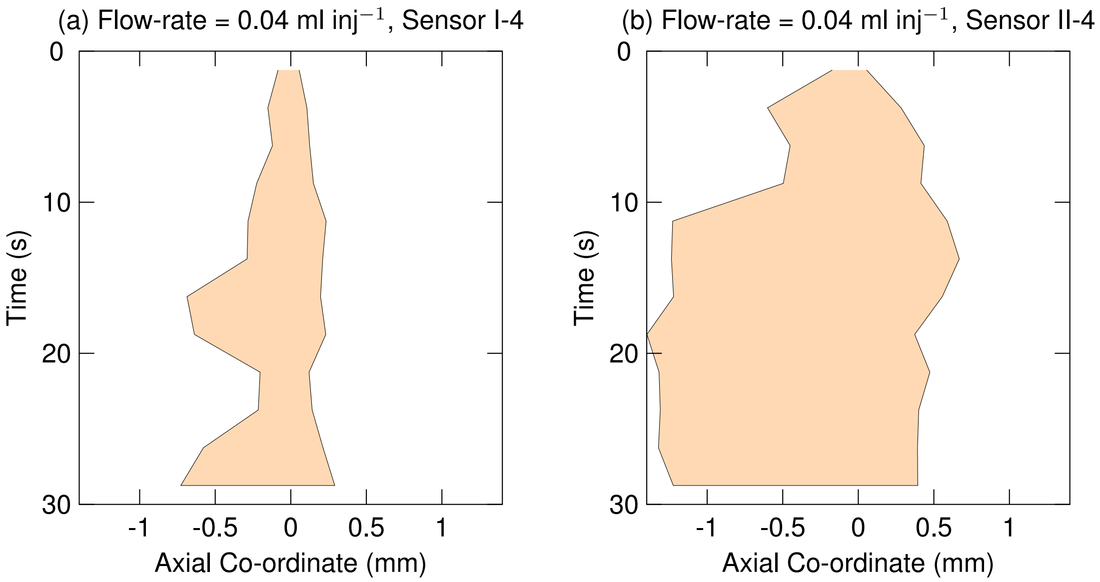

Figure 5.14: Experimental inlet and cavitation boundaries taken on the upstrokes at 5 cycle intervals

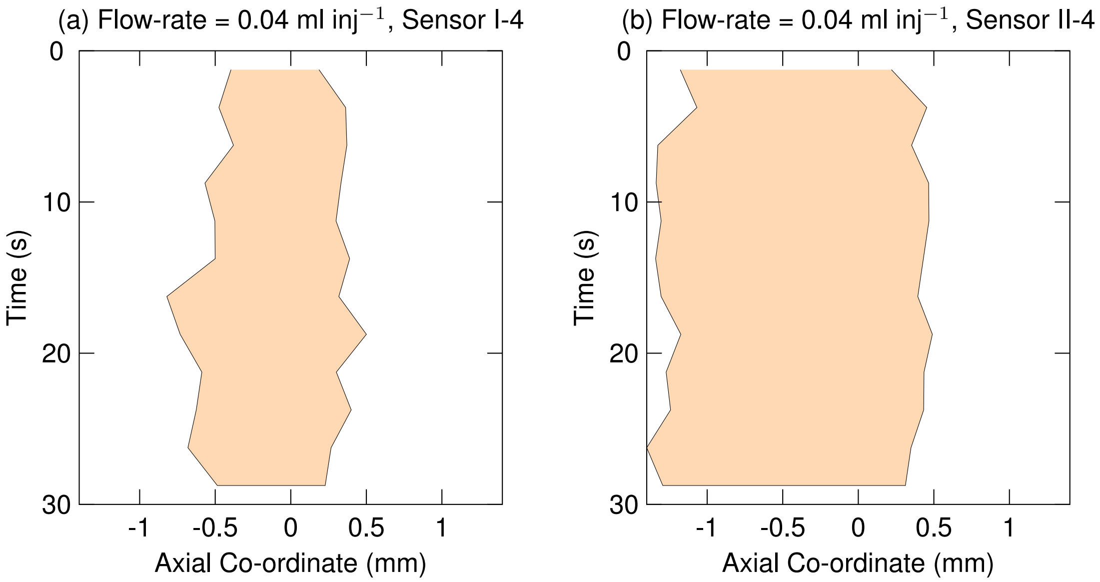

Figure 5.15: Experimental inlet and cavitation boundaries taken on the downstrokes at 5 cycle intervals

almost fully-flooded throughout the test. In the case of sensor I-4, while not fully flooded, the conjunction between piston-ring and cylinder liner is more filled than in the case of the upstroke.

There are two possible causes for the different position of the inlet boundary; either more lubricant available on the downstroke, or the minimum oil-film thickness is lower. Figure 5.16 shows the minimum oil-film thickness at both sensor I-4 and II-4 during the test. Looking at sensor II-4, it is not the case that there are lower oil-film thicknesses on the downstroke during the first few cycles of the test. It is only following the sixth cycle ($t = 3$ seconds) this becomes the

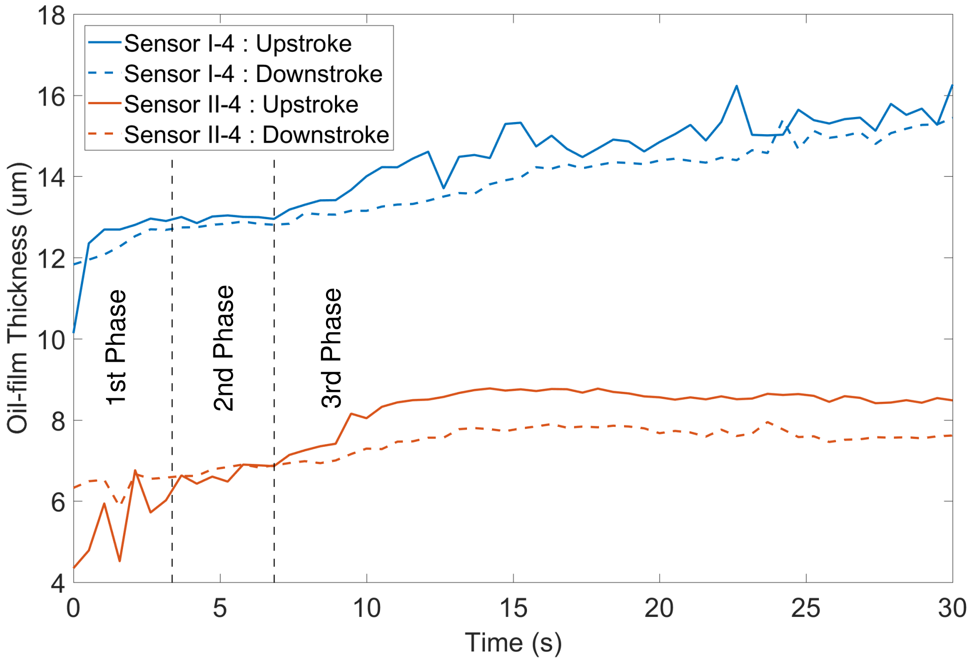

Figure 5.16: Minimum oil-film thickness on upstroke and downstrokes at sensors I-4 and II-4 (31.2mm from top dead centre) : Flow-rate = 0.04 ml inj^{-1}

case. With sensor I-4 the upstroke oil-film thickness is consistently greater during the test, with the exception of the first cycle, and a cycle at around 25 seconds into the test.

For the purposes of the analysis, figure 5.16 is to be categorised into three phases. The period between the start of the test and $t = 3$ seconds, where the downstroke minimum oil-film thickness is greater than that of the upstroke. The period between $t = 3$ seconds and $t = 7$ seconds where the oil-film thickness on upstroke and downstroke are similar. The period from $t = 7$ seconds where the oil-film thickness on the upstroke is notably greater than that of the downstroke.

During the first of these phases the results of figures 5.14 and 5.15, show the piston-ring to be more starved on the upstroke than the downstroke at sensor II-4. During the same period figure 5.16 shows the minimum oil-film thickness was lower on the upstroke than the downstroke, and that upstroke oil-film thickness is increasing. The increase in lubricant availability for the downstroke is a result of the low oil-film thicknesses near to top dead centre, where the piston-ring velocity is low. Here the minimum oil-film thickness drops to its lowest value during the cycle, and subsequently the ring becomes fully flooded. As the piston-ring commences the downstroke, any lubricant in excess of that required to fully-flood the piston-ring is scraped down the cylinder liner (see figure 5.17), to be consumed further down the stroke as the oil-film thickness rises. This action is an important mechanism for lubricant transport, and while the piston-ring continues to be fully flooded the excess will be scraped further down the cylinder. As the oil-film thickness rises, so too will lubricant flow past the piston-ring and the excess will become consumed, leading to the inlet boundary moving towards the centre of the piston-ring.

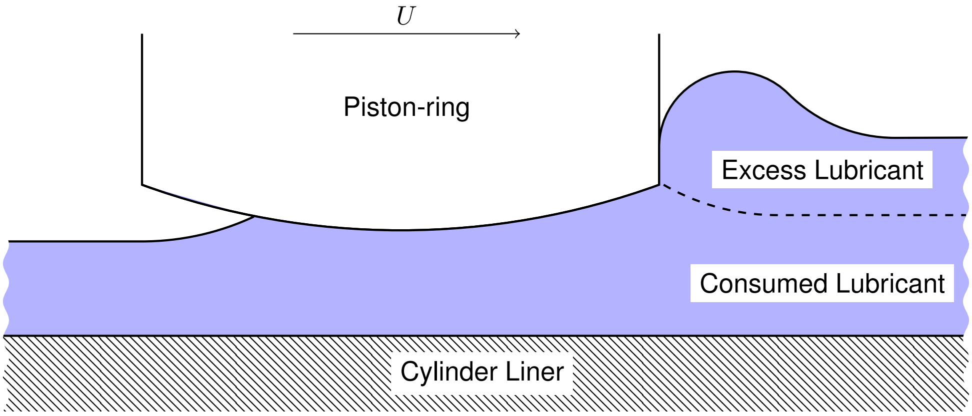

Figure 5.17: The scraping mechanism of the lubricant volume exceeding that which can be consumed past the piston-ring

On the upstroke there is no excess, with the velocity of the piston-ring as it approaches the transducers from midstroke being sufficiently high to allow the piston-ring to be supported by the hydrodynamic pressure generated by a lubricant film extending only partly towards the leading edge. Consequently, as the piston-ring passes sensor II-4 it is seen to be starved.

From $t = 3$ seconds to $t = 7$ seconds, as the lubricant continues to be scraped down from top dead centre, the increased thickness of the lubricant film on the cylinder liner allows the measured minimum oil-film thickness on the upstroke to converge with that of the downstroke. During this time the inlet boundary should be seen to be moving towards the leading edge of the piston-ring. Figure 5.14 does not show this. This does not negate there being an increase in lubricant availability, however. Since the lubricant is still largely concentrated near the top of the stroke the oil-film thickness begins to rise in the vicinity of midstroke. This negative squeeze action requires the available lubricant to fill the increased volume between piston-ring and cylinder liner, leading to the inlet boundary being nearer the centre of the piston-ring. Since the piston-ring is flooded on the downstroke there is no notable increase in oil-film thickness apparent for the downstroke during this phase of the test as an increasing volume of lubricant becomes resident on the cylinder liner.

Lastly, during the period from seven seconds into the test, the oil-film thickness on the upstroke increases further as the piston-ring becomes fully flooded. In addition to the piston-ring becoming fully flooded, the more developed lubricant film will provide increased film extent circumferentially, and will cause the negative squeeze action to diminish, both contributing to this rise in oil-film thickness of between one and two micrometers.

The starvation boundary analysis has also been performed at transducer II-5 (figure 5.18), with the oil-film thickness development shown in figure 5.19. Here the piston-ring can be seen to be fully flooded from 12 seconds into the test on both the upstroke and downstroke, with this increase occuring over the course of several seconds in the latter case. The most notable rise in oil-film thickness in figure 5.19 occurs between 7 and 12 seconds for the upstroke, with only very marginal changes on the downstroke in this phase of the test. The timing of this change in the position of the starvation boundary corresponds well with the changes in oil-film thickness seen in figure 5.19, suggesting a link between the position of the inlet boundary and oil-film thickness. The change seen in the position of the inlet boundary for the downstroke does not lead to a similar rise in oil-film thickness, however. Again, oil-film thickness in the first ten seconds of the test is higher for the downstroke, while after this time the upstroke oil-film thickness becomes the greater.

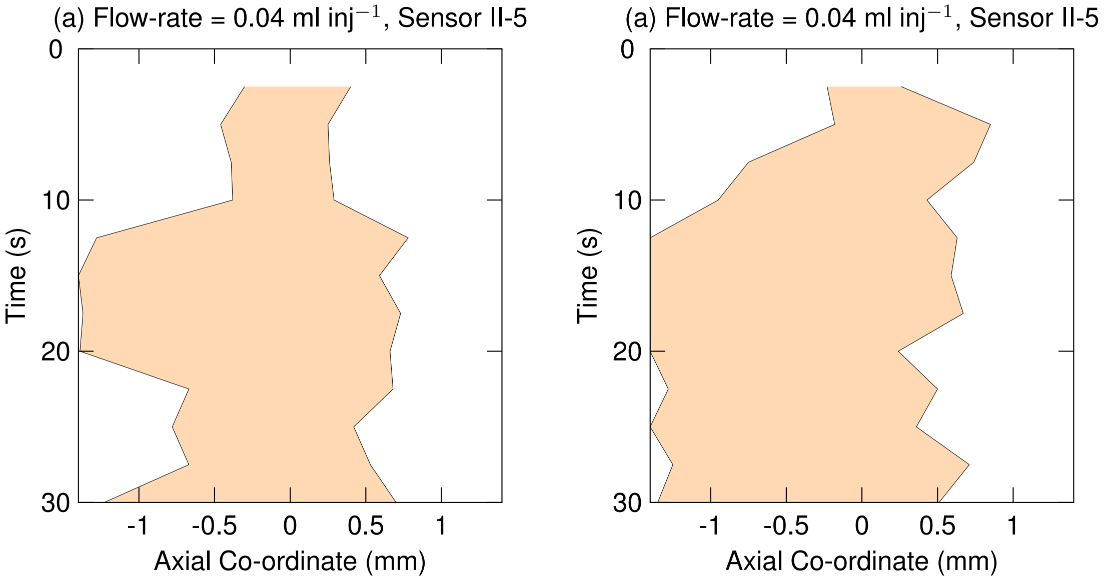

Figure 5.18: Experimental inlet and cavitation boundaries taken at 5 cycle intervals for (a) upstroke and (b) downstroke

The response of the oil-film thickness under the piston-ring at this transducer appears to have the form, on the upstroke at least, of a first order system. The characteristic parameter of this system is the time constant, which is defined as the time taken for a parameter to vary by 63% of the total change. In this case, the final value is likely to be the minimum oil-film thickness once the lubricant film has completely developed over the entire cylinder liner, and the oil-film thicknesses has reached a cyclic steady state. Considering this transducer is remote by some distance from the region where lubricant is injected, there is also a time delay before the transient begins. This time delay is another important feature of the response and here is in the region of 8 seconds.

An expression representing a response of this type is shown in equation 5.3, where h_0 represents the minimum oil-film thickness, H the oil-film thickness measured on the cycle at which the transient response begins, H_0 is the magnitude of the change between the initial value and the steady state, and τ is the time constant. The time delay before the beginning of the response

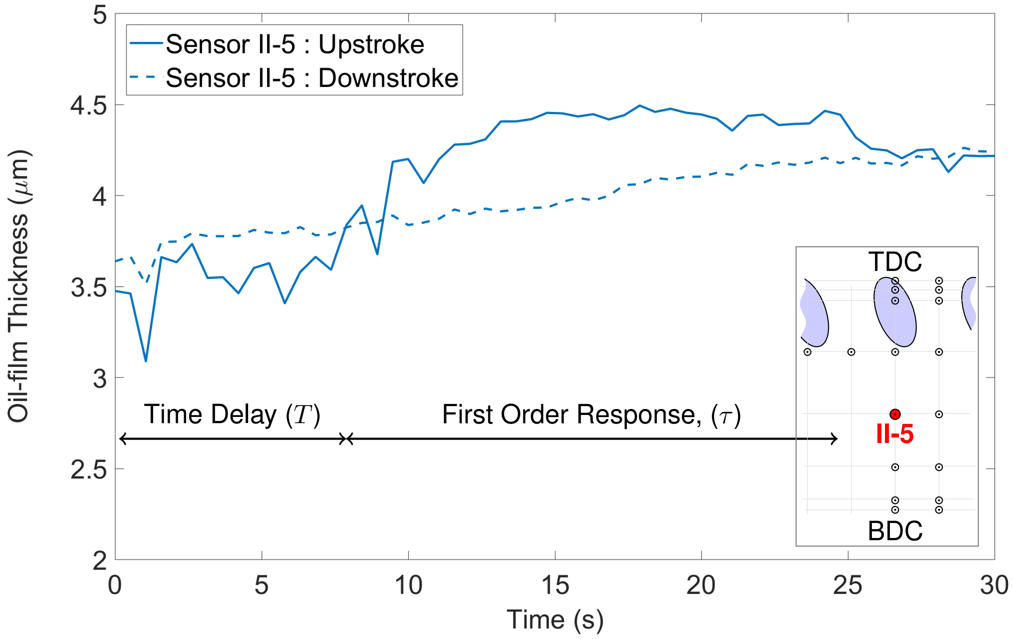

Figure 5.19: Minimum oil-film thickness on upstroke and downstrokes at sensor II-5 (58.5 mm from top dead centre)

is T. The equation can also be written in terms of engine cycles using the conversion $n = ft$, where n is the number of cycles, and f is the engine frequency in Hertz. While it may be thought the initial oil-film thickness value (H) should be zero, the volume of lubricant delivered on the first injection event is sufficient to allow the piston-ring to achieve the oil-film thickness seen at several transducers on the first cycle.

$$h_0 = \begin{cases} H, & \text{if } t < T \\ H + H_0\left(1 - e^{-\frac{t-T}{\tau}}\right), & \text{otherwise} \end{cases} \tag{5.3}$$

The Deborah number is the ratio of material relaxation time (the time taken for a material to adjust to applied stresses) and the time scale of an experiment (Reiner, 1964). Deborah numbers less than one suggest Newtonian fluid flow, while Deborah numbers greater than one indicate non-Newtonian behaviour with visco-elastic stiffening leading to the fluid behaving in an increasingly solid-like manner.

In this case, the experimental timescale covers the part of the stroke during which the piston-ring undergoes a sudden change in oil-film thickness as the more lubricated region of the cylinder is reached. This is typically between the sensors at II-4 and II-3. At two cycles per second, this distance is covered in a time of approximately 0.04 s, and given that engine oil has a relaxation time of the order of 10^{-4} to 10^{-6} the Deborah number can be estimated to be in the range 0.0025 – 0.25. This suggests the Deborah number is likely to be below one, and that the first order increase seen in oil-film thickness between these sensors seems intuitively aligned with expectations and the assumption of Newtonian flow considered acceptable.

However, an increase in lubricant relaxation time or a change in one of the experimental parameters such as engine speed could lead to Deborah numbers greater than one, leading to a visco-elastic stiffening of the fluid. It is also possible the rapid increase in oil-film thickness seen on the first cycle or two occurs because the boundary between lubricated and unlubricated regions of the cylinder is comparable to a step change and the experimental timescale smaller than estimated above. On these strokes this may be small enough for the Deborah number to become greater than one, leading to visco-elastic stiffening of the fluid and a sudden change in oil-film thickness. Further investigations examining relaxation times and the effects this has on the development of the lubricant film would very much be worthwhile.

Lastly, figure 5.20 shows the upstroke and downstroke inlet boundary for sensor II-4 at the lower injector flow-rate of 0.01 ml inj^{-1}. In comparison to the higher flow-rate, the migration of the inlet boundary towards the leading edge is a couple of seconds later for both strokes. While it would be expected that the lubricated area takes longer to grow in size when the volume of oil being injected is lower, the close proximity of the transducer to this area would suggest it should not be a long delay.

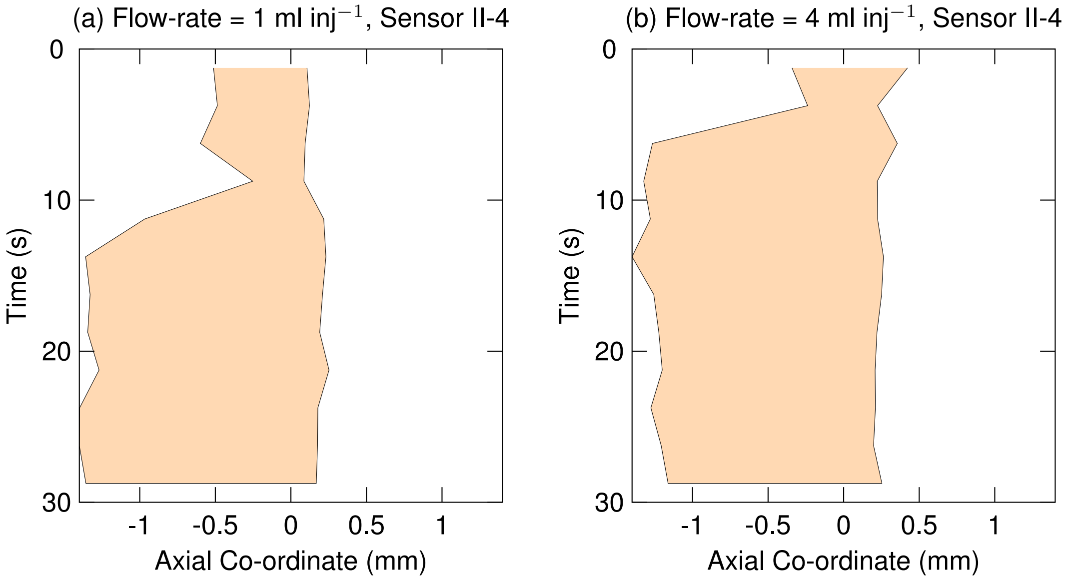

Figure 5.20: Comparison of experimental inlet and cavitation boundaries on upstroke and downstroke taken at 5 cycle intervals for both injector flow-rates

5.4 Result Verification Using Video Footage

Figure 5.21 shows a series of stills from video footage of the test with injector flow-rate 0.04 ml inj^{-1}. Four of the transducers are labeled. The images are taken at intervals in the first half of the test, and provide valuable evidence to support the results of the film extent analysis (5.3.3). Looking at figure 5.21a, a small area of lubricant is visible near to top dead centre. in the proximity of the block II sensors. It's limits are just above sensor II-3, and extending approximately 45° around the circumference of the liner. This region of oil appears to be relatively thick, in that it is probably sufficient to fully flood the piston-ring. Elsewhere on the liner there doesn't appear to be any evidence of lubricant, although it is not possible to confirm this conclusively from the video.

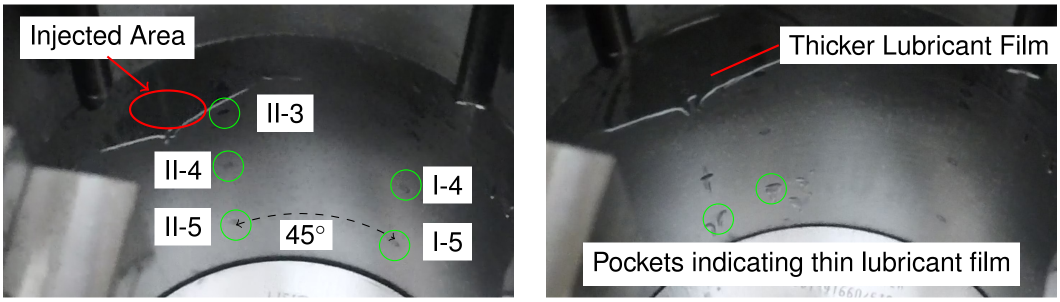

(a) t = 2 second

(b) t = 6 seconds

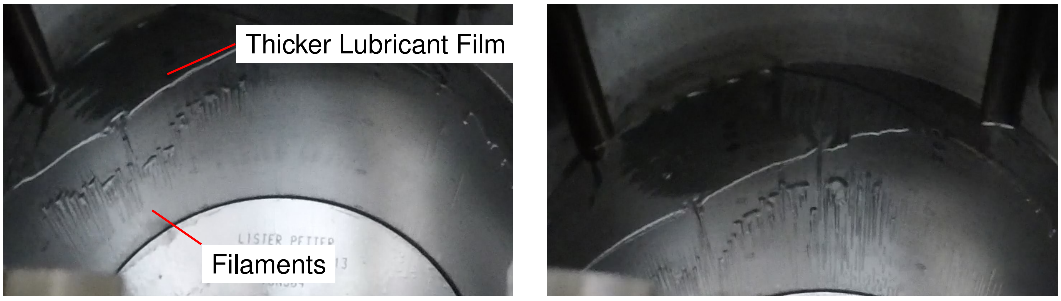

(c) t = 10 seconds

(d) t = 20 seconds

Figure 5.21: Video stills: Flow-rate = 0.04 ml inj^{-1}

As the test proceeds, the effects of cavitation become visible as filaments and pockets in the trailing lubricant, providing evidence of the widening extent of the lubricating film on the cylinder liner. Figure 5.21b, for example, has several of these features in the midstroke region, while there is much clearer evidence at 10 and 14 seconds as the extent of the lubricant film increases around the cylinder liner, and importantly over sensor II-4. Notably, this film cannot be seen to extend as far as sensor I-4 at 10 seconds (figure 5.21c), despite figure 5.10 showing the rise in oil-film thickness at around this time. It is nearer to 20 seconds into the test when clear evidence of lubricant in the proximity of sensor I-4 becomes apparent. This is not to say that lubricant is not present prior to this, especially considering the short distances to other areas of the cylinder with these cavitation features.

Figures 5.22 and 5.23 show results from tests at two of the injector flow-rates, 0.01 ml inj^{-1}

and 0.04 ml inj^{-1}. Each graph shows lines of minimum oil-film thickness changes against time at several transducers as the piston-ring travels past them during both (from left to right) the upstroke and downstroke. Results at sensors I-3 and II-3 to I-6 and II-6 (8.7 mm to 81.7 mm below top dead centre) are shown, with negative crank angles indicating the position before top dead centre during the upstroke. The tests were 30 seconds in duration, so oil-film thickness development over the course of 60 cycles is shown.

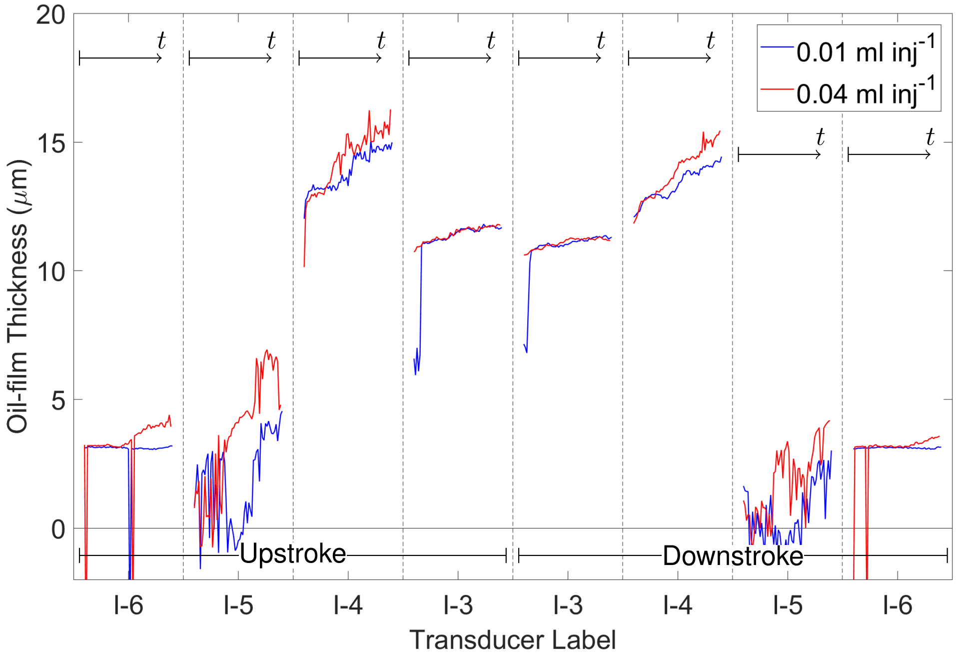

Figure 5.22: Graphs of minimum oil-film thickness vs time at sensors I-3 to I-6

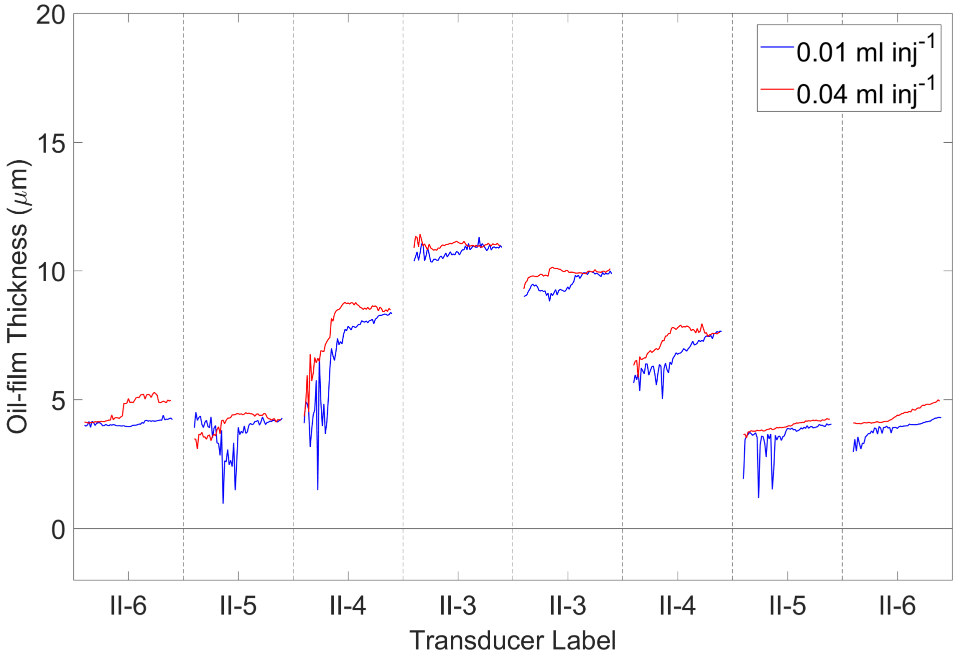

Figure 5.23: Graphs of minimum oil-film thickness vs time at sensors II-3 to II-6

These figures show thicker oil-film thickness at the top of the stroke than at the midstroke. This is not typical of oil-film thickness in internal combustion engines, because the higher velocities and lower gas-pressure forces near midstroke tend to lead to thicker films. Here it is more expected though, since there is constant load and initially a deficit of oil in the bottom half of the stroke due to the localised lubricant delivery in the upper part of the cylinder liner.

Inspecting the results for the higher flow-rate of 0.04 ml inj^{-1}, these show the features in the results at sensors I-4 and II-4 are also evident in the results from other transducers. At sensors I-3 and II-3 (8.7 mm below top dead centre) for example, the oil-film thickness appears to be steady (II-3), or show a very slight increase (I-3). Transducer II-3 is in the area in which lubricant is sprayed, and as such should be well lubricated from the outset of each test. The oil-film thickness at sensor I-3 sees a marginal increase at about ten seconds. This corresponds to the results shown in figure 5.21, which show little evidence of lubrication near to sensor I-3 until after six seconds of the test.

At sensors I-5 and II-5 (58.5 mm below top dead centre) the oil-film thickness is very unsteady until well into the test, particularly at sensor I-5. The unsteady oscillation of the piston-ring signal during contact between itself and the transducer lead to variable minima on each pass, this result manifests as a fluctuating minimum oil-film thickness value in the graph in figure 5.22. Again, at around ten seconds into the test this oscillation ceases, and the oil-film thickness begins to rise. For sensor II-5 this rise occurs earlier in the test - at approximately 7 seconds.

At sensors I-6 and II-6 (81.7 mm below top dead centre) the oil-film thickness is steady, before the rise at about half-way through the test. This rise is more rapid at sensor II-6 than sensor I-6, which is due to the relatively fast action of lubricant being scraped down the cylinder liner compared with the slower transport circumferentially.

5.5 Discussion

Since the engine is up to test speed when lubricant is first injected, it can be assumed that several of the parameters in Reynolds equation (equation 3.1) remain constant over each cycle of the test (ie. viscosity, piston-ring geometry, and velocity at any given transducer location). Considering the load on the piston-ring to also be constant, there are three possible causes for an increase in oil-film thickness.

1. An increase in film extent in the axial direction
2. An increase in film extent in the circumferential direction
3. An increase in the velocity of the piston-ring towards the cylinder liner (squeeze effect)

To explain the first two of these points, consider the piston-ring at a given oil-film thickness, and assume the viscosity, piston-ring velocity, and piston-ring geometry to remain constant. An increase in film-extent will lead to an increase in hydrodynamic pressure (the integral of the pressure field over the piston-ring face). Consequently the magnitude of the pressure field must be reduced to maintain equilibrium, which requires an increase in minimum oil-film thickness. This is true regardless of the direction in which the film extent is increasing. With the latter point, an increase in the velocity of the piston-ring towards the cylinder liner will lead to an increase in hydrodynamic pressure resulting from the squeeze action. Again, an increase in oil-film thickness would reduce the magnitude pressure generated by the sliding motion, allowing the equilibrium to be maintained.

Also, mass conservation dictates that lubricant flow past the inlet of the piston-ring must equal the mass flow out. Not all of this must be past the trailing edge of the piston-ring. However, since there may be some mass flow in the circumferential direction in the event of squeeze action, the mass flow out will be greater than the mass flow in due to the reduction in volume of the area underneath the piston-ring. An increasing oil-film thickness leads to the opposite effect, and mass flow in will be greater than it is out. If the piston-ring is fully flooded, lubricant will be scraped down the cylinder liner (in the manner shown in figure 5.17) until the excess diminishes, or it is deposited at bottom dead centre.

Given the tendency for oil-film thicknesses to be thicker on the downstroke during the early part of the tests, there must be more lubricant available on the downstroke, or there is a difference in the squeeze effect on each stroke. The first possibility is that lubricant is being scraped down the cylinder liner from near the top of the cylinder during the downstroke, providing sufficient lubricant to fully flood the piston-ring. Normally, should this be the case, there would be enough lubricant flow past the piston-ring to fully-flood it again for the following upstroke. However with the film extent also extending circumferentially this may not be the case here. There is also the possibility this behaviour results from an unusual squeeze action at the limit of the lubricant film. Typically there is minimal squeeze action towards the middle of the stroke, but with the lower stroke being poorly lubricated early during the test, oil-film thicknesses remain low. As the piston-ring reaches the lubricated area towards the top of the stroke the oil-film thickness rises, diminishing the hydrodynamic pressure field and leading to a lower than typical oil-film thickness. The opposite may be occurring on the downstroke. With the oil-film thickness dropping as it reaches the limits of the lubricated area, the squeeze action augments the pressure field and leads to a greater than normal oil-film thickness.

Considering the inlet boundary analysis there appears to be evidence - in the case of sensors I-4, II-4, and II-5, the oil-film thickness occurring on the upstrokes at around ten seconds into the tests result from an axial increases in film extent. The timing of these rises indicates the development of the lubricant film towards these locations from the area it is delivered to from the injectors. Oil-film thickness in some cases continue to rise beyond this (sensor I-4), which given the ring is already flooded can only be caused by the film extending further around the circumference of the cylinder liner.

It is apparent from these results that while the delivery of lubricant is to the upper region of the cylinder liner, there is one or more mechanisms whereby this lubricant is transported to other areas of the cylinder liner. The inlet boundary analysis showed the piston-ring to be fully flooded on the downstroke more often than not, and so the scraping action of lubricant down the cylinder liner is thought to be the primary mechanism for transport. Circumferentially, Poiseuille flow is the only hydrodynamic mechanism and so it may be be expected this be slower than axial transport. There is however also a mechanism whereby the oil that is being scraped down the cylinder liner by the piston-ring spreads under a force due to acceleration of the piston. This may accelerate the spreading of lubricant circumferentially.

5.6 Conclusions

Midstroke oil-film thicknesses are low at the beginning of the tests, due to an atypical lubricant-film distribution near midstroke with lubricant concentrated towards top dead centre. This effect lessens as the tests continue and the lubricant film develops.

Increases in oil-film thickness can be seen to result from an increase in both axial and circumferential film extent.

The response of the piston-ring to the increase in availability of lubricant, and the time taken for lubricant to be transported to different parts of the cylinder liner can be approximated as a first order dynamic response with time delay (equation 5.3). Further testing is needed determine the influence of lubricant flow-rate on the key characteristics of this response (the time constant - τ, and time delay - T).

The development of the lubricant film in time can be tracked at a number of transducers through changes in oil-film thickness and the migration of the inlet boundary towards the leading edge of the piston-ring.

The increases in oil-film thickness during transition from starved to flooded conditions are fast relative to the length of the test. Given this occurs even at the lower flow-rate of 0.01ml inj^{-1}, it would likely be helpful to conduct more experiments at a reduced flow-rate in order to further investigate these effects. It would also be beneficial to run the tests for longer to allow for a more complete development of the lubricant film on the cylinder liner.

Lubricant is transported down the cylinder through the scraping of lubricant in excess of the volume needed to fully flood the piston-ring. This action must be incorporated into the piston-ring lubrication model if the lubricant film development is to be modelled appropriately.

Chapter 6

The Influence of Lubricant Injection Volume and Time on Oil-film Thickness Development

6.1 Introduction

The response of oil-film thickness to a step change in lubricant injector flow-rate has been shown (in chapter 5) to take the form of a first order system with time delay (equation 5.3). For the piston-ring system, this involves parameters including the oil-film thickness at the beginning of the transient phase (H), the magnitude of the change during the transient phase (H_0), the time delay (T), and the time constant (τ). The purpose of this chapter is to investigate the transient phase of this response in more detail, along with factors affecting the response, such that a complete system model can be proposed.

Specifically, results from a series of tests will be inspected to determine the cause of the variable H, the time constant will be evaluated to analyse which parameters may contribute to this dynamic characteristic, and periodic features of the response resulting from the injection of lubricant are also be discussed.

6.2 Method

A series of tests have been conducted using the experimental equipment described in chapter 4. While the tests followed a similar method to those outlined in chapter 5, here the tests were 60 seconds in duration and lubricant was injected at periodic intervals to reduce the overall lubricant injector flow-rate below the specified minimum of the injector. With periodic injection, lubricant was sprayed only once every third, sixth, or tenth cycle, leading to an average injector flow-rate (q_{ave}) that is the quotient of the injector flow-rate setting and the period between injection events. In order to effect a step change in lubricant supply, the engine was brought up to speed before the first lubricant injection event.

The tests were performed at three lubricant injector flow-rate settings, 0.02 ml inj^{-1}, 0.04 ml inj^{-1}, and 0.08 ml inj^{-1}. On each injection event, lubricant was injected onto the cylinder liner in 4 locations as described in chapter 4, and shown in figure 4.19. Only the compression ring was employed in these tests, and oil-film thickness for this piston-ring was measured using fourteen capacitance transducers arranged in an array, as shown in figure 5.1.

As with the first set of experiments, lubricant injection commenced as the piston reached 82 mm below top dead centre on the downstroke, and the injector valve was held open for 200 milliseconds. The sprayed lubricant covers the first three sensors in block II (top dead centre to 31 mm below top dead centre). Other engine and experimental parameters remain unchanged from the tests in described chapter 5. The cylinder liner was cleaned thoroughly with solvent after each test to ensure there was minimal residual lubricant present at the start of each run.

6.3 Results

6.3.1 Minimum Oil-film Thickness

Figures 6.1a to 6.1f show oil-film thickness measurements from a series of tests. These figures are arranged in pairs for the sensors in block I and block II, with each graph showing lines of oil-film thickness change in time at a number of sensors on both upstroke and downstroke. The tests were 60 seconds in duration and the development of minimum oil-film thickness throughout this time is shown. There are four sets of results on each chart for the different periodic injection frequency settings, and three pairs of graphs for each of the lubricant injector flow-rate settings. The results for the tests performed with lubricant injection on every cycle are thirty seconds in length. In order to allow a more complete development of the lubricant film, the tests conducted at lower injector flow-rates are twice this length.

As with the similar charts in chapter 5, these graphs show some expected features, such as higher oil-film thicknesses towards the middle of the stroke where the velocity is higher, and lower oil-film thickness in the bottom half of the stroke where there is initially no lubricant present. The flow-rate setting on the lubricant injectors is held constant for all tests on each chart. As such a period of one equates to three times more oil than for a period of three. Likewise this is more than for the tests with period of six and for a period of ten.

Oil-film thickness on the charts generally reduces as the period increases, or at the very least remains equal. The notable exception is for results with period setting equal to six, which shows the lowest oil-film thicknesses at all sensors in block I, and conversely the highest oil-film thickness at all sensors in block II. This is true at all injector flow-rates. At the other periodic injection settings there is a more intuitive trend, with results showing oil-film thicknesses at period of one tend to be the highest, and the results at period 3 being higher, or very similar to a period of ten.

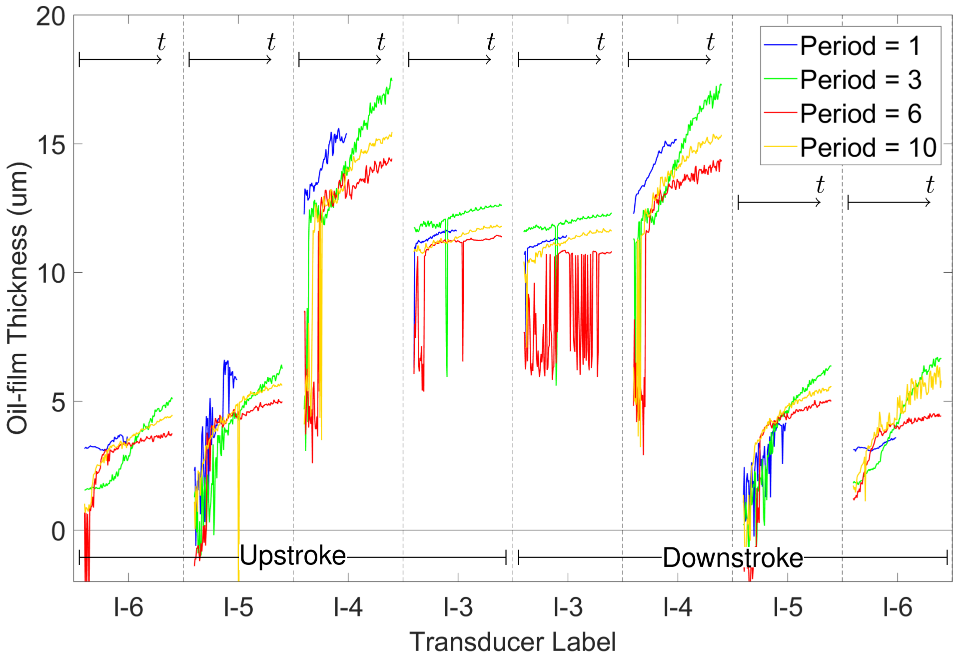

(a) Flow-rate 0.02 ml inj^{-1} : Block I

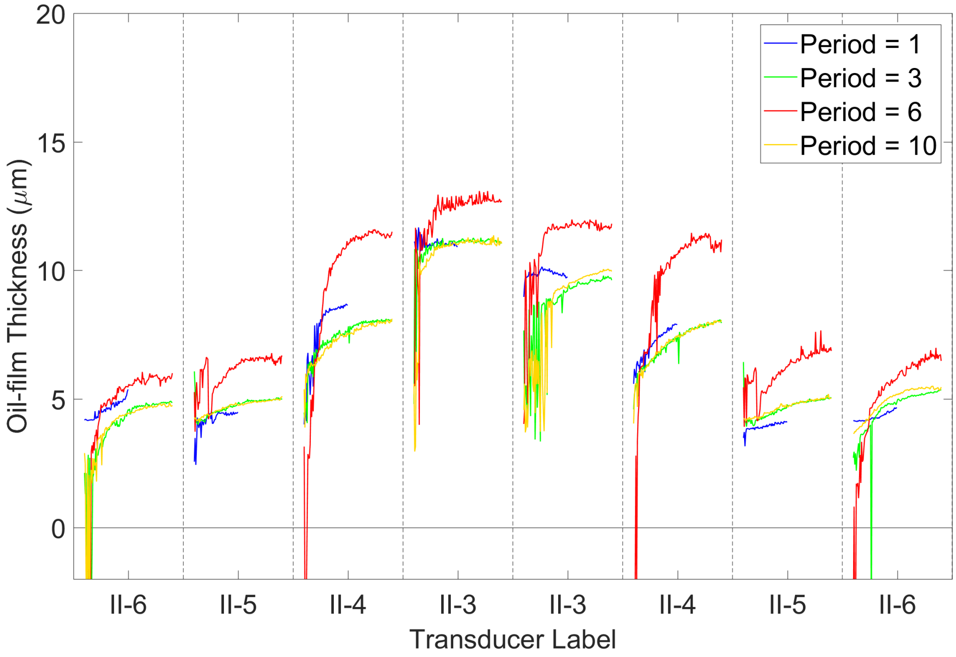

(b) Flow-rate 0.02 ml inj^{-1} : Block II

Figure 6.1: The influence of injection period and flow-rate on the time-variation of oil-film thickness

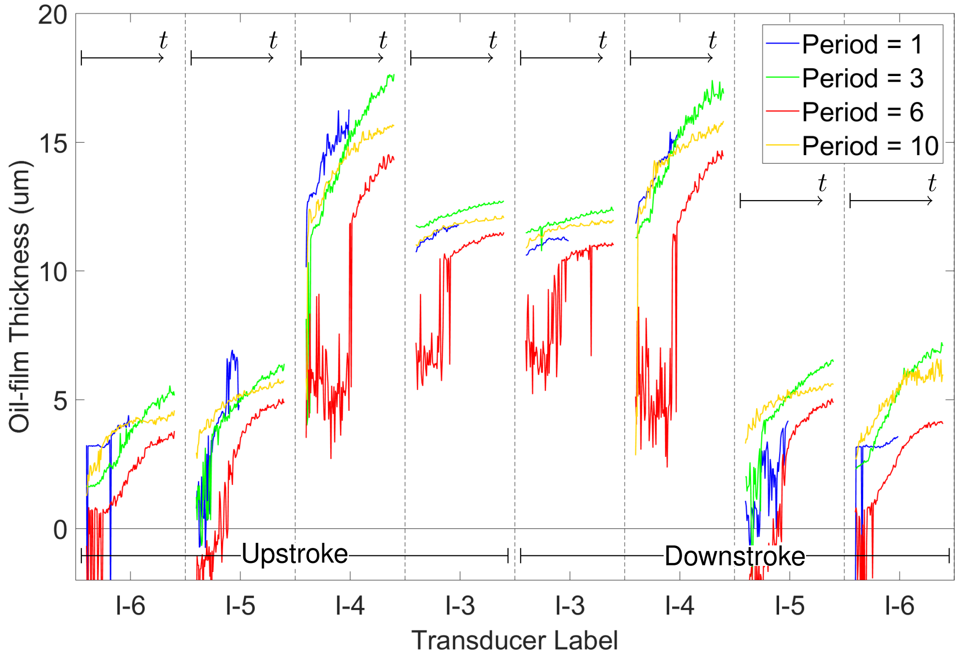

(c) Flow-rate 0.04 ml inj^{-1} : Block I

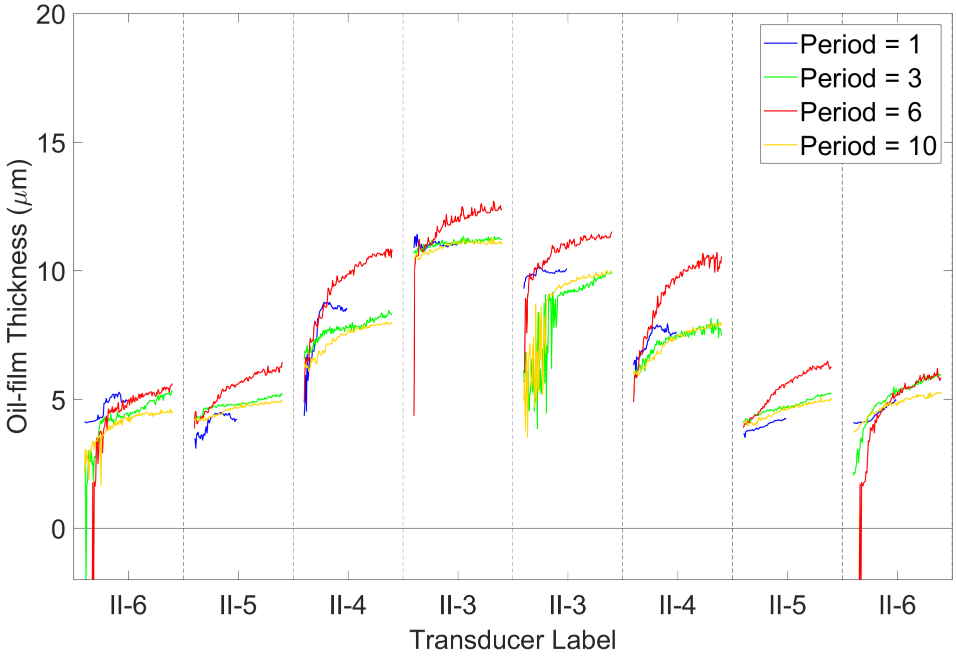

(d) Flow-rate 0.04 ml inj^{-1} : Block II

Figure 6.1: The influence of injection period and flow-rate on the time-variation of oil-film thickness

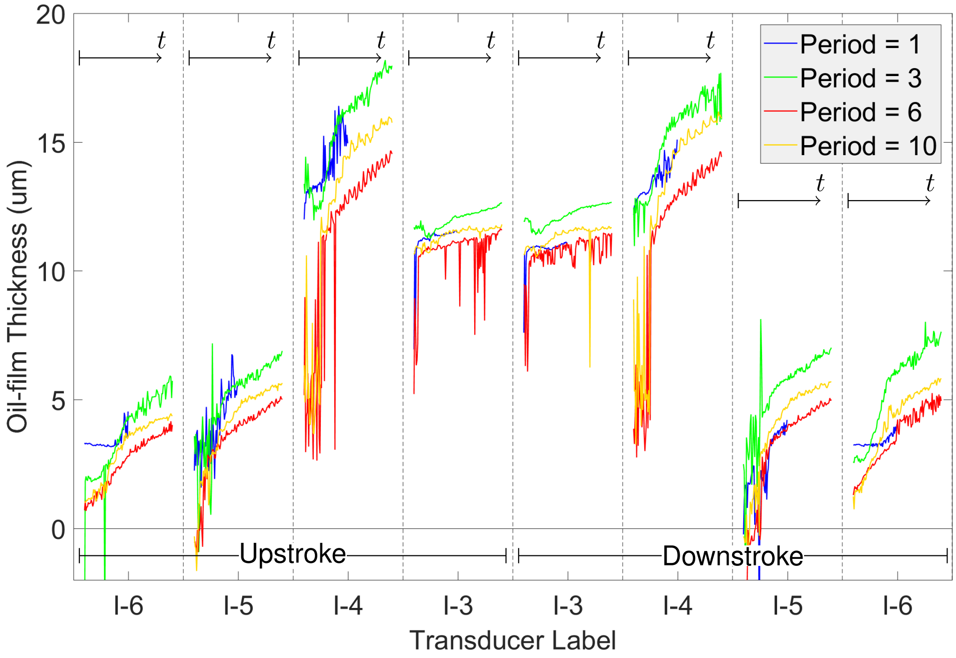

(e) Flow-rate 0.08 ml inj^{-1} : Block I

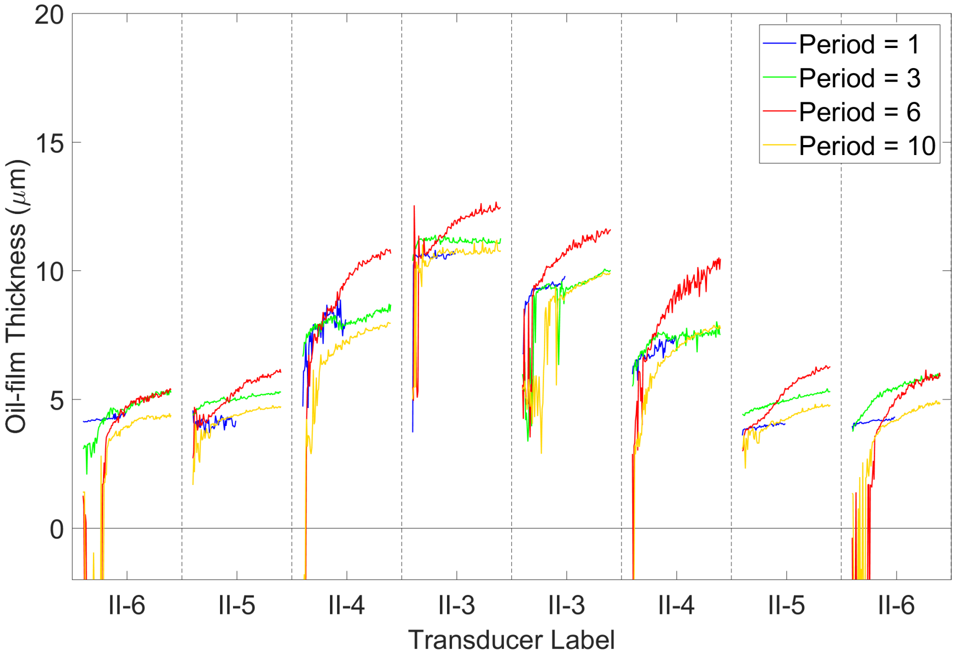

(f) Flow-rate 0.08 ml inj^{-1} : Block II

Figure 6.1: The influence of injection period and flow-rate on the time-variation of oil-film thickness

This suggests the results with periodic injection on every sixth cycle (period = 6) may be spurious, with the oil-film thickness being the highest of all tests at block II, and the lowest at block I. There is no evidence, but it is possible a temporary fault developed with the injector delivering lubricant to position C (on figure 4.19) such that the lubricant distribution was not axis-symmetric, and leading to the piston-ring being pushed towards the area where lubricant was absent. This is most evident in the results near top dead centre shown in figure 6.1c.

While many of the oil-film thickness results in block II show very similar values at the different periodic injections setting, there is a noticeable difference between for period 3 and period 10 at sensors II-5 and II-6, with the former being greater by approximately one micrometre. The cause of this difference appears to be due to the response at the lower injector flow-rate commencing at a later time. This may indicate a lower rate of lubricant transport to the transducers located towards the bottom of the stroke. With the higher flow-rate lubricant appears to be transported immediately to these same locations, likely due to axial scraping of lubricant by the piston-ring from the area where it is injected.

In block II, the results for periodic injection every third and tenth cycle are very similar, particularly towards the top of the cylinder near transducers II-3, II-4, and II-5. At sensor II-6 there is a difference in the rate of increase towards the end of the test at flow-rate 0.04 ml inj^{-1} (figure 6.1d), with the higher gradient occurring for the higher average lubricant injector flow-rate. This is also true at many of the transducers in block I, and could again be due to a lower rate of lubricant transport to these areas of the cylinder leading to lower rates of increase in oil-film thickness. At the transducers in the proximity of injected lubricant the differences in oil-film thickness at different injection frequencies are less, suggesting the lubricant film is thick enough to flood the piston-ring regardless of the average lubricant flow-rate. As lubricant is spread more widely, the thickness of the oil-film is decreased. Therefore at transducers more distant from the area where lubricant is injected (ie. I-4 to I-6) the difference in lubricant availability leads to more apparent differences in oil-film thickness.

The results in some cases appear to reach a steady state, while in other cases the oil-film thickness can be seen to be still increasing. Again this is particularly evident at transducers more distant from where lubricant is injected. Near to the injected area the piston-ring can become saturated with lubricant allowing the piston-ring to reach its steady-state oil-film thickness. At the transducers towards the bottom of the stroke, and at those sensors in block I, the lubricant film is still developing at the end of the tests, hence the continued rise in oil-film thickness.

With respect to the different injector flow-rate settings, the results at each setting (0.02 ml inj^{-1}, 0.04 ml inj^{-1}, and 0.08 ml inj^{-1}) show relatively little difference in oil-film thickness at each cylinder liner location. Figure 6.2 highlights this for sensor II-4, with the oil-film thickness from the

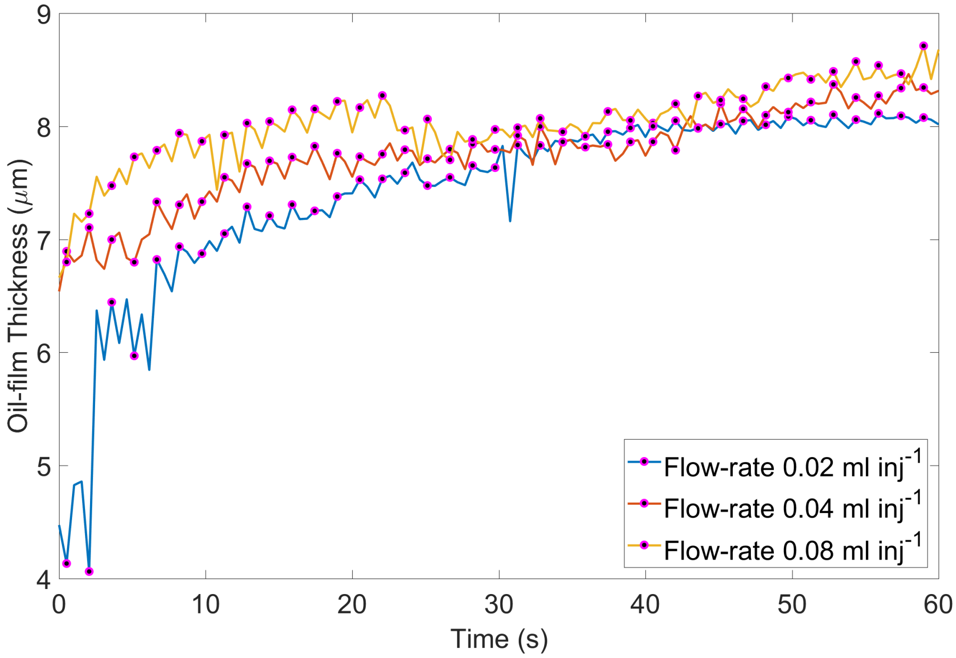

Figure 6.2: Effect of flow-rate on oil-film thickness - Sensor II-4 : Period = 3. The markers indicate the cycles on which lubricant is injected into the cylinder.

three tests following a very similar trend throughout the test, within a range of approximately 1 μm or less. The markers on this figure indicate lubricant injection events, in this case every third cycle. Considering also the proximity of the lines for periods of three and ten, and that the change in average lubricant volume injected per cycle (q_{ave}) is by a factor of more than 10, it is surprising there are not more notable differences in the oil-film thickness data (figure 6.3). This may highlight that the lubricant injector flow-rates used during these tests are still in excess of that needed to fully flood the piston-ring inlet under motored conditions, or it may be that a wider distribution of lubricant is needed.

While oil-film thickness results are all very similar at the block II transducers, in block I the increases are often more slow for lower average lubricant injector flow-rates (ie. for period = 10). This suggests lubricant transport occurs around the cylinder liner at a lower rate than occurs axially, with the latter being assisted by the scraping action of lubricant down the liner described in chapter 5. The scraping action appears to occur very quickly regardless of average lubricant injector flow-rate, with only transducer II-6 showing any notable difference (in figures 6.1b, 6.1d, and 6.1f) as the lubricant injection frequency is reduced.

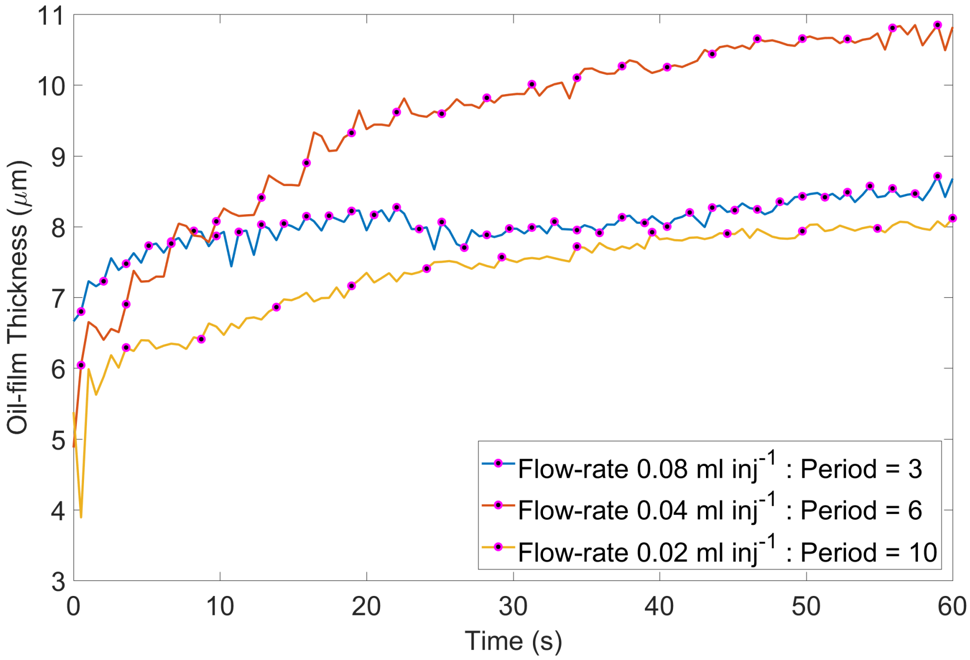

Figure 6.3: Oil-film thickness at maximum and minimum average flow-rates - Sensor II-4

6.4 Transient Response Characterisation

Determination of the dynamic characteristics of a system is essential for control system design, and many of the results above show the form of a first order exponential rise as the primary element of the initial transient (ie. figure 6.4). The results shown in figure 6.3 for example show this form following the step change in lubricant supply, with the oil-film thickness rising most quickly at the beginning of the tests before reaching a (near) steady state value by the end of the tests (after 60 seconds). The time constant (τ) is the key characteristic of this response, relating to the time taken for oil-film thickness to reach a steady state following a change in lubricating conditions. Specifically, the time constant is the time taken for the response vary by 63% of the total change in oil-film thickness, with three times the time constant being the time taken for 95% of the change.

In addition to the first order transient there are small scale oscillations evident, appearing to become less frequent as the interval between lubricant injection events is increased. This type of behaviour would be typical of a dynamic system that is subjected to a periodic forcing function.

In this section these transient phenomena are inspected and evaluated.

6.4.1 Evaluation of System Time Constant

Minimum oil-film thickness response for the tests performed can be approximated to the response of a first order system to a step input, of the form given in equation 6.1. Here h_0 represents the minimum oil-film thickness, H the oil-film thickness measured on the cycle at which the transient

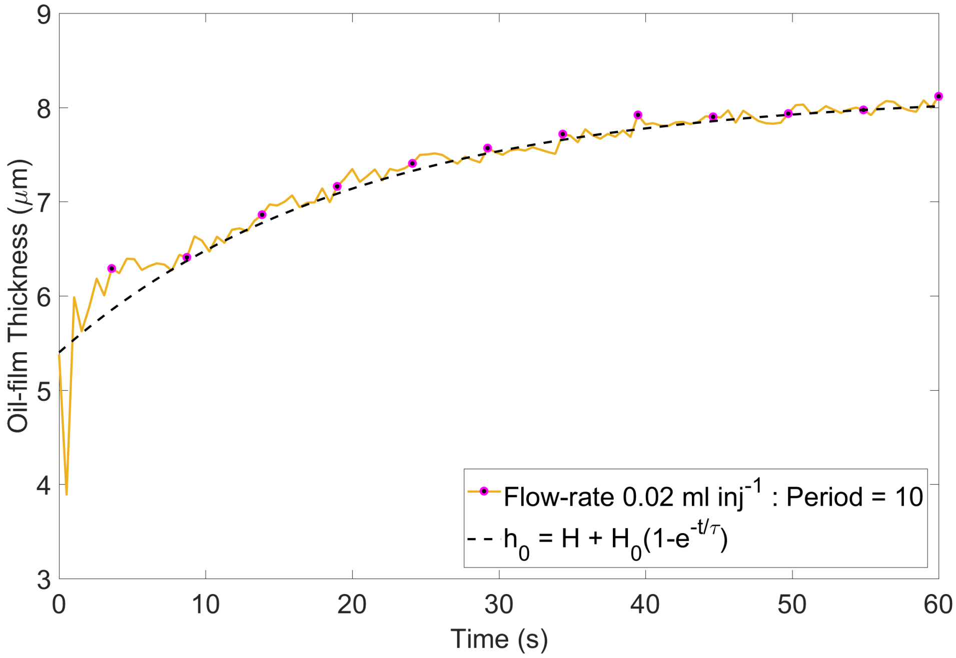

Figure 6.4: Comparison of oil-film thickness result with a first order exponential system response to a step input

begins, H_0 is the magnitude of the change between the initial value and the steady state, and τ is the time constant.

$$h_0 = \begin{cases} H, & \text{if } t < T \\ H + H_0\left(1 - e^{-\frac{t-T}{\tau}}\right), & \text{otherwise} \end{cases} \tag{6.1}$$

It is apparent from the results shown in the results shown in figure 6.1 the magnitude of change (H_0) is not consistent across all tests. Considering the oil-film thickness is a function of the viscosity, piston-ring velocity, and load this is to be expected. While load and viscosity are assumed to remain constant during these tests, velocity at different crank positions is not. Consequently this magnitude will be greater during the part of the stroke with the highest velocities.

In order to evaluate the time constant, graphs of minimum oil-film thickness against time must be assessed to find the time taken for 63% of the change to occur. Figures 6.5a and 6.5b show how this is done. Firstly, the magnitude of the change in oil-film thickness between the beginning of the response and the steady state is assessed, and a value corresponding to 63% of this change found. The time taken for the response to reach this value from the beginning of the transient phase can then be evaluated.

Time constants have been assessed in this way for transducers II-3 (8 mm below top dead centre), II-4 (31 mm below top dead centre), II-5 (58 mm below top dead centre), and II-6 (82 mm below top dead centre) at three injector flow-rate settings and three periodic injection frequencies.

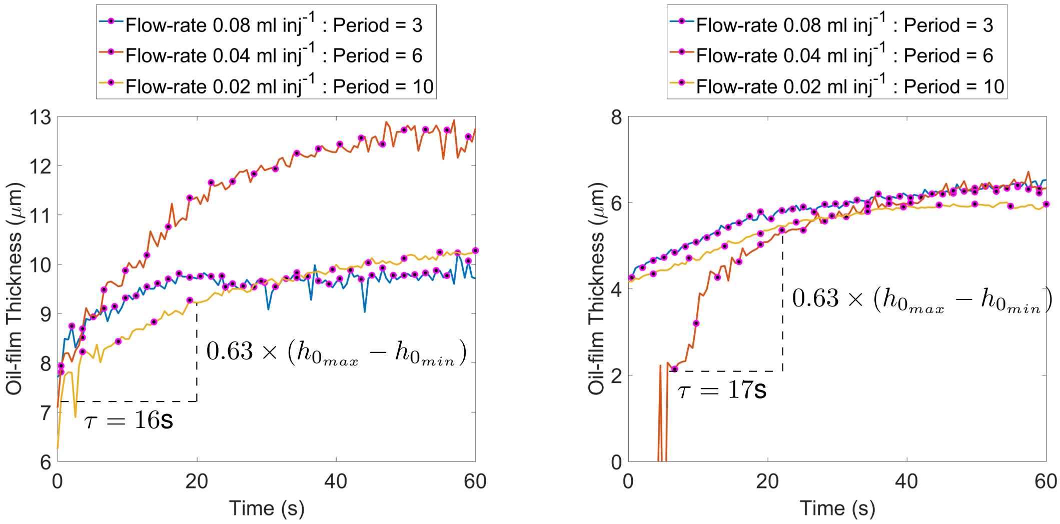

(a) Transducer II-4

(b) Transducer II-6

Figure 6.5: Determination of time constant at transducers II-4 and II-6

The results are presented in table 6.1. Only the transducers in block II are considered because the delay in commencement of the system response has led to many of the transients at block I transducers being incomplete. However, because the piston-ring is responding to changes in the developing lubricant film, it is thought the time constant should not be dependent on circumferential location.

		P3	P6	P10
Injector Flow-rate	Transducer		τ (s)	
0.02 ml inj^{-1}	II-3	11	3	17
	II-4	18	12	16
	II-5	23	13	23
	II-6	13	12	17
0.04 ml inj^{-1}	II-3	21	14	14
	II-4	21	16	20
	II-5	35	21	21
	II-6	13	12	19
0.08 ml inj^{-1}	II-3	33	20	17
	II-4	10	13	15
	II-5	30	19	22
	II-6	22	16	10

Table 6.1: Evaluated time constants at transducers II-3, II-4, II-5, and II-6, for injector periods of 3, 6, and 10.

Figure 6.6 shows the above results organised by average flow-rate. Here the time constant for sensor II-5 tends to be the longest with an average of 23 seconds. The time constants for sensors II-3, II-4 and II-6 are less in all cases, with averages of 16.7, 15.7 seconds and 14.9 seconds respectively. Thicker oil-film thicknesses tend to occur in the middle of the stroke where

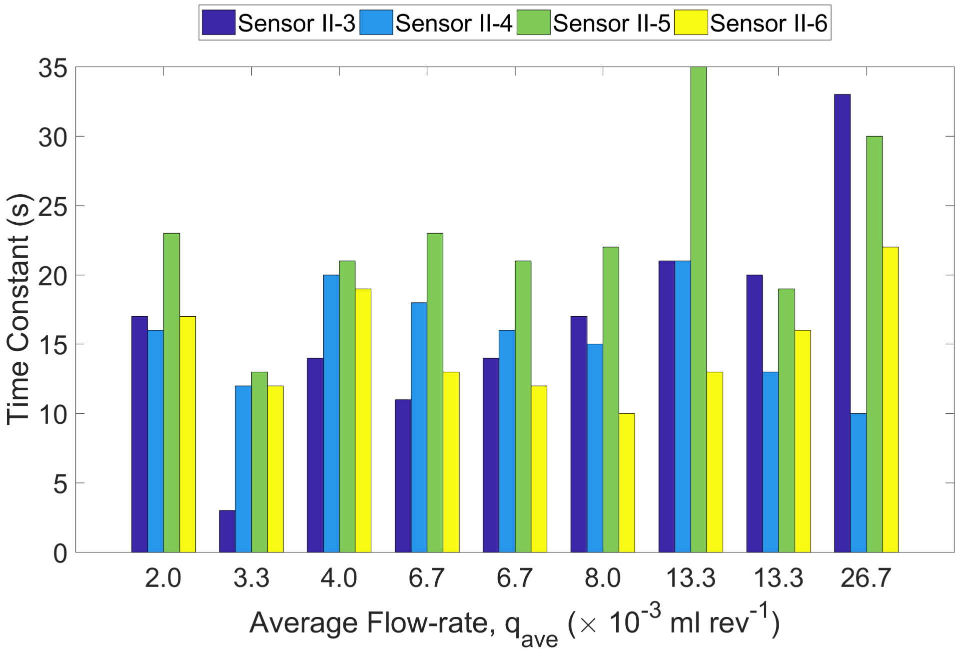

Figure 6.6: Time constant in seconds evaluated at transducer II-4, II-5, and II-6 over a range of average injector flow-rates

the velocity is greatest (the velocities at transducers II-3 to II-6 are 0.39 ms^{-1}, 0.62 ms^{-1}, 0.64 ms^{-1}, and 0.49 ms^{-1}). Additionally the oil-film thickness results suggest a thicker lubricant film near to the top of the stroke in the proximity of the lubricated area. Consequently, it appears a link may exist between the thickness of the lubricating film and the time constant.

The effect of average lubricant flow-rate is less apparent. The longest time constants are indeed towards the right-hand side of the graph where the lubricant flow-rate, and hence expected lubricant film-thicknesses are greatest. The average for the three greatest lubricant flow-rates is 21.1 seconds. At the lower flow-rates there appears to be less of an effect, with the averages being 15.6 seconds and 16 seconds for the lowest three and middle three flow-rates respectively.

6.4.2 Periodic Effects

Another aspect of the transient response are oscillations evident on the oil-film thickness graphs when lubricant is injected periodically. Figure 6.7 shows the oscillations following the frequency of lubricant injection (the graph with periodic injection every sixth cycle is shown separately for clarity). The markers on the graphs indicate the stroke on which lubricant is injected, with the peak occurring on the same or following upstroke. While there are likely to be transient effects due to several causes, such as contact between the piston-ring and cylinder liner, oscillation caused in this manner will likely be irregular (ie. at $t = 2$ seconds in figure 6.7a).

Figure 6.8 shows how the amplitude of the oscillations reduces as distance from the lubricated

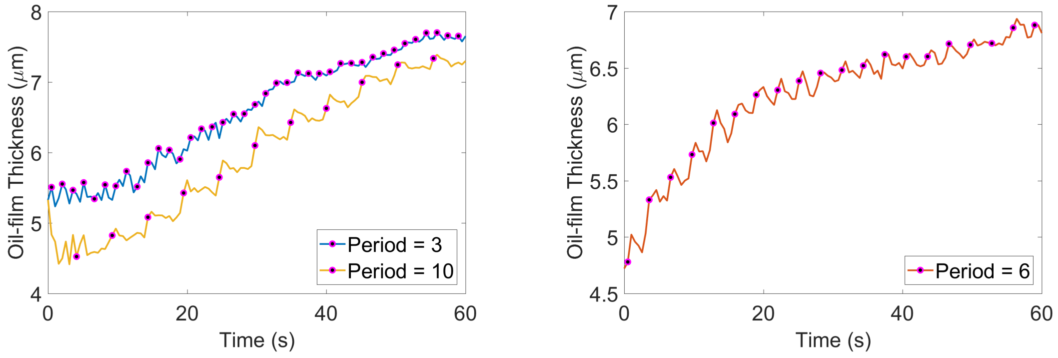

(a) Lubricant injection every 3rd and 10th cycle (b) Lubricant injection every 6th cycle

Figure 6.7: Periodic oil-film thickness oscillations at sensor IV-4 in response to periodic lubricant injection

area increases. Considering the lubricant is delivered to the top of the stroke it would be logical that once this has been more widely (and thinly) distributed the effects of the periodic injection is diminished.

Figure 6.9 shows the amplitude also varies at different circumferential positions. Lubricant is injected slightly above the sensors II-4 and IV-4, and these show noticeably larger scale oscillations than at the other two transducers. It is also interesting that transducers I-4 and II-4 are positioned either side of the thrust face, with transducers III-4 and IV-4 being 90° around the cylinder liner. With the amplitude of the oscillations being lesser at I-4 and II-4, it is apparent the thrust action of the piston suppresses the oscillations slightly. Certainly, the oscillations are at their most clear and most regular at sensor IV-4 which is both proximal to lubricant injection and without thrust action from the piston.

Inspecting the results at transducer IV-4 in more depth (figure 6.10a and 6.10b) shows the effect of lubricant injector flow-rate are minimal, certainly in the first half of the tests. In the latter stages, however, the amplitude of the oscillatory behaviour diminishes at the lower injector flow-rates as the oil-film thickness approaches a steady state. Lastly, the amplitude of the oscillations are greater on the upstroke than the downstroke. Again, with excess lubricant being transported to the top of the cylinder at the end of the upstroke

The cause of the oscillations in oil-film thickness becomes clear on inspection of the film extent during the first 30 seconds of tests at this sensor (figures 6.11a and 6.11b). In figure 6.11a spikes in the film extent can be seen approximately every five seconds (ie. at around 4 seconds, 9 seconds, 20 seconds). These results are from a test in which lubricant is injected every ten cycles, and since the engine speed is 120 rpm this equates to every five seconds. Additionally, from the injector signal data the first injection event is known to have occurred on the 9th cycle, which correlates with the first spike at $t = 4.5$ seconds.

Figure 6.11b shows results when the lubricant injection period was set to every third cycle.

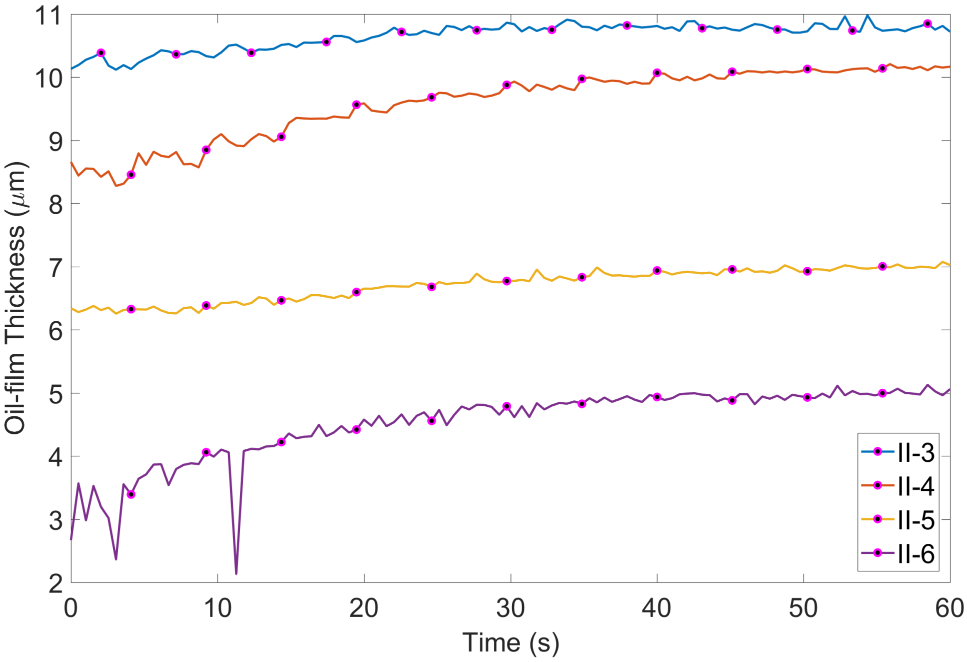

Figure 6.8: Periodic effects at different axial positions (period = 10)

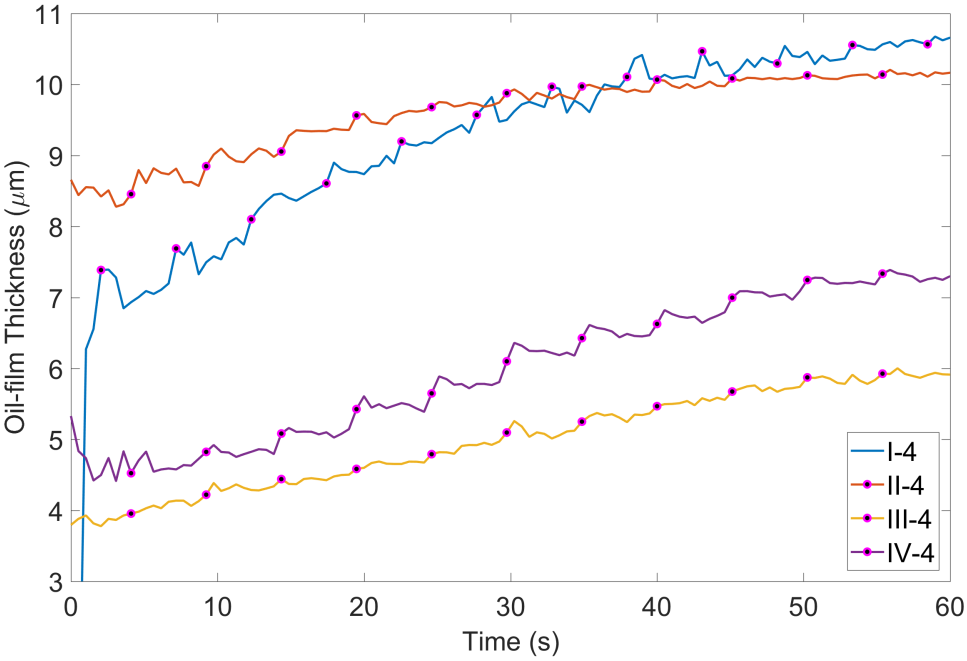

Figure 6.9: Periodic effects at different circumferential locations (period = 10)

Spikes of a similar magnitude to those in figure 6.11b are not present, even when the inlet boundary is near the centre of the piston-ring at the beginning of the test. There is still evidence of more frequent spikes at a smaller scale, however. This is more apparent during the first ten seconds of the test as the contact fills. Later in the test the magnitude of the oscillations becomes similar to those seen between injection events in figure 6.11a.

In all these cases, the amplitude of the oscillations is a fraction of the magnitude of change

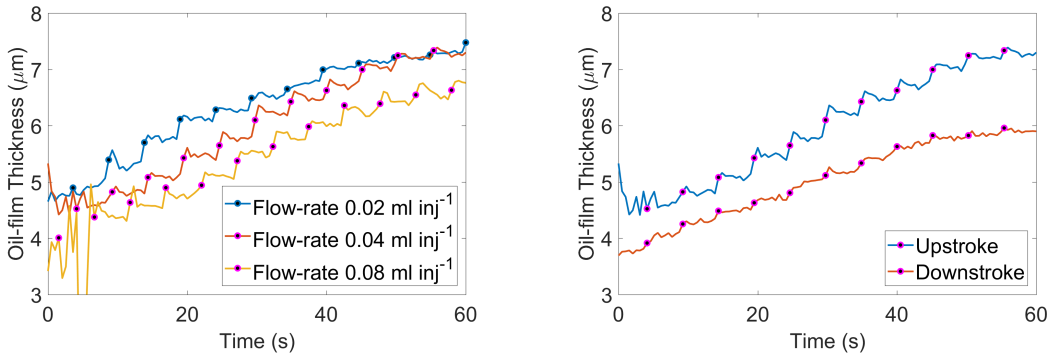

(a) Effect of flow-rate on Oscillations (b) Oscillations on upstroke and downstroke

Figure 6.10: Factors affecting the magnitude of oil-film thickness oscillations at transducer IV-4

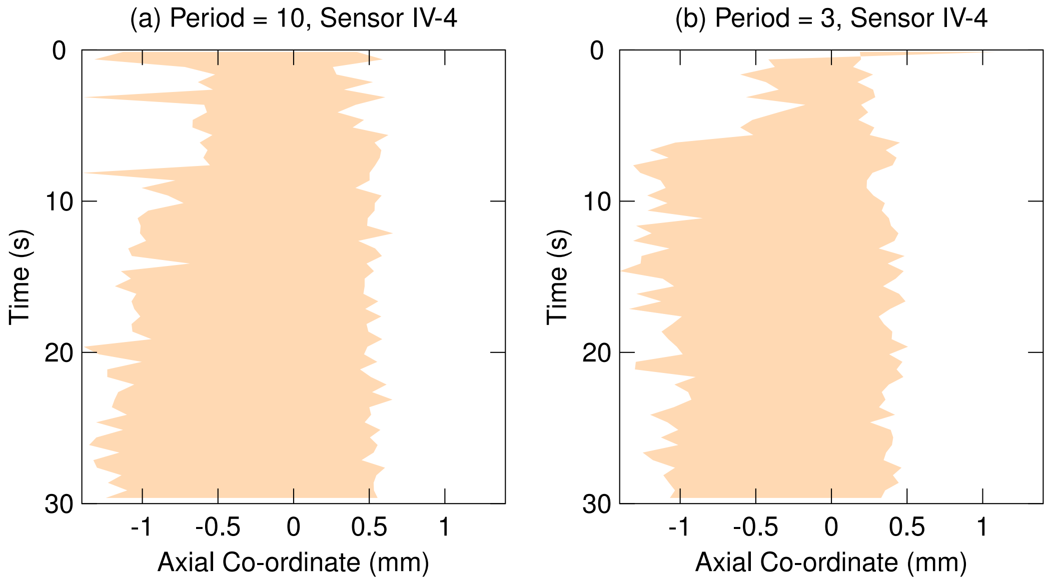

Figure 6.11: Upstroke inlet and cavitation boundaries taken every cycle : Flow-rate = 0.04 ml inj^{-1}

in minimum oil-film thickness between the start and end of the tests, with even the largest scale oscillations at sensor IV-4 having an amplitude less than one micrometer. In addition, this periodic transient behaviour is unlikely to have a significant effect on the first order system response discussed in section 6.4.1, with dynamic systems typically adhering to the principle of superposition. It is expected that lubricant consumption by evaporation would increase the magnitude of the oscillations, but with this not being a factor here this will need further experiments involving a firing engine.

6.4.3 Initial Oil-film Thickness, H

Many of the experimental results show an initial value of oil-film thickness of several micrometers. On figure 6.12b for example, at the higher flow-rate the oil-film thickness on the first stroke is almost seven micrometers. At the lowest flow-rate a fast rise from four to six micrometers is

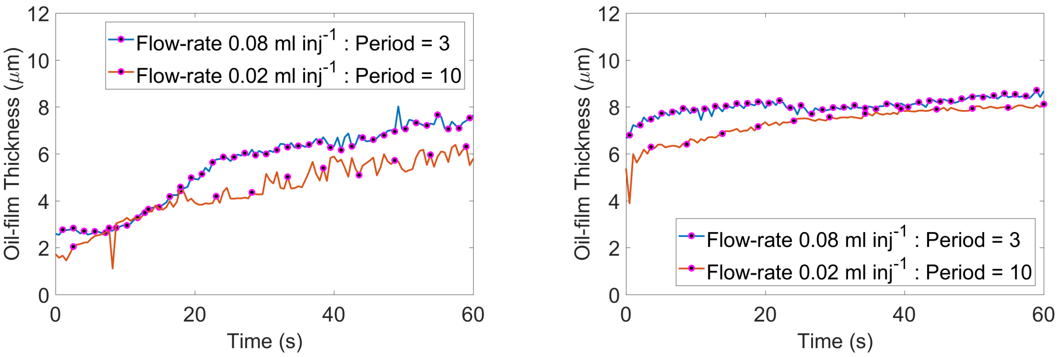

(a) Transducer I-6 (b) Transducer II-4

Figure 6.12: Comparison of oil-film at the highest and lowest average lubricant injector flow-rates, at transducers I-6 and II-4

apparent within the first three cycles. Considering the proximity of transducer II-4 to the lubricant injected onto the cylinder liner, it is likely that lubricant is very quickly transported to this part of the cylinder liner in sufficient quantity to support the piston-ring hydrodynamically. At the lower average injector flow-rate this takes two additional cycles compared to the higher flow-rate, due to the volume of injected lubricant being lower. The first order response follows this initial, fast increase in oil-film thickness.

At transducer I-6 there is also an initial oil-film thickness, here approximately two micrometers. This value is close to the lower limit for fluid film lubrication (LLFFL) for these surfaces (the cylinder liner has average roughness, $R_a = 0.42$, and the piston-ring has $R_a = 0.12$). At the higher lubricant injector flow-rate (0.08 ml inj^{-1}, period = 3), a steady rise in oil-film thickness follows, before a knee in the graph where the gradient reduces at $t = 22$ seconds. The gradient at the lower injector flow-rate (0.08 ml inj^{-1}, period = 3) is also low. However here there is no knee apparent, which could be due to the flow-rate being so low that the two phases of the response merge.

Transducer II-4 is approximately 10 mm below the location where lubricant is injected, while transducer I-6 is more distant at 70 mm below and 45° (approx. 40mm) around the cylinder liner. While the injected lubricant can be scraped down to transducer II-4 by the piston-ring very quickly from slightly higher up the stroke, the flow-rate of lubricant to I-6 relies on circumferential flow caused by hydrodynamic pressure differentials as the piston-ring passes. As such the flow of lubricant to this part of the cylinder liner is much lower and the initial phase of the response occurs more slowly. While the proposed first order model also could be used to fit these results, a two component model (with characteristics for the faster and slower elements of the response) may be more appropriate to account for the more prolonged increase in the rate of lubricant transport at transducers more distant from the area where lubricant is injected.

As discussed in section 5.3.3, in regions of the cylinder near to where lubricant is injected the change in lubricating film thickness is likely to be more sudden than at areas more distant. As such there is the possibility a visco-elastic stiffening of the lubricant forces the more sudden changes in oil-film thickness seen at transducers in these areas. Further work would be useful to investigate these effects further.

6.5 Discussion

A time constant characterising the response in oil-film thickness has been determined at four of the transducers in block II (II-3 to II-6), with those towards the centre of the stroke being longer than those towards the ends of the stroke. This increase could be linked to the development of a thicker lubricant film at midstroke, which due to the constant load and viscosity, would tend to occur in this part of the stroke where the velocity is highest. In the engine used for these tests velocities are greatest between sensors II-4 and II-5. Figure 6.13 shows how the lubricant film develops from a volume concentrated near top dead centre, to a more fully developed oil-film. Once the film becomes more developed the thickest region is towards midstroke.

At transducer II-3, the time constant appears to be longer with increasing lubricant injector flow-rate. This trend is not apparent at the other transducers. With lubricant being injected onto transducer II-3 it is likely the oil-film thickness nears its maximum very quickly, and the results in figure 6.1 agree with this. Subsequently, the time constant evaluated for this transducer, particularly at the injector higher flow-rates, is for an oil-film thickness response that is near steady-state, and as such may be affected.

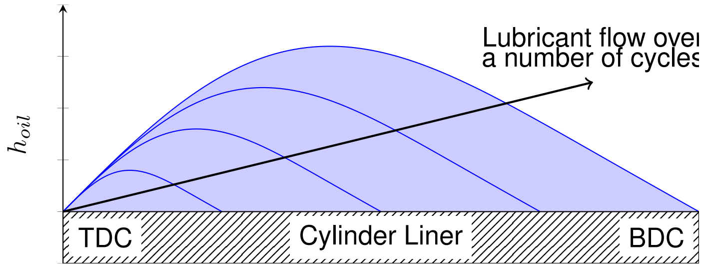

Figure 6.13: Development of lubricant film thickness on the cylinder liner

Conversely, while the use of the coefficient H to account for the fast rise in oil-film thickness at the beginning of the tests is adequate in many cases, more distant from the injected lubricant it does not appear to fit so well. This may be due to the rate of lubricant transport varying at different transducer locations.

Conservation of mass for a control volume (6.14) at a location on the cylinder liner can be expressed as in equation 6.2. The lubricant density is considered to be constant, and thickness of the lubricant film denoted as h_{oil}. As the piston-ring passes there is lubricant flow into and out of the control volume. Axially, this is primarily due to the scraping of lubricant ahead of the piston-ring. While there may also be some lubricant flow resulting from the hydrodynamically generated pressure differential, this is likely to be small compared to the lubricant flow caused by the scraping action of the piston-ring. Circumferentially the lubricant flow is caused only by the pressure differential.

$$\rho A \frac{dh_{oil}}{dt} + \rho q_{out_{ax}} + \rho q_{out_{circ}} = \rho q_{in_{ax}} + \rho q_{in_{circ}} \tag{6.2}$$

Near to the injected lubricant (ie. near the top of the stroke and in line with the block II transducers), and early in the test when the thickness of the control volume (h_{oil}) is thin, the mass flow of lubricant into the control volume due to the scraping action ($q_{in_{ax}}$) will be relatively high. The piston-ring inlet is likely to be fully flooded, and the initial increase of oil-film thickness relatively high and relatively fast. Some of this lubricant will subsequently be scraped out of the control volume ($q_{out_{ax}}$) in the same manner, with the difference remaining in the control volume being equal to the lubricant flow past the piston-ring. This net flow of lubricant into the control volume is the sum of the Couette and Poiseuille flow, as shown in equation 3.18, and as such is a function of the oil-film thickness on a given pass, piston-ring velocity, viscosity, and the pressure differential in the axial direction.

At some point during the downstroke the excess lubricant being transported by scraping becomes entirely consumed. This will occur further down the stroke on each subsequent cycle as the lubricant film on the cylinder liner develops. Initially, at the lower end of the stroke (but still in line with block II), there will be no lubricant flow into the control volume, although this will begin to increase as the test continues. The rate of this increase will be lower more distant from the injected lubricant. On figure 6.1b, for example, the effect of this change in the rate of lubricant transport can be seen as a lower gradient at transducer II-6 than at II-3 near the beginning of the tests.

Around the cylinder liner from the location of the injected lubricant (ie. in block I) there is no flow into the control volume from lubricant scraping until sufficient lubricant has been transported due to the pressure differential ($q_{in_{circ}}$ and $q_{out_{circ}}$). This is likely to occur earlier near the top of the

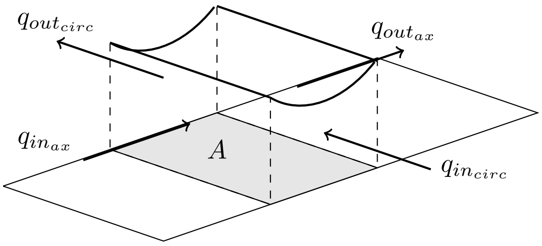

Figure 6.14: Lubricant film control volume

stroke than the bottom (where squeeze action augments the circumferential flow) with lubricant scraping commencing once the thickness of the lubricant film is sufficient. This will lead to a lower rate of increase again in the thickness of the lubricant film.

While this initial phase of the response in oil-film thickness appears to change in different areas of the cylinder liner, the first order fit equation still appears to adequately model the second part of the response. This second phase may be due to the continued filling of the piston-ring circumferentially, which (as seen in the video evidence presented in chapter 5) occurs quickly near the top of the stroke where there is a relatively thick lubricating film, but more slowly elsewhere. With the oil-film thickness response at transducers I-4, I-5, and I-6 appearing to continue beyond the end of the test, this supports the idea the lubricant film is continuing to develop circumferentially. The circumferential filling will also lead to increases in the oil-film thickness at transducers in block II, and the latter phase of the response may result from this. The effects of squeeze action at the extremes of the stroke should help to accelerate this by generating a greater pressure differential, leading to an increase in Poiseuille flow, and consequently higher time constants near midstroke. This would fit the trend seen in the time constant results at most lubricant injector flow-rates.

There was no clear effect on the time constant resulting from changes in average lubricant injector flow-rate, which perhaps occurs because the lubricant injector flow-rates are still relatively high. This leads to the rapid development of the lubricant film over the stroke where transducers II-3 to II-6 are located, to the form shown in figure 6.13, with the piston-ring very quickly becoming fully flooded. A lack of oil-consumption through evaporation will also contribute to this effect. Consequently, the form of the response in oil-film thickness seen at each transducer is very similar regardless of the lubricant injector flow-rate, since the lubricant film builds quickly (relative to the length of the tests) to the same steady-state value. It is expected a lower average lubricant injector flow-rate would lead to clearer differentiation between the steady-state oil-film thickness (H_0).

While the above response to lubricant flow is the dominant feature of the response, an oscillatory behaviour was also observed where the oscillations occurred at the same frequency at which lubricant was injected. In these tests the magnitude of these oscillations were small relative to the first order response discussed above. In an operational engine, however, lubricant consumption through evaporation may lead to an increase in the oscillations. This would likely be the case in large two stroke marine diesel engines where lubricant is often delivered every four or five cycles. Ideally, an investigation of these effects using an operating marine diesel engine, leading perhaps to a frequency response analysis, would be helpful to understand the significance of this secondary component to the transient response. The motivation being that the oscillations could, given small oil-film thicknesses and a larger amplitude, lead to contact between the piston-ring and cylinder liner. Before performing this investigation using a marine engine it may be prudent to conduct a feasibility study using a suitable piston-ring lubrication model.

6.6 Conclusions

A two-part transient behaviour in oil-film thickness occurs following a step change in lubricant injector flow-rate.

1. The primary aspect of the behaviour is a first order rise in response to the change in lubricant availability.
2. The second aspect of the behaviour involves periodic oscillations in oil-film thickness at a frequency matching that of the periodic lubricant injection. The oscillations reduce in magnitude towards the thrust face.

Near to the injected lubricant, the first order rise takes the form shown in equation 6.3, with the time constant being the key parameter of the response. This time constant appears to be a function of the axial co-ordinate, due to an increase in the rate of circumferential filling near top and bottom dead centre due to squeeze action. The development of a thicker lubricant film around midstroke also influences the time constant.

There is a fast initial response in oil-film thickness due to an increase in axial film extent. Near to the injected lubricant this increase can be represented as a step change, H. At transducers near the bottom of the stroke, and around the cylinder from the injected lubricant, the step change in oil-film thickness is less appropriate due to a lower rate of lubricant transport to this part of the cylinder. Here a ramp component could be used to precede the first order rise.

There is no clear pattern in the time constants over the range of (relatively high) lubricant injector flow-rates used.

Periodic lubricant injection leads to changes in the position of the inlet boundary, which leads to oscillations in piston-ring oil-film thickness at the same frequency. This could be incorporated into equation 6.3 by using a sinusoidal (or similar) multplier. However, it has been omitted as the nature of the behaviour is not yet fully understood.

$$h_0 = \begin{cases} H, & \text{if } t < T \\ H + H_0\left(1 - e^{-\frac{t-T}{\tau}}\right), & \text{otherwise} \end{cases} \tag{6.3}$$

Chapter 7

Axial and Radial Oil-transport in the Cylinder

7.1 Introduction

Lubricant transport is a key factor for piston-ring lubrication in large marine diesel engines because of localised lubricant delivery to a limited area of a large cylinder liner. It is apparent from the results of chapters 5 and 6 there is a time delay for the transport of oil from the delivery point to other areas where lubricant is needed, which can impact both the lubrication of the piston-rings as well as neutralisation of the fuel sulphur content. Inadequate piston-ring lubrication can lead to increased rates of wear due to both of these factors, resulting in reduced time between overhaul for the components involved.

The purpose of this investigation is to examine the rate at which lubricant is transported around a cylinder liner, and the factors affecting this. In order to achieve this only one lubricant injector was used to allow the development of the oil film from the injected area to be examined.

7.2 Method

A series of tests were carried out using the equipment described in chapter 4. For these tests lubricant was sprayed onto the cylinder liner from a single lubricant injector, and the oil-film thickness monitored using the transducers installed in the cylinder liner in the arrangement shown in 4.19. The tests were repeated using lubricant injection to two different locations (position A and position B) in order to effectively widen the instrumented coverage of the liner from 45° to 135° (figure 7.1). For the first lubricating position (position A) the transducers in block II are in line with the lubricant, and those in block I are 45° circumferentially around the cylinder liner. For the second lubricating position (position B) the transducers in block II are 90° circumferentially around the cylinder liner from the injected lubricant, and those in block I are 135° around the cylinder liner. For clarity, the axial position of the transducers will be referred to as S1, S2, and so on. The same lubricant injector is used to inject lubricant at both position A and position B. The tests have been carried out at two injector flow-rates (0.04 ml inj^{-1} and 0.08 ml inj^{-1}) and two frequencies of injection (every third cycle, ie. period = 3, and every sixth cycle, ie. period = 6).

An algorithm has been used to extract the minimum oil-film thickness on each upstroke and downstroke from the recorded transducer data. This allows the time dependency of oil-film thickness to be analysed, with availability of lubricant at the transducer locations being indicated by

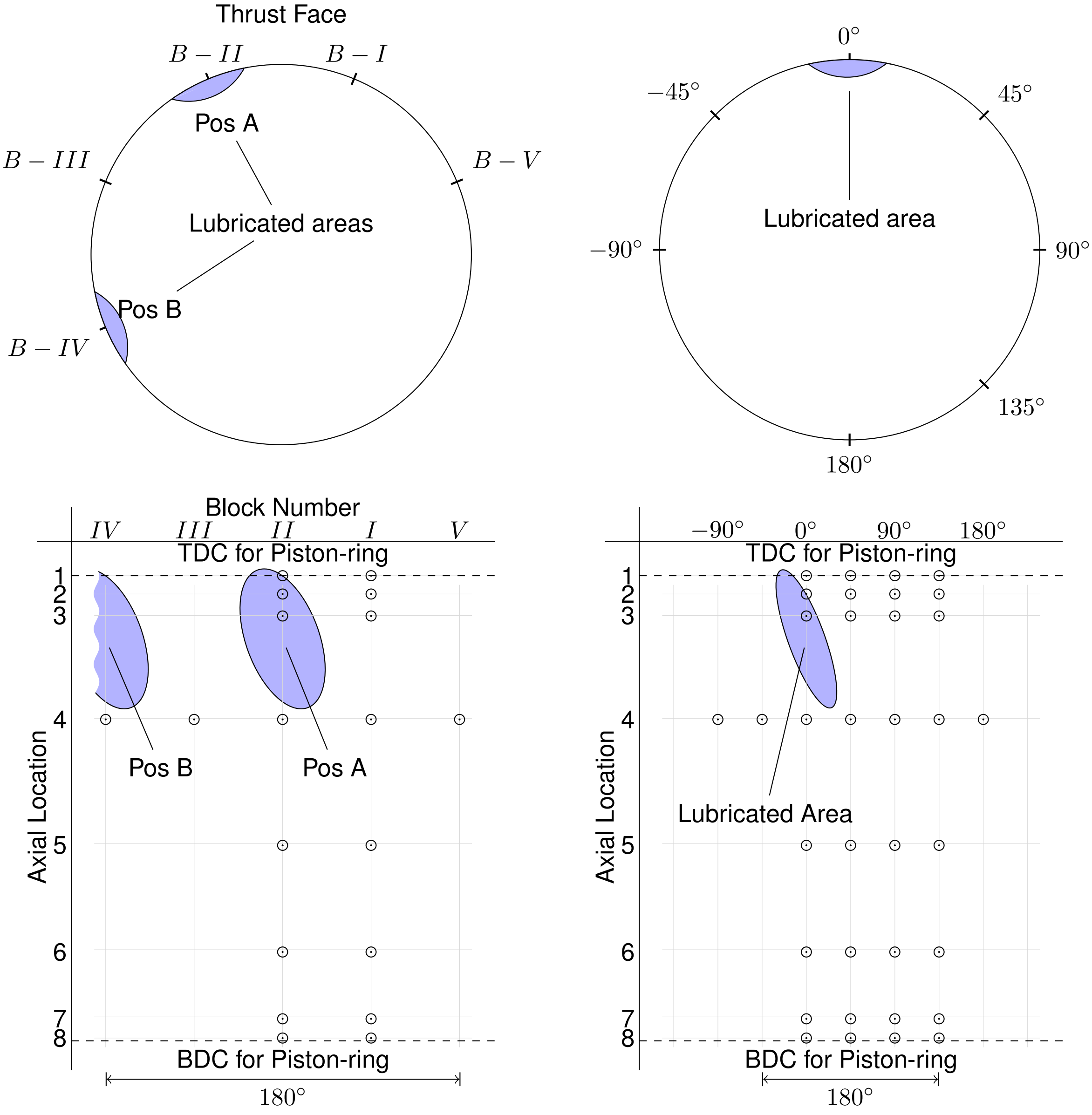

(a) True lubricant and transducer locations

(b) Relative transducer locations

Figure 7.1: Location of lubricant injection and sensors

notable changes in the oil-film thickness. The results for many of the transducers show initial contact between the piston-ring and cylinder liner, indicated by highly unsteady minimum oil-film thickness measurements at a relatively low oil-film thickness. At some transducers this is different due to their being slightly recessed into the cylinder liner. In either case, lubricant is considered to be available for lubricating the piston-ring once the oil-film thickness begins to rise. The timings of the change in conditions were recorded.

Additionally, piston-ring signals from the logged transducer data have been compared to a simulated signal representing the true profile of the piston-ring, where a change in the inlet boundary from near the centre of the piston-ring towards the leading edge is considered to be an indication that lubricant has been transported to that part of the cylinder.

Evidence from video footage taken from some of the tests was also utilised to help confirm the results based on the above methods.

7.3 Results

7.3.1 Minimum Oil-film Thickness

Figure 7.2 shows the oil-film thickness from measurements taken on the upstroke at sensor I-6 and II-6, which related to an axial position 82 mm below top dead centre. Each line on the graph represents a different position circumferentially around the cylinder liner, with the legend outlining how far around these are from the injected lubricant. The 0° and 90° positions are recorded by transducer II-6, and 45° and 135° by transducer I-6.

At the start of the tests, measurements from each transducer are different by approximately two micrometers, which is thought to be due to the calibration process from each sensor. Accounting for this, there are clear rises (marked A and B on the figure) from the initial datum at the 0° and 45° positions, at $t = 20$ seconds and $t = 30$ seconds. Considering the distance of these positions from the injected area, and that the cylinder liner is thoroughly cleaned and dried prior to each test, it is logical to conclude these increases are due to the arrival of lubricant at these locations. Of course it could also be that because the piston-ring is relatively stiff, an increase at one location also contributes to an increase at the second location. The characteristics of the increases in oil-film thickness at these transducer locations have the form of a first order response.

At the 90° and 135° positions there is a less marked change. It appears there is an increase at the former at around $t = 45$ seconds (marked C), while at the latter (marked D) there is no apparent evidence that lubricant reaches this part of the cylinder liner.

Figures 7.3 and 7.4 both show a number of these results sets, where again each line is a graph of minimum oil-film thickness changes in time (all tests were 60 seconds in length). These

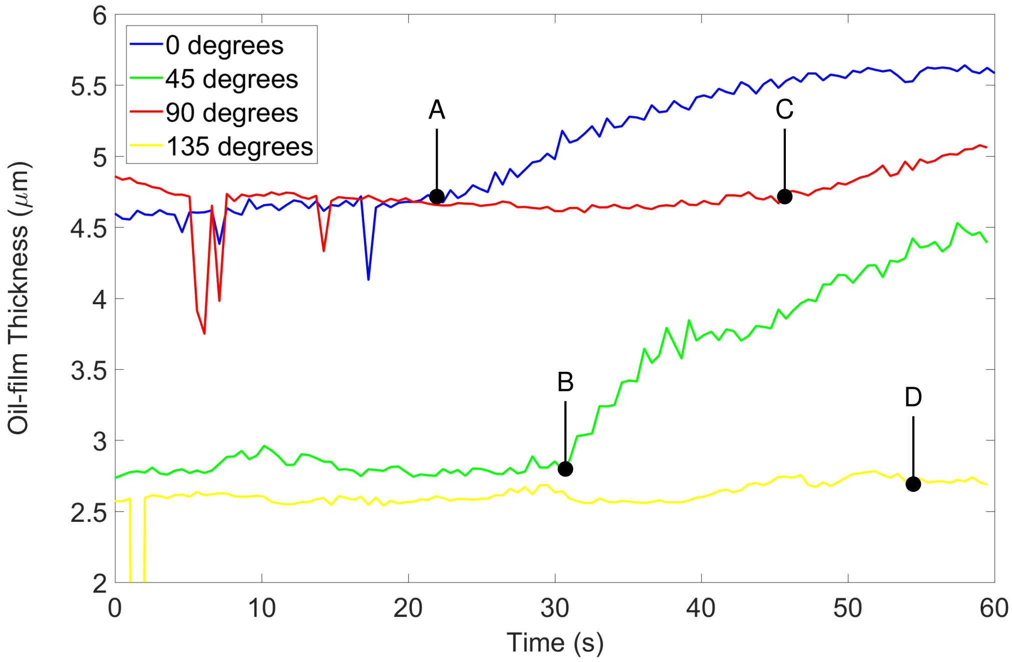

Figure 7.2: Upstroke minimum oil-film thickness around the cylinder liner at sensor S6, for lubricant injection with a period = 3

are arranged to show the oil-film thickness on both the upstroke and downstroke (from left to right) at a number of crank angle positions relating to when the piston-ring passes a transducer. The different lines at each sensor location show oil-film thickness at four circumferential positions at increasing distance from the point of lubricant injection (0°).

Taking the transducer at S5 in figure 7.3 as an example, the blue line shows the oil-film thickness at the same circumferential co-ordinate as the injected lubricant, albeit further down the liner. Here there is a step change in oil-film thickness just prior to 15 seconds into the test ($t = 15$ seconds) following a period of highly fluctuating values. Moving around the cylinder liner 45°, here the green signal shows a change at approximately 30 seconds into the test. At 90° around from the injected area the rise in oil-film thickness commences at about $t = 45$ seconds, shown by the red signal. Finally, 135° around from the injected area the yellow line shows no clear change throughout the test.

The signals are particularly noisy before their rise in oil-film thickness, partly due to the oil-film thickness data being more unpredictable when contact occurs, due to oscillations of the signal as the piston-ring is dragged along the cylinder liner in the absence of effective lubrication. Figure 7.5 shows one such signal for early during the test at the higher flow-rate. Markers have been included to highlight the position of the datapoints. In the area around the minimum oil-film thickness, the signal is briefly consistent with the sawtooth appearance that is often recorded when contact occurs between piston-ring and cyliner liner. It would be expected the signal becomes smooth

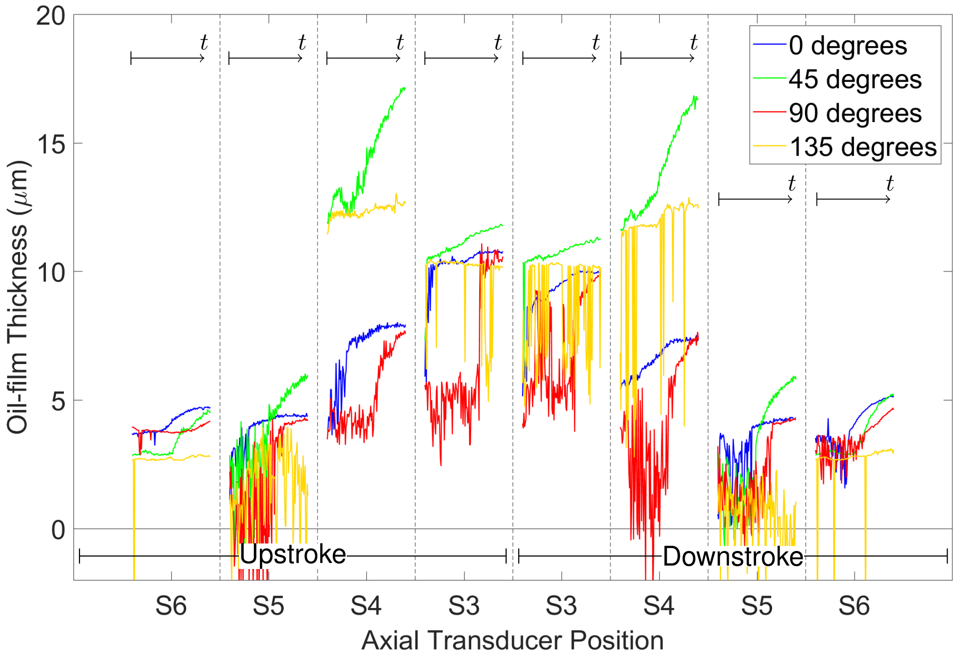

Figure 7.3: Minimum oil-film thickness development at a number of axial and circumferential locations : Flow-rate 0.04 ml inj^{-1} : Period = 3

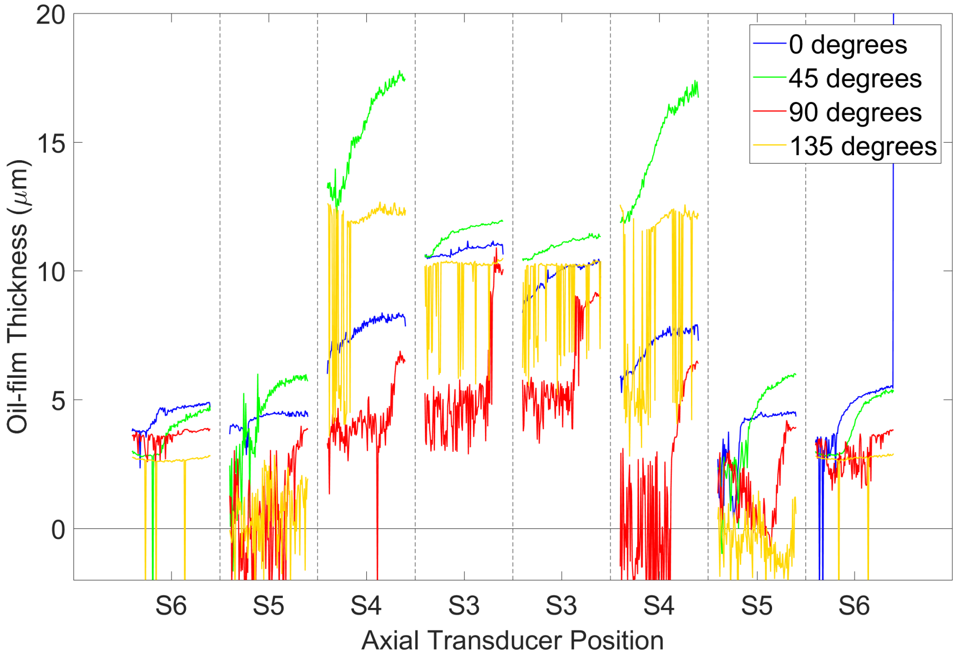

Figure 7.4: Minimum oil-film thickness development at a number of axial and circumferential locations : Flow-rate 0.08 ml inj^{-1} : Period = 3

either side of this where the separation is greater, but this is not the case. With lubricant being limited around most of the circumference of the cylinder liner, the piston-ring could be subjected to sudden movements resulting in this behaviour. Figure 7.5 shows how the signal changes with the presence of lubricant, becoming smoother around the centre of the piston-ring.

There is also a disparity in the results for transducer S4 (31 mm below top dead centre).

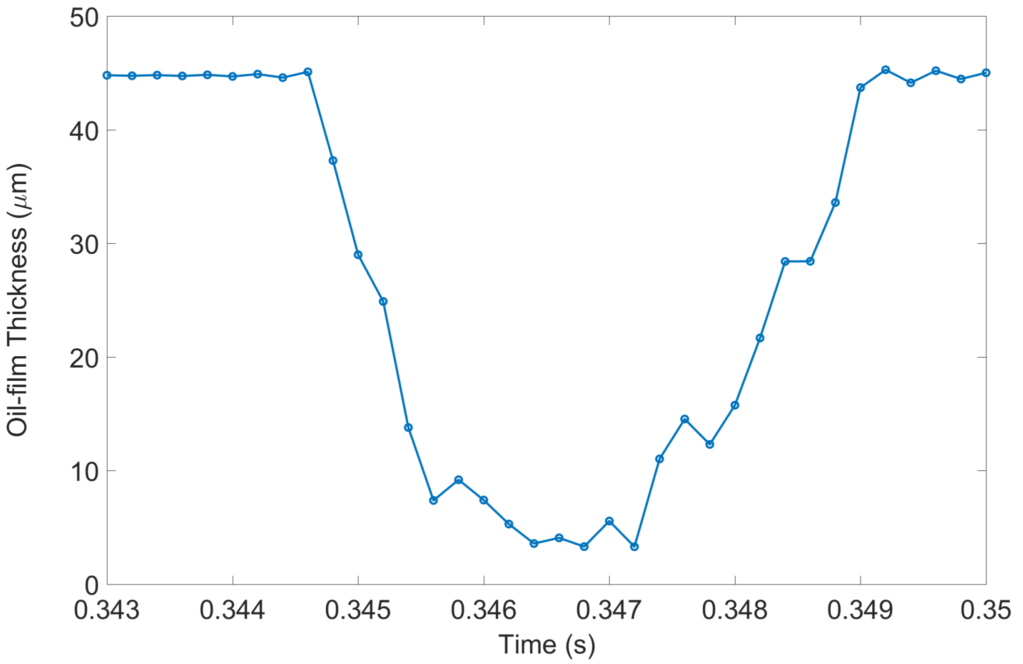

Figure 7.5: Noisy measurements of minimum oil-film thickness at sensor II-4 resulting from contact between piston-ring and cylinder liner

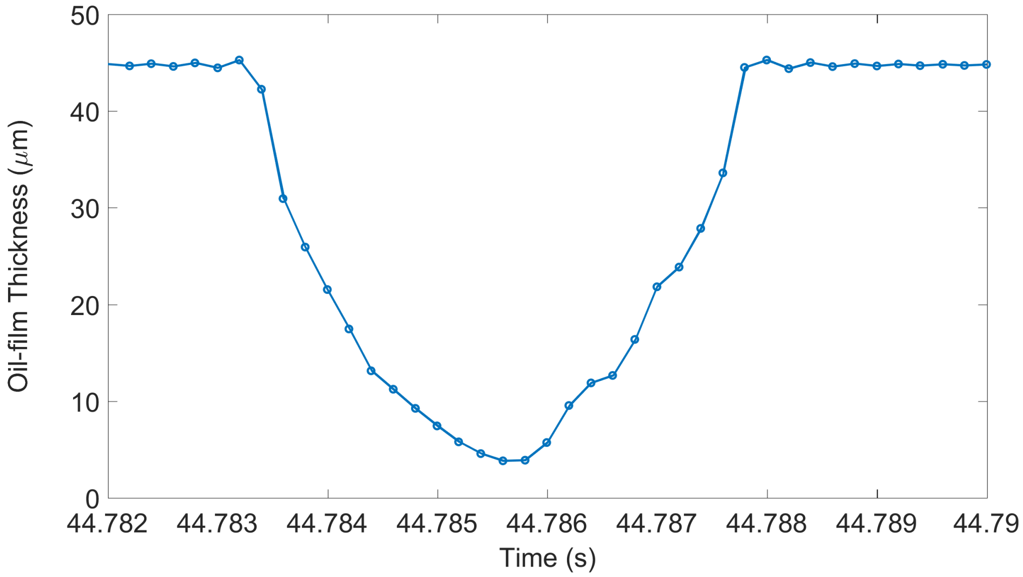

Figure 7.6: A more typical oil-film thickness signal at II-4 as lubricant becomes available

The two higher signals correspond to the block I transducer, while the lower signals are from the block II transducer, suggesting a difference between the two transducers. Results from these transducers were acquired using the same amplifier channel, and as such the discrepancy must results from the offset values applied for one or both of these sensors.

As discussed in chapter 4, the offset values were determined both prior to and after the experiments using white-light interferometer scans of a replica taken at each transducer location.

	Sensor I-4	Sensor II-4
Pre-test	2.7	1.1
Post-test	5.0	-2.2

Table 7.1: Offset values for sensor I-4 and II-4

Generally the post-test offsets have been applied. The pre- and post-test offsets are shown for these transducers in table 7.1. While the difference between the offsets prior to testing was only 1.6μm, afterwards it was 7.2μm - which is roughly the difference between the results from each sensor. Although the quality of the scans for these transducers appeared to be good, if one of the replicas was compromised (ie. through stretching) it could adversely affect the scans and lead to this discrepancy. It should not, however, affect the values of oil-film thickness relative to an initial datum.

In other respects the oil-film thickness results show evidence of behaviour that is more expected. As before, oil-film thicknesses increase away from top dead centre where velocity is higher - until the limit of lubricant availability is reached. The changes in oil-film thickness are generally greater in the mid-stroke region than near the dead centres. Examining the results for different flow-rates, rises in oil-film thickness appear to occur in most cases a little sooner for each higher flow-rate - for example at transducer S6 the step change on the upstroke moves from around $t = 25$ seconds to $t = 10$ seconds as the rate of lubricant supply increases.

7.3.2 Evaluating the Rate of Lubricant Transport

The oil-film thickness data from all sensors has been inspected closely to determine the timing of any rises in oil-film thickness. These results are shown in tables 7.2 and 7.3. In some cases several results are recorded at a single cylinder location, due to the multiple transducers at S4 and the change in location of the lubricated area. Where there is no evidence of lubricant reaching the sensor this is indicated as '-'. If it was not possible to determine the timing the table has been left blank.

As an example, at the lower flow-rate of 0.04 ml inj^{-1} the rise seen in oil-film thickness at S6 (82 mm below top dead centre) occurs at $t = 26$ seconds, while at the higher flow-rate this occurs at $t = 16$ seconds. Circumferentially, the increases at a position 45° around from the injection location occur in the region of $t = 30$ seconds at the lower flow-rate, and after about $t = 20$ seconds at the higher flow-rate. Moving further, to 90° around from the injected area the timings appear to be converging as there is less than 5 seconds difference between the two flow-rates.

The results generally follow a trend suggesting the time it takes for lubricant to reach the transducers increases as their distance from the lubricated area increases. Which is of course

	Angle from Injected Area						
Sensor	-90	-45	0	45	90	135	180
3			6	3	42		
4	9/23	12/14	14	27/28/16	38/34	30	48
5			14/26	30	41		
6			26	30	40	40	
8			-	-	-		
POS A	IV	III	II	I	V		
POS B			IV	III	II	I	V

Table 7.2: Timing (in seconds) of lubricant availability based on oil-film thickness changes - flow-rate 0.04ml inj^{-1}

	Angle from Injected Area						
Sensor	-90	-45	0	45	90	135	180
3			0	8	40/53	55	
4	42/27	8/7	10	28/8/10	39/21/20	-	-
5			14	20	46	-	
6			16	23	40	-	
8				35		-	
POS A	IV	III	II	I	V		
POS B			IV	III	II	I	V

Table 7.3: Timing (in seconds) of lubricant availability based on oil-film thickness changes - flow-rate 0.08ml inj^{-1}

logical. Considering that a quarter of the circumference is 77.1 mm and the stroke length 101.2 mm, transport occurs more quickly axially than it does circumferentially. In fact at both flow-rates the lubricant extends to all the transducers at 45° and 90° around the liner at very similar times.

Some of the values in the tables do not appear to be consistent, for example the 3 seconds taken for lubricant to be transported 45° around the liner at the sensor 3 position. Figure 7.3 shows the oil-film thickness rising steadily from very early during the test. It is possible this increase in oil-film thickness is due to the increase in oil-film thickness at the sensor proximal to the lubricated area, rather than an indication of lubricant at this sensor. Looking closely there is a very slight step increase at halfway through the test that could be the arrival of lubricant. This too corresponds to a change in oil-film thickness at the lubricated area however, so the cause cannot be confidently stated. The result at an angle of 135° from the injected area could be caused in a similar manner.

Several of the sensor 4 measurements at both injector flow-rates vary considerably, for example at the same relative location it appears to take as little as 8 seconds, or up to 28 seconds for lubricant to extend to 45° around the cylinder liner from the lubricated area. Similar results occur further around the cylinder liner at both injector flow-rates. It tends to be that the longer timing is for lubricant injection to position B, from where the lubricant must move towards the thrust face. Conversely, for lubricant delivery to position A, the transport of oil is generally away from the thrust face. As such it appears the thrust action of the piston against the cylinder liner hastens lubricant transport away from this area.

7.3.3 Result Verification Using Film Extent

In order to verify whether the above rises seen in oil-film thickness were due to the availability of lubricant, the piston-ring signals were inspected against the true ring shape. This allowed the starvation boundary to be examined. Examples of these signals for the above tests are shown in figures 7.7 and 7.8. These are taken from results for the transducers at S4, where (a) to (d) show signals at increasing circumferential distance from the region of lubricant injection. Only signals at 20 second intervals are shown, although signals at 2.5 second intervals were inspected.

Figure 7.7a for example, shows that all the signals after the initial cycle follow the true ring shape, suggesting fully flooded conditions. The oil-film thickness signal in figure 7.3 suggested this occured at $t = 14$ seconds, while the signals in figure 7.7a indicated lubricant availablity at $t = 16$ seconds. Continuing around the liner, figures 7.7b and 7.7c show the timing at 45° and 90° was later, occurring between 20 and 40 seconds, and between 40 and 60 seconds respectively. Figure 7.7d shows that lubricant never reached the transducer at a circumferential location of 135°

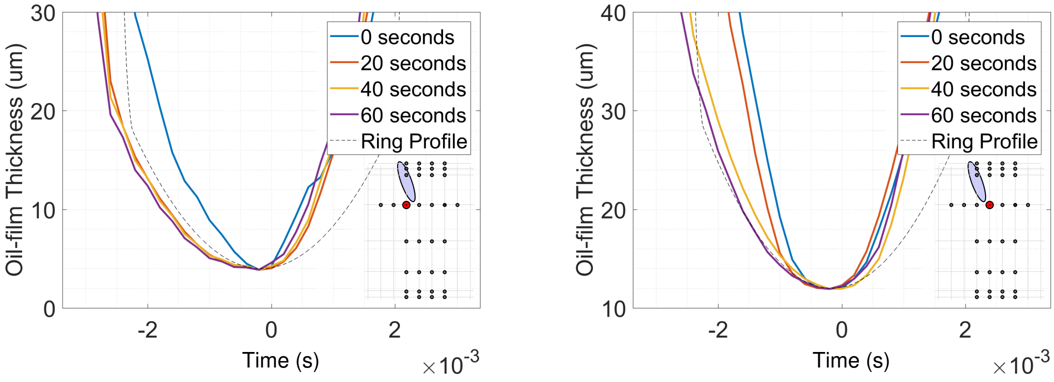

(a) 0° from injection point (b) 45° from injection point

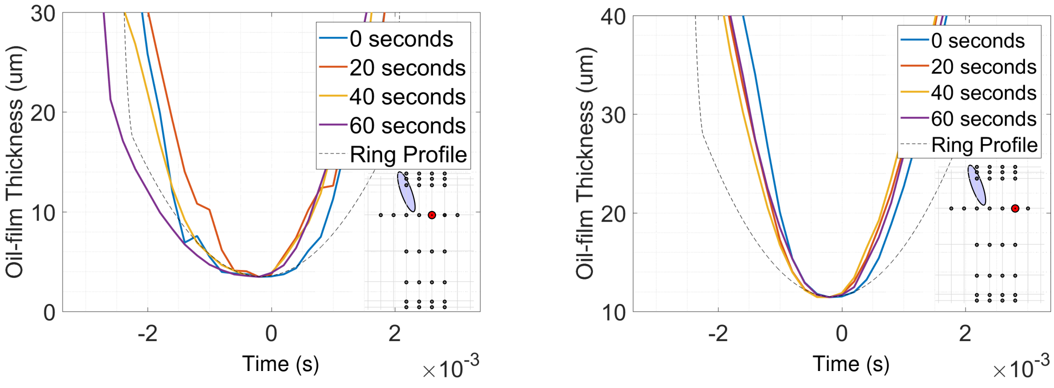

(c) 90° from injection point (d) 135° from injection point

Figure 7.7: Ring signals at S4: Flow-rate = 0.04 ml inj^{-1}, Period = 3

from the injection point.

The results shown in figure 7.8 show a similar trend. Lubricant is available just below the injection region almost immediately in this case (figure 7.8a). At 45° (7.8b) lubricant availability occurs again between 20 and 40 seconds. This time however, the true timing appears to be at $t = 17$ seconds as opposed to the 27 seconds it takes at the lower flow-rate. Again, figure 7.8d shows lubricant never reaches 135° around the cylinder liner. Figure 7.8c is maybe less clear. The jagged nature of the signals are evidence of contact between the piston-ring and transducer. Only the 60 second signal does not show this, here the signal follows the ring shape from the apex of the ring face towards the leading edge, before diverging upwards. This shows there is lubricant available but not in a quantity necessary to fully flood the piston-ring.

As with the timings taken from the piston-ring signals, the results from this analysis are shown in tables 7.4 and 7.4. Where there is no evidence of lubricant reaching the sensor this is indicated as '-'. If it was not possible to determine the timing the table has been left blank. This was the case with the sensors I-6 and II-6 at a flow-rate of 0.04 ml inj^{-1}.

The two results for sensor S4 (31 mm below top dead centre), 90° around from the lubricant spray, are quite dissimilar. However they correlate closely with the timings obtained from the

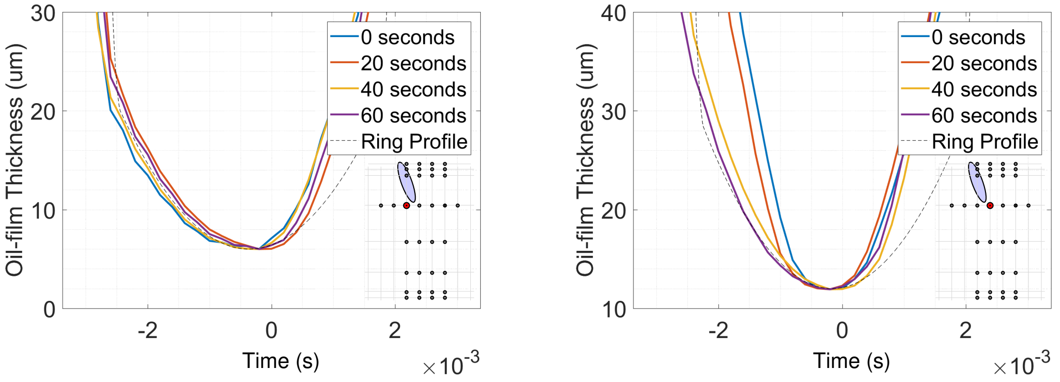

(a) 0° from injection point

(b) 45° from injection point

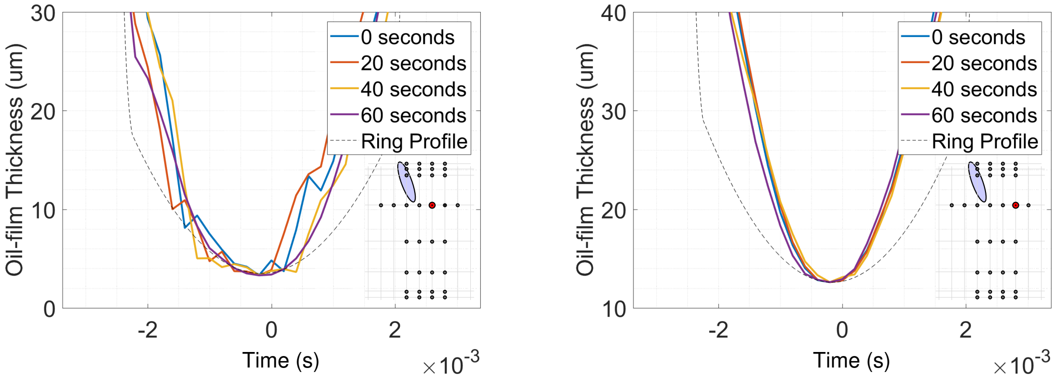

(c) 90° from injection point

(d) 135° from injection point

Figure 7.8: Ring signals at S4: Flow-rate = 0.08 ml inj^{-1}, Period = 3

	Angle from Injected Area						
Sensor	-90	-45	0	45	90	135	180
S3			5	22	42	-	
S4	35	22	16/20	27	35	-	-
S5			17	32	40	-	
S6							
POS A	IV	III	II	I	V		
POS B			IV	III	II	I	V

Table 7.4: Timing of lubricant availability based on piston-ring signals - flow-rate 0.04ml inj^{-1}

	Angle from Injected Area						
Sensor	-90	-45	0	45	90	135	180
S3			0	10	50	-	
S4	47	12	0	17	45/25	-	-
S5			0	10	50	-	
S6				10	50	-	
POS A	IV	III	II	I	V		
POS B			IV	III	II	I	V

Table 7.5: Timing of lubricant availability based on piston-ring signals - flow-rate 0.08ml inj^{-1}

minimum oil-film thickness ($t = 39$ seconds and $t = 20$ seconds). As with the timings obtained from changes in oil-film thickness, the difference is thought to be due to the thrust action of the piston, with the faster timing being recorded when lubricant was being transported away from the thrust face. The piston-ring signals are presented in figure 7.9, and show that while there is evidence of some lubricant being available at this time, it is highly starved, and intermittent (ie. the 12.5 second, 37.5 second, and 50 seconds signals).

7.3.4 Result Verification Using Video Footage

In order to further confirm these results, evidence has been taken from video footage of the tests. Extracts from these videos are shown in figures 7.10 and 7.11. These stills show two regions of lubricant film in most cases, a thicker film near top dead centre, and a thinner film that is evident further down the stroke. This latter film is difficult to see, although the cavitation fingers help to visualise this.

At the lower flow-rate of 0.04 ml inj^{-1}, the extent of the thicker film at $t = 15$ seconds (figure 7.10a) is almost at 45° circumferentially around the cylinder, and approximately 25 mm below top dead centre. The thinner film appears to extend to around 40 mm below top dead centre. The circumferential transport is in agreement with the results in table 7.4, in fact it is very close for the case where lubricant is injected to position A - where lubricant is transported away from the thrust face. The axial transport evidence from the piston-ring signals suggested lubricant

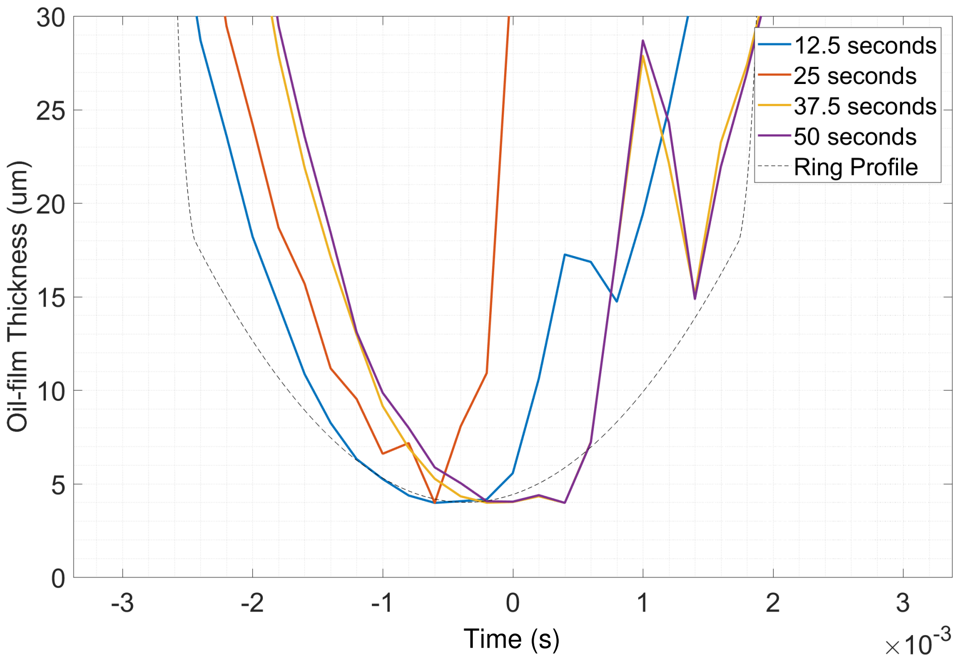

Figure 7.9: Ring signals for sensor V-4: Flow-rate = 0.08 ml inj^{-1}, Period = 3

extended to this point just after this time, at $t = 16$ seconds. Since a 2.5 second interval was used for inspecting these signals, and the oil-film thickness changes in table 7.2 suggest it occured at $t = 14$ seconds, then it can be accepted that the video and the data agree.

At $t = 30$ seconds (figure 7.10b) the thicker film has extended further, to approximately 60° around from the lubricant spray. Here the thinner film is down to at least S6 transducer (82 mm below top dead centre). This time there is a full correlation with the data collected from the oil-film thickness and the inspection of piston-ring signals. Given the data suggests the lubricant extends to 90° around from the injected area at around $t = 40$ seconds, again this agrees with the video evidence in figure 7.10b, which shows the film extent just beyond this point at 45 seconds.

Likewise, at the higher flow rate the extent of the thicker lubricant film circumferentially at $t = 15$ seconds (figure 7.11a) is just reaching 45°, at $t = 30$ seconds (figure 7.11b) is nearing the 90° transducer, and at $t = 45$ seconds (figure 7.11c) has passed it. Axially, this thicker film sits between the S3 and S4 transducers until 45 seconds, at which point it sits just above the sensor at this point. No notable change in oil-film thickness is seen despite the proximity of this thicker film to the transducer. The thinner film can just be seen to have passed the S5 sensor at $t = 15$ seconds, and certainly beyond the S6 sensor at $t = 30$ seconds.

Once more this agrees strongly with the data collected in tables 7.2 to 7.5, providing important information about the lubricant transport, and validation of the analysis performed using the oil-film thickness data.

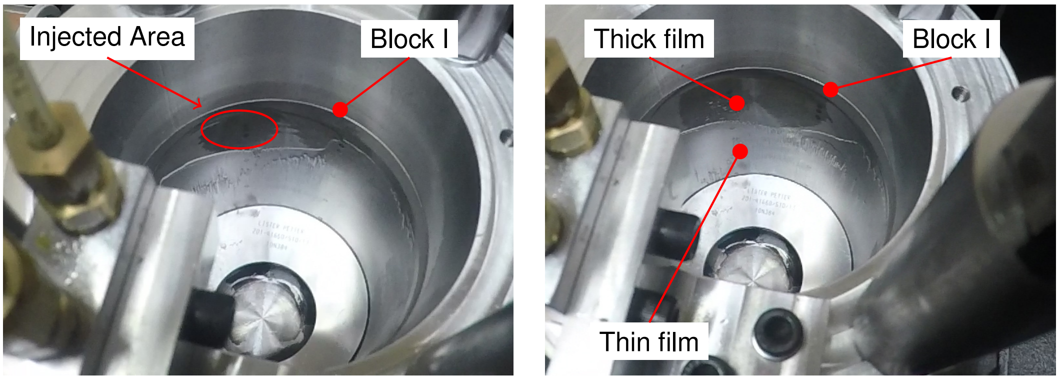

(a) t = 15 seconds (b) t = 30 seconds

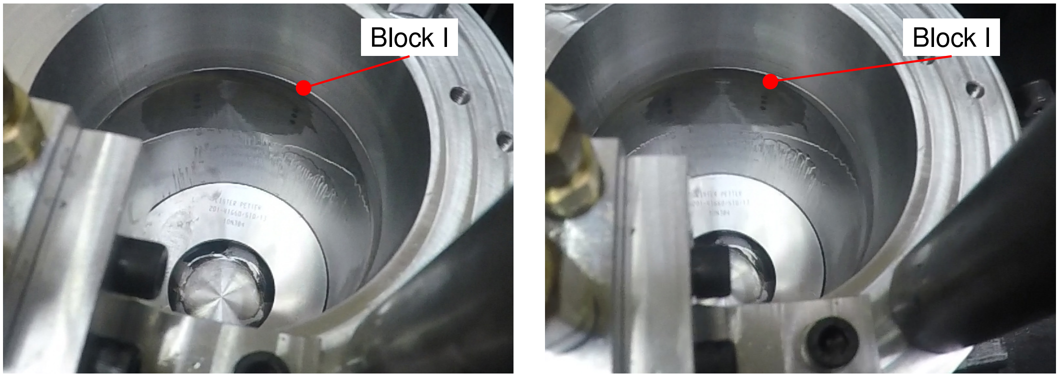

(c) t = 45 seconds (d) t = 60 seconds

Figure 7.10: Video stills: Flow-rate = 0.04 ml inj^{-1}, Period = 3

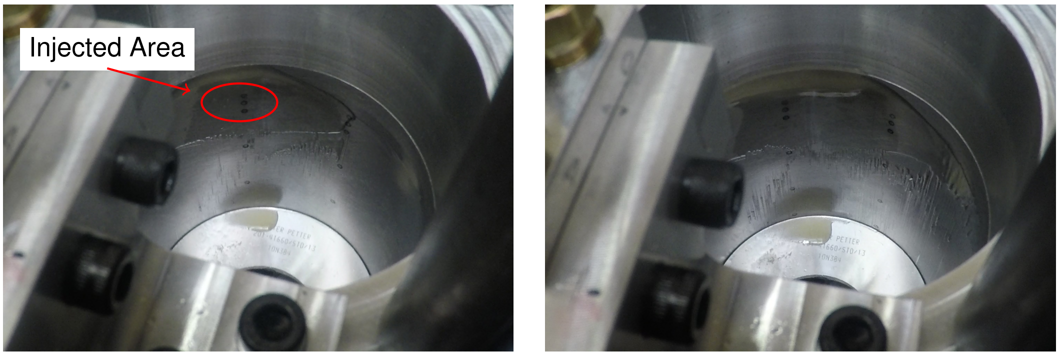

(a) t = 15 seconds (b) t = 30 seconds

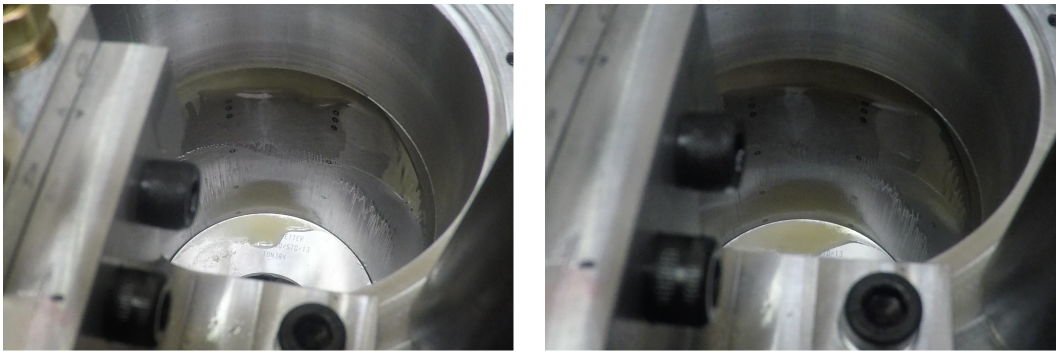

(c) t = 45 seconds (d) t = 60 seconds

Figure 7.11: Video stills: Flow-rate = 0.08 ml inj^{-1}, Period = 3

7.4 Discussion

Using the results in tables 7.2 and 7.3, the lubricant transport at a number of time intervals can be mapped (figures 7.12 and 7.13). These maps show contour lines representing the extent of the lubricant film on the cylinder liner at ten second intervals. The co-ordinates for the contour lines have been determined by interpolating the information from the tables for the timing at each transducer location.

Where there were duplicate results at a given location with different timings, this was resolved by taking an average of the highest and lowest values. Where there was a third result this was discarded to prevent weighting the average towards one or other of the injector positions (ie. which relate to lubricant transport being either towards or away from the thrust face).

Figure 7.12 shows the development of the lubricant film on the cylinder liner at the lower lubricant injector flow-rate of 0.04 ml inj^{-1}. The lubricant appears to be transported axially more quickly than it is circumferentially, however the axes on the diagram are not equal. Looking at the 20 second contour, the circumferential distance around the cylinder liner from 0° to 45° is 40 mm, which is comparable to the axial distance of 58 mm to sensor position S5. It appears that for the lower lubricant flow-rate the coverage at twenty seconds extends halfway down the stroke, and around a quarter of the circumference. At forty seconds it covers half of the cylinder liner, extending to near bottom dead centre and 90° either side of the lubricated area circumferentially.

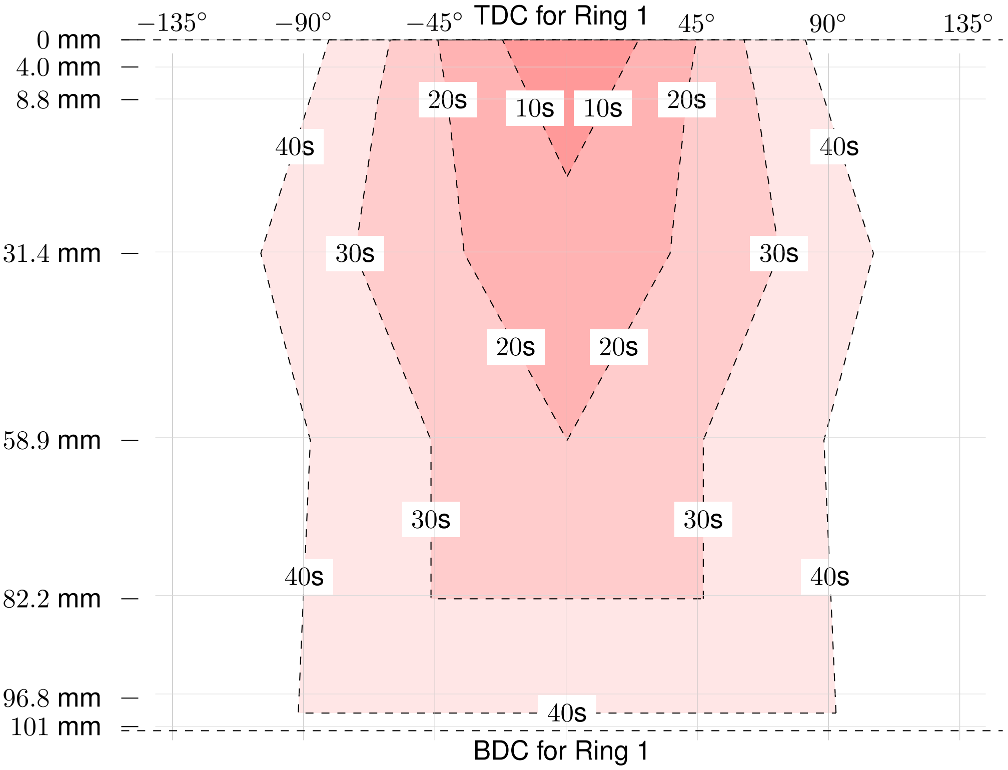

Figure 7.12: Map of lubricant transport : Flow-rate 0.04 ml inj^{-1} : Period = 3

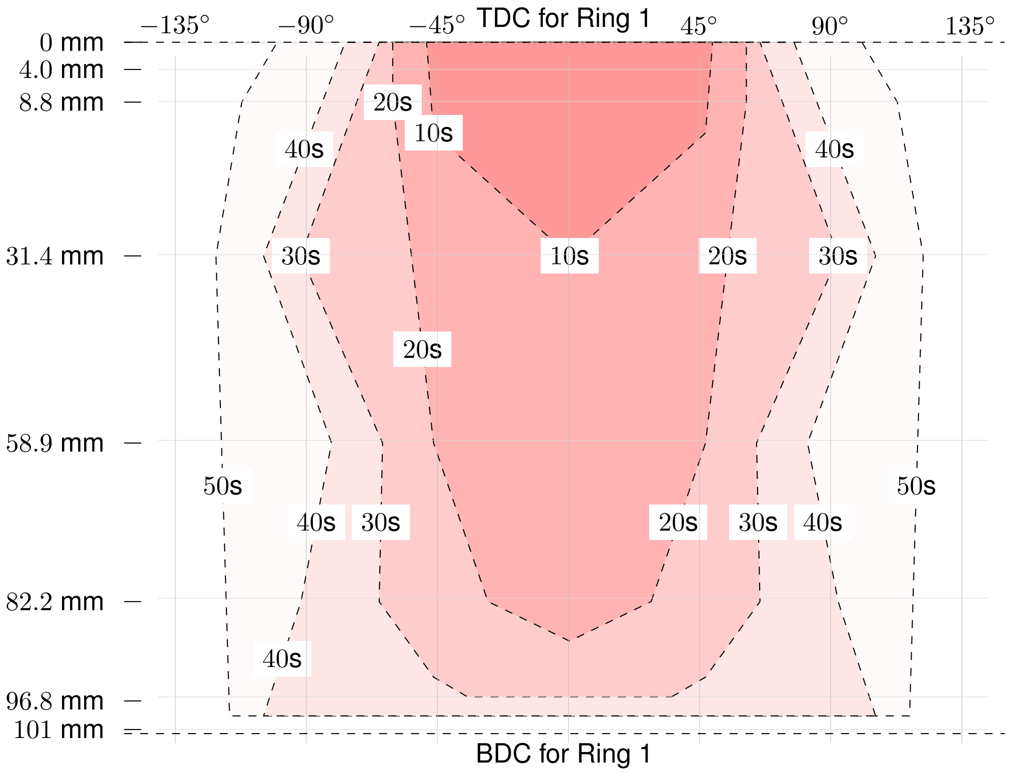

Figure 7.13: Map of lubricant transport : Flow-rate 0.08 ml inj^{-1} : Period = 3

At the higher injector flow-rate (0.08 ml inj^{-1}) the lubricant appears to be transported approximately 50% more quickly. Axially, lubricant is beyond 80 mm down the cylinder liner after 20 seconds, whereas at the lower flow-rate it was nearer 55 mm. Circumferentially too, the lubricant is at around 60° here but was at 45° at the lower flow-rate. The rate of lubricant transport is in the region of fifty percent faster again. Beyond this, lubricant transport appears to slow, since by forty seconds the coverage is similar to how it was at the lower flow-rate.

The times deduced for lubricant to become available at each transducer have been plotted (figure 7.14) against a scaled parameter for the rate of cylinder liner coverage per unit volume of lubricant injected (D/q_{ave}). The average injector flow-rate (q_{ave}) is defined as the average quantity of lubricant injected per engine cycle. The distance from the point at which lubricant is injected is denoted D. For the above tests lubricant was injected every third cycle, so an injector flow-rate setting equal to 0.04 ml inj^{-1} equates to a true injected flow-rate of 0.013 ml per engine cycle. In addition to the data discussed above, the results of an additional two tests at a lower injection period are included in the plot.

$$T = 1.31 \times 10^{-5} \left(\frac{D}{q_{ave}} \right) - 2.3 \tag{7.1}$$

A trendline has been fitted to the data giving equation 7.1 ($R^2 = 0.64$). While there are some data points that deviate from this line, these tend to be further into the tests, and for the data

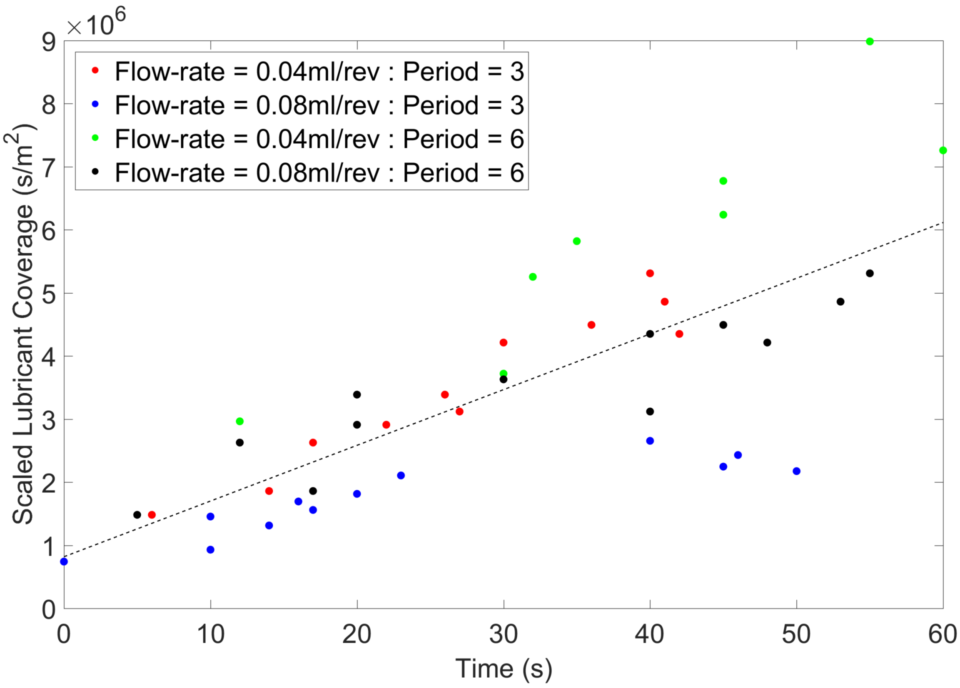

Figure 7.14: Scatter plot of time taken for lubricant to reach a transducer against the inverse of the lubricant coverage parameter

points from the transducers most distant from where lubricant is injected. It may be that the rate of lubricant transport reduces as it extends further around the cylinder, such as 90° either side of the injected area. Another cause for the relatively low correlation is that transport axially and circumferentially is caused by different mechanisms. Axially, lubricant exceeding the volume required to fully flood the piston-ring is transported through a scraping action by the piston-ring when the inlet is fully flooded. This is not the case circumferentially, where it is dependent only on the hydrodynamic pressure differential generated as the piston-ring passes. Subsequently, transport in this direction is much slower.

Considering the consistency of units for equation 7.1 it is likely the coefficient will be a function of some length scale (bore diameter, or piston-ring geometry). It would likewise be logical to assume viscosity and engine speed are also factors that could influence the coefficient.

With lubricant being transported through more than one mechanism (ie. scraping of the lubricant ahead of the piston-ring, and resulting from differentials in the hydrodynamic pressure field), and considering the magnitude of changes in piston-ring velocity and oil-film thicknesses over the course of an engine stroke, the correlation of data to this equation is good. In order to develop the investigation further it would be necessary to perform experiments over a much wider range of the variables of influence, potentially following the application of dimensional analysis and even the development of a specialist test-rig. It is possible that a relationship such as that in equation 7.1 is adequate for predicting lubricant transport in marine engines, since there is typically eight lubricant injectors. Consequently, the required lubricant need only be transported 45° around the cylinder liner which is within the region of figure 7.14 with better fit. Trials on a large marine diesel engine would be needed to determine whether this is true.

7.5 Conclusions

A method has been developed for mapping changes in the lubricant film in the cylinder following a change in lubricant supply and thus assessing the the rate of lubricant transport axially and circumferentially. While this can be done by comparing piston-ring signals with a simulated ring profile, it can be more efficiently inferred from changes in oil-film thickness.

Time delays between lubricant injection and transport to different areas of a cylinder liner can be relatively long, leading to poorly lubricated conditions in parts of the engine stroke normally associated with satisfactory oil-film thicknesses and minimal asperity contact.

Rates of lubricant transport follow an approximately linear relationship to the ratio between the distance from the lubricated area and the average lubricant injector flow-rate. This is true up to around 90° either side of the lubricated area.

Lubricant transport away from the thrust face occurs at a higher rate than lubricant transport towards it.

Chapter 8

Validating a Model for Oil-film Thickness Development

8.1 Introduction

Simulation plays an integral role in modern engineering for a number of reasons. Key among these are that testing of complex systems can be performed at low risk and at relatively low cost. Additionally, simulation can support experimental investigations, providing detailed examination of physical effects that are difficult to measure.

A piston-ring lubrication model has been developed (described in chapter 3) to simulate the developing oil-film thickness in an engine subjected to periodic lubricant injection. Lubricant delivery leads to a non-uniform distribution of oil that is subsequently transported axially through a scraping action of lubricant in excess of that needed to flood the piston-ring.

In this chapter, results from the experiments and the model are compared.

8.2 Method

The development of oil-film thickness for the engine used in the experiments has been simulated over a range of lubricant injector flow-rates. As with the experiments, only the compression ring was in the model, with geometrical parameters such as the ring-face profile, connecting rod and stroke length, and cylinder bore diameter being incorporated. Lubricant viscosity was considered constant at 0.375 Pa.s (the viscosity of the Motaquip 20W-50 mineral oil at room temperature), and cylinder pressure constant at atmospheric pressure. A nominal lubricant-film thickness of 0.8 micrometers was distributed evenly over the cylinder liner at the start of each simulation to enable the model to run.

The distribution of lubricant on the cylinder liner following an injection event was set to approximate that of the experiment, as shown in figure 8.1.

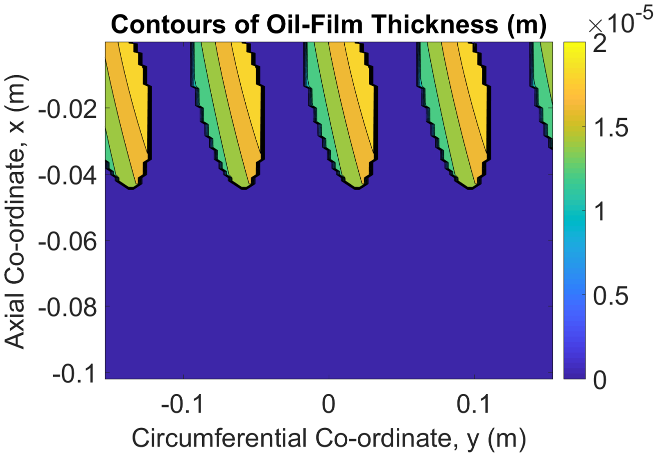

Figure 8.1: Distribution of lubricant following injection event at flow-rate 0.04 ml inj^{-1}

The model calculated oil-film thickness at every crank angle based on a quasi-static equilibrium of forces. The convergence criterion between piston-ring load and hydrodynamic pressure was set at 0.2%, while the convergence criteria for the computed pressure and degree of filling residuals in the flow-continuity algorithm were set to 0.002% and 0.001% respectively.

Experimental results used in this chapter are taken from chapters 5, 6, and 7, with the methods used to obtain these results being described in the respective chapters.

8.3 Validation of Piston-ring Lubrication Model

As with any simulation of physical phenomena, the validity of the results is dependent on the assumptions and simplifications made regarding the physics during implementation of the model. While this lubrication model has previously been verified against Reynolds equation, as well as empirical results for load carrying capacity (see chapter 3), a further validation of the time-variation of oil-film thickness, inlet boundary, and lubricant transport is necessary. The following results and discussion aim to validate these aspects of the piston-ring lubrication model.

8.3.1 Minimum Oil-film Thickness

Figures 8.2 and 8.3 show minimum oil-film thickness for both experimental and simulated results at two lubricant injector settings - 0.01 ml/rev and 0.04 ml/rev. Each line is a plot of oil-film thickness against time, with results being shown for a number of transducers in both block I and block II (between 4 mm and 100 mm below top dead centre). Results from the model are also shown.

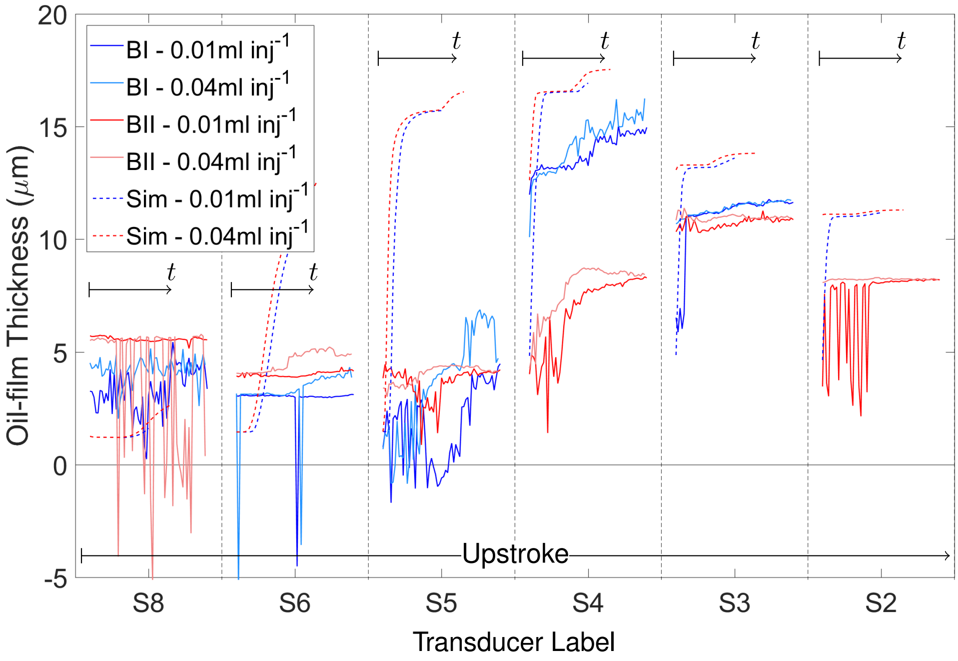

Figure 8.2: Time-variation of minimum oil-film thickness on upstrokes at axial transducer positions 2 to 8 (dashed = predictions, solid = experimental)

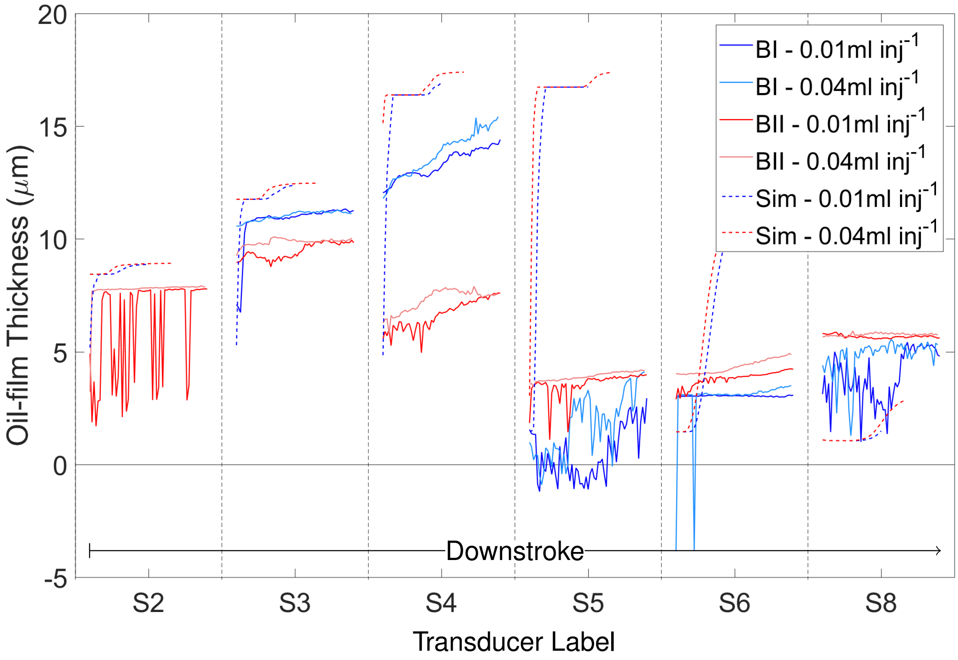

Figure 8.3: Time-variation of minimum oil-film thickness on downstrokes at transducer positions 2 to 8 (dashed = predictions, solid = experimental)

The model assumes the piston-ring and cylinder liner to be concentric, consequently there is only a single graph at each flow-rate. The transducer label (ie. S4) therefore represents only the axial position for the simulated results, being the axial co-ordinate correspondent with transducers I-4 and II-4. Figure 8.2 shows results for the upstroke, and figure 8.3 the downstroke.

In figure 8.2 both simulated and experimental results show greater oil-film thicknesses in the upper part of the stroke than the lower. This is a consequence of the top of the cylinder being sprayed with lubricant and therefore having much thicker lubricant film. While the experiment and simulation show close agreement throughout for the upper part of the stroke, with oil-film thickness increasing with distance from top dead centre as the velocity increases, as the tests progress the simulation shows the oil-film thickness further down the stroke climbs considerably more than seen in the experimental results. The exception here is at transducer location S8 (2 mm above bottom dead centre), where the simulated oil-film thickness returns to a value similar to that of the experiment.

The results from the model suggest the oil-film thickness rises from 2 μm to over 15 μm at S5 as lubricant is transported down the cylinder liner. The experimental results on the other hand show a change of much lower magnitude (0 μm to 6 μm at S5). The voltage signal from the transducer is shown in equation 4.17 to be inversely proportional to the area of the capacitor plate, which in the case of the oil-film thickness transducers is the electrode. In some cases the electrode is known to smear during honing, increasing its area and effectively reducing the measured oil-film thickness. It is possible the transducer electrodes at S5 and S6 have smeared in this way, more so perhaps than near the top of the cylinder, thus compressing the results. Heating of the injected lubricant from the warm cylinder may lead to lower than expected viscosity in the experiment and thus predicted oil-film thicknesses greater than those measured. This heating effect will have a greater effect on smaller volumes of lubricant due to their having lower thermal inertia. The subsequent reduction in viscosity may be an additional cause for lower oil-film thicknesses seen in the experimental results, and is not accounted for in the predicted oil-film thickness due to the isothermal assumption.

Another factor which may cause such a difference is the manner in which the model handles axial lubricant transport. The model assumes that lubricant being transported axially maintains its circumferential co-ordinate. In the experiment, however, as the piston accelerates, a body of fluid being transported may be expected to spread to some extent. As such the model may predict faster axial lubricant transport, and slower circumferential lubricant transport, than seen in the experiment.

Figure 8.4 shows the predicted development of the lubricant film on the cylinder liner for a test replicating those of chapter 7. The lubricant film can be seen to quickly extend axially throughout the stroke. While there is some circumferential development of the lubricant film further down the stroke, this is the result of lubricant being scraped from near the injected lubricant rather than from pressure driven flow. Further up the stroke there is very little development of the lubricant film in the circumferential direction. The lubricant supply parameters of the model were set at a flow-rate equal to 0.04 ml inj^{-1}, with periodic injection every third cycle.

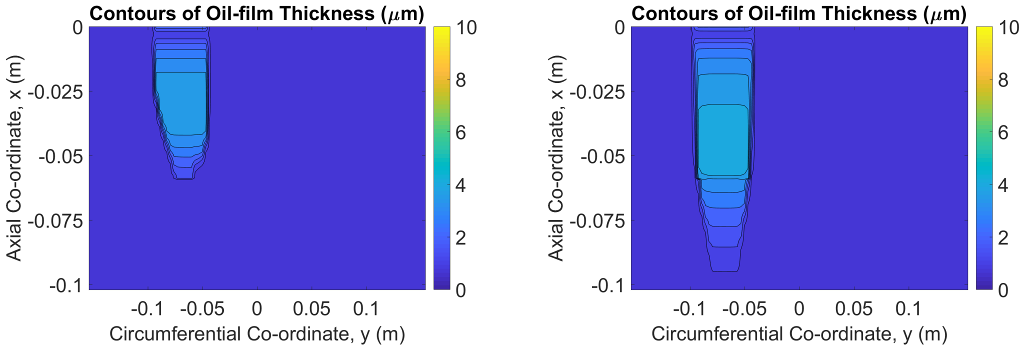

(a) 1st Cycle ($t = 0$ s)

(b) 10th Cycle ($t = 5$ s)

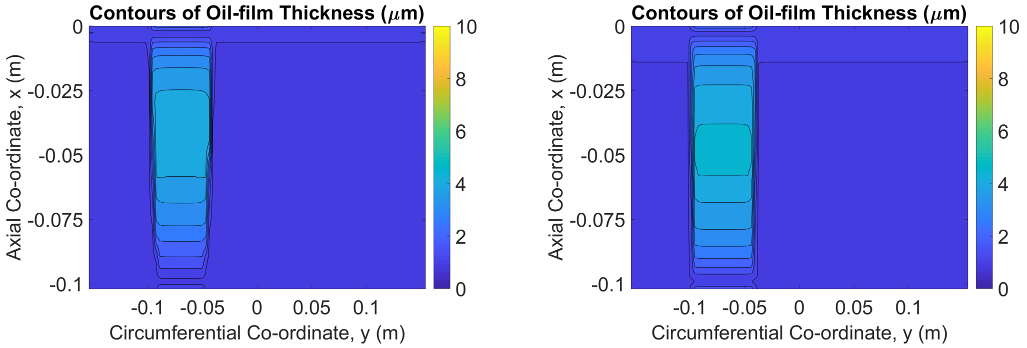

(c) 20th Cycle ($t = 10$ s)

(d) 40th Cycle ($t = 20$ s)

Figure 8.4: Thickness of the lubricant film on the cylinder liner following each labelled cycle a lubricant injector flowrate of 0.04 ml/rev and injection period = 3

With the lubricant supply parameters for the experiment and the model being equal, the results in figure 8.4 should be comparable to those of figure 7.12. However, the experimental results show the lubricant film to be still very concentrated near the area of lubricant injection after ten seconds ($t = 10$ s) of the test, while the model has predicted oil transport to very near bottom dead centre (8.4). Circumferentially, the experiment has shown the lubricant film extends to 45° either side of the injected lubricant after twenty seconds ($t = 20$ s), in the top half of the stroke at least. This is a quarter of the circumference of the cylinder liner. The model shows slightly less circumferential transport, with coverage being just below 80° (20% of the circumference). These results again show the model to predict higher axial and lower circumferential lubricant transport than seen in the experiment.

Considering only the experimental results, there is a clear difference with the experimental oil-film thickness results from sensors I-4 and II-4, with the former having notably greater oil-film thickness. This is particularly curious given that lubricant is delivered towards the block II sensors, and as such would perhaps be expected to have the greater oil-film thickness. The transducer calibration process has two stages: calibration of the amplifier to find the relationship between voltage and oil-film thickness, and taking surface scans of each transducer giving an offset between the transducer electrode and the cylinder liner. Considering results for both these channels use the same amplifier channel, the issue must lie with the surface scan. While the scan for this transducer appeared to be of satisfactory quality it is feasible an error occurred with the evaluation of the offset. Regardless, the increase seen at each sensor is of similar magnitude and as such it is still possible to evaluate the changes in oil-film thickness for these tests.

While there is in some cases notable differences in the magnitude of oil-film thickness, the form of the simulated results appears to reflect well those from the experiments (figures 8.5a and 8.5b). Again focussing towards the top of the stroke, there is very fast rise at the beginning of the tests. This is true for the simulated results at transducer positions S2 to S4, as well as some experimental ones (ie. transducer I-3 on both upstroke and downstroke). As discussed in 6, this may be due to a rapid rise in oil-film thickness as the lubricant film is established by a large volume of lubricant being injected repeatedly onto this part of the cylinder liner, or through the scraping of lubricant in relatively large quantities by the piston-ring to locations further down the stroke. In the simulation this initial rise occurs marginally more slowly at the location of sensor II-4 than at II-3 because of the reliance on lubricant transport to increase the volume at this position. As discussed (in section 5.3.3) the Deborah number has been estimated to be below one and hence visco-elastic effects are thought to be neglible. Since the model is based on a quasi-steady balance of piston-ring forces there is no accounting for this effect and as such the predictions suggest the estimations to be adequate.

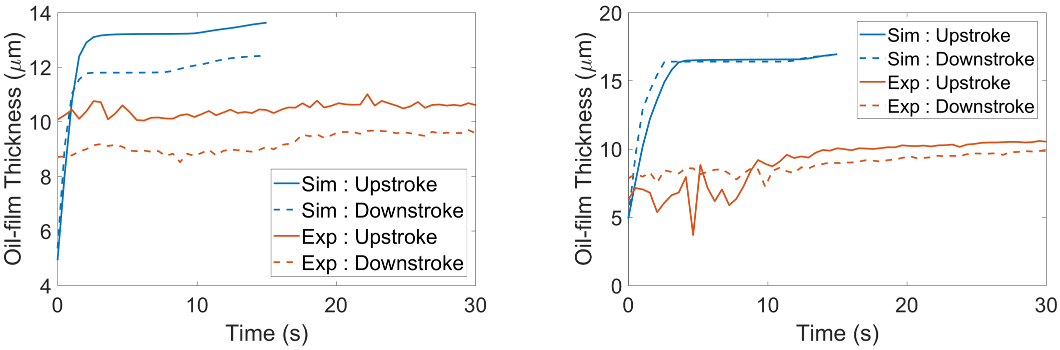

(a) Sensor II-3

(b) Sensor II-4

Figure 8.5: Upstroke and downstroke oil-film thickness at transducers II-3 and II-4, for a lubricant injector flow-rate 0.01 ml inj^{-1}

It is possible using the model to inspect the volume of lubricant being transported axially. Figure 8.6 shows this at transducers S3 to S7 for the first twelve cycles, where the volume shown is the summed rate of transport from around the circumference of the piston-ring. At each transducer, there is an increase in volume cycle on cycle, before the lubricant transport plateaus, or reduces very slightly, from thereon in. There is lubricant transport to transducers S3 and S4 from the first cycle, with transport to locations further down the cylinder liner commencing on increasingly later cycles. Considering transducer S4 (31.2 mm below top dead centre), there are increases in lubricant transport over the first eight cycles, which corresponds very closely to duration of the initial increase in oil-film thickness seen for simulated oil-film thickness in 8.5b. From the eighth cycle there is a slight reduction in the volume of lubricant transport, which may be due to an increasing rate of circumferential flow reducing the volume being transported axially. Further down the stroke, the volumes of lubricant transport being transported are much lower, hence the more gradual increase in oil-film thickness seen in these parts of the stroke.

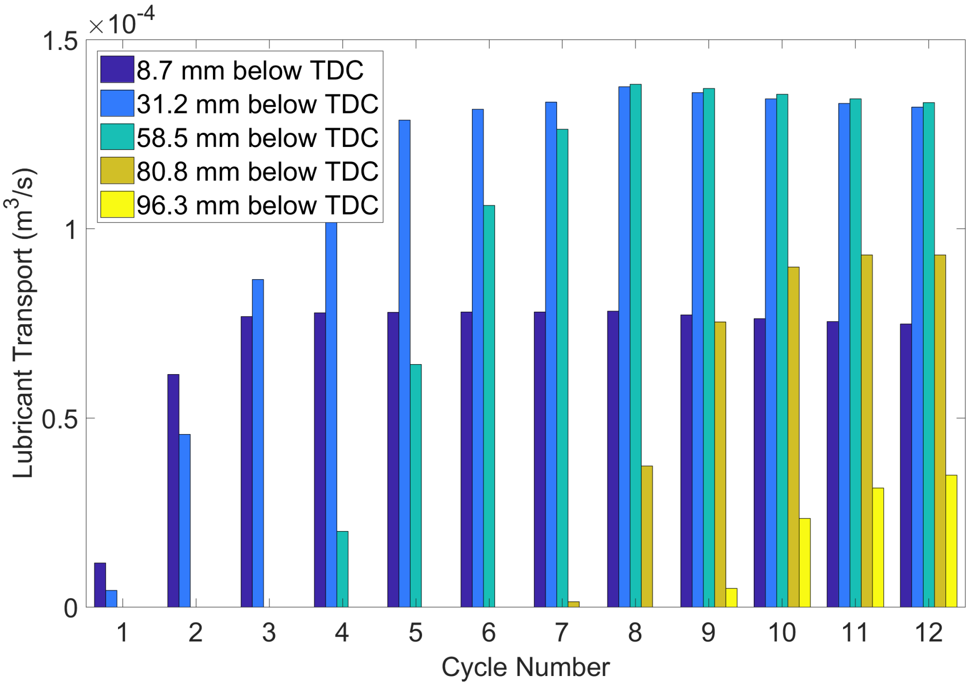

Figure 8.6: Simulated lubricant transport at the axial location of sensors 3 to 7

Consider the control volume analysis in chapter 6, and equation 6.2 alongside this, regarding the link between the timing of increases seen in oil-film thickness and lubricant transport. It is apparent from the results in 8.6 that axial lubricant transport ($q_{in_{ax}}$) is driving an increase in thickness of the lubricant film, and subsequently the initial phase of the response in oil-film thickness. Additionally, while the rate of supply from the lubricant injectors has undergone a step change, as distance from the injected area increases, the change in the rate of lubricant supply becomes decreasingly sudden, and as such so does the speed of the response seen in oil-film thickness. That the change in lubricant supply undergoes this more gradual change makes the corresponding response in oil-film thickness difficult to characterise, as it follows the form of this system input. Further testing and more extensive analysis is necessary in order explore these effects in more detail.

The rate of lubricant transport becomes more constant once the oil-film thickness further up the stroke plateaus, following the piston-ring inlet becoming fully flooded. The subsequent reductions in axial transport are perhaps caused by an slight increase in the rate of circumferential flow.

It is during this phase, where there is perhaps a more steady rate of lubricant transport circumferentially, where the response in oil-film thickness follows the form of a first order system, and allowing the time constant to be estimated.

Another aspect of the results shown in figure 8.5 is that upstroke oil-film thickness is greater throughout the tests at sensor II-3, while it is initially lower on the upstroke at sensor II-4. Again the simulated results reflect this same trend. At sensor II-3, there is sufficient lubricant to fully flood the piston-ring inlet on both upstroke and downstroke from the outset. As the piston-ring approaches top dead centre the oil-film thickness is reducing, and the resulting squeeze action allows the piston-ring to be supported at greater oil-film thickness. At transducer II-4, the initial lubricant distribution leads to an increasing oil-film thickness during the upstroke, and a reducing oil-film thickness on the downstroke. As such, the squeeze action occurs on the downstroke. Figure 8.7 shows the simulated lubricant flow past the leading and trailing edges of the piston-ring on both upstroke and downstrokes for the first ten cycles. During the first five cycles, there is greater lubricant flow past the trailing edge on the downstroke, indicating the occurrence of squeeze action. Here, as the volume between piston-ring and cylinder liner reduces, a reduction in lubricant flow past the leading edge, and an increase past the trailing edge must occur. The converse is true on the upstroke, indicating a negative squeeze action whereby an increase in lubricant flow past the leading edge is required to fill the increased volume between the cylinder liner and piston-ring surfaces. This same action leads to a reduction in the flow past the trailing edge. As the test proceeds these effects reduce as the peak oil-film thickness moves towards the location of transducer II-4, negating any squeeze effects. Here (at $t = 3$ seconds) the oil-film thickness on the upstroke and downstroke converge.

8.3.2 Starvation and Cavitation

A method to determine film extent for the experiment was described in 5, where this film extent could be tracked for the duration of the tests. Figure 8.8 shows the experimental film extent at transducers II-4 and II-5. At sensor II-4 the inlet boundary migrates towards the leading edge at approximately ten seconds, while at II-5 it occurs later (at $t = 13$ seconds), and at a slower rate. Referring back to figures 8.2 and 8.3, in both cases these changes in inlet boundary correspond with an increase in oil-film thickness. Prior to this time, there are fluctuations in the minimum oil-film thickness at both transducers, perhaps indicating contact between transducer and cylinder liner. Such fluctuations cease much earlier in the test at transducer II-4 at the higher flow-rate, since the increased volume of lubricant being delivered to the cylinder liner allow transport to sensor II-4 to occur more quickly. It appears that the fast rises in oil-film thickness near the beginning of the tests does occur due to an increase in filling of the piston-ring in the axial direction, leading

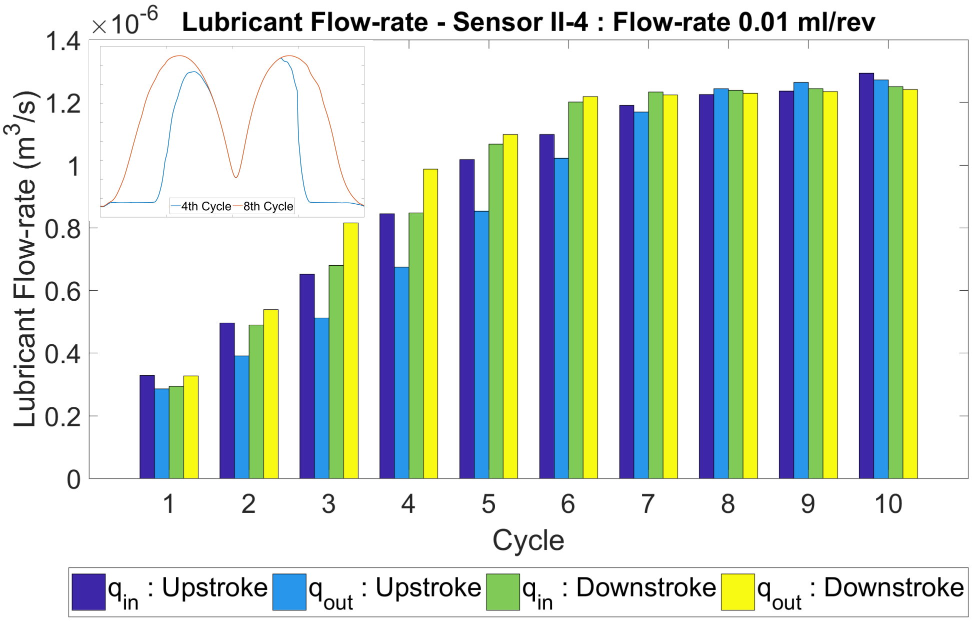

Figure 8.7: Simulated lubricant flow past the leading and trailing edge of the piston-ring (sensor position II-4, flow-rate 0.01 ml inj^{-1}). The inset shows oil-film thickness on the 4th and 8th cycles, to highlight the rapid change in oil-film thickness near midstroke, leading to squeeze effects as the lubricant film develops

to the transition from boundary or mixed lubrication, to hydrodynamic.

While the rises in oil-film thickness occur a short time into the test at these locations for the experiment, the transition in the results from the simulation occur earlier. At S4, for example, the magnitude of this rise is greater and over a longer time-frame at the lower flow-rate. Inspection of the degree of filling between the piston-ring and cylinder liner for the simulated results allows the cause of this to be inspected, and is shown in figure 8.9 for the transducer location S4, and in figure 8.10 for S5. A degree of filling of 100% indicates the computational cell between piston-ring and cylinder liner is filled with lubricant, whereas a degree of filling below 100% shows a partially filled cell. The leading edge of the piston-ring is along the bottom edge of each contour plot. Figure 8.9 shows the inlet boundary at the lower flow-rate of 0.01 ml inj^{-1} moves towards the leading edge over the first four cycles, and as with the experimental results this corresponds with the sharp increase in oil-film thickness. At S5 (figure 8.9) the transition occurs more slowly, with the inlet boundary almost reaching the leading edge of the piston-ring by the twelfth cycle. During this time the circumferential filling also increases by a factor of approximately two.

In both the experiment and the simulation then, the first increase in oil-film thickness observed occurs due to the inlet boundary moving towards the leading edge of the piston-ring. The oil-film thickness must respond by increasing in order to maintain the equilibrium between the hydrodynamic load capacity and the piston-ring force, leading to the integral of lower hydrodynamic

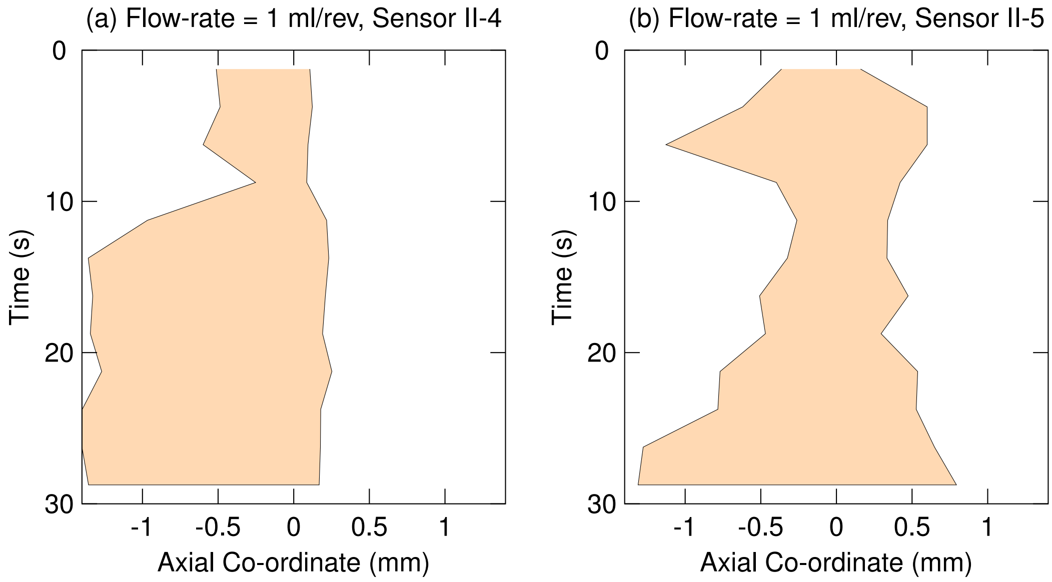

Figure 8.8: Comparison of upstroke inlet and cavitation boundaries taken at 5 cycle intervals at transducers II-4 and II-5

pressures over a larger area.

The timing of these increases may be dependent on the distribution of lubricant from the injectors. In the model the area over which lubricant is distributed is unaffected by the lubricant injector flow-rate setting. At S3 there is no increase evident at the higher flow-rate, but there is at the lower flow-rate due to a thinner lubricant film on the cylinder liner on the first upstroke. At S4 where the initial lubricant volume is lower again the rise is seen at both injector flow-rates. At S5 and S6 the rises are similar at both injector flow-rates, albeit with a slight difference in the timing, being a cycle or two later at the lower flow-rate. The very slight delay in the commencement of the rise at S5 and S6 is due to the need for lubricant to be transported to this part of the cylinder liner.

The experimental results for block II show there is sufficient lubricant to flood the piston-ring inlet on the first cycle, and as such the rise is not present here. As already seen, at II-4 there is a delay before the initial increase in oil-film thickness, suggesting the there is a delay in lubricant availability while it is transported to this sensor. This is less apparent at the higher flow-rate where oil-film thickness begins to rise from the beginning of the test. It appears that lubricant is not injected onto this transducer, certainly at the lower flow-rate. This may also be true at the higher flow-rate, with an increased lubricant volume injected reducing the time required for lubricant transport to sensor II-4. However, it could be the area over which lubricant is distributed reduces at lower lubricant injector flow-rates, which is not the case for the model.

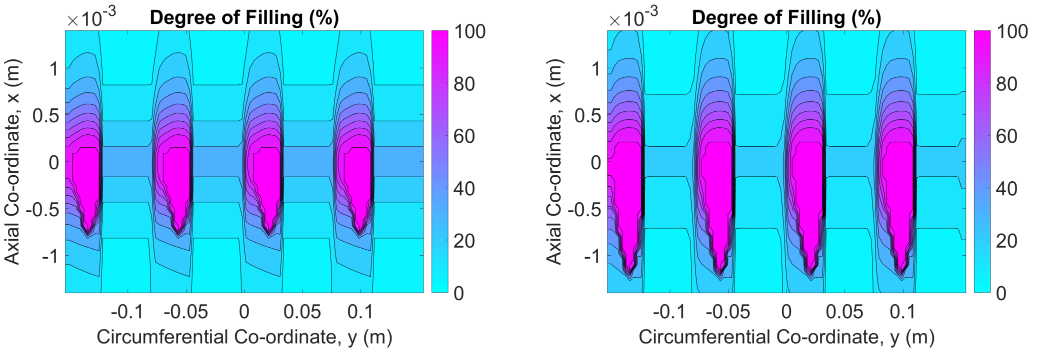

(a) 1st Cycle

(b) 2nd Cycle

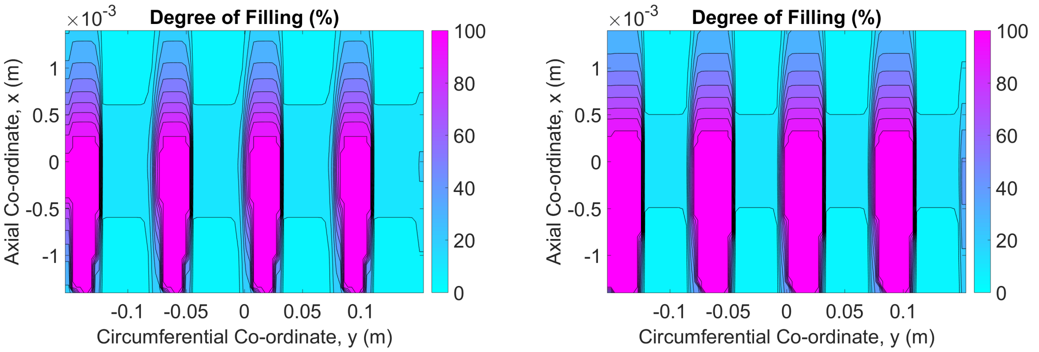

(c) 3rd Cycle

(d) 4th Cycle

Figure 8.9: Degree of filling showing the increased area of piston-ring generating hydrodynamic pressure at the location of sensor 4, at a lubricant injector flow-rate 0.01 ml/rev

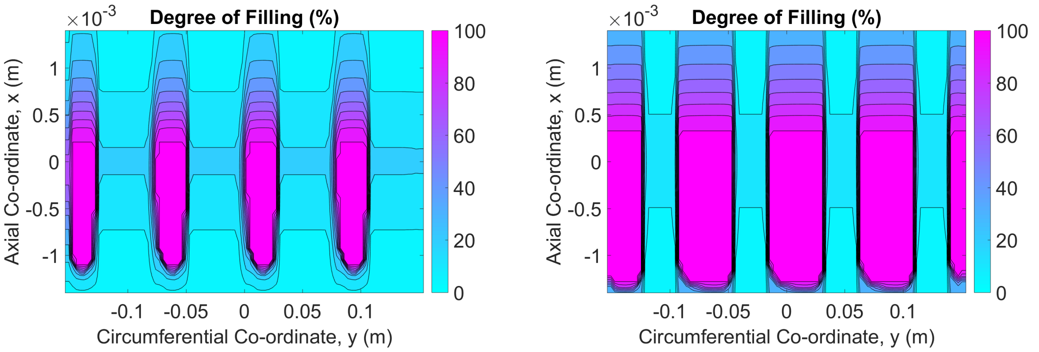

(a) 6th Cycle

(b) 12th Cycle

Figure 8.10: Degree of filling showing the increased area of piston-ring generating hydrodynamic pressure at the location of sensor 5, at a lubricant injector flow-rate 0.01 ml/rev

Following the initial rise in oil-film thickness discussed above, there is a plateau with relatively little increase. After this there is a further rise in oil-film thickness as the lubricant film on the liner further develops. This is most clear for transducers I-4, I-3, and II-3, but is also evident for others - particularly on the downstroke. This behaviour is also apparent in the simulated results, with a magnitude of change of a similar order to that seen in the experiment - typically only one or two micrometres. The cause of this latter increase appears to be due to an increase in the circumferential filling, although this occurs much more slowly than the change in inlet boundary discussed above. Figure 8.11 shows the degree of filling at the axial position of transducer II-4, which corresponds to a time before ($t = 6$ seconds) and after ($t = 12$ seconds) the start of this second rise in oil-film thickness (seen in 8.5b). Here there is a slight increase (of two computational cell on each side) in the width of each filled region, which leads to this increase.

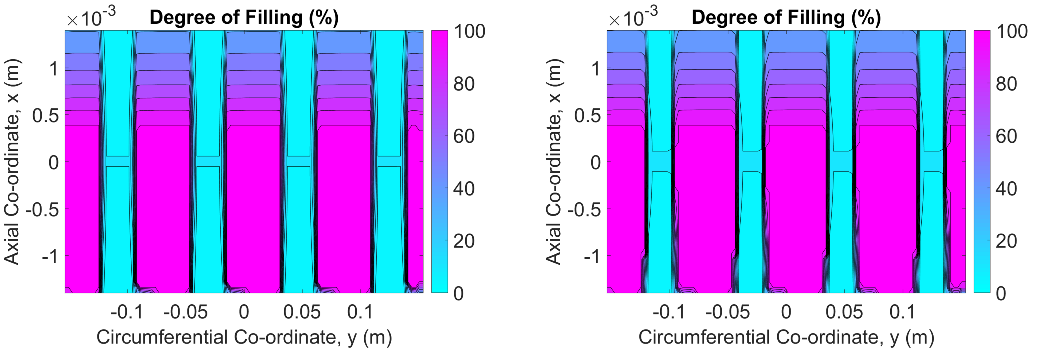

(a) 12th Cycle

(b) 24th Cycle

Figure 8.11: Degree of filling showing the increased area of piston-ring generating hydrodynamic pressure at the location of sensor 4, at a lubricant injector flow-rate 0.01 ml/rev

While this second rise in oil-film thickness again plateaus, likely due to the subsequent reduction in hydrodynamic pressure causing a lower rate of circumferential lubricant flow, it is expected the gap between piston-ring and cylinder liner should fill completely if the simulation were continued long enough. Likewise, this must be the case for the second oil-film thickness increase in the experiment, since the film extent at transducer II-4 is already fully flooded prior to this time. As with the results from the model, only an increase in circumferential filling could lead to oil-film thickness increasing further.

8.4 Discussion

The results of the model show a very good correlation with experimental results near the top of the stroke, with the error being in the range 15% to 30%, with the exception of the results at transducer II-4. For the predicted results oil-film thickness at the end of the upstroke is greater than at the start of the downstroke by around three micrometers. In the experimental results, contact is seen to occur at S2 on both upstroke and downstroke at the lower flow-rate, but in the second half of the test contact ceases on the upstroke, suggesting marginally greater oil-film thickness than at the start of the downstroke. While the difference on the two strokes is less than predicted by the model, the trend is the same with the minimum oil-film thickness occurring just after top dead centre as a result of the squeeze effect.

Further down the stroke the difference between the predicted and experimental results increases. In addition, the increase at both S5 and S6 occurs sooner for the predicted results. Both of these attributes suggest lubricant transport in the model occurs more quickly. While there may be a small difference between the volume and the distribution of lubricant from the injectors in the model and the experiment, it is possible also the volume of lubricant being scraped down the cylinder is over-predicted. Further, inspection of the development of the lubricant film in figure 8.4 shows circumferential lubricant transport is predicted to be slower than the experimental results show.

The difference observed in oil-film thickness and lubricant transport in the lower half of the stroke may be due to thrust force acting on the piston normal to the cylinder liner. This force is transmitted from the connecting rod as it accelerates the piston and is greatest near midstroke where S5 is located, perhaps leading to the lower oil-film thicknesses observed. As a consequence, more of the injected lubricant may be scraped upwards to the top of the cylinder, leaving a lower volume of lubricant to be scraped downwards on the following stroke. Inertial spreading of the body of lubricant being scraped by the piston-ring may be another factor, since the force applied to accelerate it will lead to some circumferential flow. This would lead to lower axial lubricant transport, and greater circumferential transport, perhaps reducing the differences between predicted and measured results.

Despite these differences, the response seen in the predicted oil-film thickness shows a similar form to the results of the experiments. This includes the fast initial increase in oil-film thickness, shown to be due to the inlet boundary moving towards the leading edge, followed by a slower increase in oil-film thickness as the lubricant film on the cylinder extends circumferentially. Further, as discussed for the experimental results in chapter 6, the initial response is predicted to be faster in areas near to the injected lubricant.

$$\tau \frac{dh_0}{dt} + h_0 = \alpha \frac{dh_{oil}}{dt} + \beta h_{oil} \tag{8.1}$$

The fit equation proposed in chapter 6, comprising a step change in oil-film thickness followed by a first order response, appears then to adequately represent this two phase response. A system model for this behaviour could be proposed such as that shown in equation 8.1. The right-hand side of the equation drives the response of oil-film thickness, and has been shown to be closely linked with the supply of lubricant to a given location. The term h_{oil} relates to the lubricant injector supply rate, following a change in which the magnitude of change in oil-film thickness during the two phases of the response being determined by the coefficients α (fast) and β (slow). These coefficients are likely to be dependent on their location in the cylinder and could be determined for a marine engine through testing. For example, the second coefficient (β) represents the steady-state oil-film thickness at a given rate of lubricant supply. The left-hand side of the equation characterises the speed of the response for oil-film thickness with the time constant, τ. The limitation of this model is with the speed of the response following the change in lubricant injector supply being modelled as a step change. It is a reasonable first approximation, however, and would permit the design and trialling of potential control solutions for an oil-film thickness control system. Further testing on a marine engine would allow the coefficients to be determined, along with an evaluation of the suitability of the model for large marine diesel engines.

In order to better fit the initial response in oil-film thickness a higher order model could be used, with the step change in oil-film thickness being replaced with a second exponential function. This may allow for the slower increases in oil-film thickness more distant from the injected lubricant to be better represented using a second time constant. Figure 8.12 shows how the first order model compares to experimental data from transducer II-4, along with a fit to a potential second order model. It may be that a higher order model such as this becomes necessary at lower lubricant supply rates.

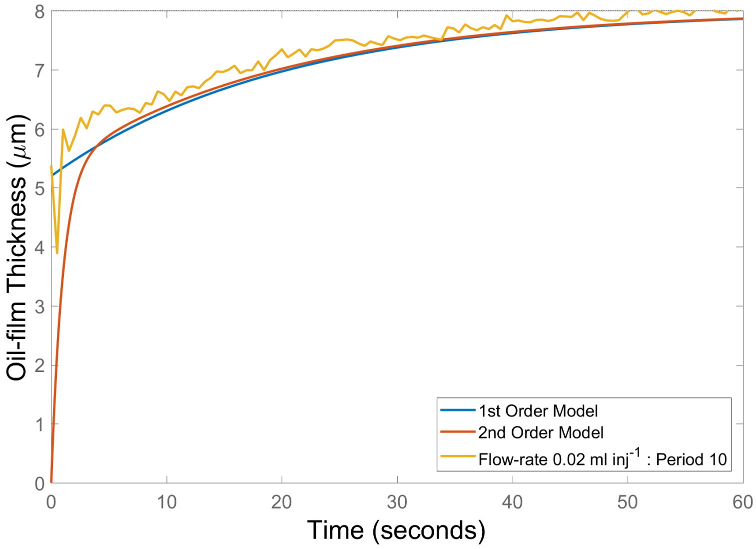

Figure 8.12: Comparison of first and second order models to experimental results

8.5 Conclusions

A three-dimensional piston-ring lubrication model, which includes the effects of axial and circumferential lubricant flow resulting from both pressure differentials and the scraping action of the piston-ring, has been developed and validated. The model can predict the development of the lubricant film and subsequently oil-film thickness and film extent when subjected to a non-uniform lubricant supply.

The results for oil-film thickness and film extent taken from the piston-ring lubrication model are comparable to those from the experiments. Oil-film thickness predictions near top dead centre are approximately 20%, while lubricant transport axially is predicted to be faster than seen in the experimental results.

There is in both cases a two phase response in oil-film thickness as the oil-film evolves, firstly in the axial direction, and secondly in the circumferential. The axial development of the lubricant film has been shown to lead to the inlet boundary migrating to the leading edge of the piston-ring, and subsequently a relatively fast increase in oil-film thickness. This occurs as a result of lubricant transport in the axial direction, largely as a result of lubricant being scraped down the cylinder liner by the piston-ring. The rate at which the transition occurs is dependent on distance from the injected lubricant, with a reduced rate of this transition at increasing distances.

Increased filling in the circumferential direction follows at a reduced rate, because lubricant transport in this direction relies on pressure based flow. This can be seen using degree-of-filling results from the model, although it is implied with the experiment from oil-film thickness increases occurring beyond the piston-ring becoming fully-flooded. This latter increase corresponds with the behaviour being characterised using a time constant analysis seen in investigation 6.

A system model for the response in oil-film thickness to a change in lubricant supply has been proposed to allow potential control solutions to be investigated. The coefficients in the model can be determined by experiment on a large marine diesel engine.

Chapter 9

Conclusions and Recommendations for Further Work

9.1 Introduction

Understanding the response of the lubricant film to changes in lubricant supply or engine operating conditions is necessary to enable further development of systems and components involved in cylinder lubrication in marine engines. Characterising the dynamics of changes in oil-film thickness is required if feedback control systems are to be implemented and cylinder oil consumption reduced. Ensuring an adequate oil supply to areas away from lubricant injection is essential to prevent excessive wear and corrosion of components following a reduction in lubricant supply, during a transition to slow steaming, or upon switching between high and low sulphur content fuels.

The aim of this research project was to investigate the effect of lubricant supply on piston-ring lubrication in internal combustion engines. This has been achieved through the development of a test apparatus with a bespoke, adjustable lubricant injector supply system, capable of delivering a range of volumes of lubricant to the cylinder liner. The test apparatus was fitted with a number of capacitance based oil-film thickness transducers to provide information about the developing oil film.

The apparatus has been used to conduct a number of investigations with the aim of understanding how the lubricant film develops in time when subjected to repeated lubricant injection. Oil-film thickness has been observed to be greater at the top of the stroke near to lubricant injection, leading to non-typical oil-film thickness profiles. Oil-film thickness data and film extent has been analysed to ascertain the manner in which lubricant was being transported axially.

The development of the lubricant film has been evaluated over a range of lubricant injector flow-rates and has been shown to have a two part response due to axial and circumferential oil transport. The first part of the response has been shown to be relatively fast, more so in the proximity of the injected lubricant. The second part of the response has the form of a first order exponential rise, the time constant being longer near midstroke where a thicker lubricant film develops and where squeeze effects are less.

A method has been developed for quantifying the development of the lubricant film in time. This includes the tracking of film extent both axially and circumferentially using oil-film thickness data and by comparison of the piston-ring signal to a simulated signal representing the true profile of the piston-ring. The method has been utilised to show lubricant film development at a number of lubricant injector flow-rates and a model proposed to approximate this behaviour.

In addition to the experimental work, a piston-ring lubrication model has been developed to predict the development of oil-film thickness as a function of time when the injection of lubricant causes a non-uniform distribution. The model has been verified and validated against empirical and experimental data.

9.2 Achievement of Aims

The aims of this project were to determine the effect of lubricant supply on piston-ring lubrication in internal combustion engines, with a particular focus of the effects on large, two-stroke marine diesel engines, where lubrication of the piston-rings is achieved using the injection of oil at discrete locations on the cylinder liner. The achievement of these aims are summarised below.

1. *To develop a test apparatus whereby lubricant can be delivered to the cylinder liner at a number of different supply rates, and where oil-film thickness can be measured using capacitance transducers*

   A test apparatus has been developed with the capability to allow investigations involving a developing lubricant film in a motored internal combustion engine. The system incorporates lubricant injectors that can deliver lubricant to the cylinder over a range of flow-rates and injection frequencies and position. Capacitance based oil-film thickness transducers have been manufactured, installed, and calibrated at a number of locations in the cylinder to provide information about the changing oil-film thickness and lubricating film.

2. *To conduct experiments at a number of lubricant supply rates, in order to investigate the effect of lubricant supply on piston-ring oil-film thickness at different locations on the cylinder liner*

   The impact that a change in lubricant injector supply rate to the cylinder has on the development of oil-film thickness and film extent has been quantified. The response of oil-film thickness at a given location can be modelled using a time delay, a fast increase approximated as a step change, and a slow increase represented as a first order response with a time constant. A system model for this behaviour has been proposed, with coefficients that can be determined by experiment.

3. *To develop methods for characterising the development of the lubricant film, and to investigate the mechanisms by which this lubricant film development occurs*

   A method has been developed for observing the rate at which lubricant is transported both axially and circumferentially. The timing of changes in oil-film thickness or film extent at different cylinder locations has been interpolated to generate contour maps showing the development of the lubricant film. The variation of film extent in time has been measured. Comparison of the oil-film thickness signal to a simulated signal has been made to ascertain the variation in time of inlet and cavitation boundaries following a change in operating conditions.

4. *To develop a piston-ring lubrication model capable of simulating a developing lubricant distribution over a number of engine cycles, following lubricant injection to different areas of the cylinder liner*

   A theoretical model has been developed to predict the development of a lubricant film over time from an initial non-uniform distribution. The model uses the principle of conservation of mass to compute hydrodynamic pressure and degree of filling at each computational cell, with oil-film thickness being determined by considering an equilibrium of the forces acting on the piston-ring. The model includes an algorithm to generate non-uniform lubricant distributions. Oil-film thickness predictions to within 30% of experimental data have been computed in the top half of the stroke. Errors in the predictions increase in magnitude towards the bottom of the stroke due to an over-prediction in the rate of axial lubricant transport.

9.3 Conclusions

A test engine was developed to allow investigations relating to the time variation of oil-film thickness resulting from a step change in lubricant injector supply rate. This included the measurement and analysis of data acquired using capacitance based oil-film thickness transducers, which allows the transition from boundary to hydrodynamic lubrication to be seen, along with corresponding changes in film extent and oil-film thickness as the lubricant film develops further. While these tests were carried out under motored conditions, without the cylinder head, further developments would (for example) allow for tests to be carried out with greater combustion chamber pressures near top dead centre.

Using data from experiments using this engine, the development of a lubricant film on the cylinder liner has been observed by analysing the time variation of oil-film thickness and the development of axial and circumferential film extent. Using this information it has been possible to attribute the causes of the observed behaviour in oil-film thickness. This behaviour typically involves an initial transition from boundary to hydrodynamic lubrication in the early stages of the tests, with a corresponding rise in oil-film thickness being the result of increased axial film extent. Continued increases in oil-film thickness once the piston-ring is fully flooded imply an increase in circumferential film extent. A delay in the first phase has been linked to the distance of a transducer from the area of injected lubricant.

The rate at which the initial development in oil-film thickness occurs appears to be dependent on distance from the injected lubricant, with regions nearby undergoing a rapid transition from having highly starved to fully flooded ring inlet, with a similarly fast increase in oil-film thickness. More distant from the injected lubricant there appears to be a slower increase in both film extent and oil-film thickness, although further investigation into the form of this initial response, and factors affecting the rate at which it occurs is required.

The second phase of the development in oil-film thickness has been observed to follow the form of a first order system response. An attempt has been made to characterise this response by evaluating time constant, where this showed a trend for higher response times for areas of the cylinder liner with the development of a thicker film (ie. near midstroke). Squeeze action may also lead to a faster response due to increased pressure differentials driving the circumferential flow. While no apparent trend was observed regarding the time constants and the rate of lubricant supply, it is thought that lower injector flow-rates may lead to longer response times.

Oscillations in oil-film thickness resulting from periodic lubricant injection have been observed, whereby the frequency and amplitude of the oscillations are linked to the frequency of lubricant injection. These oscillations have lower amplitude at higher frequencies, and greater amplitude away from the thrust face. It would be interesting to investigate these oscillations further, particularly in a firing engine where fuel consumption through evaporation would radically change the behaviour.

Following on from the above investigations on the development of oil-film thickness and film extent, a study was carried out into the rate at which lubricant is transported around the cylinder liner. The method involved a single lubricant injector, and the determination of lubricant availability at the piston-ring from oil-film thickness measurements and analysis of film extent. Contours showing the development of the lubricant film have been ascertained from these timings by linear interpolation. Lubricant transport was found to occur at a higher rate axially than circumferentially, due to an additional mechanism whereby lubricant is scraped down the cylinder liner at times where the ring inlet is fully flooded. Lubricant flow-rates circumferentially are largely due only to pressure differentials and are therefore slower. The circumferential lubricant transport occurs at a higher rate away from the thrust face than it does towards it.

A two-dimensional piston-ring lubrication model, which includes the effects of axial and circumferential lubricant flow resulting from both pressure differentials, and from the above scraping action of the piston-ring, has been developed and validated. The model can predict the development of the lubricant film and subsequently oil-film thickness and film extent when subjected to a non-uniform lubricant supply. Results from the model show particularly good correlation with experimental results in the top half of the cylinder. Further analysis is needed regarding the differences in predicted and measured oil-film thickness is further down the cylinder liner, with potential causes being the area of the transducer electrode and its effect on the voltage output, or the highly one-dimensional lubricant transport seen for the model leading to excessively high rates of axial lubricant transport.

Despite this, results from the model confirm the findings above, that oil-film thickness responds in two phases due to different rates of lubricant transport axially and circumferentially. Data pertaining to film extent and rate of lubricant transport axially through scraping has been extracted, and shows the lubricant transport increasing cycle on cycle during the initial phase of the response. Inspection of the film extent shows the piston-ring to be fully flooded following this phase in regions near to the injected lubricant. Increases in circumferential film extent from the model have been shown to be the cause of the second phase.

9.4 Further Work

9.4.1 Experimental Research

A test engine has been developed to allow investigations relating to the time variation of oil-film thickness resulting from a step change in lubricant injector supply rate. This included the measurement and analysis of data acquired using capacitance based oil-film thickness transducers. While many aspects of these investigations have been successful, there is certainly scope for further development in order to perform future investigations.

Currently, the design of the test-rig is such that the cylinder is open and at atmospheric pressure, and a means of capping the cylinder so as to generate higher combustion chamber pressures near top dead centre is feasible. In doing so, the impact of increased pressure on rates of lubricant transport and oil-film thickness development could be investigated, which may permit better understanding as to these findings extrapolate for a firing marine diesel engine. Additional injection points could be incorporated to investigate the differences between spraying lubricant above and below the piston. The effect a more complete ring pack has on the development of oil-film thickness and oil transport could also be investigated.

Experiments looking at the development of the lubricant film following a single injection event (of varying volume, viscosity, and at different speeds and locations), rather than repeated events. A greater density of oil-film thickness transducers could be fitted to the engine to give better resolution of the development of the lubricant film. Using the techniques described herein involving oil-film thickness and film extent along with predicted lubricant flow past the piston ring (by predicting the point of maximum pressure using Reynolds equation with the measured parameters and then computing Poiseuille and Couette) could allow a more detailed examination of lubricant flow in the cylinder. This could be carried out with the engine in its current configuration, with the thrust action of the piston, or could incorporate a crosshead similar to those in large marine diesel engines to remove this effect. In a similar manner, it would be interesting to investigate the development of the lubricant film from steady state following a cease in lubricant injection.

Throughout this work an assumption of isothermal conditions and constant viscosity has been adopted. Given the capacity of the lubricant to cool the liner and existing oil film will vary at different rates of lubricant supply, leading to a change in lubricant viscosity and subsequently oil-film thickness, there is value in conducting further experiments to investigate the significance of this effect. As part of this investigation the appropriateness of the Newtonian flow assumptions (and hence hydrodynamic conditions) should be carried out using a suitable non-dimensional approach, for example by evaluating relaxation time of the lubricant and hence the contribution of viscoelastic effects using the Deborah number, elasticity number, or similar.

Investigations relating to local and transient heating and the resulting viscosity change could additionally be carried out on a firing engine during start-up. While the cylinder temperature and bulk lubricant temperature in the sump will initially both be similar at ambient temperature, there will quickly form a temperature gradient due the relatively fast heating of the cylinder from combustion and friction. As such, there will be a period of time where the lubricant is being heated once resident on the liner or in the ring-pack while the bulk temperature in the sump comes up to its steady-state operating temperature. With enough oil-film thickness transducers fitted it would also be possible to map the development of the lubricant film on the cylinder during this time.

Of course it would be a natural progression to conduct trials on a firing marine diesel engine, where investigations into the effect of changes in the lubricant film following a step change between two non-zero lubricant injector supply rates could be performed. By doing this at different engine conditions, for both increases and decreases in lubricant flow-rate to examine hysteresis effects, the behaviour of the oil-film could be thoroughly understood. This includes determination of the relationship between lubricant supply, cylinder location, and the coefficients in the proposed system model to enable a control system to be devised. It would be possible to examine the effects of lubricant consumption through evaporation on any periodic effects and rates of lubricant transport to areas susceptible to corrosive wear could be quantified by examining the timing of changes in oil-film thickness. Ultimately, this could lead to a control system for oil-film thickness being developed and trialled to allow reductions in cylinder oil consumption and increased time between overhaul.

9.4.2 Computational Research

With the model there is clear scope for simulations using parameters reflecting those of an operational marine diesel engine, including combustion chamber pressure. Any number of studies could be carried out in such a configuration, including how engine load and lubricant viscosity may effect the likelihood of corrosive wear for example, or investigating the effects of different lubricant distributions following injection events.

Development of the model could also continue. Incorporating a temperature gradient both spatially and temporally would enable predictions of oil-film thickness and other important information from a cold start, for example. Adapting the model to account for asymmetric geometry and non-concentric piston-ring/cylinder liner interface would also be worthwhile. A more complete ring pack, with inter-ring gas pressures could also be included.

For a more complete behaviour, the model could be developed to includes the piston skirt and piston crown, with ring tilt being computed using by equilibrium of forces, and forces normal to the cylinder liner being evaluated and applied to assess the effect this has on oil-film thickness and lubricant transport on both thrust and anti-thrust faces. This would be applicable to more conventional engines rather than large crosshead marine engines, and would enable detailed simulation of piston-ring lubrication during transient phases in engine operation, such as an acceleration event.

References

Aabo, K (2005). *Operation on Low-Sulphur Fuels: Two-Stroke Engines*. Pamphlet. Copenhagen, Denmark.

Adamkiewicz, Adam and Drzewieniecki, Jan (2018). “Operational Evaluation of Piston-rings-Cylinder Liner Assembly Wear in High Power Marine Diesel Engines”. *Tribologia* 271, pp. 5–15.

Amoser, M (2001). “Insights Into Piston-Running Behaviour”. *Marine News* No. 2 - 2001, pp. 23–27.

[Anon] (2006a). *MARPOL Annex VI: Operation in SOx Emission Control Areas, how to comply*. Pamphlet.

[Anon] (2006b). *Review of Maritime Transport*. Report.

[Anon] (2007). *Maritime Air Emissions and MARPOL Annex VI: Strategies and Consequences*. Pamphlet.

[Anon] (2008). “A New Cylinder Oil for all Sulphur Fuels”. *Marine Engineers Review* 2008.January, pp. 42–42.

[Anon] (2009). “Shipping emissions levy proposed”. *Professional Engineering* 22.5, pp. 6–6. ISSN: 0953-6639.

[Anon] (2010a). *Piston Ring Geometry of Running Service*. Web Page.

[Anon] (2010b). *The World Merchant Fleet in 2005*. Magazine Article.

[Anon] (2015). *Fuel Switching: Monitoring to Prevent Damage*.

[Anon] (2017). *The Global Fleet Revealed*.

[Anon] (2018a). *IMO Marine Engine Regulations*.

[Anon] (2018b). *Shipping industry faces calls to clean up emissions*.

Association, International Air Transport et al. (2009). “A global approach to reducing aviation emissions”. *IATA, Montreal*.

Avan, Emin Y, Mills, Robin S, and Dwyer-Joyce, Rob S (2010a). “Simultaneous film thickness and friction measurement for a piston ring-cylinder contact”. *STLE/ASME 2010 International Joint Tribology Conference*. American Society of Mechanical Engineers, pp. 191–193.

Avan, Emin Yusuf, Mills, Robin, and Dwyer-Joyce, Rob (2010b). “Ultrasonic imaging of the piston ring oil film during operation in a motored engine-towards oil film thickness measurement”. *SAE International Journal of Fuels and Lubricants* 3.2, pp. 786–793.

Avan, Emin Yusuf, Mills, Robin, and Dwyer-Joyce, Rob (2011). *Frictional Characteristics of Ultrasonically Measured Lubricant Films in a Simulated Piston Ring Liner Contact*. Tech. rep. SAE Technical Paper.

Bassani, R and Ciulli, E (1996). “Lubricant Film Thickness and Shape using Interferometry and Image Processing”. *Elastohydrodynamics ’96: Fundamentals and Applications in Lubrication and Traction*. Ed. by D. Dowson. Vol. 32. Tribology Series. Amsterdam: Elsevier Science B.V., pp. 81–90.

Bewsher, S.R. et al. (2019). “Boundary friction characterisation of a used cylinder liner subject to fired engine conditions and surface deposition”. *Tribology International* 131, pp. 424 –437. ISSN: 0301-679X.

Bhushan, B (2001a). *Modern Tribology Handbook Vol. 1*. Vol. Principles of Tribology. CRC Press LLC. ISBN: 0-8493-8403-6.

Bhushan, B (2001b). *Modern Tribology Handbook Vol. 2*. Vol. Materials, Coatings, and Industrial Applications. CRC Press LLC. ISBN: 0-8493-8403-6.

Bhushan, B and Gupta, B (1991). *Handbook of Tribology: Materials, Coatings, and Surface Treatments*. New York: McGraw-Hill.

Blau, P (1992). *ASM Handbook: Volume 18 - Friction, Lubrication, and Wear Technology*. 10th ed. ASM International. ISBN: 0871703807.

British-Standards-Institution (1998). *Surface texture profile method - Terms, definitions, and surface texture parameters: Geometrical product specification (GPS)*. Standard BSEN4287:1998. London, UK.

Castrol (2013). *Product Data Sheet - Cyltech 50S*.

Castrol (2014). *Product Data Sheet - Cyltech 80AW*.

Castrol (2015). *Product Data Sheet - Castrol Magnatec 5W-20 E*.

Castrol (2017). *Product Data Sheet - Cyltech 70*.

Christensen, Ole (2010). “Cylinder lubrication of two-stroke crosshead marine diesel engines”. *Wartsila Technical Journal*.

Clark, G.H. (1970). “The Design of Pistons and Piston Rings”. *Marine Diesel Lubrication*. London: Burmah-Catrol Marine. ISBN: 090258703X.

Collins, B., Sanderson, M.G., and Johnson, C.E. (2009). “Impact of increasing ship emissions on air quality and deposition over Europe by 2030”. *Meteorologische Zeitschrift* 18.1, pp. 25–39. ISSN: 0941-2948.

Corbett, J.J. and Koehler, H.W. (2003). “Updated emissions from ocean shipping”. *Journal of Geophysical Research-Atmospheres* 108.D20, pp. 4650–4664. ISSN: 0148-0227.

Corbett, J.J. and Winebrake, J.J. (2008). “Emissions tradeoffs among alternative marine fuels: Total fuel cycle analysis of residual oil, marine gas oil, and marine diesel oil”. *Journal of the Air & Waste Management Association* 58.4, pp. 538–542. ISSN: 1047-3289.

Corbett, J.J. et al. (2007). “Mortality from ship emissions: A global assessment”. *Environmental Science & Technology* 41.24, pp. 8512–8518. ISSN: 0013-936X.

Corbett, J.J., Wang, H.F., and Winebrake, J.J. (2009). “The effectiveness and costs of speed reductions on emissions from international shipping”. *Transportation Research Part D-Transport and Environment* 14.8, pp. 593–598. ISSN: 1361-9209.

Courtney-Pratt, J. and Tudor, G. (1946). “An Analysis of the Lubrication between the Piston Rings and Cylinder Wall of a Running Engine”. *Proceedings of the Institution of Mechanical Engineers* 155, pp. 293–299.

Douglas, J.F. (2005). *Fluid Mechanics*. Pearson/Prentice Hall. ISBN: 9780131292932.

Dow, T.A., Schiele, C.A., and Stockwell, R.D. (1983). “Technique for Experimental Evaluation of Piston Ring - Cylinder Film Thickness”. *Journal of Lubrication Technology-Transactions of the Asme* 105.3, pp. 353–360. ISSN: 0022-2305.

Dowson, D. (1993). “Piston Assemblies; Background and Lubrication Analysis”. *Engine Tribology*. Ed. by C.M. Taylor. Tribology Series. London: Elsevier Science Publishers BV, pp. 213–240.

Dowson, D. and Higginson, G.R. (1977). *Elasto-hydrodynamic lubrication*. International series on materials science and technology. Pergamon Press. ISBN: 9780080213026.

Dragsted, J et al. (2004). “An Insight into Advanced Cylinder Lubrication Issues”. *CIMAC Congress 2004*.

Dwyer-Joyce, R.S., Drinkwater, B.W., and Donohoe, C.J. (2003). “The measurement of lubricant film thickness using ultrasound”. *Proceedings of the Royal Society of London.Series A: Mathematical, Physical and Engineering Sciences* 459.2032, pp. 957–976.

Elrod, H.G. and Adams, M.L. (2017). “Computer Program for Cavitation and Starvation Problems”, pp. 37–41.

Eriksen, L (2003). “Developments in Cylinder Liner Lubrication”. *Information Conference*. Institut fur Schiffsbetriebsforschung.

ExxonMobil (2017). *Switching Between High and Low Sulfur Fuels*.

Eyring, V. et al. (2005). “Emissions from international shipping: 1. The last 50 years”. *Journal of Geophysical Research-Atmospheres* 110.D17, p. 110. ISSN: 0148-0227.

Eyring, Veronika et al. (2007). “Brief summary of the impact of ship emissions on atmospheric composition, climate, and human health”. *Document submitted to the Health and Environment sub-group of the International Maritime Organization* 6.

Fatjo, G. Garcia-Atance, Smith, E.H., and Sherrington, I. (2014). “Mapping lubricating film thickness, film extent and ring twist for the compression-ring in a firing internal combustion engine”. *Tribology International* 70, pp. 112 –118. ISSN: 0301-679X.

FormLabs (2017). *Materials Data Sheet - Photopolymer Resin for Form 1+ and Form 2*.

French, P (2008). “Emissions Reductions All At Sea”. *Ethical Corporation* December 2008/January 2009, pp. 28–29.

Fuglestvedt, J. et al. (2009). “Shipping Emissions: From Cooling to Warming of Climate-and Reducing Impacts on Health”. *Environmental Science & Technology* 43.24, pp. 9057–9062. ISSN: 0013-936X.

Furuhama, S. and Sumi, T. (1960). “A dynamic Theory of Piston-Ring Lubrication”. *Bulletin of JSME* 4.16, pp. 744–752.

Garcia-Atance Fatjo, Gonzalo, Smith, Edward H, and Sherrington, Ian (2017). “Piston-ring film thickness: Theory and experiment compared”. *Proceedings of the Institution of Mechanical Engineers, Part J: Journal of Engineering Tribology*, p. 1350650117722257.

George, Libby and Ghaddar, Ahmad (2018). *New rules on ship emissions herald sea change for oil market*.

Gohar, R and Rahnejat, H. (2008). *Fundamentals of Tribology*. London: Imperial College Press. ISBN: 978-1-84816-184-9.

Gore, M. et al. (2017). “A combined analytical-experimental investigation of friction in cylinder liner inserts under mixed and boundary regimes of lubrication”. *Lubrication Science* 29.5, pp. 293–316. eprint: https://onlinelibrary.wiley.com/doi/pdf/10.1002/ls.1369.

Grice, N, Sherrington, I, and Smith, E (1990). *A Capacitance Based System for High Resolution Measurement of Lubricant Film Thickness*. Conference Paper.

Hamilton, G and Moore, S (1974). “Measurement of the Oil Film Thickness between the Piston Rings and Liner of a Small Diesel Engine”. *Proceedings of the Institution of Mechanical Engineers* 188.20, pp. 253–261.

Havil, P (2008). “One Lube Oil For All”. *Marine Engineers Review* March, pp. 23–24.

Hoffman, Joe (1993). *Numerical Methods for Engineers and Scientists.* eng. McGraw. ISBN: 0071129626.

Hutchings, I.M. (1992). *Tribology: Friction and Wear of Engineering Materials*. Edward Arnold. ISBN: 0-340-56184-X.

Lansdown, A.R. (2004). *Lubrication and Lubricant Selection - A practical Guide*. 3rd ed. Tribology in Practice. Bury St. Edmunds: Professional Engineering Publishing.

Lauritsen, S, Dragsted, J, and Buchholz, B (2001). “Swirl Injection Lubrication - A New Technology to Obtain Low Cylinder Oil Consumption without Sacrificing Wear Rates”. *CIMAC Congress, Hamburg 2001*, pp. 921–931.

Leduc, M (2001). *Diesel Duck The Marine Diesel Engine*. URL: http://www.dieselduck.info/machine/01\%20prime\%20movers/diesel_engine/diesel_engine.01.htm (visited on 09/14/2017).

Leighton, M et al. (2017). “Combined lubricant–surface system perspective: Multi-scale numerical–experimental investigation”. *Proceedings of the Institution of Mechanical Engineers, Part J: Journal of Engineering Tribology* 231.7, pp. 910–924. eprint: https://doi.org/10.1177/1350650116683784.

Lewis, M.G. (1974). “Miniature Mutual-Inductive Proximity Transducer”. *Journal of Physics E-Scientific Instruments* 7.4, pp. 269–271. ISSN: 0022-3735.

Lincoln-Industrial (2002). *Product Data - SL-43 Injector*.

Lister-Petter (2011). *TR1 G Build Engine Datasheet*.

Ma, M-T, Sherrington, I, and Smith, E (1996). “Implementation of an Algorithm to Model the Starved Lubrication of a Piston-ring in Distorted Bores: Prediction of Oil-flow and Onset of Gas Blow-by”. *Proceedings of the Institution of Mechanical Engineers Part J-Journal of Engineering Tribology* 210, pp. 29–44.

Marklund, O. and Gustafsson, L. (2001). “Interferometry-based measurements of oil-film thickness”. *Proceedings of the Institution of Mechanical Engineers Part J-Journal of Engineering Tribology* 215.J3, pp. 243–259. ISSN: 1350-6501.

Mason, R (2009). *Copenhagen: Support for a Global Tax on Shipping and Aviation Grows*. Newspaper Article.

MathWorks (2018). *mldivide*. URL: https://uk.mathworks.com/help/matlab/ref/mldivide.html (visited on 11/12/2018).

Maung, Z (2007). “Swept Up by Environmental Currents”. *Ethical Corporation* June 2007, pp. 48–48.

Micro-Epsilon (2012). *Product Data - Capacitive Displacement Sensors*.

Mills, R, Vail, JR, and Dwyer-Joyce, R (2015). “Ultrasound for the non-invasive measurement of internal combustion engine piston ring oil films”. *Proceedings of the Institution of Mechanical Engineers, Part J: Journal of Engineering Tribology* 229.2, pp. 207–215.

Mills, Robin, Avan, Emin Yusuf, and Dwyer-Joyce, Rob (2014). “Ultrasonic mapping of lubricant film thickness along a piston skirt and its use to indicate piston secondary motions”. *5th World Tribology Congress, WTC 2013*. Vol. 3. Politecnico di Torino (DIMEAS), pp. 1877–1880.

Mills, RS (2014). “2D Mapping of Piston Skirt Lubricant Film Thickness Using Ultrasound”.

Mittler, R., Mierbach, A., and Richardson, D. (2009). “Understanding the Fundamentals of Piston Ring Axial Motion and Twist and the Effects on Blow-by”. *Proceedings of the 2009 Spring Technical Conference of the Asme Internal Combustion Engine Division*, pp. 721–735.

Moore, S (1993). “The Measurement of Piston Ring Oil Film Thickness in a Two-Stroke Marine Diesel Engine”. *20th International Congress on Combustion Engines*. CIMAC.

Moore, S (1998). “The Complexities of Piston Ring Lubrication in a Large Two-Stroke Marine Diesel Engine”. *Cimac Congress 1998, Copenhagen*, pp. 575–586.

Mortier, R.M., Fox, M.F., and Orszulik, S.T. (2010). *Chemistry and Technology of Lubricants*. 3rd ed. London: Springer.

Munro, R (1999). “Pistons, Rings and Liners”. *Diesel Engine Reference Book*. Ed. by B Challen and R Baranescu. 2nd Edition. Oxford: Butterworth-Heinemann. Chap. 14.

Penner, J.E. et al. (2000). *Aviation and the Global Atmosphere*. Report.

Pevzner, L.A. (1998a). “Aspects of marine low-speed, cross-head diesel engine lubrication”. *Lubrication Engineering* 54.6, pp. 16–21. ISSN: 0024-7154.

Pevzner, L.A. (1998b). “Cylinder lubrication and feed control in relation to low-speed, cross-head engine load and speed”. *Lubrication Engineering* 54.6, pp. 22–28. ISSN: 0024-7154.

Reiner, Marcus (1964). “The deborah number”. *Physics today* 17.1, p. 62.

Reynolds, Osborne (1886). “IV. On the theory of lubrication and its application to Mr. Beauchamp tower’s experiments, including an experimental determination of the viscosity of olive oil”.

Philosophical Transactions of the Royal Society of London 177, pp. 157–234. eprint: http://rstl.royalsocietypublishing.org/content/177/157.full.pdf+html.

Richardson, D. and Borman, G. (1991). *Using Fiber Optics and Laser Flourescence for Measuring Thin Oil Films with Application to Engines*. Conference Paper.

Ritch, E (2009). *Report: Shipping Sector Could Cut CO2 by 25% - At No Cost*. Web Page.

Sanda, S. et al. (1993). “Development of scanning laser-induced-flourescence method for analyzing piston oil film behaviour”. *Intstitution of Mechanical Engineers Conference Publications* 10.C465/014, pp. 155–164. ISSN: 0144-0799.

Schenk, C, Hengeveld, J, and Aabo, K (2000). “The Role of Temperature and Pressure in Wear Processes in Low Speed Diesel Engines”. *6th Int. Symp. Marine Engineering (Tokyo, Japan)*, pp. 14–19.

Schinas, O. and Stefanakos, Ch.N. (2014). “Selecting technologies towards compliance with MARPOL Annex VI: The perspective of operators”. *Transportation Research Part D: Transport and Environment* 28, pp. 28 –40. ISSN: 1361-9209.

Schirru, M. et al. (2015). “Viscosity Measurement in a Lubricant Film Using an Ultrasonically Resonating Matching Layer”. *Tribology Letters* 60.3, p. 42. ISSN: 1573-2711.

Schirru, M. M. et al. (2018). “In situ Measurement of Journal Bearing Lubricant Viscosity by Means of a Novel Ultrasonic Measurement Technique Using Matching Layer”. *Tribology Transactions* 61.1, pp. 157–167. eprint: https://doi.org/10.1080/10402004.2017.1285970.

Schirru, Michele M and Dwyer-Joyce, Rob S (2016). “A model for the reflection of shear ultrasonic waves at a thin liquid film and its application to viscometry in a journal bearing”. *Proceedings of the Institution of Mechanical Engineers, Part J: Journal of Engineering Tribology* 230.6, pp. 667–679. eprint: https://doi.org/10.1177/1350650115610357.

Schmid, H and Weisser, G (2005). “Marine Technologies for Reduced Emissions”. *2nd Annual Conference on Green Ship Technology, Amsterdam*. Wartsila.

Schrooten, L et al. (2009). “Emissions of maritime transport: A European reference system”. *Science of the Total Environment* 408.2, pp. 318–323. ISSN: 0048-9697.

Sherrington, I (2000). *Lubrication Control System*. Patent.

Skeie, R.B. et al. (2009). “Global temperature change from the transport sectors - Historical development and future scenarios”. *Atmospheric Environment* 43.39, pp. 6260 –6270. ISSN: 1352-2310.

Smith, H (1986). “Marine Lubrication Demands in the Nineties”. *Proc.of Shipping Economics in the Nineties*, pp. 63–69.

Stachowiak, G and Batchelor, A (2005). *Engineering Tribology*. Oxford: Elsevier Butterworth-Heinemann.

Stark, M.S. et al. (2005). “Measurement of lubricant flow in a gasoline engine”. *Tribology Letters* 19.3, pp. 163–168. ISSN: 1573-2711.

Tian, T. (2002a). “Dynamic behaviours of piston rings and their practical impact. Part 1: ring flutter and ring collapse and their effects on gas flow and oil transport”. *Proceedings of the Institution of Mechanical Engineers Part J-Journal of Engineering Tribology* 216.J4, pp. 209–227. ISSN: 1350-6501.

Tian, T. (2002b). “Dynamic behaviours of piston rings and their practical impact. Part 2: oil transport, friction and wear of ring/liner interface and the effects of piston and ring dynamics”. *Proceedings of the Institution of Mechanical Engineers Part J-Journal of Engineering Tribology* 216.J4, pp. 229–247. ISSN: 1350-6501.

Weimar, H-J. and Spicher, U. (2003). “Crank-Angle Resolved Oil Film Thickness Measurement Between Piston Ring and Cylinder Linder in a Spark Ignition Engine”. *ASME Internal Combustion Engine Division Spring Technical Conference*. ASME, pp. 349–359.

Welsh, M (2002). *Considerations for Using Low-Sulphur Fuel*. Web Page.

Woodyard, D (2004). *Pounder's Marine Diesel Engines*. 8th Edition. Oxford: Elsevier Butterworth-Heinemann.

Zetterdahl, Maria et al. (2016). “Impact of the 0.1% fuel sulfur content limit in SECA on particle and gaseous emissions from marine vessels”. *Atmospheric Environment* 145, pp. 338 –345. ISSN: 1352-2310.

Appendices

Appendix A

Finite Difference Expressions in Full

A.1 Finite difference expressions for conservation of mass: hydrodynamic pressure and degree of filling

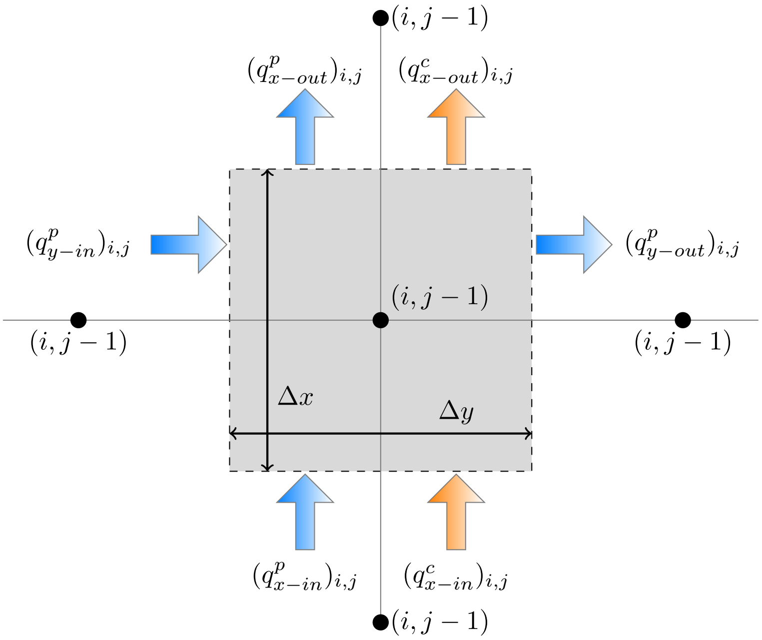

Figure A.1: Oil-film thickness parameters, where $b =$ ring-face height, $h =$ distance from cylinder liner to ring-face, $h_0 =$ minimum oil-film thickness, $q =$ lubricant flow-rate, $R =$ ring-face radius, $U =$ piston-ring speed.

Given that conservation of mass states

$$\boxed{\begin{array}{c}\text{Rate of change}\\ \text{of mass in a cell}\end{array}} + \boxed{\begin{array}{c}\text{Mass flux out}\\ \text{of a cell}\end{array}} = \boxed{\begin{array}{c}\text{Mass flux into}\\ \text{of a cell}\end{array}}$$

$$\rho\Delta x\Delta y\left.\frac{\partial\theta h}{\partial t}\right|_{i,j}+\rho\left(q^{c}_{x,out}\right)_{i,j}+\rho\left(q^{p}_{x,out}\right)_{i,j}+\rho\left(q^{p}_{y,out}\right)_{i,j}=\rho\left(q^{c}_{x,in}\right)_{i,j}+\rho\left(q^{p}_{x,in}\right)_{i,j}+\rho\left(q^{p}_{y,in}\right)_{i,j} \tag{A.1}$$

The expressions for the above terms, ie. for rate of change of mass in a cell;

$$\rho\Delta x\Delta y\left.\frac{\partial\theta h}{\partial t}\right|_{i,j}=\rho\Delta x\Delta y\left\{\left(\theta_{i,j}\frac{h_{i,j}-h^{n-1}_{i,j}}{\Delta t}\right)+h_{i,j}\left(\frac{\theta_{i,j}-\theta^{n-1}_{i,j}}{\Delta t}\right)\right\}$$

Mass flux in for both Couette and Poiseuille flow;

$$\begin{aligned}
\left(q^{c}_{x,in}\right)_{i,j}&=\rho\Delta y\frac{U}{2}\left\{\theta_{i-1,j}h_{i-1,j}\left(1-g_{i-1,j}\right)+g_{i-1,j}h_{i-1,j}+g_{i-1,j}g_{i,j}\left(\frac{h_{i,j}-hi-1,j}{2}\right)\right\}\\
\left(q^{p}_{x,in}\right)_{i,j}&=-\rho\Delta y\frac{1}{12\eta}\left(\frac{h_{i-1,j}+h_{i,j}}{2}\right)^{3}\frac{\left(g_{i,j}p_{i,j}-g_{i-1,j}p_{i-1,j}\right)-\left(g_{i,j}-g_{i-1,j}\right)p_{b}}{\Delta x}\\
\left(q^{p}_{y,in}\right)_{i,j}&=-\rho\Delta x\frac{1}{12\eta}\left(\frac{h_{i,j-1}+h_{i,j}}{2}\right)^{3}\frac{\left(g_{i,j}p_{i,j}-g_{i,j-1}p_{i,j-1}\right)-\left(g_{i,j}-g_{i,j-1}\right)p_{b}}{\Delta y}
\end{aligned}$$

And likewise the mass flow out;

$$\begin{aligned}
\left(q^{c}_{x,out}\right)_{i,j}&=\rho\Delta y\frac{U}{2}\left\{\theta_{i,j}h_{i,j}\left(1-g_{i,j}\right)+g_{i,j}h_{i,j}+g_{i,j}g_{i+1,j}\left(\frac{h_{i+1,j}-hi,j}{2}\right)\right\}\\
\left(q^{p}_{x,out}\right)_{i,j}&=-\rho\Delta y\frac{1}{12\eta}\left(\frac{h_{i,j}+h_{i+1,j}}{2}\right)^{3}\frac{\left(g_{i+1,j}p_{i+1,j}-g_{i,j}p_{i,j}\right)-\left(g_{i+1,j}-g_{i,j}\right)p_{b}}{\Delta x}\\
\left(q^{p}_{y,out}\right)_{i,j}&=-\rho\Delta x\frac{1}{12\eta}\left(\frac{h_{i,j}+h_{i,j+1}}{2}\right)^{3}\frac{\left(g_{i,j+1}p_{i,j+1}-g_{i,j}p_{i,j}\right)-\left(g_{i,j+1}-g_{i,j}\right)p_{b}}{\Delta y}
\end{aligned}$$

Gathering all these terms into the expression of conservation of mass

$$\begin{aligned}
\rho\Delta x\Delta y&\left\{\left(\theta_{i,j}\frac{h_{i,j}-h^{n-1}_{i,j}}{\Delta t}\right)+h_{i,j}\left(\frac{\theta_{i,j}-\theta^{n-1}_{i,j}}{\Delta t}\right)\right\}=\\
&+\rho\Delta y\frac{U}{2}\left\{\theta_{i,j}h_{i,j}\left(1-g_{i,j}\right)+g_{i,j}h_{i,j}+g_{i,j}g_{i+1,j}\left(\frac{h_{i+1,j}-hi,j}{2}\right)\right\}\\
&-\rho\Delta y\frac{1}{12\eta}\left(\frac{h_{i,j}+h_{i+1,j}}{2}\right)^{3}\frac{\left(g_{i+1,j}p_{i+1,j}-g_{i,j}p_{i,j}\right)-\left(g_{i+1,j}-g_{i,j}\right)p_{b}}{\Delta x}\\
&-\rho\Delta x\frac{1}{12\eta}\left(\frac{h_{i,j}+h_{i,j+1}}{2}\right)^{3}\frac{\left(g_{i,j+1}p_{i,j+1}-g_{i,j}p_{i,j}\right)-\left(g_{i,j+1}-g_{i,j}\right)p_{b}}{\Delta y}\\
&-\rho\Delta y\frac{U}{2}\left\{\theta_{i-1,j}h_{i-1,j}\left(1-g_{i-1,j}\right)+g_{i-1,j}h_{i-1,j}+g_{i-1,j}g_{i,j}\left(\frac{h_{i,j}-hi-1,j}{2}\right)\right\}\\
&+\rho\Delta y\frac{1}{12\eta}\left(\frac{h_{i-1,j}+h_{i,j}}{2}\right)^{3}\frac{\left(g_{i,j}p_{i,j}-g_{i-1,j}p_{i-1,j}\right)-\left(g_{i,j}-g_{i-1,j}\right)p_{b}}{\Delta x}\\
&+\rho\Delta x\frac{1}{12\eta}\left(\frac{h_{i,j-1}+h_{i,j}}{2}\right)^{3}\frac{\left(g_{i,j}p_{i,j}-g_{i,j-1}p_{i,j-1}\right)-\left(g_{i,j}-g_{i,j-1}\right)p_{b}}{\Delta y}
\end{aligned}$$

Appendix B

Engineering Drawings

B.1 Transducer Grinding Clamp

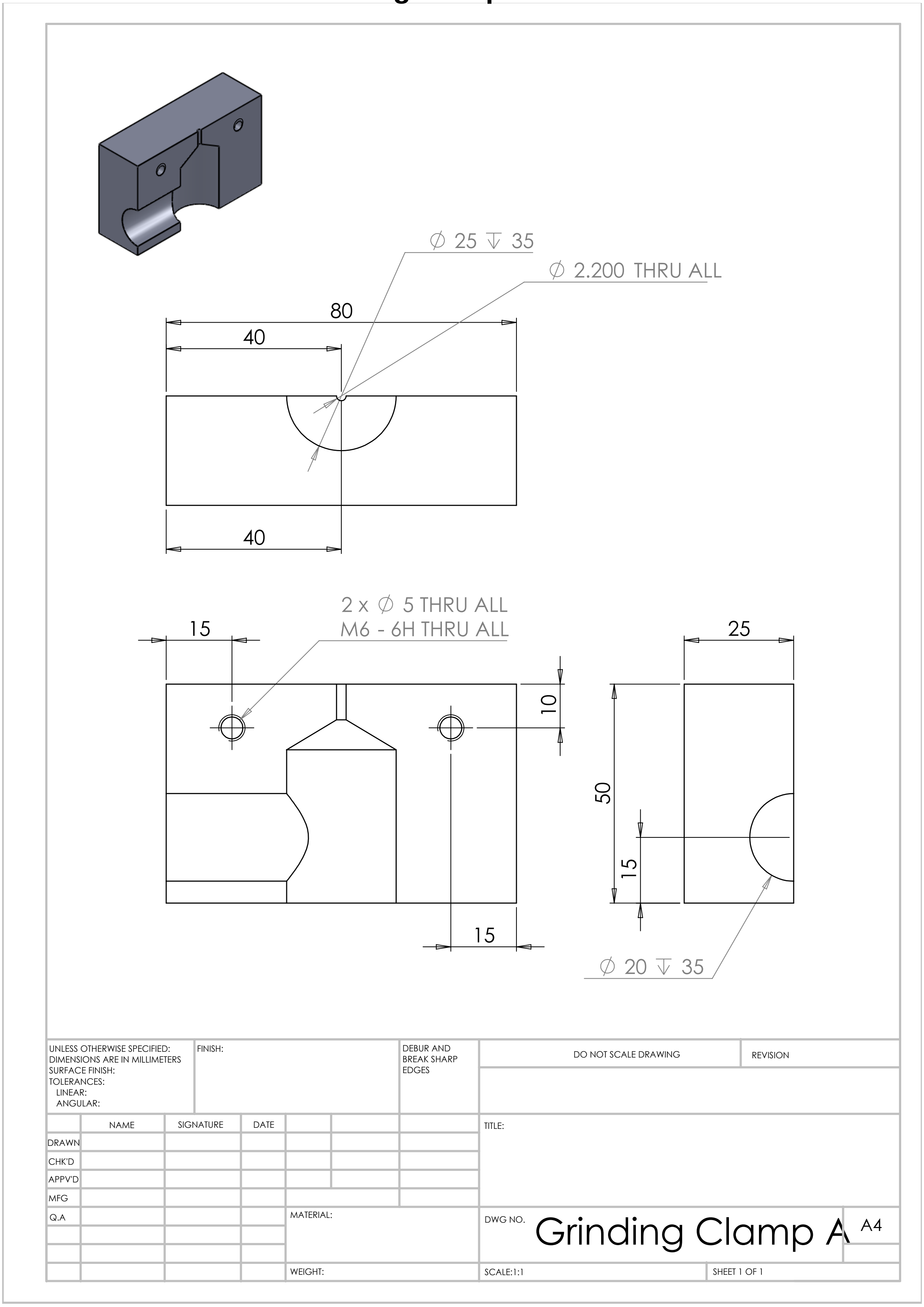

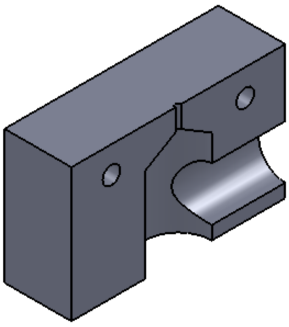

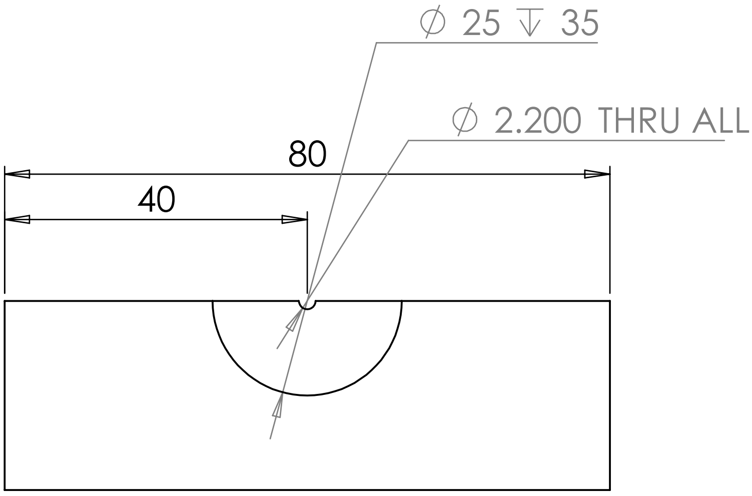

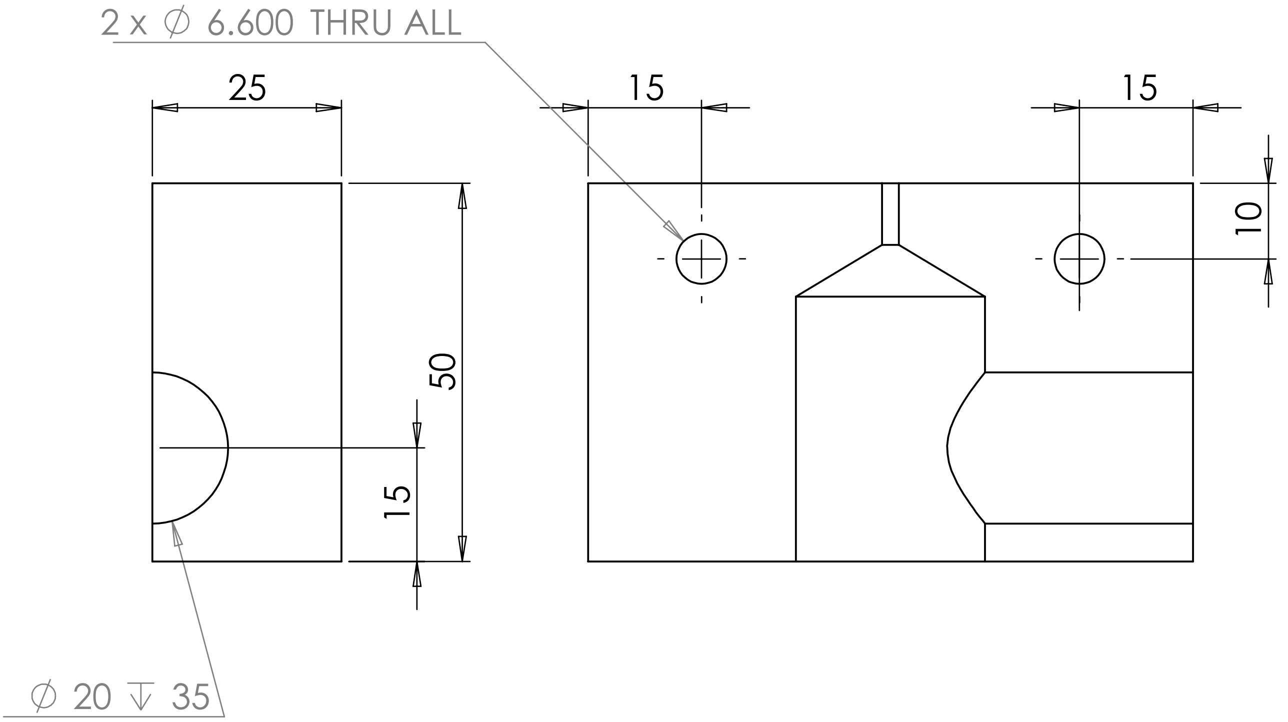

UNLESS OTHERWISE SPECIFIED: DIMENSIONS ARE IN MILLIMETERS SURFACE FINISH: TOLERANCES: LINEAR: ANGULAR:	FINISH:	DEBUR AND BREAK SHARP EDGES	DO NOT SCALE DRAWING

	NAME	SIGNATURE	DATE
DRAWN			
CHK'D			
APPV'D			
MFG			
Q.A			

REVISION

TITLE:

MATERIAL:

WEIGHT:

DWG NO. Grinding Clamp B

A4

SCALE:1:1

SHEET 1 OF 1

B.2 Drilling of Holes for Transducers

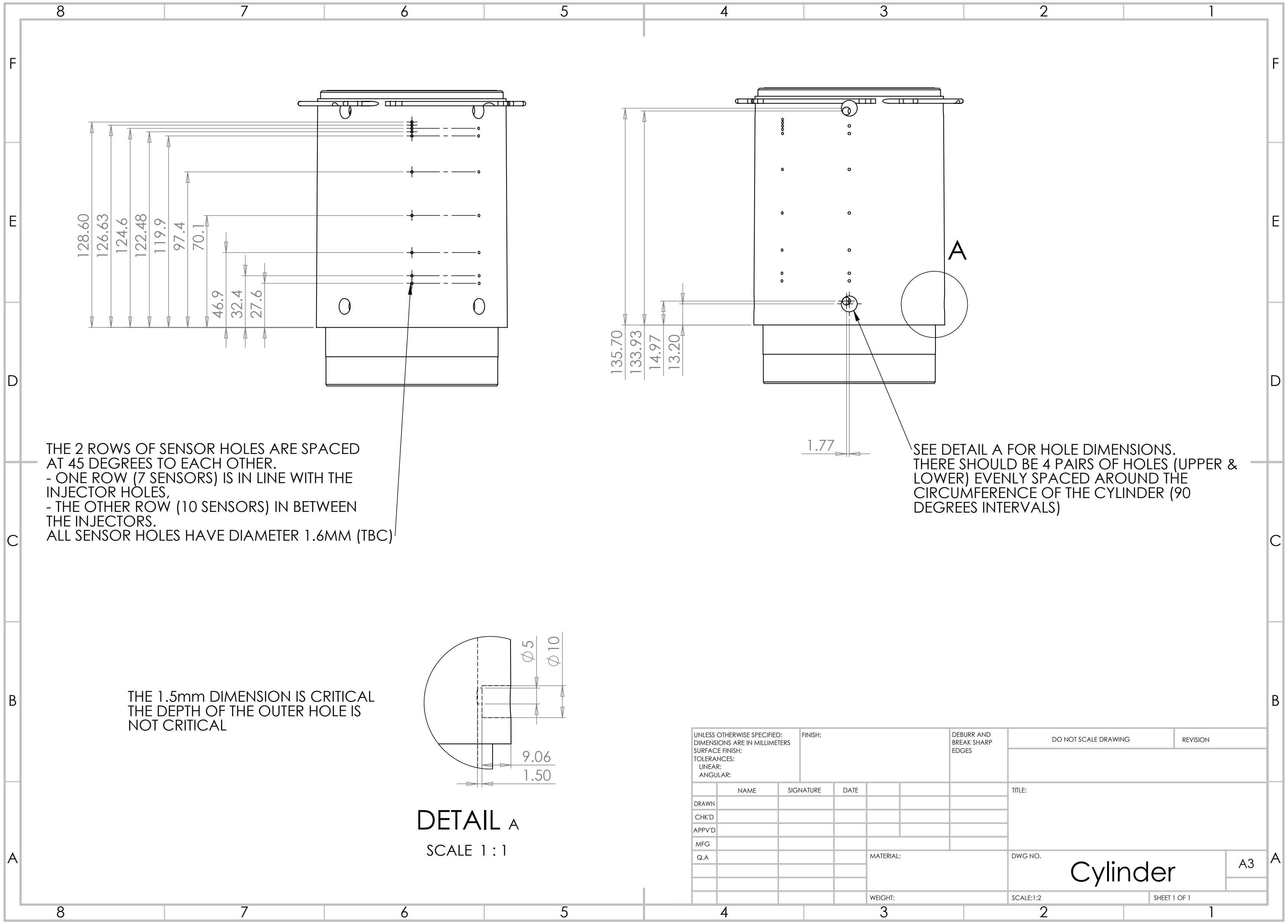

THE 2 ROWS OF SENSOR HOLES ARE SPACED AT 45 DEGREES TO EACH OTHER.
- ONE ROW (7 SENSORS) IS IN LINE WITH THE INJECTOR HOLES,
- THE OTHER ROW (10 SENSORS) IN BETWEEN THE INJECTORS.
ALL SENSOR HOLES HAVE DIAMETER 1.6MM (TBC)

SEE DETAIL A FOR HOLE DIMENSIONS. THERE SHOULD BE 4 PAIRS OF HOLES (UPPER & LOWER) EVENLY SPACED AROUND THE CIRCUMFERENCE OF THE CYLINDER (90 DEGREES INTERVALS)

THE 1.5mm DIMENSION IS CRITICAL
THE DEPTH OF THE OUTER HOLE IS NOT CRITICAL

DETAIL A
SCALE 1 : 1

B.3 Hall Effect Trigger Bracket

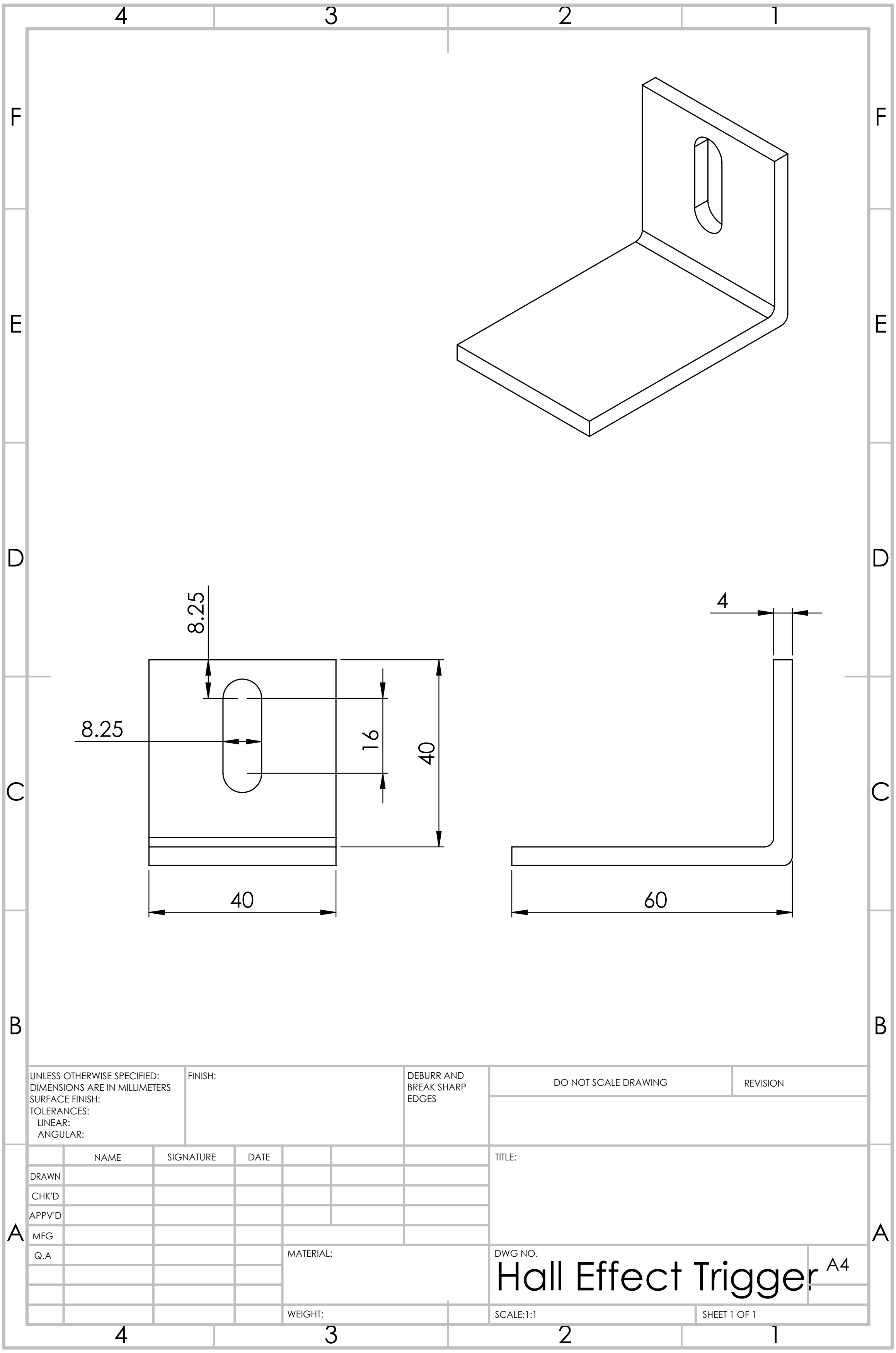

Appendix C

Specification Sheets

C.1 Signal Amplifier Datasheet

FYLDE
MODULAR
INSTRUMENTATION

FE-420-CD capacitive displacement amplifier and oscillator

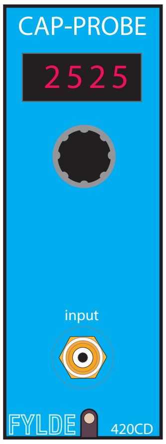

- MODULAR ASSEMBLY COMPRISING :-
- INTERNAL HI STABILITY OSCILLATOR
- DIGITAL DISPLAY OF DISTANCE
- INTERNAL SCALING & LINEARISATION
- SYSTEMS FROM 1 TO 16 CHANNELS
- MINIATURE 2U COMPACT SYSTEM
- MAINS OR DC POWER
- 10V OUTPUT
- WIDE BAND STABLE MEASUREMENTS
- DESIGNED AND PRODUCED IN THE UK

The measurement of displacement using capacitive displacement transducers is an established principle based on the variation of capacity between a transducer probe and an electrically conductive and grounded surface.

The principle of measurement demands the application of a highly stable high frequency oscillator, together with a special high impedance amplifier which detects the spacing between the probe and the movable target area.

In the FYLDE system a very precise & stable sinewave oscillator energises the probe via a low noise screened cable. Amplification of the resulting signal is developed in the amplifier module which comprises:-

a. A high impedance input stage
b. A precision rectifier
c. 3 pole active filter
d. Automatic scaling stage.

Linearity in the measurement depends on the transducer design and the distance to be measured, but amplifier performance involving bandwidth, linearity and stability are important factors in maintaining a measurement standard. Internal scaling and linearisation are available to allow for a more precise display of distance

The integral mains power supply provides isolation of signal earths. The isolation may be maintained when operating from a d.c. battery supply, using a Fylde FE-605-DCC. converter in place of the mains transformer.

FYLDE Electronic Laboratories Ltd., 49/51 Fylde Road Preston PR1 2XQ, UK Phone +44 1772 257560 http://www.fylde.com

Output voltage from the amplifier is in the range 0 to 10 volts. The output is inversely proportional to capacitance and therefore proportional to distance between the probe and the grounded surface to be measured. Scaling of probe outputs is a simple menu selection which sets the zero distance and full scale or mid scale distance.

The module is suitable for measuring both dynamic and static distance to an electrically earthed target. Fylde can supply suitable probes and typical measuring distance can extend from zero to approximately 3 mm. (We recommend that probe to target distance is limited to the probe's innerdiameter.) Cable lengths can extend to 3 meters (2m is the recommended cable length.)

Presentation of the the equipment is in modular form. Fylde supply instrument enclosures to accept 2,4,8,or 16 modules.

A Microdot coaxial connector on the front panel connects to the capacitance probe. A menu based system is provided that allows scaling of the analog output as well as inputing data so that the digital display may provide a linear readout of distance.

User interface is via a front panel rotary control with an integrated push button, or by remote RS232C control.

All analog outputs are on the rear panels of instrument cases.

Modules in the system are compatible with other standard modules in the Fylde miniature signal conditioning system and may be mains (230V or 115V) energised. Alternatively, 12V DC power may be obtained on request.

Oscillator frequency	16kHz (built in).
Capacitance Range	0.03pF to 3pF typical.
Rectifier	Full wave precision.
Filter type	3 pole Butterworth programmed by plug in resistor network.
Max Cut off frequency	8 kHz.
Rise time	300μs (1kHz cut off freq.)
	50μs (8 kHz cut off freq.)
Output	0 to +10V at 5 mA.
Scale	Automatic by settingZero and Mid or Full scale distance.
Gain stability	< 0.1% per °C.
Input connector	micro-dot.
Cable length	2 metres recommended.
Power requirement	Mains 240V 50Hz or 110 60Hz or 12V DC when using FE-605-DCC.
Front Panel Control	Rotary Control with Push Button
Digital readout	4 digit display of Distance, calibrated using a10pt calibration table.
	Menu system allows calibration of Analog Output and Front Panel Digital Display
Serial output	Optional RS232 digital output.

C.2 Epoxy Resin Datasheet

Permabond®
Engineering Adhesives

PERMABOND® ET538
Two-Part Epoxy
Technical Datasheet

Features & Benefits

- Adhesion to a wide variety of substrates
- Full cure at room temperature
- Easy to apply
- High shear and peel strength
- Good impact strength
- Good chemical resistance
- Non-drip rheology

Description

PERMABOND® ET538 is a structural, room temperature curing epoxy adhesive that has excellent adhesion to a wide variety of surfaces such as wood, metal, ceramics and many plastic and composite materials. It exhibits good resistance to petrol, oils and water and has an extended cure time making it suitable for larger applications and batch production processes. Its thixotropic "non-slump" nature makes it suitable for gap filling or vertical application.

Physical Properties of Uncured Adhesive

	ET538A	**ET538B**
Chemical composition	Epoxy Resin	Polyamine Hardener
Appearance	White	Dark grey
Viscosity @ 25°C	20rpm: 50,000-100,000 mPa.s *(cP)* 2.5rpm: 150,000-300,000 mPa.s *(cP)*	20rpm: 20,000-40,000 mPa.s *(cP)* 2rpm: 30,000-90,000 mPa.s *(cP)*
Specific gravity	1.1	1.4

Typical Curing Properties

Mix ratio	1:1 by volume 100:130 by weight
Maximum gap fill	5 mm *0.2 in*
Usable / pot life @23°C	120-150 mins
Handling time @23°C	3-5 hours
Working strength @23°C	24 hours
Full cure @23°C	72 hours

Typical Performance of Cured Adhesive

Shear strength* (ISO4587)	Steel: 18-20 N/mm^2 *(2600 - 2900 psi)* Zinc: 17-20 N/mm^2 *(2500 - 2900 psi)*
Peel strength (aluminium) (ISO4578)	60-80 N/25mm *(13-18 PIW)*
Hardness (ISO868)	70-80 Shore D
Elongation at break (ISO37)	4-8%
Glass transition temperature Tg	45-55°C *(113-131°F)*
Dielectric strength	15-25 kV/ mm
Thermal conductivity	0.55 W/(m.K)

**Strength results will vary depending on the level of surface preparation and gap.*

Strength Development

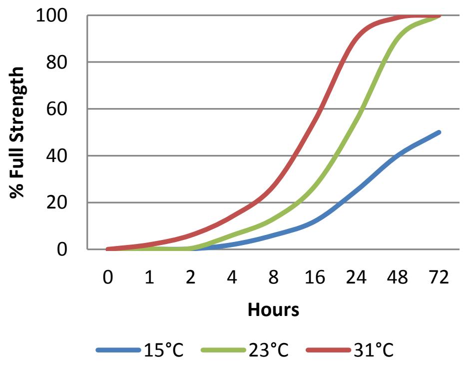

Graph shows typical strength development of bonded components. An increase of 8°C in temperature will halve the cure time. Lower temperatures will result in a slower cure time.

Hot Strength

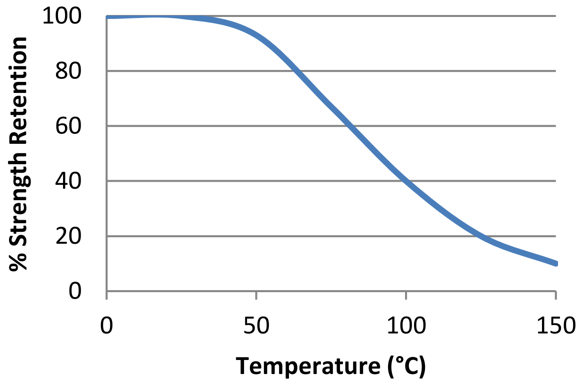

"Hot strength" shear strength tests performed on mild steel. Fully cured specimens conditioned to pull temperature for 30 minutes before testing at temperature.

ET538 can withstand higher temperatures for brief periods (such as for paint baking and wave soldering processes) providing the joint is not unduly stressed. The minimum temperature the cured adhesive can be exposed to is -40°C (-40°F) depending on the materials being bonded.

Additional Information

This product is not recommended for use in contact with strong oxidizing materials.
Information regarding the safe handling of this material may be obtained from the safety data sheet.

Users are reminded that all materials, whether innocuous or not, should be handled in accordance with the principles of good industrial hygiene.

This Technical Datasheet (TDS) offers guideline information and does not constitute a specification.

Storage & Handling

Storage Temperature	5 to 25°C ***(41 to 77°F)***

Surface Preparation

Surfaces should be clean, dry and grease-free before applying the adhesive. Use a suitable solvent (such as acetone or isopropanol) for the degreasing of surfaces. Some metals such as aluminium, copper and its alloys will benefit from light abrasion with emery cloth (or similar), to remove the oxide layer.

Directions for Use

1. Dual cartridges:
   a) Insert the cartridge into the application gun and guide the plunger into the cartridge.
   b) Remove the cartridge cap and dispense material until both sides are flowing.
   c) Attach the static mixer to the end of the cartridge and begin dispensing the material.
2. Apply material to one of the substrates.
3. Join the parts. Parts must be joined within 120-150 minutes of mixing the two epoxy components.
4. Large quantities and/or higher temperature will decrease the usable life or pot life.
5. Apply pressure to the assembly by clamping for 5 hours or until handling strength is obtained.
6. Full cure will be obtained after 72 hours at 25°C (77°F). Heat can be used to accelerate the curing process.

Video Links

Surface preparation:
https://youtu.be/8CMOMP7hXjU

Two-part epoxy directions for use:
https://youtu.be/GRX1RyknYqc

www.permabond.com
• UK: 0800 975 9800
• General Enquiries: +44 (0)1962 711661
• US: 732-868-1372
• Asia: + 86 21 5773 4913
info.europe@permabond.com
info.americas@permabond.com
info.asia@permabond.com

C.3 Formlabs Grey Datasheet

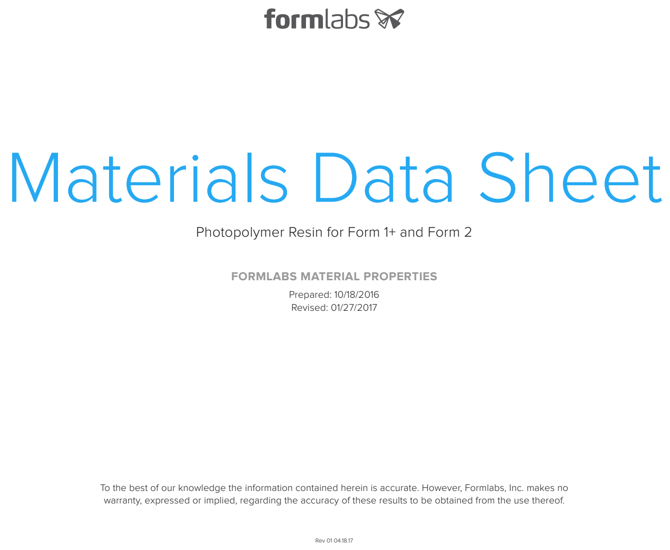

formlabs

Materials Data Sheet

Photopolymer Resin for Form 1+ and Form 2

FORMLABS MATERIAL PROPERTIES

Prepared: 10/18/2016
Revised: 01/27/2017

Rev 01 04.18.17

CLEAR FLGPCL03[1]

	METRIC[2]		IMPERIAL[2]		METHOD
	Green[3]	Postcured[4]	Green[3]	Postcured[4]	
Mechanical Properties					
Ultimate Tensile Strength	38 MPa	65 MPa	5510 psi	9380 psi	ASTM D 638-10
Young's Modulus	1.6 GPa	2.8 GPa	234 ksi	402 ksi	ASTM D 638-10
Elongation at Failure	12 %	6.2 %	12 %	6.2 %	ASTM D 638-10
Flexural Modulus	1.25 GPa	2.2 GPa	181 ksi	320 ksi	ASTM C 790-10
Notched IZOD	16 J/m	25 J/m	0.3 ft-lbf/in	0.46 ft-lbf/in	ASTM D 256-10
Thermal Properties					
Heat deflection temp. @ 264 psi	42.7 °C	58.4 °C	108.9 °F	137.1 °F	ASTM D 648-07
Heat deflection temp. @ 66 psi	49.7 °C	73.1 °C	121.5 °F	163.6 °F	ASTM D 648-07

NOTES:

[1] Clear material properties are representative of all Standard Resins: Clear, White, Black and Grey.

[2] Material properties can vary with part geometry, print orientation, print settings and temperature.

[3] Data was obtained from green parts, printed using Form 2, 100 µm, Clear settings, without additional treatments.

[4] Data was obtained from parts printed using Form 2, 100 µm, Clear settings and post-cured with 1.25 mW/cm^2 of 405 nm LED light at 60 °C for 60 minutes.

HIGH TEMP FLHTAM01

	METRIC[1]		IMPERIAL[1]		METHOD
	Green[2]	Post-Cured[3]	Green[2]	Post-Cured[3]	
Mechanical Properties					
Ultimate Tensile Strength	33 MPa	51.1 MPa	4790 psi	7410 psi	ASTM D 638-14
Young's Modulus	1.5 GPa	3.6 Gpa	222 ksi	525 ksi	ASTM D 638-14
Elongation at Break	9 %	2 %	9 %	2 %	ASTM D 638-14
Flexural Strength at Break	41.2 MPa	106.9 MPa	5980 psi	15500 psi	ASTM D 790-15
Flexural Modulus	1.1 GPa	3.3 GPa	158 ksi	478 ksi	ASTM D 790-15
Notched IZOD	12.3 J/m	14 J/m	0.23 ft-lbf/in	0.26 ft-lbf/in	ASTM D 256-10
Water Absorption	N/A	0.21 %	N/A	0.21 %	ASTM D 570-98
Thermal Properties					
Heat Deflection Temp. @ 1.8 MPa	42.3 °C	130 °C	108.1 °F	266 °F	ASTM D 648-16
Heat Deflection Temp. @ 0.45 MPa	55.9 °C	289 °C	132.6 °F	552.2 °F	ASTM D 648-16
Thermal Expansion (0 – 150 °C)	120.9 µm/m/°C	87.5 µm/m/°C	67.2 µin/in/°F	48.6 µin/in/°F	ASTM E 831-13

NOTES:

[1] Material properties can vary with part geometry, print orientation, print settings and temperature.

[2] Data was obtained from green parts, printed using Form 2, 100 µm, High Temp settings, without additional treatments.

[3] Data was obtained from parts printed using Form 2, 100 µm, High Temp settings and post-cured with 80.5 mW/cm^2 of 365 nm fluorescent light for 60 minutes.

TOUGH FLTOTL03

	METRIC[1]		IMPERIAL[1]		METHOD
	Green[2]	Post-Cured[3]	Green[2]	Post-Cured[3]	
Mechanical Properties					
Ultimate Tensile Strength	34.7 MPa	55.7 MPa	5040 psi	8080 psi	ASTM D 638-14
Young's Modulus	1.7 GPa	2.7 GPa	239 ksi	387 ksi	ASTM D 638-14
Elongation at Break	42 %	24 %	42 %	24 %	ASTM D 638-14
Flexural Strength at 5% Strain	20.8 MPa	60.6 MPa	3020 psi	8790 psi	ASTM D 790-15
Flexural Modulus	0.6 GPa	1.6 GPa	90.3 ksi	241 ksi	ASTM D 790-15
Notched IZOD	32.6 J/m	38 J/m	0.61 ft-lbf/in	0.71 ft-lbf/in	ASTM D 256-10
Thermal Properties					
Heat Deflection Temp. @ 1.8 MPa	32.8 °C	45.9 °C	91.1 °F	114.6 °F	ASTM D 648-16
Heat Deflection Temp. @ 0.45 MPa	40.4 °C	48.5 °C	104.7 °F	119.3 °F	ASTM D 648-16
Thermal Expansion (23 – 50 °C)	159.7 µm/m/°C	119.4 µm/m/°C	88.7 µm/m/°F	66.3 µm/m/°F	ASTM E 831-13

NOTES:

[1] Material properties can vary with part geometry, print orientation, print settings, and temperature.

[2] Data was obtained from green parts, printed using Form 2, 100 µm, Tough settings, without additional treatments.

[3] Data was obtained from parts printed using Form 2, 100 µm, Tough settings and post-cured with 2.5 mW/cm^2 of 405 nm LED light for 120 minutes at 60°C.

DURABLE FLDUCL01

	METRIC[1]		IMPERIAL[1]		METHOD
	Green[2]	Post-Cured[3]	Green[2]	Post-Cured[3]	
Tensile Properties					
Ultimate Tensile Strength	18.6 MPa	31.8 MPa	2.7 ksi	4.61 ksi	ASTM D 638-10
Tensile Modulus	0.45 GPa	1.26 GPa	65.7 ksi	183 ksi	ASTM D 638-10
Elongation	67 %	49 %	67 %	49 %	ASTM D 638-10
Flexural Properties					
Flexural Stress at 5% Strain	4.06 MPa	27.2 MPa	0.59 ksi	3.95 ksi	ASTM D 790-10, Procedure A
Flexural Modulus	0.16 GPa	0.82 GPa	23.4 ksi	119 ksi	ASTM D 790-10, Procedure A
Impact Properties					
IZOD Impact Strength	130.8 J/m	109 J/m	2.46 ft-lbf/in	2.05 ft-lbf/in	ASTM D 256-10, Test Method A
Temperature Properties					
Heat Deflection Temp. @ 0.45 MPa	< 30 °C	43.3 °C	< 86 °F	110 °F	ASTM D 648-07, Method B
Thermal Expansion from 23 to 50°C	117.0 µm/m/°C	145.1 µm/m/°C	65.0 µin/in/°F	80.6 µin/in/°F	ASTM E831-14

NOTES:

[1] Material properties can vary with part geometry, print orientation, print settings, and temperature.

[2] Data was obtained from green parts, printed using Form 2, 100 µm, Durable settings, without additional treatments.

[3] Data was obtained from parts printed using Form 2, 100 µm, Durable settings and post-cured with 2.5 mW/cm^2 of 405 nm LED light for 120 minutes at 60°C.

FLEXIBLE FLFLGR02

	METRIC[1]		IMPERIAL[1]		METHOD
	Green	Postcured[2]	Green	Postcured[2]	
Mechanical Properties					
Ultimate Tensile Strength[3]	3.3 – 3.4 MPa	7.7 – 8.5 MPa	483 – 494 psi	1110 – 1230 psi	ASTM D 412-06 (A)
Elongation at Failure[3]	60 %	75 – 85 %	60 %	75 – 85 %	ASTM D 412-06 (A)
Compression Set[4]	0.40 %	0.40 %	0.40 %	0.40 %	ASTM D 395-03 (B)
Tear Strength[5]	9.5 – 9.6 kN/m	13.3 – 14.1 kN/m	54 – 55 lbf/in	76 – 80 lbf/in	ASTM D 624-00
Shore Hardness	70 – 75 A	80 – 85 A	70 – 75 A	80 – 85 A	ASTM 2240
Thermal Properties					
Vicat Softening Point[6]	231 °C	230 °C	448 °F	446 °F	ASTM D 1525-09

NOTES:

[1] Material properties can vary with part geometry, print orientation, print settings and temperature.

[2] Data was obtained from parts printed using Form 2, 100 µm, Flexible settings and post-cured with 80.5 mW/cm^2 of 365 nm fluorescent light for 60 minutes.

[3] Tensile testing was performed after 3+ hours at 23 °C, using a Die C dumbbell and 20 in/min cross head speed.

[4] Compression testing was performed at 23 °C after aging at 23 °C for 22 hours.

[5] Tear testing was performed after 3+ hours at 23 °C, using a Die C tear specimen and a 20 in/min cross head speed.

[6] Thermal testing was performed after 40+ hours with a 10 N loading at 50 °C/hour. Cracks formed in samples during testing.

CASTABLE FLCABL02

	METRIC	IMPERIAL	METHOD
Mechanical Properties[1]			
Ultimate Tensile Strength	11.6 MPa	1680 psi	ASTM D 638-10
Young's Modulus	220 MPa	32 ksi	ASTM D 638-10
Elongation at Failure	13 %	13 %	ASTM D 638-10

NOTES:

[1] Data was obtained from parts printed using Form 2, Castable 50 µm Fine Detail settings and post-cured with 2.5 mW/cm^2 of fluorescent bulb UV light, centered at 405 nm

DENTAL SG FLDGOR01

	METRIC	METHOD
	Postcured	
Flexural Properties		
Flexural Strength	≥ 50 MPa	ISO 20795-1:2013
Flexural Modulus	≥ 1500 Mpa	ISO 20795-1:2013
Hardness Properties		
Hardness Shore D	≥ 80D	per ISO 868:2003
Impact Properties		
Charpy Impact Strength Unnotched	12 – 14 kg/m^2	ISO 179:2010

Dental SG is tested at NAMSA, Chasse sur Rhône in France, and is certified biocompatible per EN-ISO 10993-1:2009/AC:2010:

- Non-mutagenic.
- Non-cytotoxic.
- Not induce any erythema or edema reactions.
- Not a sensitizer.
- Not cause systemic toxicity.

The product is in compliance with ISO Standards:

- EN-ISO 20795-1:2013 (Dentistry – Base Polymers – Part 1: Denture Base Polymers)
- EN-ISO 7405:2009/A1:2013 (Dentistry – Evaluation of biocompatibility of medical devices used in dentistry)
- EN-ISO 10993-1:2009/AC:2010 (Biological evaluation of medical devices – Part 1 – Evaluation and testing)

NOTES:

[1] Material properties can vary with part geometry, print orientation, print settings and temperature.

[2] Data refers to post-cured properties obtained after exposing green parts to 108 watts each of Blue UV-A (315 – 400 nm) and UV-Blue (400 – 550 nm) light, in a heated environment at 60 °C (140 °F), with six (6) 18W/71 lamps (Dulux L Blue) and six (6) 18W/78 lamps (Dulux blue UV-A).

SOLVENT COMPATIBILITY

Percent weight gain over 24 hours for a printed and post-cured 1 x 1 x 1 cm cube immersed in respective solvent:

	24 HR WEIGHT GAIN (%)				
Mechanical Properties	CLEAR	HIGH TEMP	TOUGH	DURABLE	FLEXIBLE
Acetic Acid, 5 %	< 1	< 1	2.8	1.3	1.3
Acetone	sample cracked	< 1	sample cracked	sample cracked	33
Isopropyl Alcohol	< 1	< 1	2.1	5.1	9.8
Bleach, ~5 % NaOCl	< 1	< 1	1.7	< 1	1.1
Butyl Acetate	< 1	< 1	1.6	7.9	16
Diesel	< 1	< 1	< 1	< 1	not tested
Diethyl glycol monomethyl ether	1.7	< 1	6.6	7.8	30
Hydrolic Oil	< 1	< 1	< 1	< 1	not tested
Skydrol 5	1	not tested	1.2	1.3	not tested
Hydrogen Peroxide (3 %)	< 1	< 1	2.1	1	1.3
Isooctane	< 1	< 1	< 1	< 1	< 1
Mineral Oil, light	< 1	< 1	< 1	< 1	not tested
Mineral Oil, heavy	< 1	< 1	< 1	< 1	not tested
Salt Water (3.5 % NaCl)	< 1	< 1	1.5	< 1	< 1
Sodium hydroxide (0.025 %, pH = 10)	< 1	< 1	1.5	< 1	1
Water	< 1	not tested	1.6	< 1	not tested
Xylene	< 1	not tested	< 1	6.5	29
Strong Acid (HCl Conc)	distorted	not tested	distorted	distorted	not tested